AUTOMATED CONTROL OF LASER SYSTEMS FOR MICROMACHINING

Shadi Karazi

(BEng)

A thesis submitted for the degree of

Doctor of Philosophy

Supervisor

Dr Dermot Brabazon

School of Mechanical and Manufacturing Engineering

Dublin City University

January, 2013

Declaration

I hereby certify that this material, which I now submit for assessment on the programme of study leading to the award of Ph.D. is entirely my own work, that I have exercised reasonable care to ensure that the work is original, and does not to the best of my knowledge breach any law of copyright, and has not been taken from the work of others save and to the extent that such work has been cited and acknowledged within the text of my work.

Signed: ……………………....………

ID No.: 56122942

Date: January 2013

List of Papers

This thesis describes original work that has not previously been submitted for a degree in Dublin City University or at any other University. The investigations were carried out in the School of Mechanical and Manufacturing Engineering, Dublin City University under the supervision of Dr Dermot Brabazon. This work has been disseminated through the following publications.

Journal Papers:

Karazi S.M., Issa A., Brabazon D., Comparison of ANN and DoE for the prediction of laser-machined micro-channel dimensions, Optics and Lasers in Engineering, Volume 47, Issue 9, September 2009, Pages 956-964, ISSN 0143-8166, DOI:10.1016/j.optlaseng.2009.04.009.

Karazi S.M., Brabazon D., Analysis and prediction of dimensions and cost of laser micromachining internal channel fabrication process, European Physical Journal, Volume 6, July 2010, 25002, pp.1-8, ISBN:978-2-7598-0565-5, DOI:10.1051/epjconf/20100625002.

Karazi S.M., Brabazon D., Determination of laser processing parameters using response surface and neural network models for micro-channel production in polycarbonate. This paper has been submitted to "Optics and Laser Technology Journal - Elsevier" and it is under review.

International Peer Reviewed Conference Papers:

Karazi S.M., Ben Azouz A., Brabazon D., Dimensions and cost prediction modelling of Nd:YVO$_4$ laser internal micro-channel fabrication in PMMA, Nano Science and Technology Institute NSTI-Nanotech 2010 Conference and Expo, Anaheim, California, U.S.A, June 2010, Vol. 2, Pages 492-495, ISBN 978-1-4398-3402-2, 2010.

Ben Azouz A., **Karazi S.M.**, Brabazon D., M. Vazquez, M. Macka and B. Paull, Effect of laser processing parameters and glass type on topology of micro-channels, Nano Science and Technology Institute NSTI-Nanotech 2010 Conference and Expo, Anaheim, California, U.S.A, June 2010, Vol. 2, Pages 496-499, ISBN 978-1-4398-3402-2, 2010.

Karazi S.M., Brabazon D., An artificial neural network for dimensions and cost modelling of internal micro-channels fabricated in PMMA using Nd:YVO$_4$ laser, International Manufacturing Conference IMC28, Dublin City University, Dublin, Ireland, Pages 34-36, 30th August – 1st September 2011.

Karazi S.M., Brabazon D., Evaluation of the effect of Nd:YVO$_4$ laser parameters on internal micro-channel fabrication in polycarbonate, Proceedings of the International Conference on Neural Computation Theory and Applications NCTA 2011, University Paris-Est Créteil (UPEC), Paris, France, Pages 254-259, 24th-26th October 2011, ISBN: 978-989-8425-84-3, DOI: 10.5220/0003683202540259.

Karazi S.M., Brabazon D., Control of laser micromachining via artificial neural network (ANN) and response surface methodologies (RSM), 15th Annual Sir Bernard Crossland Symposium, Dublin City University, Dublin, Ireland, 28th – 29th March 2012.

Karazi S.M., Ben Azouz A., Brabazon D., Laser micromachining control: numerical and statistical modelling techniques, 15th international conference on advances in materials & processing technologies AMPT2012, University of Wollongong, Wollongong, Australia, 23rd to 26th September 2012.

Ben Azouz A., Murphy S, **Karazi S.M.**, Vasquez M., Brabazon D., Fast fabrication process of cyclic olefin copolymer microfluidic sensing systems, 15th international conference on advances in materials & processing technologies AMPT2012, University of Wollongong, Wollongong, Australia, 23rd to 26th September 2012.

Seminars and Posters:

Karazi S.M., Brabazon D., Analysis and prediction of dimensions and cost of laser micromachining internal channel fabrication process, Engineers Ireland, Dublin, Ireland, 25th May 2010. Young Engineer Paper Prize (won 3rd place).

Karazi S.M., Ben Azouz A., Brabazon D., Dimensions and cost prediction modelling of Nd:YVO$_4$ laser internal micro-channel fabrication in PMMA, Nano Science and Technology Institute NSTI-Nanotech 2010 Conference and Expo, Anaheim, California, U.S.A, June 2010.

Ben Azouz A., **Karazi S.M.**, Brabazon D., Vazquez, Macka M., Paull B., Effect of laser processing parameters and glass type on topology of micro-channels, Nano Science and Technology Institute NSTI-Nanotech 2010 Conference and Expo, Anaheim, California, U.S.A, June 2010.

Karazi S.M., Brabazon D., Analysis and prediction of dimensions and cost of laser micromachining internal channel fabrication process, International Symposium on Experimental Mechanics ICEM14, Poitiers, France, 7th July 2010.

Ben Azouz A., **Karazi S.M.**, Vázqueza M., Paull, B., Brabazon D., Internal Laser Processing of Polycarbonate for the Purpose of Microfluidic Fabrication, Conference on Analytical Sciences Ireland 2011 - 6th CASi, Dublin City University, Ireland, 21 – 22 February 2011.

Karazi S.M., Brabazon D., An artificial neural network for dimensions and cost modelling of internal micro-channels fabricated in PMMA using Nd:YVO$_4$ laser, International Manufacturing Conference IMC28, Dublin City University, Dublin, Ireland, 30th August 2011.

Ben Azouz A., **Karazi S.M.**, Vázqueza M., Paull, B., Brabazon D., Laser Processing of PMMA and Polycarbonate for the purpose of internal fabrication of microfluidic channels, photonics Ireland conference 2011, Dublin, Ireland, 7th -9th of Sep 2011.

Karazi S.M., Brabazon D., Evaluation of the effect of Nd:YVO4 laser parameters on internal micro-channel fabrication in polycarbonate, Proceedings of the International Conference on Neural Computation Theory and Applications NCTA 2011, University Paris-Est Créteil (UPEC), Paris, France, 24th October 2011.

Acknowledgments

In the name of Allah, the Most Gracious and the Most Merciful. Alhamdulillah, all praises be to Allah for the strengths and His blessing in completing this study.

I would like to sincerely thank my supervisor Dr Dermot Brabazon for his support throughout the study. I want to especially thank him for his guidance, encouragements, ever-inspiring expertise, and sourcing out collaborations. I am truly grateful for everything he has done to help me get to where I am now. I would like to gratefully thank Dr Abdul-Ghani Olabi for his sound advices and concern during my entire study.

Heartfelt thanks to Dr Khaled Benyounis, Dr Muhammad Morshed, Dr Sumsun Naher, and my colleague Aymen Ben-Azouz for the regular exchange of ideas and collaboration that assisted with the progress of this work. I would also like to extend my thanks to technicians in the mechanical and manufacturing engineering school in DCU for the technical support throughout the study.

Due thanks go to my young family in Ireland (my wife Yasmin, my two sons Hadi and Kareem, and my little angel Sarah), and my family in Syria (my parents, brother, and sister). I would like to warmly thank them all for their generous unconditional support, continuous encouragement, and for making me feel loved and cherished all the time.

I genuinely show gratitude to all my office colleagues, school of mechanical and manufacturing engineering, NCPST, and all DCU staff and students for making my time here so enjoyable. There are too many to thank, but a special thanks has to go to those who have been such great friends Abed, Abdulaleem, Ahmad, Hussam, Mustafa. I apologise if your name is included here, this only means that you are closer to my heart than you are to my mind.

I gratefully acknowledge the financial support and scholarship from the University of Aleppo.

Abstract

In this thesis, the effects of process parameters on the resulting feature morphology and dimensions within line length scales and micro-fluidic devices is presented. Positioning stages, laser systems, and autonomous control systems were developed and designed for the machining of micro-channels on glass sheet and inside polycarbonate and PMMA samples. The developed real time closed loop control system was set-up via reconfigurable I/O Field-Programmable Gate Array (FPGA). In-depth analyses of the positional performance of the developed $Nd:YVO_4$, and Nd:YAG laser systems were carried out. The results of these analyses indicated that the developed 3D translation stage of the $Nd:YVO_4$ laser system is better with accuracy and repeatability values less than 65 μm for all the three axes. In particular, CO_2 (1.5 kW, 10.6 μm) and $Nd:YVO_4$ (2.5 W, 1.064 μm) laser systems were investigated experimentally and through system models in order to better understand the effects of laser and motion parameters on the process control. Predictive models, that relate the laser machining parameters (laser power; P, pulse repetition frequency; PRF, and sample translation speed; U) to the geometry and cost of the produced micro-channels, were developed. Detailed designs of experiments (DoE) were conducted and results from developed predictive models based on Artificial Neural Network (ANN) and Response Surface Methodology (RSM) techniques were compared with the actual results. Statistical estimators were used to evaluate these models and compare their predictive and generalization ability. Results showed that although the ANN models provided the highest prediction accuracy, both RSM and ANN modelling techniques could be utilised as effective predictive tools for resultant laser micro-machined dimensions and selection of laser micromachining parameters.

Contents

x

Nomenclature

μFIA   Micro-flow injection analysis

μTAS   Micro-total analysis systems

2D   Two dimensional

3D   Three dimensional

ANN   Artificial Neuron Network

ANOVA   ANalysis Of VAriance

ArF   Argon fluoride

BK7   Borosilicate crown glass (Schott brand)

C4D   Capacitively coupled contactless conductivity detection

CCD   Contactless Conductivity Detection

CCD camera Charge-Coupled Device camera

CNC   Computerized Numerical Control

CW   Continuous Wave

d.f.   Degree of freedom

DC   Direct Current

DIC   Differential Interference Contrast microscopy

DoE   Design of Experiment

DPSS   Diode Pumped Solid State

E∞   Absolute maximum percentage error

e_i Percentage error

FCC   Face-Centred Cubic

fs   Femtosecond

Gbits   Gigabit

GUI   Graphical User Interface

HAZ   Heat Affected Zone

I/O   Input/Output

IC   Integrated Circuit

IR   Infrared

KrF   Krypton fluoride

LASER   Light Amplification by Stimulated Emission of Radiation

LCD   Liquid Crystal Display

LCP   Liquid Crystal Polymer

LED   Light Emitting Diode

MEMS   MicroElectroMechanical System

MOEMS   Micro-Opto-ElectroMechanical system

MPE   Mean Percentage Error

NA   Numerical Aperture

Nd: YAG	Neodymium-doped yttrium aluminium garnet
Nd:YVO$_4$	Neodymium-doped Yttrium Orthovanadate
NIST	National Institute of Standards and Technology
nJ	Nano-joule
ns	Nanosecond
OEM	Original Equipment Manufacturer
OVAT	One-Variable-At-a-Time
P	Laser power
PAC	Programmable Automation Controller
PC	PolyCarbonate
PDMS	Poly(dimethylsiloxane)
PMMA	Poly(methyl methacrylate)
PPR	Pulse Per Revolution
PRF	Pulse Repetition Frequency
PS	Polystyrene
RF	Radio Frequency
RMS	Root Mean Square
RSM	Response Surface Methodology
SEM	Scanning Electron Microscope
sf6	Sulphur hexafluoride

SI	International System of Units
SLM	Selective Laser Melting
SPC	Statistical Process Control
TB	Terabyte
TFT	Thin Film Transistor
TMM	Tool Maker's Microscope
TTL	Transistor–Transistor Logic
U	Translation speed
UV	Ultraviolet
XRD	X-Ray Diffraction

List of Figures

xxiv

List of Tables

Chapter 1

INTRODUCTION

Laser micro-fabrication is a materials-processing technique that employs lasers to induce managed thermal alterations of material shape and dimensions at micrometre scale.

Table 1-1 provides a broad overview of the application of lasers in different areas with diverse objectives [1, 2]. This list is not comprehensive; however, it serves to demonstrate the diversity of laser applications.

Table 1-1: A broad spectrum of laser applications.

Applications of lasers	Low power applications	Communication	Optical fibre communication, telecommunication, optical data storage and computation
		Metrology	Holography, length/velocity measurement, inspection, interferometry, alignment
		Reprography	Printing of various kinds, scanning, data storage
		Entertainment	Laser light beam show, pointers, audio acoustic recording
	High power applications	Military	Weapon guide, atomic fusion, surveillance
		Chemical	Spectroscopy, isotope separation, photochemical deposition, pollution control
		Medical	Angioplasty, tumour therapy, skin/dental/ eye surgery, dermatology
		Heat source	Forming, joining machining, rapid prototyping, manufacturing, coating/ deposition, surface engineering

Laser micromachining processes include the drilling, cutting, milling, and engraving of materials with micro-dimensional tolerances. In spite of the fact that laser micromachining is a technically complex manufacturing process, research work has enabled the fabrication of increasingly precise, smooth, and clean components at high speed [3-5]. Laser micromachining is used for micro-channel and micro-electro-mechanical systems (MEMS) production within many applications. These include telecommunications, glass cutting, micro-sensors [6-8]; micro-vias, ink jet printer nozzles, biomedical catheter drilling, thin-film scribing [9]; micro-fluidic channels for blood/protein analysis [10]; optical vibration sensors [11]; 3D binary data storage [12-24]; and novelty fabrications [25].

Laser machining processes use laser induced heating on the surface or inside the bulk of the work piece to have a controlled removal of substance, they include laser assisted drilling, cutting, marking, milling and scribing and several other forms of removal/shaping of materials with micro-dimensional tolerances. Laser micromachining is a technically complex manufacturing process, however research work has enabled the fabrication of increasingly precise, smooth, and clean components at high speed [2-5].

Laser micromachining has become increasingly important in a variety of applications because of its high repeatability, high resolution, localized material removal with micron size tolerances [26]. Figure 1-1 shows a Differential Interference Contrast (DIC) microscope image [27]. This image reveals an array of cavities written in quartz using a femtosecond laser. The colouration of the cavities is the result of interference between the light reflected at the front and at the back of each cavity. The spacing of the "voxels" is 2 μm. The different colouration of the cavities is caused by the interference between the light reflected at the front and at the back of each cavity. This figure demonstrates the potential capabilities of laser micromachining technology. Another advantage is that this technology does not need pre- or post-processing of materials, the production costs will be considerably reduced and the production quality will be improved [28]. Furthermore, due to the non-contact procedure of the machining process, tool wear was completely removed and production speed and throughput was much enhanced.
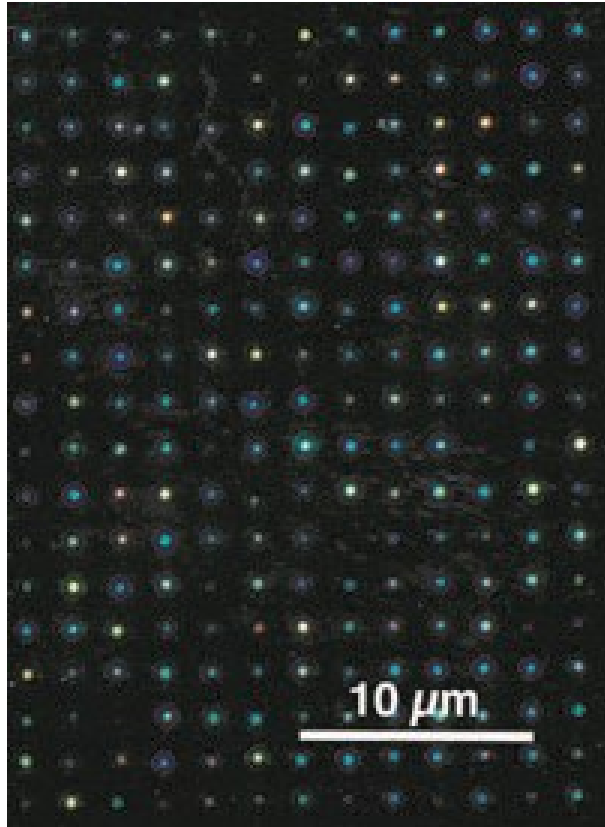
Figure 1-1: Differential Interference Contrast (DIC) image of

an array of cavities written in quartz [27].

Ablation is accomplished by tightly focusing a laser beam inside or on the surface of the target media via a microscope objective causing local heating, melting and following removal of material in the focal region [29-32]. Typically the resulting damage inside the transparent material is a micrometre-sized volume element as a result of the ability laser focus systems [32]. Figure 1-2 illustrates a broad classification of laser material processing techniques. Laser material processing techniques can be categorised into two groups. The first group does not involve notable phase change so an insubstantial amount of laser energy is needed; polymer curing is an example within this group. The second group does involve a phase change so a significant amount of laser energy is needed; laser cutting, welding, and Selective Laser Melting (SLM) are types of applications that are included in this latter group [1, 33, 34].
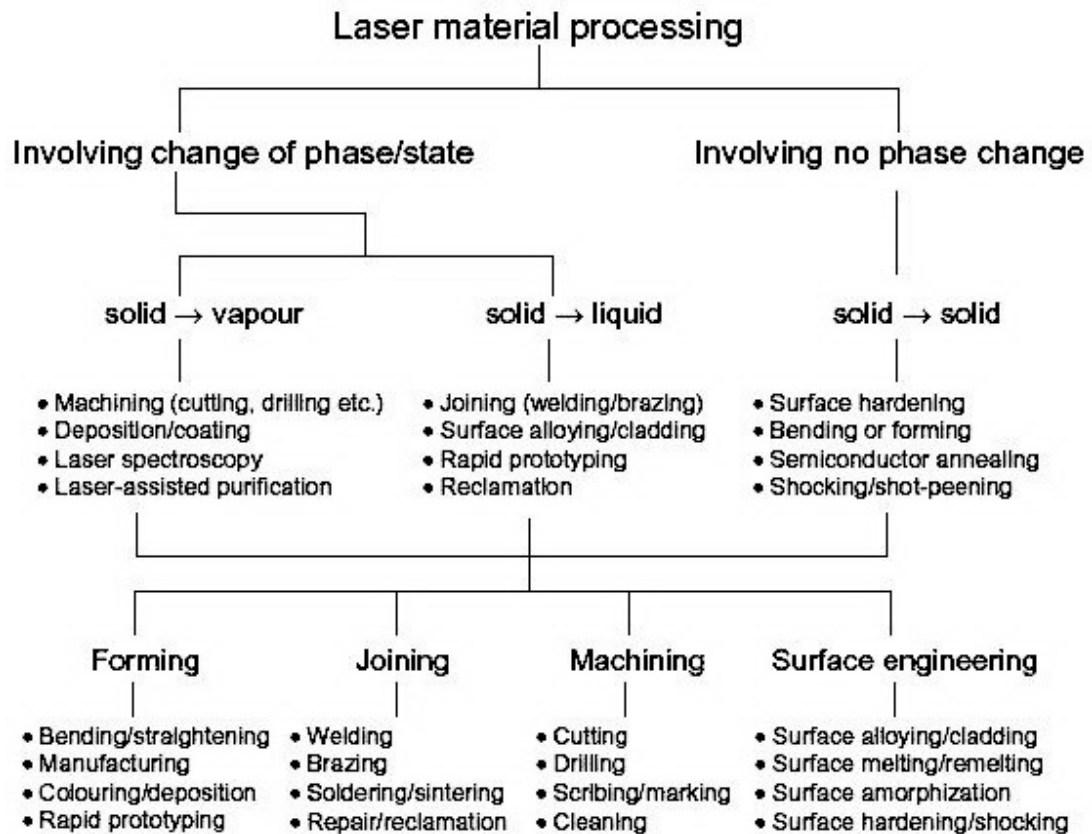
Figure 1-2: Laser material processing techniques classification [1].

In traditional physical tool based micromachining operations, the work piece endures high residual stress, which leads to subsequent post machining defects, and machining tool wear, which induces a variation in accuracy and repeatability. Since laser micromachining is a contactless processing technique, it does not suffer from these same problems. This is especially important for transparent media, and other brittle materials, where micro-cracks can easily propagate. Additionally, laser micromachining is a clean process and does not necessitate use of solvent chemicals like chemical etching process. Moreover, laser micromachining incorporates advanced computer control with programming interfaces that allow for "soft retooling". It is possible to change the beam properties by changing the inputs such as laser power, power repetition frequency (PRF), duty cycle, sample, or scan speed, etc. Lastly, laser micromachining is a low cost processing technique in terms of running costs, which makes it a great candidate for prototype work, especially where high tool-up costs must be avoided.

1.1   Study Objectives

The primary aims of this study were:

1- To evaluate the effect of CO_2 laser- micromachining parameters on the dimensional characteristics of surface micro-channels on lime-soda glass and to analyse the ability of RSM and ANN models to predict these dimensional characteristics and to determine the values of laser micromachining input parameters that should be used to attain specific dimensional characteristics. Afterwards, these models can be utilised as a tool for optimising laser input parameters for specific outputs.

In order to complete these objectives, the following work for the CO_2 laser system was initially required:

    I.   To perform a detailed design of experiment study of the process (to record the effect of the laser micromachining input parameters on the micro-channels geometry).

    II.   To construct a Response Surface Methodology (RSM) model for this process.

    III.   To construct an Artificial Neural Network (ANN) model for this process.

    IV.   To compare the capabilities of the two modelling methodologies.

2- To evaluate the effect of $Nd:YVO_4$ laser micromachining parameters on the dimensional characteristics and micromachining cost of the developed micro-channels in Polycarbonate and PMMA. Additionally, to assess the ability of RSM and ANN models to predict the geometry and process cost and to determine the values of laser micromachining input parameters that should be used to attain specific dimensional characteristics. Subsequently and for specific required outputs, these models can be utilised as a tool for optimising laser input parameters. These objectives necessitated the following plan of work, similar to that used with the CO_2 laser, but for the $Nd:YVO_4$ laser system.

Unlike the $Nd:YVO_4$ laser, the CO_2 laser system was used without any modifications since it was equipped with the Original Equipment Manufacturer (OEM)

MechTronic CNC motion system. The hardware parts of a Nd:YVO$_4$ laser system needed to be built and integrated and control software developed. In addition, building an in-house 3D sample positioning system for high resolution positioning capability utilising high-resolution rotary encoders and real time closed loop control, which is capable of repeatable micrometre level accurate positioning, was needed to fulfil this primary aim.

This hardware and software development of the Nd:YVO$_4$ laser system demanded selecting the proper hardware that will provide a real time combined monitoring, data logging, and control and can be programmed to develop the software control for sample position and laser firing. This detailed and difficult task was achieved through use of:

   I.   NI CompactRIO FPGA hardware, which is a programmable automation controller (PAC) to control the Nd:YVO$_4$ laser system; and

   II.   NI LabVIEW graphical programming for measurement and automation of the developed Nd:YVO$_4$ laser system and its 3D positioning stage.

3- To study in detail according to a recognised standard metrology method, the positional analysis of the developed motion systems of the Nd:YVO$_4$ laser system and the Nd:YAG laser system; and to compare between the two developed systems. One of these systems uses a 3D translation stage and the other one uses a galvanometer (laser scanning system) for X and Y laser beam spot translation and a Z-stage. To carry out the positional analysis study, a Mitutoyo optical microscope was used as a measurement system.

The aim of this study was to provide improved characteristics of laser-machined micro-channels thus improving the laser micromachining process. This study investigated laser micromachining using the CO$_2$ and Nd:YVO$_4$ laser systems to develop micro-channels in soda-lime, polycarbonate, and PMMA. Furthermore, this study aims to present a low-cost automated control system for laser systems for micromachining purposes (with micrometre level accurate positioning). Although micromachining systems have become increasingly used in industry, very few investigations have been carried out for micromachining systems development. The

focus of this study is the laser micromachining process modelling using RSM and ANN and micromachining laser systems development.

1.2   Thesis Outline

The thesis has been laid out in a progressive manner that initially introduces the laser micromachining process and the related background knowledge, followed by the materials and methods used in the work, the results, and discussion from the study, and followed by the conclusions. The contents of each chapter are highlighted below:

Chapter 1 – The aim of the chapter is to introduce the reader to the laser micromachining process and present study objectives and an overview of thesis content.

Chapter 2 – This chapter presents an in-depth discussion of research already undertaken on laser micromachining and its analytical approaches, outlining the existing knowledge. Additionally it assesses previous research carried out in this field, highlighting the areas where the state of the knowledge of laser micromachining can be advanced.

Chapter 3 – The materials and methods chapter presents the hardware that has been put to work and software used and developed. Furthermore, it outlines the material preparation, experimental and measurement procedures, experimental design, and the setup of the predictive models implemented in this work.

Chapter 4 – Results obtained from laser micromachining work and positional analysis are elucidated and discussed in detail in this chapter.

Chapter 5 – This chapter offers an overall discussion of the study and concludes by highlighting the most important findings and recommendations for future research work. Figure 1-3 shows the flow chart of the overall structure of the thesis.

Chapter 1
Introduction
- Introduction to laser miocromachining
- Study objectives
- Thesis outline

Chapter 2
Literature Review
- Laser Micromachining
- Applications in transparent media
- Process parameters
- Surface & internal laser micromachining
- Materials properties
- Process Analysis Approaches

- Positional analysis
- Literature review summary
- Units, and hypothesis

Chapter 3
Materials and methods
- Hardware & software setups
- Glass Experiments with CO_2 Laser System
- Polymers Experiments with $Nd:YVO_4$ Laser System
- Positional analysis

Chapter 4
RESULTS & DISCUSSION
- Glass Experiments with CO_2 Laser System
- Polymers Experiments with $Nd:YVO_4$ Laser System
- Positional analysis

Chapter 5
CONCLUSIONS
- Laser micromachining modelling
- Positional analysis for 1064 nm laser systems
- Future work

References
Appendices
- List of references
- Appendices

Figure 1-3: Flow chart of the structure of the thesis.

Chapter 2

LITERATURE REVIEW

2.1   Introduction

In this chapter, previous literature pertaining to laser micromachining process in transparent media is reviewed. The key studies relevant to this work are outlined indicating the relevant critical points of the current knowledge on this topic. Accordingly, applications of this process in transparent media, its parameters, and theoretical, experimental, statistical, and numerical studies that have been carried out by a number of researchers on different aspects of the laser micromachining process are discussed in this chapter.

2.2   Laser Micromachining Applications in Transparent Media

2.2.1   Waveguides

It is highly likely that the optical waveguide fabrication is the most studied application of micromachining in transparent media. Optical waveguides are structures that guide optical waves. They can be defined as any device that guides electromagnetic waves along a path defined by the physical construction of the device [35]. The machining of waveguides was enabled due to the fact that the laser can be used to create voxels with different refractive index. It is economically and technically feasible to use lasers for production of three-dimensional continuous internal transparent, but visible, waveguides and optical devices [36, 37].

Waveguides could be straight lines or of other geometries, Figure 2-1 illustrates the waveguide concept and a helical waveguide structure inside the bulk of glass fabricated using a femtosecond laser system.
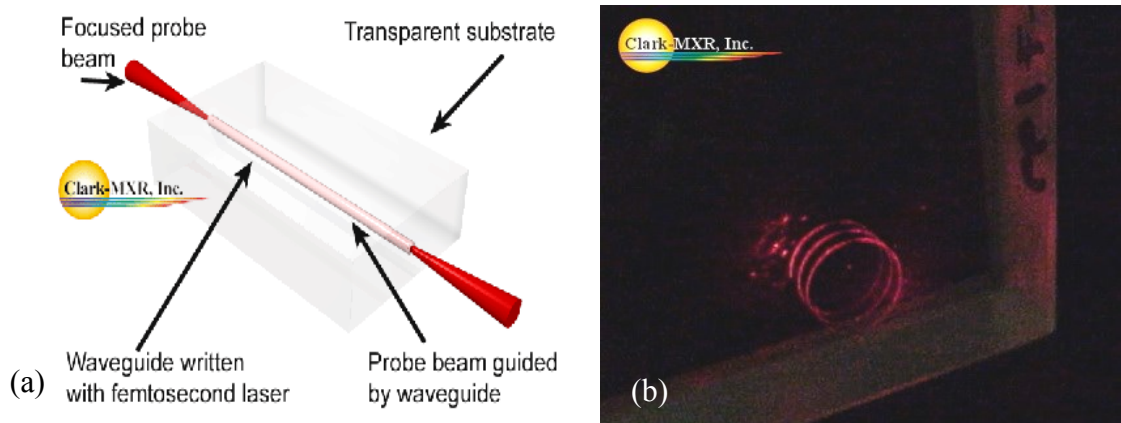
Figure 2-1: (a) Waveguide concept, and (b) helical waveguide in glass [38].

Figure 2-2 shows direct writing and self-writing techniques used by Ebendorff-Heidepriem for fabrication of waveguide structures in glasses using a UV laser. In the direct writing process, a sample is translated underneath a laser beam. On the other hand, self-writing is based on the propagation of the writing laser beam through the glass sample resulting in self-evolution of the channel gradually with time along the propagation axis [36]. Ebendorff-Heidepriem reported that the shape of the induced waveguides and surface changes depends on glass absorption properties and laser exposure conditions. The refractive index changes according to glass absorption, laser power and exposure fluence [36].
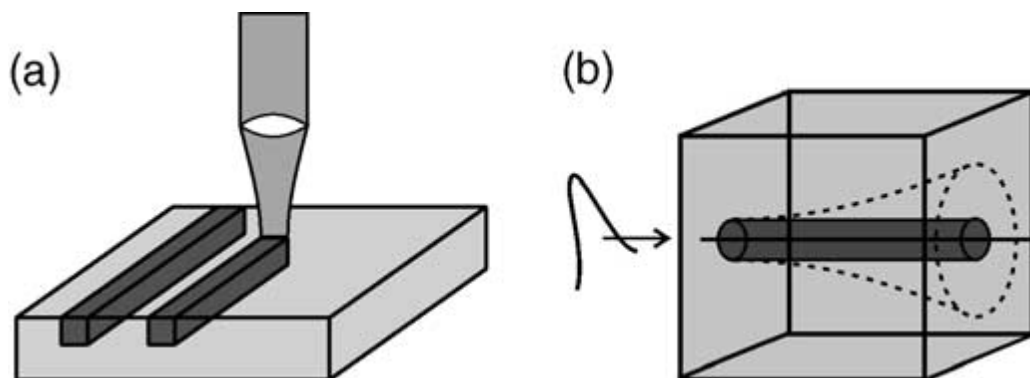
Figure 2-2: Sketch of: (a) direct writing and (b) self-writing processes [36].

Schaffer and Mazur reported the ability to write waveguides directly in three dimensions into bulk glass using ultra short pulses with nano-Joule energy from a laser oscillator [23]. This has enabled the fabrication of a wide variety of passive and

10

active optical devices for the telecommunications industry. Figure 2-3 shows an optical microscopic image of waveguides written inside bulk glass using a femtosecond laser. The sample was translated at 20 mm/s [23, 39, 40].
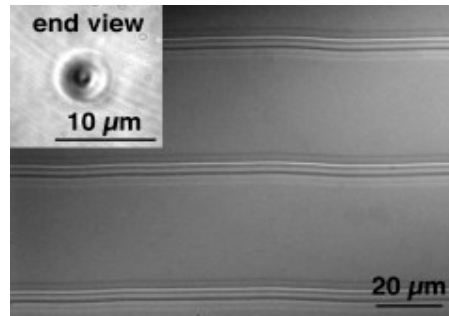
Figure 2-3: An image of single-mode optical waveguides written in glass [40].

According to other researchers in the field, 3D integrated waveguides in silicate glass using infrared or sub-UV wavelengths femtosecond lasers are feasible [41-44]. Many researchers used femtosecond laser pulses as it induces highly localized refractive-index changes in the transparent media. Using this type of laser, Shih et al. succeeded to produce magneto-optic switching inside bulk terbium-doped Faraday glass [45]; Miura et al. produced optical waveguides in inorganic glasses [46]; and Hirao et al. produced waveguides and gratings in silica, fluoride, SF_6 and chalcogenide glass [47]. Figure 2-4 shows sample waveguides produced by using a femtosecond Ti:Sapphire laser written in Silica and SF_6 glass.
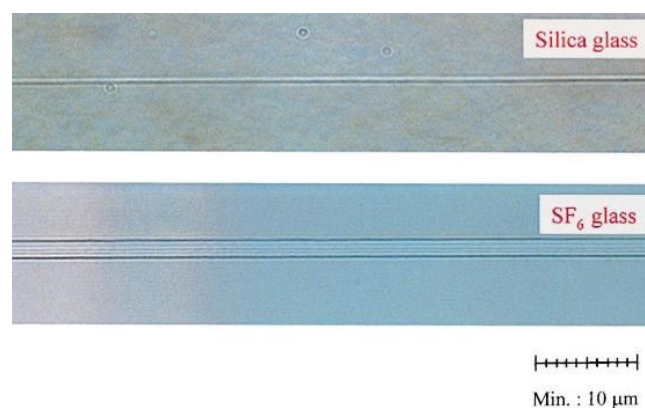
Figure 2-4: Waveguides written in silica and SF_6 glass [47].

2.2.2   Optical Data Storage

The ability of laser micromachining to create micrometre-sized refractive index changes inside of transparent media offers an opportunity for high-density optical data storage. Figure 2-5 illustrates recorded digital information in three dimensions by writing multiple planes [13].

Glezer et al. reported a novel method for high-density 3D optical data storage using ultra short laser pulses. In this work, submicron-sized bits were recorded by focusing 100 femtosecond laser pulses inside a wide range of transparent media using a 0.65 NA objective. 17 Gbits/cm^3 of 3D memory was achieved by writing an array of micro-scale spots in separate planes through the depth of the sample.
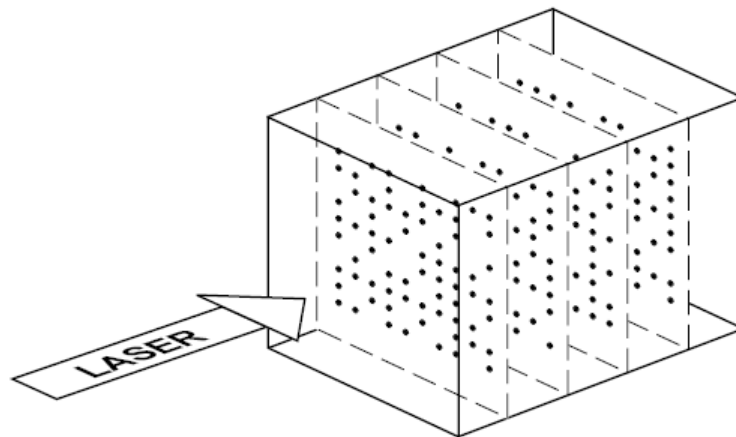
Figure 2-5: Schematic diagram of 3D optical data storage [13].

Figure 2-6 shows an optical microscopic image of binary data pattern stored inside fused silica, with 2 μm bit spacing, using a Ti:Sapphire femtosecond laser [13]. Dumonta et al. investigated the feasibility of using a laser for 2D data matrices glass labelling for Pharmaceutical industrial applications. Direct ArF excimer laser engraving on the glass surface was used in order to allow permanent marking of vials with 2D data matrix codes [48].
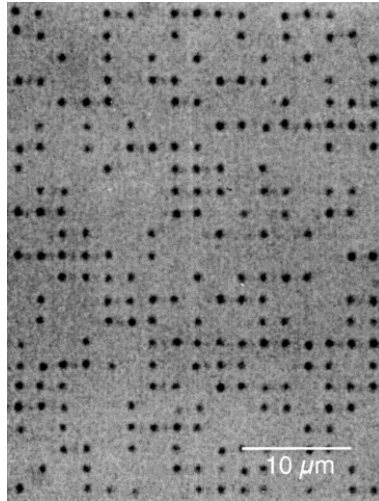
Figure 2-6: A random binary pattern written inside fused silica [13].

Other works showed the femtosecond laser irradiation capability of producing localized sub-micron structures with high contrast refractive index variation [24, 49]. Hong et al. presented an approach for high capacity optical data storage of up to 1 TB per disc [24]. Figure 2-7 shows ten layers of alphabet characters from "A" to "J" written in glass substrate with a femtosecond laser, with 10 μm layer spacing, 2 μm voxel diameter and 4 μm height.

1st Layer "A" charactar   3rd Layer "C" charactar

8th Layer "H" charactar   10th Layer "J" charactar
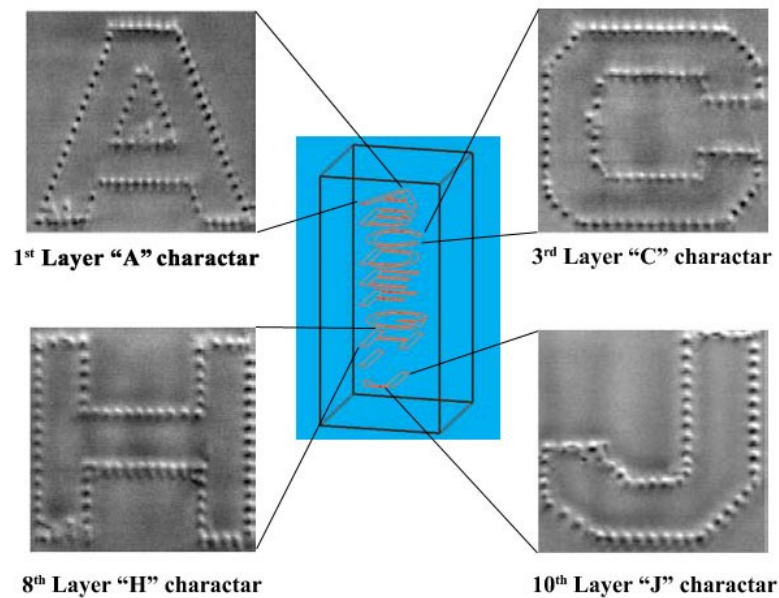
Figure 2-7: A multilayer recording in a glass substrate [24].

13

2.2.3   Micro-Fluidic Channels

Hollow 3D micro-channels in the bulk of a transparent media are used for micro-fluidic devices. These devices are normally concerned with the manipulation (transport, mixing, and sensing) of fluids at micrometre scale geometry. Rossier et al. demonstrated two different approaches for manufacturing polymer micro-fluidic chips, namely UV-laser photo-ablation and plasma etching [50]. These approaches are well suited for prototyping and mass fabrication of micro-channel networks with integrated microelectrodes for the purpose of electrochemical and biochemical analyses using UV laser photo-ablation.

Figure 2-8 (a) illustrates a plan view of a microchip fabricated by plasma etching.

Figure 2-8 (b) is a Scanning Electron Microscopic (SEM) image of the micro-channel with two 100 μm diameter disk electrodes visible within the channel [50].

Inlet/Outlet of the micro-channel   Connection pad
                              (a)   (b)
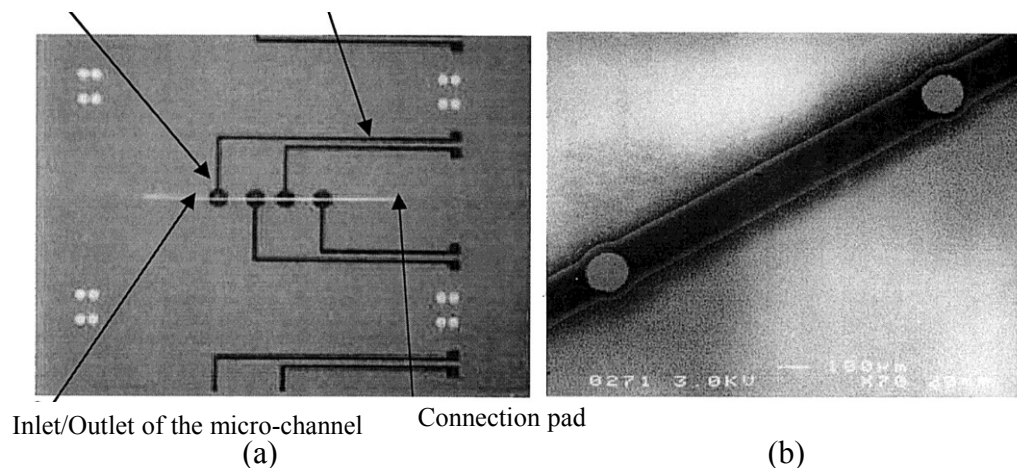
Figure 2-8: (a) Plan view and (b) SEM view of plasma etched micro-fluidic channel with two disk electrodes [50].

Detailed reviews of the applications of laser-based techniques for the fabrication of micro-fluidic devices for biochips have been presented [51, 52]. These techniques used infrared, ultraviolet and femtosecond lasers for surface treatment of micro-channels and laser ablation in polymers. From these reviews, it is noted that laser micromachining offers great process flexibility as well as the ability to micro-

machine a wide range of materials and substrates, including non-planar surfaces, and to produce structures with complex 3D geometries.

A new micro-flow injection analysis (μFIA) system on a chip coupled with chemiluminescence (CL) for the determination of uric acid without enzyme was presented in 2005 [53]. This μFIA system was produced by micromachining 200 μm wide and 100 μm deep channels in two transparent polymethyl-methacrylate (PMMA) substrates with a CO_2 laser. Uric acid was sensed by the chemiluminescence reaction between luminol and ferricyanide. This proposed method has been successfully applied to the non-separation determination of uric acid in human serum and urine.

McGinty et al. studied using two 266nm frequency quadrupled DPSS Q-switched solid state lasers, the fabrication of micro-fluidic circuits for micro-total analysis systems (μTAS) [54]. Furthermore, the authors compared their results with results achieved using a 193nm excimer laser. They concluded from their study and comparison that the excimer laser produced better micro-channel structure quality and that the 266nm frequency quadrupled DPSS laser. In particular, they concluded that the excimer offered a better solution where the quality of the structure was important for machining micro-fluidic applications in polystyrene (PS), polycarbonate (PC), polymethyl methacrylate (PMMA).

2.2.4 Micro-Electro-Mechanical Systems (MEMS)

Structures of Micro-Electro-Mechanical Systems (MEMS) are often fabricated through direct laser ablative removal of material. These laser ablative systems link mechanical and electrical technologies to produce an integrated device that utilises miniaturisation to obtain highly detailed designs in a very small volume [55]. This normally includes machining mm-μm size structures with μm-nm tolerances. Some applications include devices such as computer hard-disk drive heads, inkjet printer heads, heart pacemakers, hearing aids, pressure and chemical sensors, infrared imagers, accelerometers, gyroscopes, magneto resistive sensors and micro-spectrometers [56].

15

Sugioka et al. demonstrated the feasibility of true 3D micromachining in photosensitive glass by using a femtosecond laser operated at near-IR wavelength for lab-on-a-chip applications [57]. This 3D hollow micro-fluidic structure embedded in the glass was fabricated by direct femtosecond laser writing followed by heat treatment and successive wet etching. These researchers produced using this technique several micro-components for the lab-on-a-chip devices and investigated their performance. Figure 2-9 illustrates a fabricated microvalve device prototype with a movable microplate that can switch the flow direction of reagents.
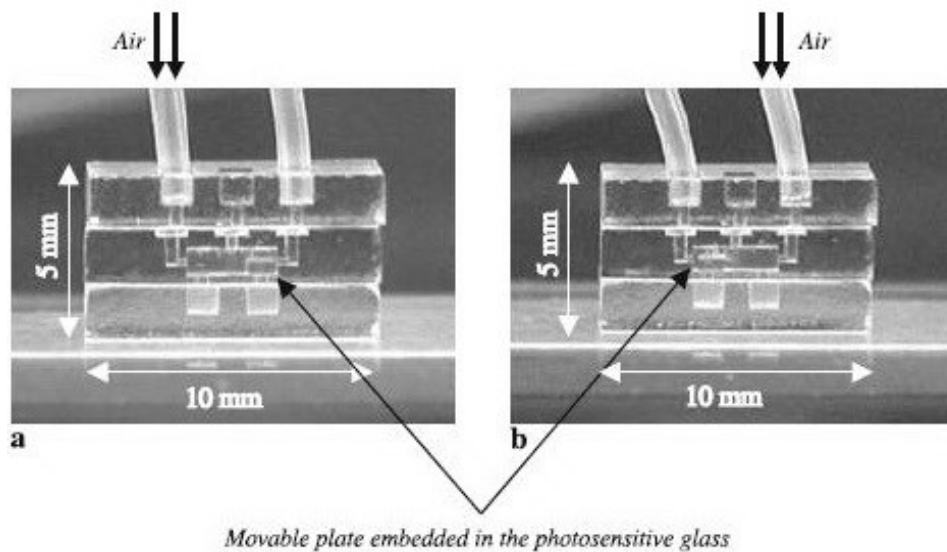
Figure 2-9: Fabricated microvalve device prototype with a movable microplate [57].

Gower et al. utilised laser micromachining for manufacturing and prototyping of MEMS and Micro-Opto-Electromechanical Systems (MOEMS) lab-on-a-chip devices, which included micro-turbines, micro-fluidic components, and micro-optical elements [58]. Table 2-1 shows a range of some selected MEMS and their potential markets.

Table 2-1: Some selected MEMS and their potential markets [59].

Devices and systems	Potential market areas
Pressure and flow sensors	Automotive industry
Chemical sensors	Aerospace
Linear actuators	Defence
Micro-motors and micro-turbines	Information technology
Fluid pumps and valves	Telecommunications
Scanning probe devices	Biotechnology
Micro-optical devices	Pharmaceutical industry
Micro-relays and switches	Medicine
Accelerometers and gyroscopes	Process technology and automation
Fluid handling systems	Measurement and microscopy
Micro-chemical analysis systems	Environmental technology

Holmes reviewed the use of high power lasers for manufacturing MEMS and the applicability of a wide range of materials for MEMS fabrication [60]. They successfully produced 3D structures for micro-fluidic devices by the "Laser-LIGA" process. The LIGA process is a stepwise process to mass replicate parts in polymer, metal or ceramic. This process consists of sequential lithographic, electroplating, and moulding steps. In LIGA, a polymer structure is produced via lithography, which is then electroplated to produce a tool for injection moulding or embossing. Projection ablation has been performed on polymer moulds using a 248 nm wavelength excimer laser then, like in conventional X-ray LIGA, the moulds were replicated by electroforming to fabricate fixed and freely moving nickel micro-turbine parts, as shown in Figure 2-10 [61].
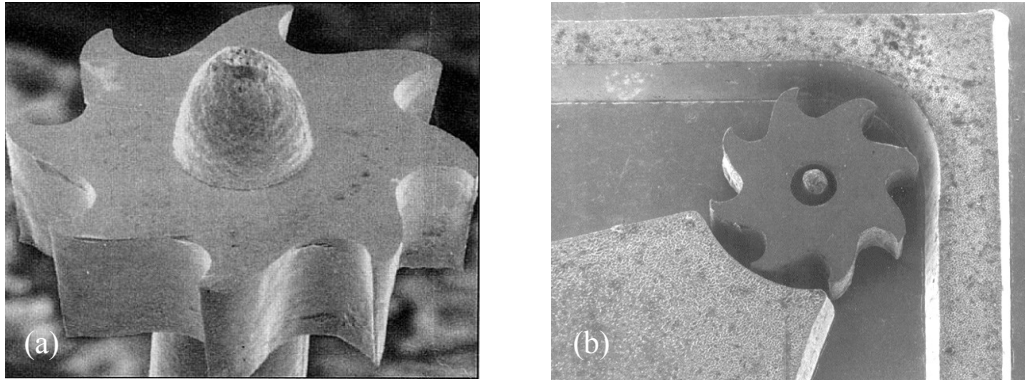
Figure 2-10: (a) Nickel rotor turbine and (b) Assembled micro-turbine prototype with turbine installed [61].

The fabrication of complex MEMS in silica and PMMA by a combination of direct femtosecond laser writing and chemical wet etching techniques was studied by Juodkazis et al. [31]. The principles and applications of polymer micro-fabrication techniques has been presented for the fabrication of micro-arrays, micro-reactors and micro-fluidic devices [10]. In 2004, a polymer-based capacitive micro-accelerometer was produced by Yung et al. [62]. Furthermore, they experimentally validated the fabricated MEMS and showed that utilising pulsed UV laser micro-processing technology on Liquid Crystal Polymer (LCP) provided a flexible and economic method for micromachining polymer-based MEMS devices.

2.2.5   Stage Micrometre

A "stage micrometre" is a transparent slide with a highly accurate scale. Typically, this scale is a system of distinct line markings, which are set regular distances apart from one another. Figure 2-11 (a) shows a stage micrometre metric scale of 10 mm total marked length with 100 divisions. On the other hand, Figure 2-11 (b) shows a dual axis linear micrometre that can be used to calibrate both X and Y directions accurately without stage micrometre rotation. This commercial glass stage micrometre had 25 μm on the metric divisions (left scale) and 0.001" on the imperial divisions (right scale) and overall slide dimensions of 1" x 3" (25.4 x 76.2 mm). It can be used to calibrate and check linear stage motion or to calibrate automatic measurement systems.

Usually it is used for calibrating optical measuring instruments (like microscope eyepiece reticles, microscope stage movement distances, etc.) to allow for accurate dimensional measurements. Generally, the stage micrometre is available with certificate to show that the dimensions on the stage micrometre have themselves been calibrated at a certified calibration laboratory [63].
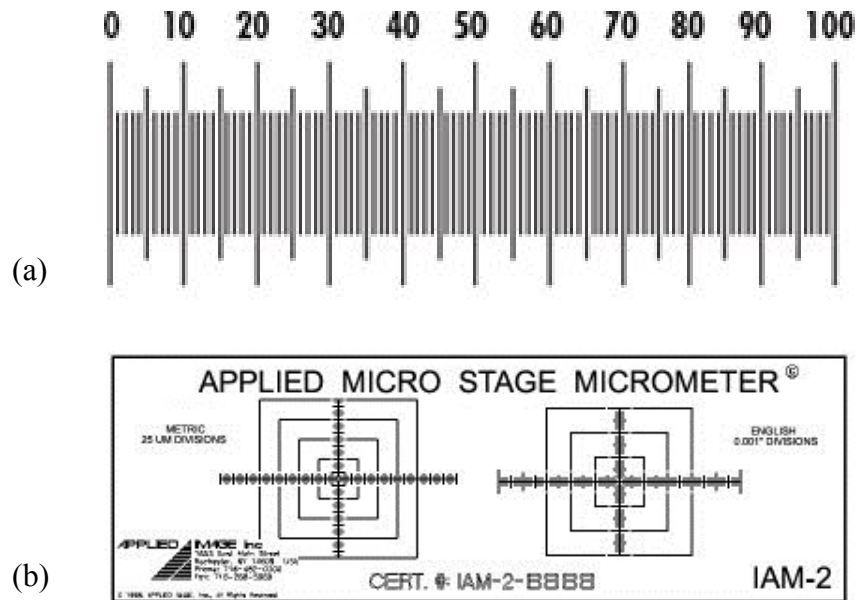
Figure 2-11: Stage micrometre (a) metric scale of 10 mm length with 100 divisions
and (b) precision calibration X-Y glass scale with
Metric (left) and imperial (right) divisions [64].

Stage micrometres normally are made from glass, due to its very low coefficient of thermal expansion, therefore keeping the distances between the lines relatively constant compared to other material choices. Although they are commonly used for calibration and metrology, precision within the manufacture of stage micrometres has not previously been examined in detail.

2.3 Laser Micromachining Process Parameters

Internal and surface laser micro-machined voxel shape and dimensions within transparent materials are considerably influenced by a number of different parameters. The practical effect of some of these parameters on the resulting microstructure, as presented in the literature, is discussed below.

2.3.1   Laser Power (P)

Laser power is the average optical power level emitted by the laser beam of light of a specific wavelength. The relationship between the average laser power and the core diameter of a machined optical waveguide in bulk glass has been previously studied. Researchers found that the core diameter is directly proportional to the average laser power [46], as illustrated in Figure 2-12.
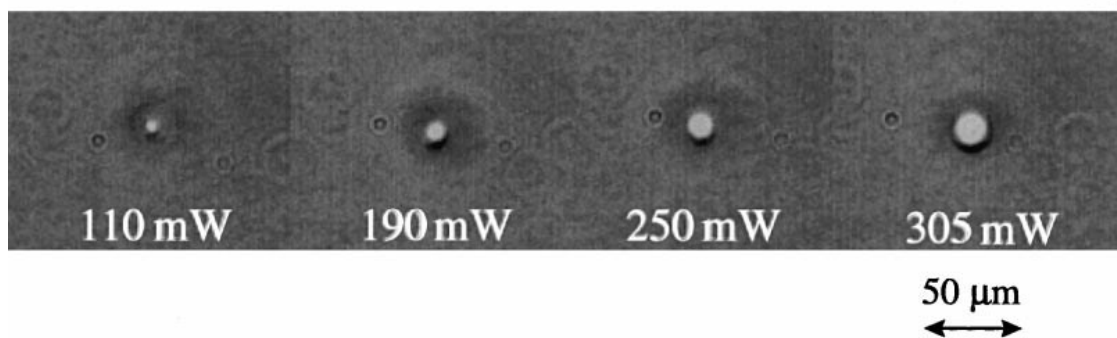
Figure 2-12: Cross sections of waveguides of different average laser powers [46].

2.3.2   Laser Wavelength (λ)

Laser wavelength is the distance between two consecutive peaks of a wave of a given frequency. In the micromachining industry in order to get a smaller spot size, shorter wavelengths should be used [65]. Other researchers compared three different lasers of dissimilar wavelengths to create micro-channels for the fabrication of micro-fluidic circuits and micro-total analysis systems (μTAS) in PS, PC, and PMMA. They found that the quality of the structure in terms of the lowest channel roughness and greatest sidewall angle was best with the laser of the shortest wavelength. Whereas, on the other hand, the other two lasers offered faster processing and higher energy efficiency [54].

Table 2-2 shows selected commercial lasers arranged according to their wavelength [66]. A laser medium is some form of optical gain medium in which lasing action occurs. This medium can be in any state of matter: solid, liquid, gas, or plasma. Operation mode describes the output capabilities of a laser whether it is continuous wave (CW) or pulsed or both. The output of the CW lasers is relatively constant with

respect to time. Q-switching is a technique for producing pulsed output from a laser by using an electro-optical shutter that prevents laser emission from the system until it is opened. In this technique, laser energy is compressed into concentrated packages (pulses). Consequently, the peak pulse energy is greater than that which comes from a CW laser of the same average power. Hence a much higher energy density can be delivered to a specific location and within a shorter period of time [35, 66].

Table 2-2: Selected commercial lasers characteristics.

Laser Type	Wavelengths (μm)	Medium	Operation mode
ArF excimer	0.193	gas	pulsed
Nd:YAG	1.064	solid	pulsed, CW
Nd:VO4	1.064	solid	pulsed, CW
CO2	10.6	gas	pulsed, CW

2.3.3   Pulse Repetition Frequency (PRF)

Pulse repetition frequency (PRF) is the number of laser pulses that are fired per second. The effect of PRF on the structures and rates of ablation within the laser micromachining process was studied by Herman et al. [67]. In their work, it was found that increasing PRF provided better precision, higher surface quality, and negligible thermal stress. Other researchers compared the time between successive pulses with the time needed for thermal diffusion out of the focal volume [68, 69]. They noticed that an accumulation of thermal energy in the focal volume would develop if the time between pulses was shorter than the thermal diffusion time, and that if the material around the laser focus heats up sufficiently it evaporates. Therefore high PRF should be used in order to ensure a uniform accumulation of heat [68, 69]. PRF controls the size of ablated regions and shape of these regions (including for example the formation of cracks).

2.3.4   Laser Pulse Width (τ)

Laser pulse width is the duration of the "on" time of the pulse. Several researchers found that laser pulse width influences the geometry and structure of the ablated areas [70-72]. A smaller laser pulse width provides less time for the heat to disperse such that a smaller heat affected zone (HAZ) would be created [65]. Recent research has shown that the use of picosecond or femtosecond laser pulses, instead of pulses of longer duration, can provide respectively very small or no HAZ [65, 73].

2.3.5   Translation Speed (U)

Translation speed is the relative linear speed between the sample and the focused laser spot. This parameter applies to different applications like optical waveguide fabrication [23, 36, 37, 39-47], glass laser texturing [74], optical data storage [13], micro-fluidic chip [50] and laser micro-channel and micro-structure fabrication [7, 54, 75, 76]. Previous research has clearly shown that the ablated structure spatial dimension is inversely proportional to the translation speed. This is a result of relatively lower energy absorbed by the irradiated region at higher speeds.

2.3.6   Pulse energy (E_P)

Pulse energy is the average laser power per laser pulse. It can be calculated according to Equation 2-1:

$$E_P = \frac{P}{PRF} \qquad\qquad \text{2-1}$$

Several researchers found that the size of ablated zone is a function of the pulse energy, with increasing pulse energy resulting in increased ablation volume [72, 74, 77].

2.3.7   Laser Intensity (*I*)

This is the laser intensity at the focal spot. It can become high enough to produce a nonlinear absorption when the laser pulse is tightly focused inside the material. The

nonlinear nature of the absorption restricts the structural changes to the focal volume [23]. It can be calculated according to Equation 2-2:

$$I = \frac{P}{\pi \, w^2}$$

2-2

where P is the laser power, w is the spot radius.

2.3.8 Pulse Fluence (F_p)

Pulse fluence is the laser pulse energy conveyed per unit area of focal spot. Several researchers found that the delivered fluence strongly affected the absorption mechanism which allowed smooth machined surfaces [30, 71]. It can be calculated according to equation 2-3:

$$F_P = \frac{E_p}{\pi \, w^2}$$

2-3

where E_P is the pulse energy and $\pi \, w^2$ is the focal spot area.

Figure 2-13 shows the produced fluence of laser pulses with energies between 100 nano-joules and 100 micro-joules into focal spots of diameter between 1 and 100 microns. Ranges of ceramic, metal and polymer ablation threshold fluences are illustrated as well. This figure indicates that even very low pulse energies are sufficient to ablate some materials, provided that the focal spot size is small and the material has a high level of absorbance at the used laser wavelength [78].

The total fluence of a number of pulses (N) is referred to as accumulated fluence. Herman et al. found that the magnitude of the induced refractive-index change in photonic device micro-fabricated in fused silica is controlled by the accumulated fluence [29, 30, 67]. The accumulated fluence can be calculated according to Equation 2-4:

$$F_{ACC} = N \frac{E_p}{\pi \, w^2}$$

2-4

23
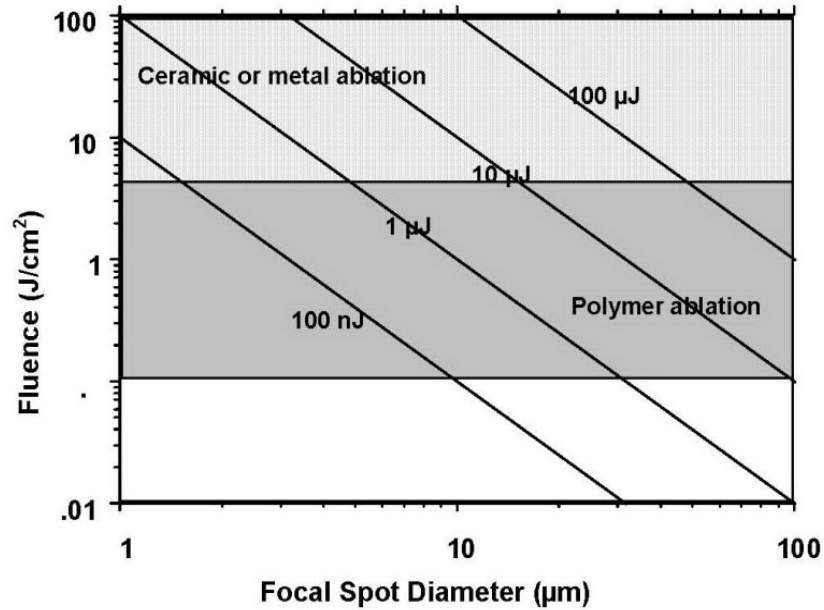
Figure 2-13: Fluence produced of variable energies and focal spot diameters [78].

2.3.9   Focal Spot Size (w)

In order to use a laser beam of a determined diameter for micromachining, it needs to be focused using a lens into a small region. There is a direct relationship between the spatial dimensions of the ablated zone and the irradiation spot size [72, 79].

The spot size can be precisely calculated only in single mode output like TEM_{00}, which is the designation for the Gaussian transverse mode [5, 35, 80]. Focal spot size is typically measured between points where the power is equal to $1/e^2$ times the power at the centre of the beam, which equates to about 86% of the focused laser energy contained in the focal spot. The focal spot size D for TEM_{00} can be estimated using Equation 2-5:

$$D = \frac{2.\lambda.f}{\pi.w} \qquad\qquad 2\text{-}5$$

where w is the beam radius at the lens inlet, λ is the laser wavelength and f is the focal length of the lens as shown in Figure 2-14.

Two important factors of focal spot are the focal length and depth of focus (also known as depth of field or focus depth). The focal length is the distance from a lens to its focal spot (focus point) and it is constant determined by the lens chosen. Depth of field is inversely proportional to the numerical aperture (NA), so to micro-machine small diameter holes, a lens of high NA is normally used to produce a smaller depth of focus [32, 81, 82]. The depth of focus is given by twice the Raleigh range for a Gaussian laser beam and can be calculated according to Equation 2-6:

$$\text{Depth of focus} = \frac{\pi . D}{\lambda} \qquad \text{2-6}$$
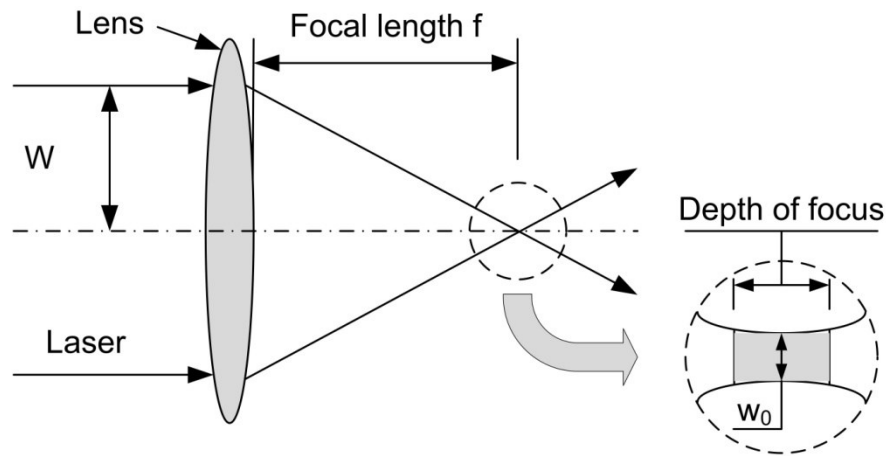
Figure 2-14: Focal length, spot size and depth of focus for a Gaussian laser beam.

2.4 Other Processing Considerations

2.4.1 Material Type

The essential quality of the ablation process depends strongly on the type of material [73]. Some selected material properties that have an influence on laser processing include absorptivity, transmittance, reflectivity, ionization potential (band gap) and thermal properties. Generally transparent materials are used to carry out micro-fabrication and micromachining studies [5]. Some investigated materials include polycarbonate (PC) [5, 54, 75, 83], polystyrene (PS) [54, 75], aluminosilicate glass [83], soda-lime glass [5, 84], fused quartz [14], polymethylmethacrylate (PMMA)

[31, 53, 54, 75], borosilicate glasses, fused silica [14], sapphire [14, 47] and silica glasses [11, 24, 31, 40, 47].

2.4.2   Focusing Method

How tightly the laser beam is focused controls the laser energy required to reach a threshold intensity that will induce permanent structural damage in the target media [23]. Furthermore, focusing controls the dimensions of the laser modified volume. In order to achieve the smallest micro-fabrication features, a laser equipped with microscope objective with a high numeric aperture (NA) should be used [32, 81, 82]. In the literature, plenty of researchers have used a variety of numerical aperture values up to 1.4 [13-23, 39, 40, 69, 85-96].

2.4.3   Number of Passes

Some researchers investigated moving the laser beam repetitively over the same region several times [7, 54, 75]. They were able to fabricate surface micro-channels on co-polyester substrates using an industrial CO_2 laser with varied aspect ratios by changing the laser power and repetition times [7].

2.4.4   Number of Pulses (*N*)

The ablated structure spatial dimension is proportional to the number of laser pulses fired into it [68]. Figure 2-15 shows the relationship between the radiuses of the fabricated structures in glass with their corresponding number of incident laser pulses (N) using a femtosecond laser. In this graph, the points represent experimental measurement and the line the calculated values of the radius from a model predicting the region temperature profile with respect to time. The model data fits well up to approximately 1000 laser pulses, after which it underestimated the radius of the structures.

26
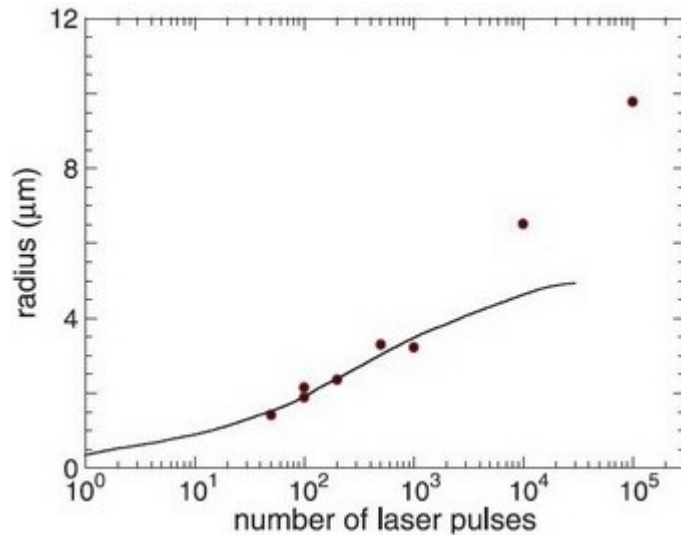
Figure 2-15: The radius of produced structure as a function of N [68].

The same effect of PRF in terms of thermal accumulation and diffusion applies to the effect of the number of pulses at a certain PRF value. Increasing the number of pulses means more energy is put into the irradiated volume, hence a greater spatial dimension for the ablated region is produced [13, 14, 16, 17, 29, 30, 39, 68, 85-89]. This could be concisely explained as increasing the number of pulses will increase the thermal energy deposited by successive pulses. In addition, because of lower thermal conductivity in the focal region, a larger volume is needed for the increased heat to disperse. Therefore, the thermal energy might not be transferred efficiently, resulting in more heating around the focal region than in normal situation based on the room-temperature value for the thermal conductivity. Accordingly, a larger structure is developed due to the melting and vaporisation of a larger volume.

Figure 2-16 shows an optical microscopic image of structures produced by a femtosecond laser fired perpendicularly to the plane of image [68, 86].
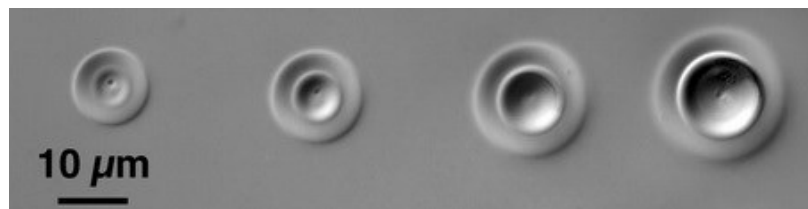
Figure 2-16: Cross section of structure developed by fs laser with 10^2, 10^3, 10^4 and 10^5 from left to right respectively.

27

2.5   Surface & Internal Laser Micromachining

2.5.1   Efficiency

Monochromaticity, coherence, and high power intensities are the very distinctive qualities of lasers [97, 98]. Laser Q-switching technique pulse formation methodology allows for high power laser pulses [3]. Several researchers have demonstrated the generation of pulsed lasing using different methods [3, 35]. Due to the high energies that can be delivered in the short pulse durations, Q-switched laser beam is efficient for ablation. Using pulsed laser beams is the only efficient way to ablate high vaporisation temperature materials since they produce high peak intensities within short time durations [99]. Extensive scientific research was conducted on laser micromachining applications in the last few decades. Micromachining laser systems used have included Ti-sapphire, (ArF) excimer, Nd:YAG, Nd:YVO$_4$, and CO$_2$ lasers [7, 54, 65, 100, 101].

Since laser wavelength and pulse duration are most significant laser beam attributes that contribute to ablation scale, both should be controlled to enable precise laser micromachining [32, 102]. The laser ability to be focused is a direct function of the laser emission wavelength [100]. Lasers of low wavelength, of a few hundred nanometres, and lasers of high wavelengths, of a few micrometres, can be used for laser micromachining applications. Numerous researchers demonstrated that for (ArF) excimer laser (193 nm), the fourth (266 nm) and third (355 nm) harmonics of Nd:YVO$_4$ or Nd:YAG (1064 nm), and CO$_2$ lasers (10.6 μm) [7, 54, 76, 79, 103]. To get an effective focal spot size, that is comparable to the emission wavelength, proper focusing of laser beams is needed [32]. The focal spot can be downsized to fractions of the emission wavelength using a tight focusing technique by means of high NA objectives lenses [32, 104]. Therefore, precision laser micromachining is feasible using laser submicron spot size.

An important factor that contributed to enhance micromachining precision is the development of ultra-short pulse duration lasers [102]. Laser pulse duration affects the absorption (and diffusion) timescales over which the thermal energy is deposited

(and transferred) to the target materials. In the ultra-short laser pulse duration situation, these timescales are very small, so confined and localised ablation with minimal or no heat affected zones [67, 105]. To ensure a uniform heat deposition and reduce the amount of micro-cracking, delivering the laser pulses at a high repetition rate is recommended for these ultra-short pulse duration lasers [102]. Other laser beam properties that affect micromachining include absorption properties of transparent materials [69, 106, 107], and internally focusing laser within the transparent material [24, 108].

Compared to other techniques such as ion-implantation, photolithography or chemical etching techniques, virtually any transparent material can be processed by laser micromachining [41, 68, 109, 110]. Moreover, laser micromachining requires less sophisticated equipment and offers a cheaper alternative for micromachining applications. Since laser micromachining is a direct writing method, so it does not normally require further steps to produce the structures. This makes the process faster compared to other techniques that require chemical etching for example [6, 111-113]. The contactless quality of lasers leads to more exact and cleaner machining, without the residual stresses (caused by mechanical forces between the sample and tool), the related post machining defects, and tool wear as per traditional machining [65, 102, 114, 115]. Additionally, a high accuracy of heat deposition into the target material using computers has led to laser micromachining of high dimensional accuracy [102, 111, 116]. Scanning the laser beam in the material enables the machining of internal and surface intricate structures in 2D or 3D [102, 117].

2.5.2   Break Down Procedure

Simply, micromachining takes place when the laser irradiation causes the material to heat up, melt and vaporise or break down. During laser-induced vaporisation, a practically totally ionised gas with excited electrons (plasma) is generated. This plasma can be observed as a glow or a flash or a bright spark in the focal region [107, 118, 119]. Research has shown that the measured average plasma temperature in the range of 5,000 to 20,000 °C is common during breakdown in most dielectric

29

materials [65, 120, 121]. There are various explanations of the laser-induced breakdown mechanisms in transparent materials [121]. The most commonly quoted dielectric materials breakdown mechanisms in the literature are avalanche ionisation, and multi-photon ionisation [65, 106, 122, 123]. These absorption mechanisms are based on the generation and growth of free electrons.

Ablation takes place at a pressure and temperature to produce high enough electrostatic forces between electrons and ions to breakdown the material and to eject the ionised species. The minimum laser fluence (energy per unit area) for which ablation can be initiated is defined as the ablation threshold or optical breakdown threshold [124]. The higher the fluence the more cutting power a laser has. During machining, the fluence is distributed over a small confined volume to allow for very close tolerance machining. Breakdown can take place in the bulk of transparent material without affecting the surface due to the ability to focus the beam. For precision micro-machining, it is important to study the required levels of laser beam fluence and other relevant parameters that will induce breakdown. Electron and phonon dynamics, following irradiation with a short laser pulse, govern the rise in temperature of the electrons and the lattice and hence any phase transitions which take place (e.g. solid-liquid and liquid-vapour) [125]. Damage occurs when the lasing energy is deposited into the material by the laser pulse causing a melting or vaporisation. The damage threshold is directly related to the relative rate of energy deposition, absorption, and thermal diffusion. Between picosecond and nanosecond pulse periods, energy is transferred from the laser-excited electrons to the lattice within the time scale of the pulse duration. This energy is transported out of the target region by thermal diffusion. Depending on the breakdown threshold based on the presence of impurity elements, can dramatically alter absorption levels [126]. All of these factors combined make it difficult to produce models that accurately predict the geometry of channels produced during the laser micromachining process.

2.5.3 Lasers Employed in Surface Micromachining

Lasers of low wavelength, of a few hundreds nanometres, and lasers of high wavelengths, of a few micrometres, can be used for laser micromachining applications.

Most of the research on surface laser micromachining applications was based on the use of short pulse width and short wavelength lasers. As an alternative to conventional methods, micro-channels were machined on the surface of polymers and glasses using different pulsed lasers of wavelength varied from femtosecond to nanosecond [50, 62, 83, 111, 126]. Sauvain et al. produced surface micro-channels on BK7 glass using a Nd:YAG laser [112]. Matsuoka et al. micro-machined surface rectangular holes of approximately (200×400 μm) on borosilicate glass using a Q-switched Nd:YAG laser [79].

Micro-channel machining on the surface of polystyrene (PS), polycarbonate (PC) and polymethylmethacrylate (PMMA) using excimer (193 nm), Nd:YAG (266 nm) and Nd:YVO$_4$ (355 nm) lasers was studied by McGinty et al.. Using a statistical design of experiments, the effects of the laser processing parameters on the resultant geometry, surface roughness and ablation rates were examined. Pulse repetition frequency, scan speed, pulse energy, and the number of passes were the studied laser input parameters. The process was modelled from the statistical analysis, which produced a prediction equation that can be used to predict the resulting channel dimensions in terms of the laser input parameters [54, 75].

2.5.4 Lasers Employed in Internal Micromachining

Various types of lasers have been employed for micromachining in transparent media. There is an extensive literature on micromachining using lasers of different emission capabilities and characteristics. Typically the pulse repetition frequencies range from a few Hz to MHz, the pulse widths range from nanosecond to femtosecond, and the laser emission wavelengths range from ultraviolet to infrared.

Laser systems used for internal micromachining have varied greatly in sophistication from one experimental set up to another. A basic configuration for internal micromachining has been shown in an ArF excimer laser setup (with a pulse width of 23 ns, a PRF of 100 Hz, and a 0.8 cm beam diameter) [91]. One the other hand, relatively advanced laser systems are becoming more common in the literature such as an ultrafast and a short wavelength (50 fs pulse width, and 157 nm wavelength) F2 (Fluoride) laser [29, 30]. Numerous types of lasers have been employed for internal micromachining including CO_2 laser [7, 70, 74, 76, 127-129], Nd:YVO$_4$ laser [54, 111, 127, 130-138], Nd:YAG laser [48, 62, 79, 99, 139], ArF Excimer laser [61, 75, 91, 114], Ti:Sapphire laser [24], Fluoride F_2 laser [29].

Schaffer et al. presented a basic laser micromachining experimental set up where femtosecond pulses are focused by a microscope objective into bulk glass, shown in Figure 2-17. Using a microscope or an objective lens, the laser pulses are focused inside the transparent material. Structural changes (voxels) were produced by moving the focused laser beam (which serves as a point source of heat) through the bulk of transparent media [40].
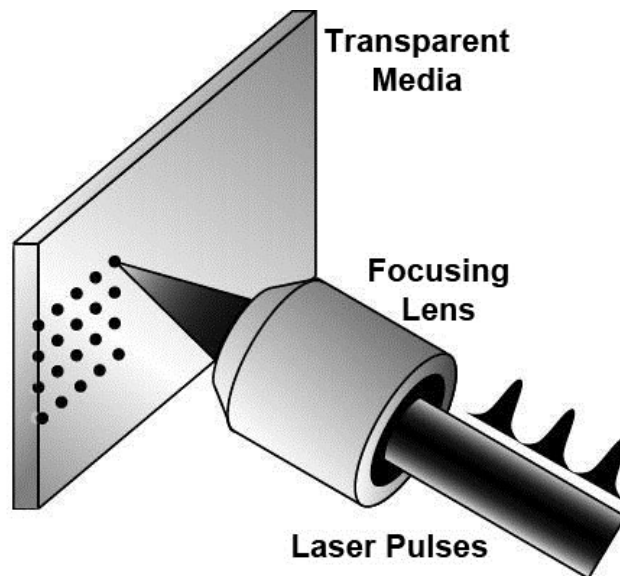
Figure 2-17: A basic internal micromachining configuration [94].

2.6 Materials properties

Since the employed material property affects laser micromachining, the related properties of soda-lime glass, polycarbonate, and PMMA are presented and discussed in the following sections. These are common microfluidic, waveguide, or micrometre stage materials, which were used in the work presented in this thesis.

2.6.1 Soda-Lime Glass

Soda-lime glass, also called soda-lime-silica glass, is the most prevalent type of glass. It is composed of SiO_4 tetrahedra connected at the oxygen atoms. The chemical ordering is very strong, each silicon atom connected to four oxygen atoms, and each oxygen atom is shared by two silicon atoms, as shown in Figure 2-18.
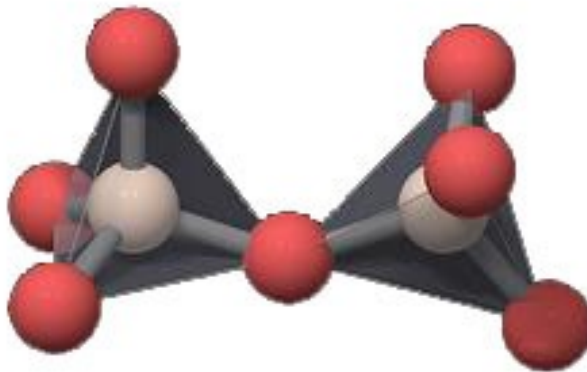
Figure 2-18: The Si-O-Si bond [140].

In soda-silica glass, the continuity of the network is disrupted by an addition of, network modifiers, like monovalent ions of Na_2O [141]. These network modifiers make the network more sophisticated so that when the components are melted together, in the cooling process, it is more difficult for the atoms to arrange themselves in suitable configurations for crystallisation to occur [142]. Figure 2-19, shows adjacent SiO_4 tetrahedral-type unit cells forming part of a continuous random network.
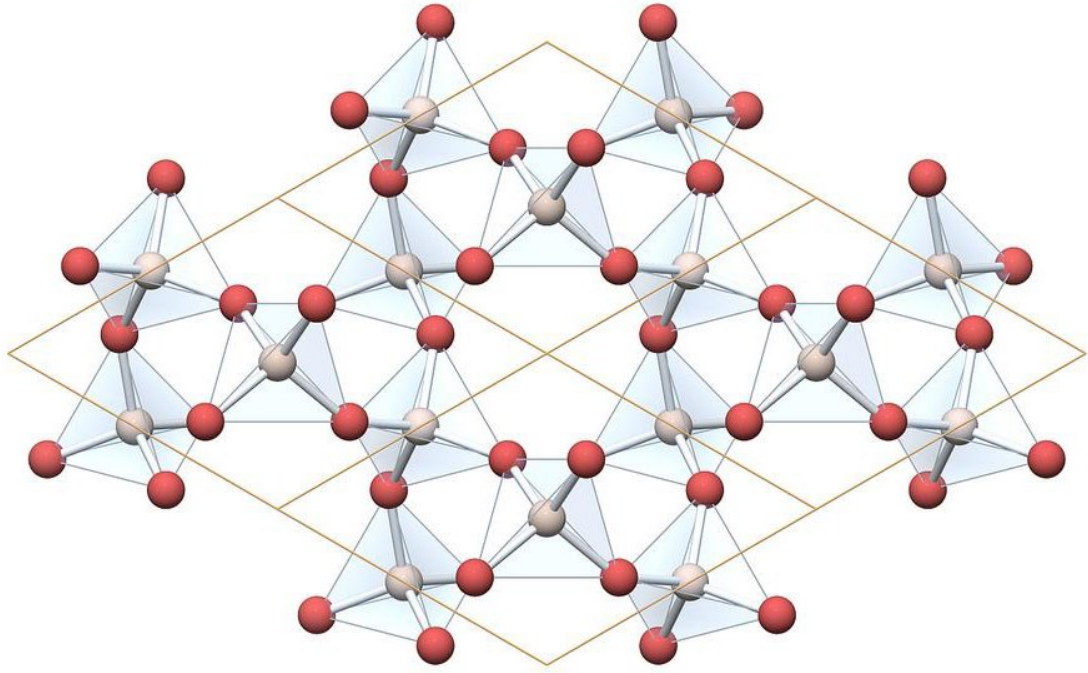
Figure 2-19: Adjacent SIO_4 tetrahedral-type unit cells [140].

Soda-lime glass is the most popular glass type based on the soda-lime silicate (sodium calcium silicate) system. Figure 2-20 shows a typical transmission spectrum of Soda-lime glass.
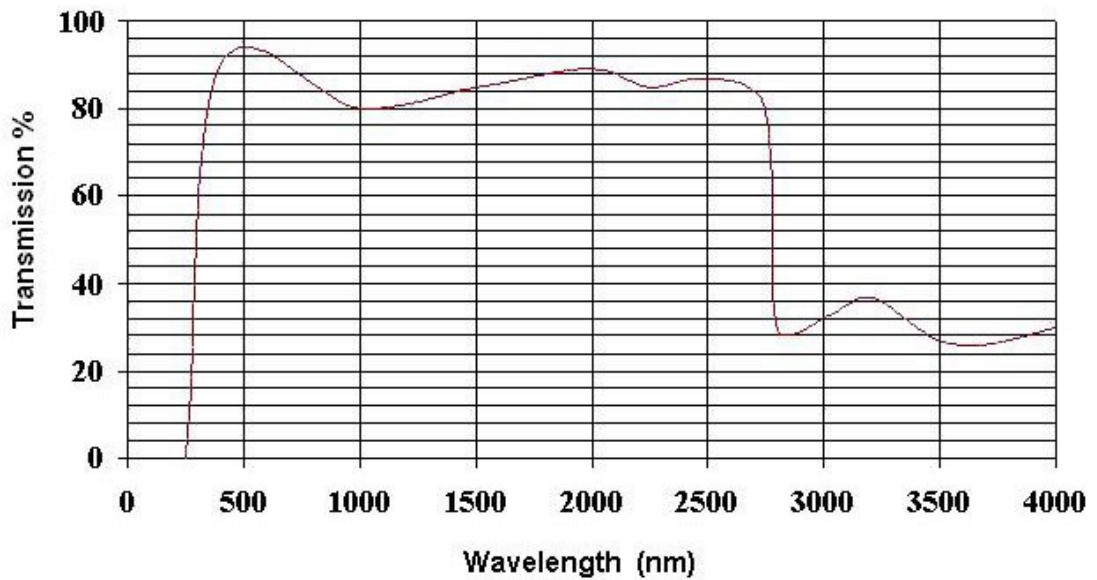
Figure 2-20: Typical transmission spectrum of Soda-lime glass [143].

This type of glass is relatively easy to melt and form, chemically durable, and not expensive. The composition of soda-lime glass varies marginally depending on the manufacturer. The typical composition of soda-lime glass is ($73\%SiO_2$ - $15\%Na_2O$ - $7\%CaO$ - $4\%MgO$ - $1\%Al_2O_3$) [141, 144, 145]. Table 2-3 lists the most commonly quoted properties of soda-lime glass.

Table 2-3**:** Selected properties of soda-lime glass.

Property	Value
Refractive index, n	1.46
% transmittance (at 1 μm)	70-80
Density, ρ (g/cm^3)	2.5
Thermal conductivity, k (W/m.°C)	1.06
Specific heat, C_P (J/g.°C)	0.87
Softening point (°C)	≈700
Melting temperature, T_M (°C)	≈1000
Vaporisation temperature, T_V (°C)	≈3427

2.6.2   Polycarbonate

Polycarbonate's chemical formula is $C_{16}H_{14}O_3$ and the bonding structure of a polycarbonate unit is shown in Figure 2-21. Polycarbonate is an amorphous substance that becomes plastic on heating, hardens on cooling. As it is a thermoplastic polymer, this process is repeatable. Usually thermoplastic materials melt at relatively high temperatures and as they cool down, below the glass transition temperature, they may become brittle. However, polycarbonate does not become as brittle as many other thermoplastics. Polycarbonate is composed of chains that have rigid segments, of monomeric units, and flexible joints. The weak Van der Waal forces connect and attach the chains directly to each other. Segments of the chains

are in continual motion, coiling, uncoiling and twisting, at any temperature above absolute zero [146].
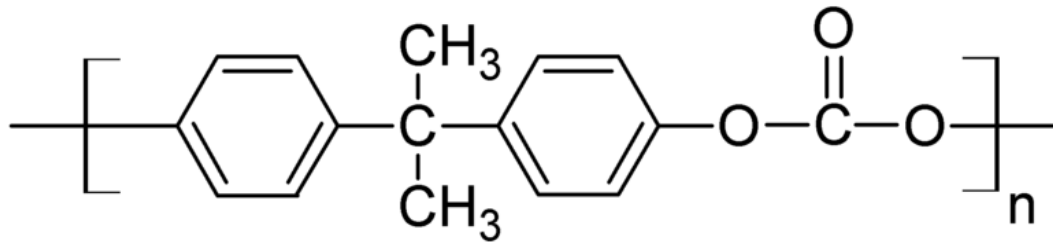
Figure 2-21: The chemical structure of polycarbonate [147].

Typically, polycarbonate is almost completely transparent throughout the entire visible region until 400 nm, blocking UV light. Figure 2-22 shows a typical IR transmittance of polycarbonate.
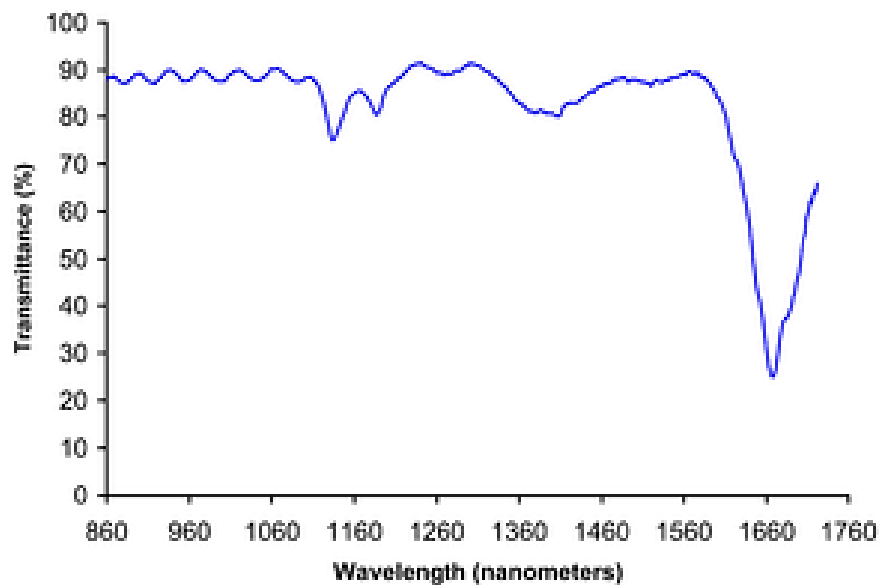
Figure 2-22: Typical transmittance spectrum of polycarbonate [147].

Table 2-4 lists the most commonly quoted properties of polycarbonate. During the manufacturing of polymers, manufacturing process conditions such as heating rates may vary which will affect the resulting material properties [146]. Table 2-4 was therefore collated from the most representative values found from different literature sources.

Table 2-4**:** Selected properties of polycarbonate.

Property	Value
Refractive index, n	1.583 – 1.586
% transmittance (at 1 μm)	89
Density, ρ (g/cm^3)	1.17 – 1.45
Thermal conductivity, k (W/m.°C)	0.19 – 0.21
Specific heat, C_P (J/g.°C)	1 – 1.2
Melting temperature, T_M (°C)	≈ 150
Glass transition temperature (Tg)	≈ 147 °C

2.6.3   PMMA

Polymethyl methacrylate (PMMA), sometimes called acrylic glass, chemical formula is $C_5O_2H_8$ and the bonding structure of a PMMA unit is shown in Figure 2-23. PMMA is also a thermoplastic polymer.
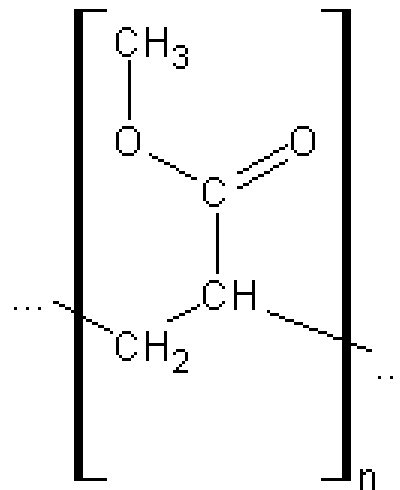
Figure 2-23: The PMMA chemical structure [148].

PMMA is transparent at visible and near infrared wavelengths, as shown in Figure 2-24. In general, the transmission properties of other transparent polymers in the visible and near-infrared are similar to PMMA [149].
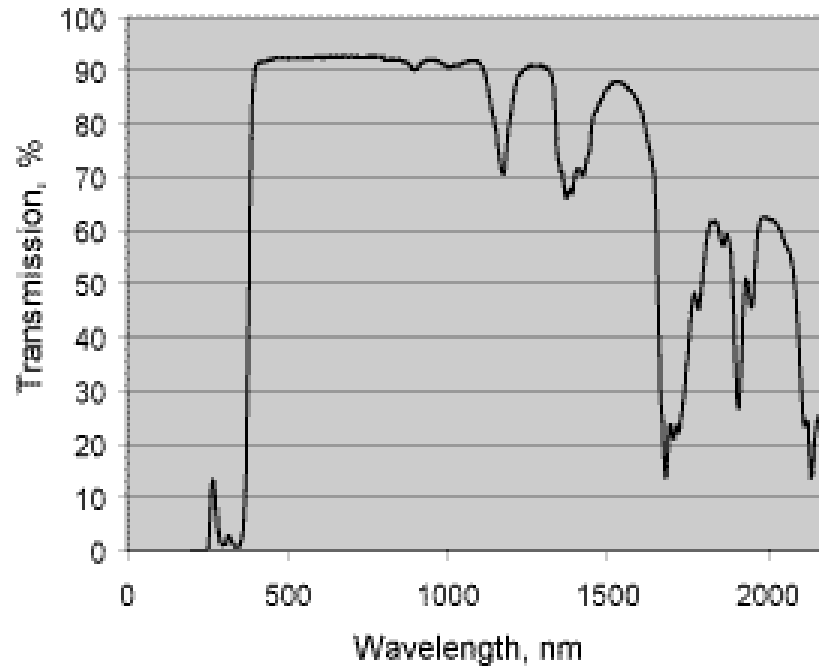
Figure 2-24: Typical transmittance spectrum of PMMA [149].

The effect of manufacturing process conditions applies to PMMA as well. Therefore, only the most commonly quoted properties of PMMA are listed in Table 2-5.

Table 2-5: Selected properties of PMMA [150].

Property	Value
Refractive index, n	1.4914
% transmittance (at 1 μm)	90
Density, ρ (g/cm^3)	1.18
Thermal conductivity, k (W/m.°C)	0.167 - 0.25
Specific heat, C_P (J/g.°C)	1.466 – 1.466
Melting temperature, T_M (°C)	≈160
Glass transition temperature (Tg)	≈ 105 °C

2.7 Design of Experiment and Response Surface Methodology

Experimental design or Design of Experiments (DOE) is the design of any information-gathering experiments where variation is present in the system under investigation. DOE is an organised methodology for examination of a system or process. A series of organised tests are designed in which systematic changes are made to the input variables of a process or system. The effects of these changes on a predetermined output are then evaluated.

2.7.1 Design of Experiment

Typically, experiments are carried out in industry to enhance the understanding and knowledge of different manufacturing processes with the objective of manufacturing high quality products. To ensure a continuous progress in process quality, it is important to be aware of the process behaviour, the extent of variability, and its influence on the process outputs. Usually, experiments are often carried out, in the engineering arena, to explore, estimate, or confirm. Exploration denotes the understanding the data from the process. Estimation denotes the specification of the effect of the process variables on the output characteristics. Confirmation involves verifying the predicted results obtained from the experiment [151].

DOE is an organised methodology for examination of a system or process. A series of organised tests are designed in which systematic changes are made to the input variables of a process or system. The effects of these changes on a predetermined output are then evaluated. DOE is significant as a formal way of maximizing information acquired while minimizing resources needed. Since it allows a conclusion on the significance to the output of input variables acting in combination with one another, as well as input variables acting alone, DOE offer more conclusions than 'one change at a time' experimental approaches.

One of the conventional and regular approaches utilized by manufacturing engineers in industry is one-variable-at-a-time (OVAT), where the engineer varies one variable at a time keeping all other variables involved in the experiment fixed. OVAT testing always holds the chance that the person who is conducting the experiments may

discover that one input variable will have a significant effect on the response (output) while failing to find that changing another variable may modify the effect of the first (i.e. where there is dependency or interaction). This OVAT approach needs considerable resources to acquire a limited amount of information about the process. Usually, OVAT experiments are time consuming, unlikely to yield the optimal condition and do not examine interaction between the process variables [151].

Methods that have statistical foundations can replace OVAT methodology. Design of Experiment (DOE) methodology plays a major role in planning, conducting, analysing, and interpreting data from experiments. If a certain quality feature of a product (the output or response) is being affected by several variables, the best tactic is to design an experiment in order to attain valid, reliable, and sound conclusions in an economical, effective, and efficient manner. It is essential to know that some factors may have strong effects on the output, others may have modest effects, and some have no effects at all. Consequently, the objective of a well-designed experiment is to determine which set of factors in the process affects the process performance most, and then the best levels for these factors to reach the sought after quality level can be determined [152].

DOE designs and arranges for all possible dependencies in the first place, and then proposes exactly what data are required to assess them i.e. whether input variables change the response when combined, on their own, or not at all [151]. DOE can be used to answer questions like "what is the key contributing factor to a problem?", "how well does the system/process carry out in the existence of noise?", "what is the best pattern of factor values to minimize variation in a response?" etc. In general, these questions are given tags as specific kinds of studies. For the type of problem-solving questions mentioned-above, DOE can be used to find the answer. Taking into account, DOE requires different experimental factors to answer different question.

The order of tasks to using this tool begins with identifying the input variables and the response (output) that is to be evaluated. For each input variable, a number of levels are determined that represent the range for which the effect of that variable

needs to be known. An experimental design is developed which tells the person who is conducting the experiments where to set each test parameter for each run of the experiment. The response is then quantified for each run. The technique of analysis is to look for variances between response (output) readings for different groups of the input changes. These variances are then accredited to single effect (the input variables acting alone) or an interaction (in combination with another input variable) [153].

Since a variety of backgrounds (e.g. design, manufacturing, statistics etc.) should be involved when identifying factors and levels, DOE is team oriented. Moreover, the team should have a full understanding of the difference between control and noise factors, because this tool is used to answer particular questions. From each performed experiment, it is crucial to obtain the maximum amount of information. Therefore, a full matrix is needed which contains all possible combinations of factors and levels. Well-designed experiments can produce significantly more information and often require fewer runs than random or unplanned experiments. Furthermore, a well-designed experiment will ensure that the assessment of the effects that had been identified as important. For instance, if there is an interaction between two input variables, both variables should be considered in the design rather than doing a "one factor at a time' experiment. An interaction occurs when the effect of one input variable is affected by the level of another input variable [151, 153, 154].

Sir R. Fisher introduced DOE in the early 1920s to determine the effect of various fertilizers on a range of land plots [151]. Since then, DOE has been employed in many domains such as engineering, physics, chemistry, etc. The use of DOE has grown rapidly in the last two decades, and has been adapted for many industrial processes such as chemical mixing, welding, and micromachining to find out the optimal conditions. Responses surface methodology (RSM) is the most-known type of DOE design; the concept of RSM was introduced in the early 50's by Box and Wilson [155, 156].

Thoughtful planning helps to avoid problems that can occur during the accomplishment of the experimental design. For example, personnel, tools

availability, funding, and the mechanical characteristics of the system may affect the ability to complete the experiment. The preparation needed before starting experimentation relies on the nature of the problem. Some of the steps that may be essential are problem definition, objective definition, developing an experimental plan, and finally, making sure the process and measurement systems are in control.

In terms of problem definition, picking a good problem statement helps make sure that the correct variables are considered. This step is used to identify the questions that need to be answered. While in terms of objective definition, a well-defined objective will guarantee that the experiment answers the right questions and produces practical, usable information. This step is used to define the goals of the experiment.

Then the experimental plan should be developed in such a way, it will provide meaningful information. At this step, it is essential to make sure that the relevant background information has been studied, like theoretical principles, and knowledge obtained through observation or previous experimentation. For instance, correct identification of which factors or process conditions affect process performance and contribute to process variability is necessary. Alternatively, if the process is already established and the influential factors have been identified, it may be required to determine the optimal process conditions.

Ideally, both the process and the measurements should be in statistical control as measured by a functioning statistical process control (SPC) system. This will guarantee that the process and measurement systems are in control. Even if it does not have the process completely in control, it must be able to reproduce process settings [157]. In addition, it is necessary to determine the variability in the measurement system.

In many process development and manufacturing applications, potentially influential variables are many. Screening reduces the number of variables by identifying the significant variables that affect product quality. This reduction allows process improvement efforts to be focused on the key variables. Screening may also propose the "optimal" or best settings for these factors, and indicate whether curvature exists

in the responses. Then, it can use optimisation methods to determine the best settings and define the nature of the curvature. General full factorial designs (designs with more than two-levels) may be particularly useful for screening experiments.

2.7.2   Response Surface Methodology (RSM)

RSM is a group of statistical and mathematical techniques that are useful for modelling and predicting the output of interest influenced by some input variables with the objective of optimizing this output [158]. RSM also describes the relationships among one or more measured outputs and the vital controllable input factors [159]. If all independent variables are measurable and can be repeated with negligible error, the response surface (output surface) can be expressed by Equation 2-7.

$$y = f(x_1, x_2, x_3, \ldots, x_k)$$ 2-7

$$y = a_0 + \sum a_i x_i + \sum a_{ij} x_i x_j + \sum a_{ii} x_{ii}^2 + \varepsilon$$ 2-8

where k is the number of independent variables.

Usually, engineers search for the conditions that would optimize the process of interest. It means that, they want to find the values of the process input parameters at which the responses reach their favourable outcome or "optimum". The optimum could be either a minimum or a maximum of a particular outcome in terms of the process input parameters. RSM is one of the optimization techniques currently in widespread usage to describe the performance of the micromachining process and find the optimum of the responses of interest. Therefore, it is essential to find an appropriate approximation for the true functional relationship between the independent variables and the response surface, in order to optimize the response "y". Generally, RSM uses a second order polynomial mathematical equation similar to Equation 2-8. A description of the general RSM procedure can be found in Appendix A respectively.

43

2.8 Artificial Neural Network (ANN)

Artificial Neural Network is a type of Artificial Intelligence (AI) originally designed to mimic the massively parallel operations of the human brain and aspects of how we believe the brain works. Neural network nodal functions can be evaluated simultaneously, thereby gaining enormous increases in processing speed [160].

A neural network can be considered as a black box that is able to predict an output pattern when it recognises a given input pattern. Once trained, the neural network is able to recognise similarities when presented with a new input pattern, resulting in a predicted output pattern.

In the fields of artificial intelligence, Artificial Neural Network (ANN) is a mathematical model that simulates the biological neural networks. A neural network is an assembly of interconnected processing elements, known as nodes or artificial neurons.

2.8.1 Introduction

Frequently, ANN is used to model complex relationships between inputs and outputs. The ability of an ANN to make predictions is based on the inter-neurons connection strengths, known as "weights", which are acquired through a set of training data by a process of adaptation called "supervised learning" [161].

The ANN on a similar principle to that of a biological neural network where each node represents a biological neuron. Figure 2-25 displays a biological and artificial neuron. Furthermore, this figure shows the obvious resemblance between the two types of neuron.
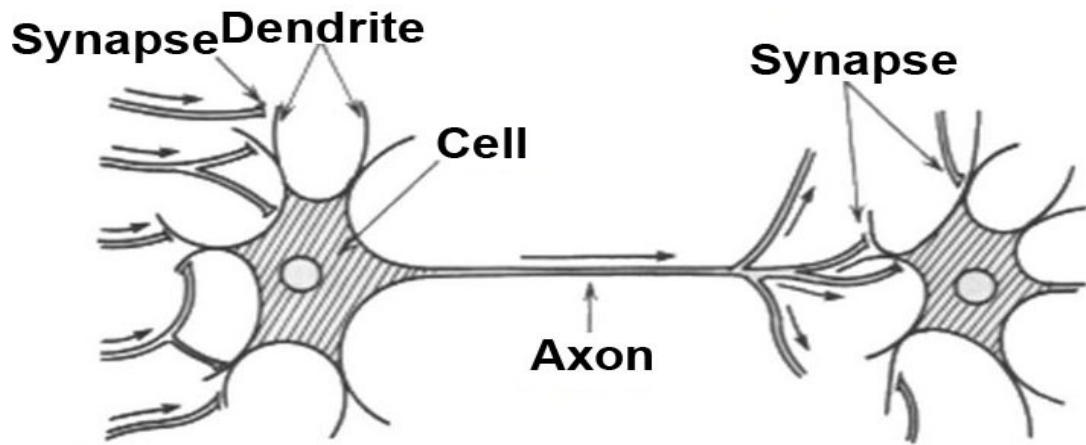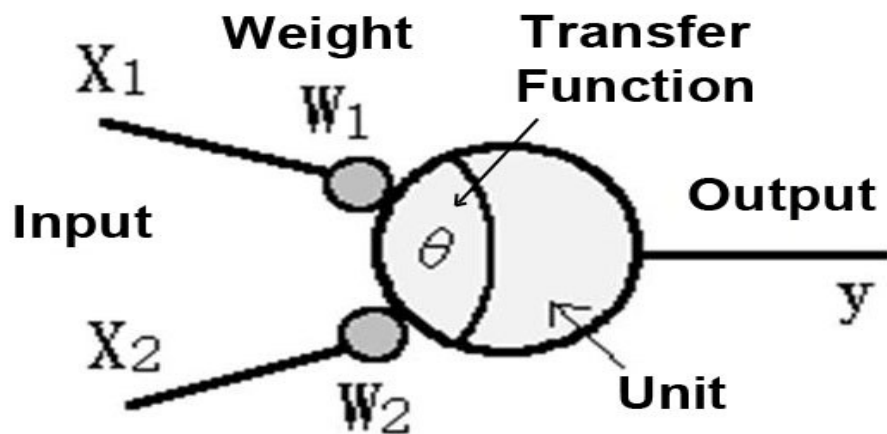
Figure 2-25: (a) Biological neuron and (b) artificial neuron.

There is a weight associated with the incoming synapse of a biological neuron. The weight of each synapse, times its input, is summed for all incoming synapses and the neuron then fires, sending a signal (electrical activity) to another neuron in the network. In ANN, almost the same principle applies. Each node in the ANN has a set of inputs (analogous to the synapses in a biological neuron). Each input connection has a quantity (the connection strength or weight) associated with it. Bias is a constant input with certain weight. Each node has a summing function for computing the weighted sum of the inputs. Moreover, it has an "activation function" (or transfer function) for limiting the amplitude of the neuron output [162]. Figure 2-26 shows a mathematical representation of a single neuron.
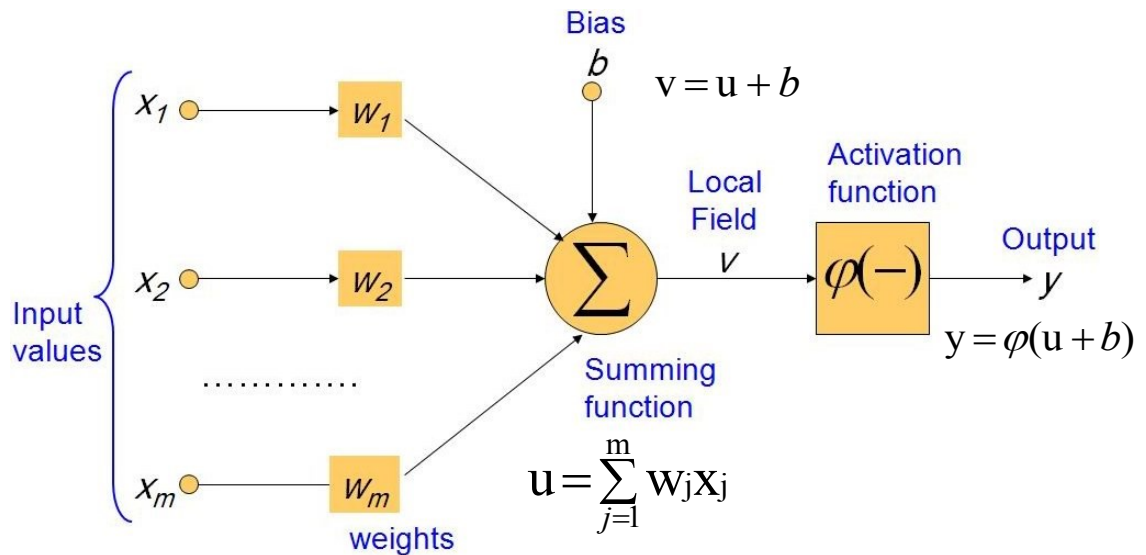
Figure 2-26: A single neuron may be represented mathematically.

The mathematical output value of a single neuron may be calculated according to formulas from Equation 2-9 to Equation 2-11.

$$u = \sum_{j=1}^{m} w_j x_j \qquad \text{2-9}$$

$$V = u + b \qquad \text{2-10}$$

$$y = \varphi(v) \qquad \text{2-11}$$

where x is a neuron with m inputs and one output $y(x)$, and w_j are weights determining how much each input should be weighted. φ is an activation function that weights how influential the output (if any) should be from the neuron, based on the sum of the input.

In order to introduce non-linearity to the neural network, the proper transfer or activation function should be selected. Activation functions vary from simple threshold functions to sigmoid or hyperbolic tangent functions. It is essential to introduce non-linearity to the ANN, as this is what provides the computational power to the network. Without this non-linearity, the network turns into a basic matrix multiplication operation.

The sigmoid transfer function is a mathematical function having an "S" shape (sigmoid curve). It takes the input, which may have any value between minus and plus infinity, and provides an output in the range 0 to 1. The sigmoid function may be written as Equation 2-12.

$$f(x) = \frac{1}{1 + e^{-t}}$$
2-12

This transfer function is commonly used in back-propagation networks of the type used in this study due to its differentiability [163]. The learning rate parameter, which is the training parameter that controls the size of weight and bias changes during learning, can be set during simulation to control the magnitude of weight and bias updates. The selection of this value significantly affects the training time of the ANN. The "momentum" technique is often utilised to decrease the likeliness for a back-propagation network to be stuck in local optima [162].

2.8.2   ANN Structure

The nodes in ANN are arranged in layers. Each of the nodes in a given layer are connected to nodes in another layer. Typically, there are three types of layers to an ANN: an input layer, one or more hidden layers, and an output layer. Figure 2-27 shows typical three layered feed forward neural network architecture, where there are three inputs, four neurons in the hidden layer, and two outputs.

The input layer is where the data vector is fed into the network. This feeds into the hidden layer, which in turn feeds into the output layer. The processing of the network occurs in the nodes of the hidden layer and the output layer. There are numerous ANN structures; however, the feed forward and recurrent structures are the most frequent. Since neural networks of feed forward structure and back-propagation algorithm offer better prediction capability [164, 165], this specific type of ANN was employed in this work.

Input Layer   **Hidden Layer**   **Output Layer**
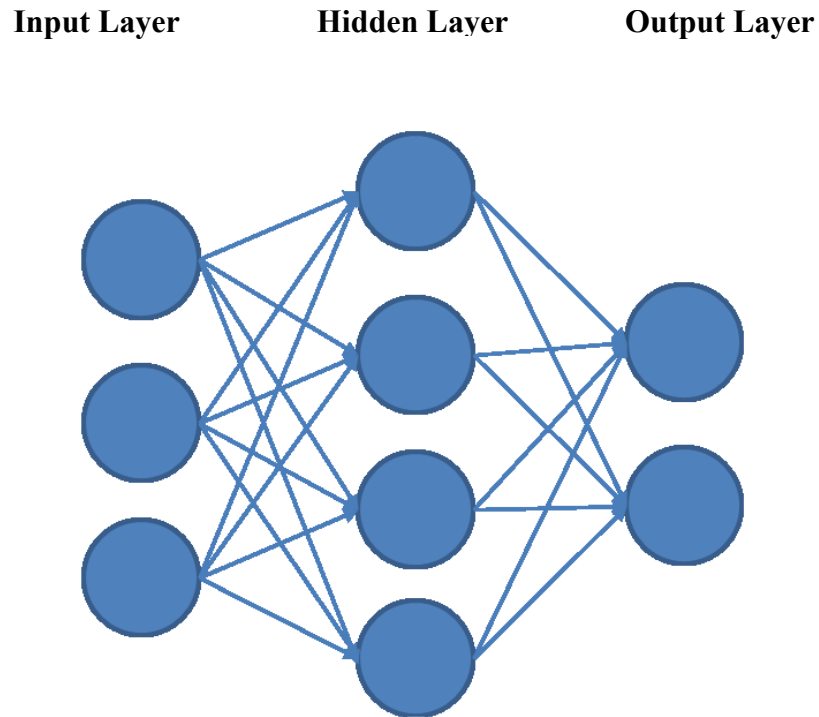
Figure 2-27: Typical three layered feed forward neural network architecture.

Feed-forward networks

Signals, in the feed forward structure, travel one way (forward), from inputs to output(s) without any backtracking along the way. Figure 2-28 shows a typical feed forward neural network. In the feed-forward network, data are uniformly processed in one direction from the input towards the output layer. Therefore, all links are unidirectional, and no cycles are present in ANNs of feed-forward structure.
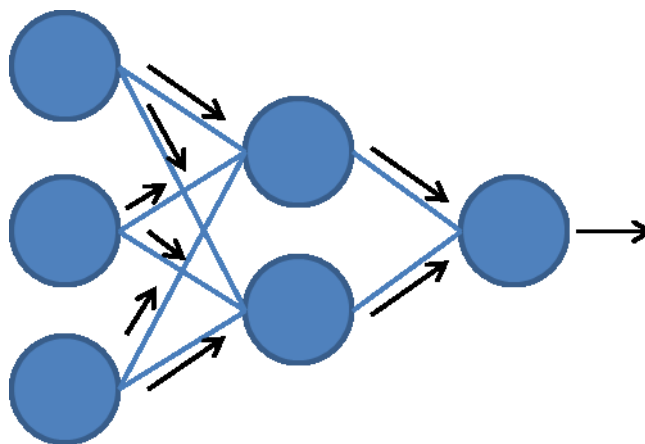
Figure 2-28: A representation of a feed-forward neural network.

Multi-layered perceptron is an ANN feed forward structure with one or more hidden layers between the input and output nodes. The advantage of multilayer perceptrons is that the number of nodes in the hidden layer can be varied to adapt to the complexity of the relationships between input and output variables [162]. One of the experimental aims of this work was to determine the number of hidden layers and the size (number of neurons) of these hidden layers that produce the best predictive performance.

Recurrent Neural Networks (RNNs)

Signals, in the recurrent structure, can travel in all directions with loops, allowing its output to be used in previously used "neurons". Therefore, these are models with bi-directional data flow. While feed-forward network propagates data from input to output, RNNs propagate data from "downstream" processing units to earlier units. Thus RNNs, have feedback connections between units of different layers or loop type self-connections [166, 167]. This implies that the output of the network not only depends on the external inputs, but also on the state of the network in the previous time step as is shown in Figure 2-29.
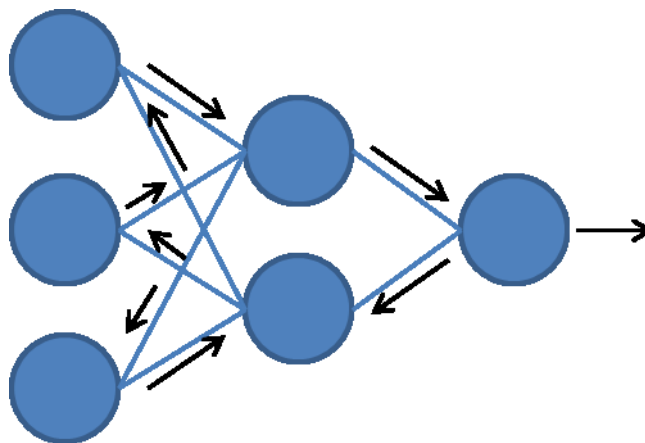
Figure 2-29: A representation of a recurrent neural network.

2.8.3   Learning Paradigms

Although it is not possible to model a human brain exactly with its enormous complexity, an ANN can be used to solve problems of considerable complexity. Learning can be achieved by proper ANN training. There are several ANN learning methods. The supervised and the unsupervised learning methods are the most common learning methods for ANN. However, the supervised ANN learning method was adopted for this work.

Supervised Learning

This method is the most common ANN learning method. In this learning method, the output of a neural network is compared to the actual output. Weights, which initially are set to random, are adjusted by the network so that the next iteration will yield a closer match to the actual output. The learning method attempts to minimize the current errors of all neurons. This global error reduction is made over time by continuously modifying the weights until acceptable network accuracy is reached. In this learning method, the ANN must be trained before it becomes useful. Training consists of presenting input and output data (training set) to the network. Supervised learning is an ideal process for prediction of an input/output functional relationship.

Unsupervised Learning

Unsupervised learning differs from supervised learning in describing data rather than predicting. This learning method, sometimes called self-supervised learning, is not common and limited to networks known as self-organizing maps. In this learning method, the network observers their performance internally and no external effects is used to adjust its weights. The network looks for uniformities (trends) in the input signals, and makes adaptations according to the function of the network. Even without being told whether it is right or wrong, the network still must have some information about how to organize itself. This information is built into the network topology and learning rules [162, 168]. Unsupervised learning is an ideal process for clustering similar data.

2.8.4   The Back-Propagation algorithm

Back-propagation algorithm is the most common supervised learning algorithm. The concept of this algorithm is to adjust the weights minimising the error between the actual output and the predicted output of the ANN using a function based on delta rule. It involves working backward from the output layer to adjust the weights accordingly, and reduce the average error across all layers. This process is repeated until the output error is minimised. The basic back-propagation algorithm adjusts the weights in the steepest descent direction [169-171].

Using this algorithm, the network training consists of three stages: (a) feed-forward of the input training pattern; (b) calculation and back-propagation of the associated error; and (c) the adjustment of the weights. By starting from the output layer, backward pass propagates the error. This process continues until the minimum error is reached. In weight update phase, input activation level and output delta are multiplied to get the gradient weight. Then weights are put in the reverse direction of the gradient by subtracting the ratio of it from the weight [172]. Since data normalisation minimises the chances of convergence to a local minimum on the error surface, convergence is more readily achieved through normalisation of the input and output data [173].

2.8.5   ANN Training, Validation and Testing

At the start of the training phase, the weights and the biases in the neural network are initialised to small random values between -0.1 and +0.1. The training process involves feeding the ANN known inputs and outputs, which gradually modify the connection weights. The back-propagation learning algorithm is implemented to modify the values of the weights. The weights eventually converge to values, which allow them to be used in predicting an unknown output.

In order to use a neural network as a predictive tool, the available data is divided into three subsets, for training, validation and testing. Overtraining (or over fitting) begins when the network starts to memorise and this render it unable to generalise due to being over trained. To avoid over training, an early stopping mechanism

should be incorporated into the ANN. As the weights and biases of the network are updated continuously to minimise the MSE (Mean Squared Error) of the training data, the error of the validation data is also calculated, and if the MSE of the validation data starts to increase, training is stopped. This is known as "cross-validation". After the training phase, the ANN is used to simulate the output of a set of test data. If the ANN returns values of the output for the test data within an acceptable margin, then the ANN can be said to be successfully trained, and may be used as a predictive tool [163, 174, 175].

2.9   Laser Micromachining Process Analysis Approaches

In order to find a set of laser micromachining parameters that provides the required micro-channel dimensions for a specific application under particular processing constraints, predictive models can be used. Several statistical and numerical approaches have been utilised to predict and optimise various laser manufacturing processes including Artificial Neural Networks (ANN) [176]; genetic algorithms [177], design of experiments [5], finite elements analysis [178], ant colony optimisation [179], and fuzzy logic [180].

Due to their non-linear, adaptive, and learning ability using collected data, ANN models have been successfully applied to a large number of problems in several domain applications. For example, many researchers have applied DoE, RSM, evolutional algorithms, and ANN techniques in the area of laser welding [129, 181-187].

Back-propagation neural network algorithms have been successfully applied by Drugos et al. to predict and improve the selection of the number of laser passes required for an automated laser sheet metal bending of aluminium and steel [188]. Lee et al. used ANN modelling to predict the process outputs from the stereo-lithography rapid prototyping process [176].

Yousef et al. used ANN to model and analyse the laser micromachining material removal process [189]. In their work, these authors wanted to develop a model that they could use to select the laser micromachining parameters that would result in the

required ablation depth and width of a conical shaped crater. The test results showed that the ANN modelled level of pulse energy corresponding to specific depth and diameter was consistent with the actual level of pulse energy to a high degree of accuracy due to the adaptive properties of ANN.

Setia et al. used back-propagation ANN to model micro-fluidic via formation using laser ablation [190]. Genetic algorithms were utilised in conjunction with the ANN models to determine the input parameters for a specific channel dimensional requirement. Experimental verification demonstrated that the models produced allowed for input parameter selection such that targeted dimensional accuracy of the ablation was improved by as much as 40% for the ablated film thickness, 30% for via diameter, 9% for via wall angle, and more than 100% for via resistance.

In recent work by Dhupal et al., research incorporated experimental observations of an Nd:YAG laser machining system into an ANN model for predicting parameter settings to achieve precise micro-grooving operations on Al_2TiO_5 [139]. In this model, a multilayered feed forward neural network was combined with DoE optimisation to enable prediction of the desired outputs of laser micro-grooves. Neurons in the input layer corresponded to air pressure, lamp current, pulse frequency, pulse width, and cutting speed. The output layer corresponded to the responses such as the width at the bottom and top sections, and depth of the micro-groove. A maximum of 5% prediction error was observed between the results based on the ANN predictive model and the actual experimental observations.

2.10 Positional Analysis and Performance Measures

Among all performance parameters, specifications for accuracy, repeatability, and resolution are the most quoted. These parameters refer to how well a component performs along the desired axis of travel and are determined primarily by the drive train mechanics. These terms are not always used correctly so complete understanding of their definitions is essential in order to compare similar components [191].

53

2.10.1 Accuracy

For a specific point of interest in 3D space, accuracy is the difference between the actual position in space and the ideal position as measured by a measurement device. Stage accuracy is influenced by the feedback mechanism (such as rotary encoder), drive mechanism (such as lead screw, linear motor), and trueness of bearing ways.

2.10.2 Repeatability

Repeatability is defined as the range of positions attained when the system is repeatedly commanded to one location under identical conditions. Repeatability is additionally qualified as being unidirectional or bidirectional. Unidirectional repeatability is measured by approaching the point from one direction, and ignores the effects of backlash or hysteresis within the system. On the other hand, bidirectional repeatability measures the ability to return to the point from both directions [192].

Accuracy and repeatability (also known as precision) can be easily understood as statistical quantities. For the example in Figure 2-30, if a large number of measurements are made where the ideal motion is 1 mm the accuracy can be defined as the difference between the mean actual motion and the ideal motion. The precision can be recorded as the range of actual motions measured within two standard deviations or 95% of all occurrences. So according to Figure 2-30 example, the accuracy is 0.05 mm and the repeatability (precision) is $\pm.08$ mm.
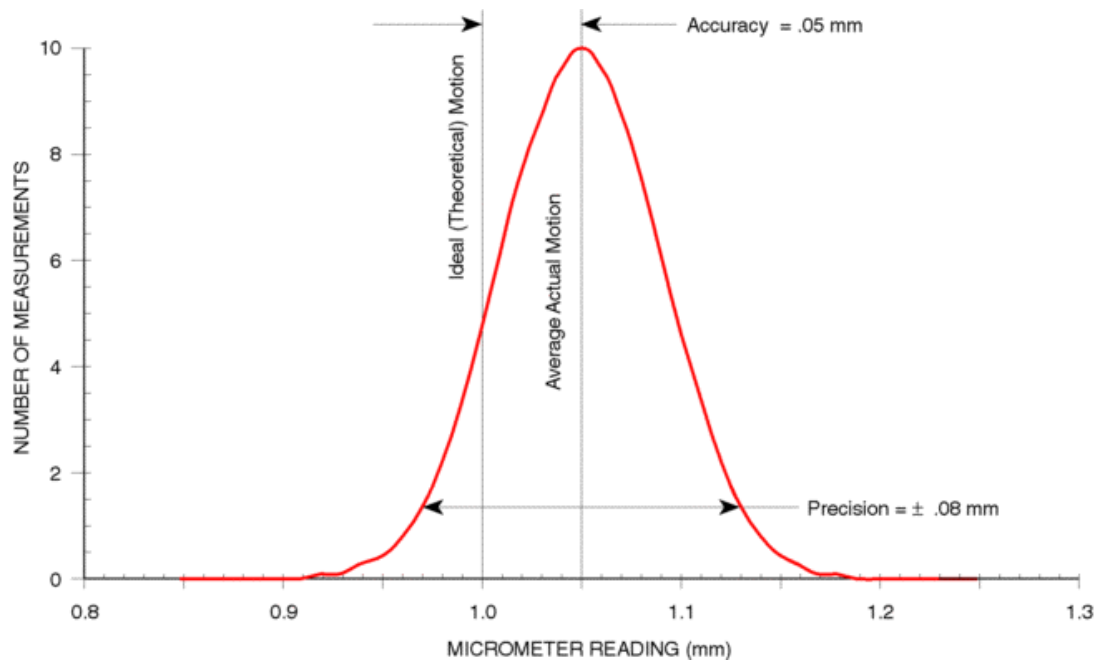
Figure 2-30: Example of statistical representation of accuracy and precision [191].

2.10.3 Resolution

Resolution is defined as the magnitude of the smallest possible movement of a positioning system. Resolution is determined by the feedback device and capabilities of the motion system. Resolution should not to be mistaken with display resolution. For example, a translation stage may have a digital readout that displays the position to four digits (i.e. 0.0001 m) which is its display resolution, while its smallest incremental movement capability is 1 mm. In this case, the position resolution is 10^{-3} m while the display resolution is 10^{-4} m [192].

2.10.4 Performance Measures Representation

Accuracy, precision, and resolution can be presented in several ways. Figure 2-31 presents a linear representation of resolution, accuracy, and repeatability of a linear robot arm.
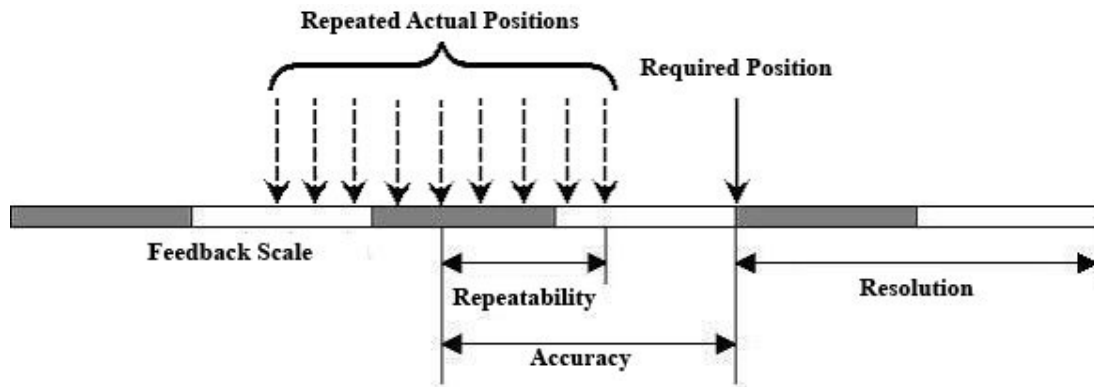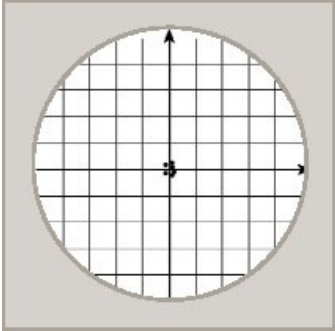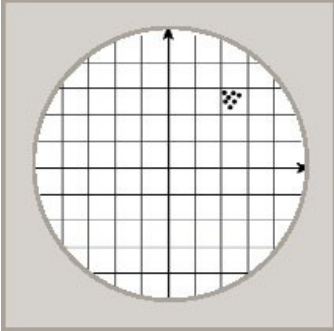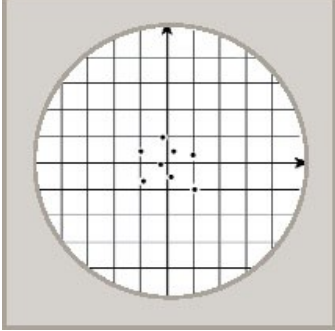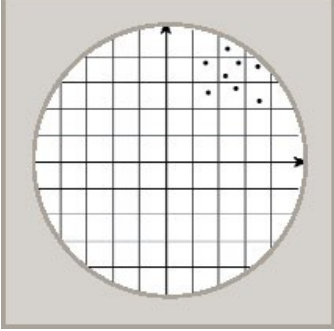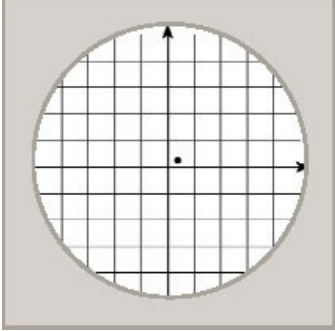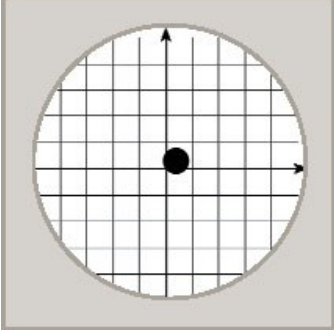
Figure 2-31: Accuracy, repeatability, and resolution linear representation [193].

These positional performance measures can be presented graphically as illustrated in Table 2-6. The target comparison analogy shown in this table is to explain the difference between accuracy and repeatability. In this analogy, repeated measurements are compared to arrows that are shot at a target. Accuracy describes the closeness of arrows to the target centre. Arrows that strike closer to the target centre are considered more accurate. The closer a system's measurements are to the accepted value, the more accurate the system is considered to be.

On the other hand, if a large number of arrows were shot, repeatability would be indicated by the size of the arrow cluster. When all arrows are grouped tightly together, the cluster is considered repeatable since they all struck close to the same spot, even if not necessarily near the target centre. The measurements are precise, though not necessarily accurate. In the last row of the table, the same analogy is used to represent fine and coarse resolution.

56

Table 2-6: Target analogy of positional performance measures.

Characteristic	Good accuracy	Poor accuracy
Good repeatability		
Poor repeatability		
	Fine resolution	Coarse resolution
Resolution		

2.11 Summary of Literature Review

In the literature review, laser micromachining applications in transparent media, the laser micromachining process parameters, internal and surface laser micromachining, the material properties of soda-lime, polycarbonate, and PMMA, and the laser micromachining process analysis approaches (such as RSM and ANN) have been presented. It can be deduced from the literature available, that the experimental work performed to date in this domain was able to describe the effects of micromachining using a large spectrum of laser systems and inspection techniques. Moreover, both surface and internal micromachining in transparent media are feasible using suitable laser choices. This process of laser micromachining in transparent materials with requirements for accurate and precise micromachining has been presented in many applications. The laser micromachining process is affected by several laser parameters including laser power, wavelength, pulse duration, and repetition frequency. Other operational parameters affect the size and geometry of the consequent structure including sample speed and type of material being processed.

Several numerical analysis techniques have been used to simulate and investigate laser micromachining process including Artificial Neural Networks (ANN) [127, 132, 134, 137, 138, 176]; genetic algorithms [177], Response Surface Methodology (RSM) [5, 127, 135, 137], finite elements analysis [178], ant colony optimisation [179], and fuzzy logic [180]. However, the prediction of the dimensions of the laser-machined micro-channels, which is an important requirement for optimisation of laser control parameters within soda lime glass, polycarbonate, and PMMA for microfluidic and micrometre scale fabrication has not been fulfilled. The lack of literature on accuracy, repeatability, and resolution of laser preparation of microfluidic channels and micrometre scales could be partially due to the large number of process variables that make it difficult to find the right parameters to get the desired dimensions of the resultant microstructure. Additionally, the large number of process variables would make it difficult to compare the reported experimental findings and relate to a specific theoretical damage mechanism. Moreover, determination of the actual damage thresholds as a function of material, laser type and processing conditions is not complete [118, 123].

Research on the use of CO_2 and Nd:YVO$_4$ lasers for the micromachining of transparent materials was limited. Nevertheless, some industries have been able to prove their potential in the field. The cost effectiveness of CO_2 and Nd:YVO$_4$ laser systems was frequently emphasised by the groups who used them. This indicates the competence and the potential of such laser systems in producing parts at lower cost compared to other laser and other processing technologies. Furthermore, since CO_2 and Nd:YVO$_4$ lasers are well known industrially and they do not require extremely sophisticated setups, their efficiency can be readily increased to match industrial production level requirements [28, 115].

RSM and ANN prediction models can be usefully employed to solve numerous industrial process control problems. These process control requirements can be driven by situations where minimum scrap is required or where structures with a high degree of precision are demanded or where laser micromachining with minimal energy is required and within plenty of other scenarios. All laser micromachining applications should benefit from optimising the geometry of microstructure utilising the above-mentioned concept, especially for the production of micro-fluidic and lab-on-a-chip devices for chemical/analytical applications and in separation science.

2.12 Units

Some important units are utilised differently within the literature, therefore considerable effort has been taken to use the international system of units (SI units) in this work or their factor units like (kilo-, milli-, etc.). The values, given in this work, are rounded, when necessary. On the other hand, the most common symbols, and abbreviations that are firmly established in the laser micromachining domain were utilised for this work. Selected parameters, symbols, and units utilised for the laser micromachining process are listed in Table 2-7.

Table 2-7: Symbols and units of some selected process parameters.

Parameter	Symbol	Unit
Laser power	P	Watts
Laser wavelength	λ	nm
Laser pulse width	τ	ns
Pulse repetition frequency	PRF	Hz
Translation speed	U	mm/s
Focal spot Diameter	W_0	μm
Laser intensity	I	W/cm^2

2.13 Hypothesis

After numerous screening trials at the start of this work, it was known that the direct writing of surface micro-channels on soda-lime glass and internal micro-channels in polycarbonate and PMMA were possible with the available CO_2, Nd:YVO$_4$, and Nd:YAG laser systems. It was hypothesised that the dimensions of the laser process parameters could be optimised and predicted for these laser systems within soda lime glass, polycarbonate and PMMA. Furthermore, it was hypothesised that the accuracy, repeatability, and resolution of the Nd:YVO$_4$, and Nd:YAG laser systems could be evaluated and micrometre level of accuracy, repeatability, and resolution could be achieved. This would allow these systems to be used for applications including microfluidic device and micrometre scale fabrication. It was hypothesised that prediction models could be developed to allow micro-channel topology prediction from the CO_2 laser surface micromachining process using RSM and ANN. Furthermore, it was hypothesised that prediction models could be developed to allow micro-channel geometry prediction and micromachining cost estimation from the Nd:YVO$_4$ laser internal micromachining process using RSM and ANN.

CHAPTER 3

MATERIALS AND METHODS

3.1 Hardware and Software Setups

3.1.1 Introduction

This section presents the hardware and software setups used in the course of this work. Three separate laser systems were investigated. These were a CO_2, a Nd:YVO$_4$, and a Nd:YAG laser system and their auxiliary pieces of hardware. Software programs developed for CAD processing, laser control, and sample positioning control, via translational stages, were examined. All programmed codes and GUIs (apart from that presented in Appendix L and Appendix O) were specifically developed for this work by the author in LabVIEW programming environment. Finally, a description of the utilised aNETka ANN software is presented.

The micromachining cost estimation assumed a linearly proportional relationship between the electrical consumption of the laser power supply and the laser power emitted by the laser head. Furthermore, it was assumed that the experimental work (such as micromachining, dimensional and non-dimensional measurements, etc.) was carried out under standard conditions for ambient temperature of 20 °C and an absolute pressure of 101.325 kPa (14.696 psi, 1 atm). These conditions were taken according to National Institute of Standards and Technology (NIST).

3.1.2 CO_2 Laser System

In order to machine micro-channels on the surface of soda-lime glass sheets, a Rofin DC 015 industrial CO_2 laser, with a maximum output power of 1500 W and 10.6 μm wavelength was used, as shown in Figure 3-1.
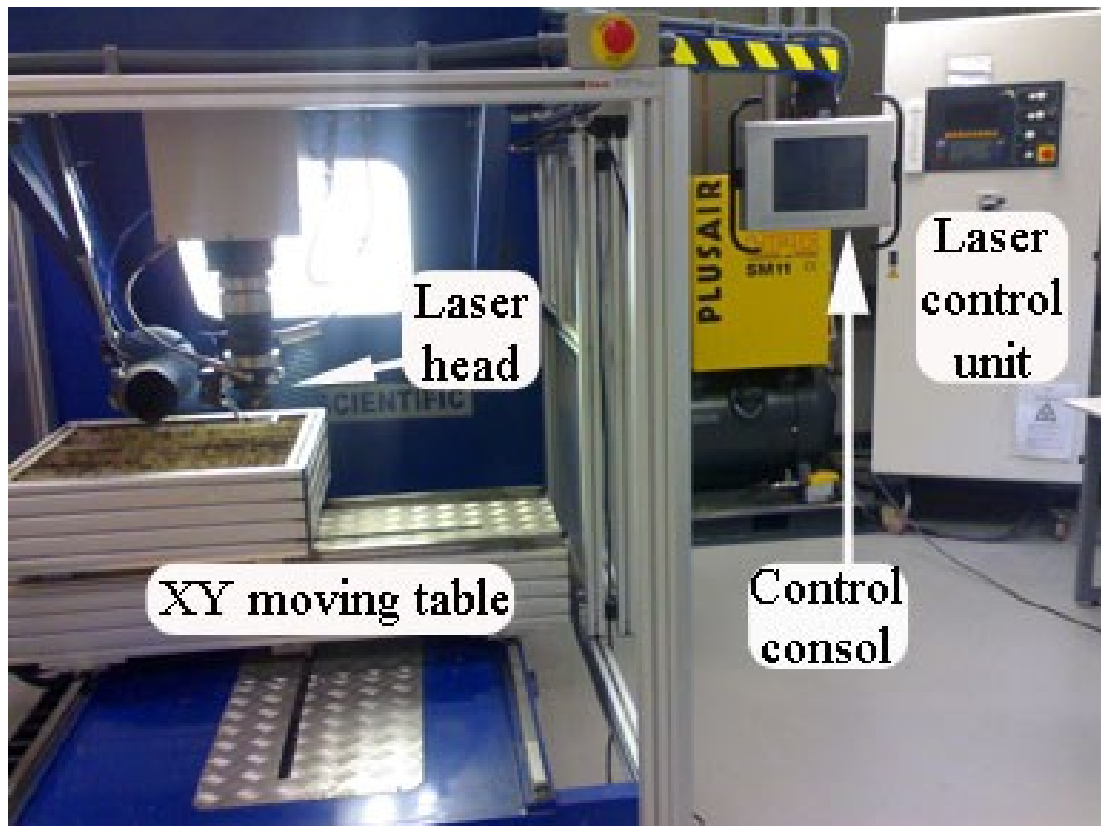
Figure 3-1: The CO_2 laser system.

The control console allowed synchronised control of the motion system and laser firing. Further description of the CO_2 laser system, laser beam, laser system control, and motion system control can be found in Appendix B. Selected specifications of the CO_2 laser system are listed in Table 3-1.

Table 3-1: Specifications of the CO_2 laser system [194, 195].

Output power	1500 W
Wavelength	10.6 μm
Excitation	Radio frequency (RF)
Operation mode	CW, pulsed
PRF range	CW or 1 - 5000 Hz
Pulse width range	26 μs – 125 ms
Translation speed	1/60 – 250/3 mm/sec
Positioning resolution	1.25 μm
Focal length	127 – 190 mm

3.1.3   Nd:YVO$_4$ Laser System

In order to machine internal micro-channels in polymers, an in-house designed and assembled Nd:YVO$_4$ laser system was used, as shown in Figure 3-2. This system was originally designed and assembled by Ahmed Issa [5]. The whole system, especially the motion control system, was redesigned from scratch and completely renovated by the current author as part of this study. This upgraded system enabled for the first time, real-time autonomous closed loop control and substantially enhanced the accuracy and reliability of the motion control system. This laser system was of 2.5 W maximum power and 1064 nm wavelength.
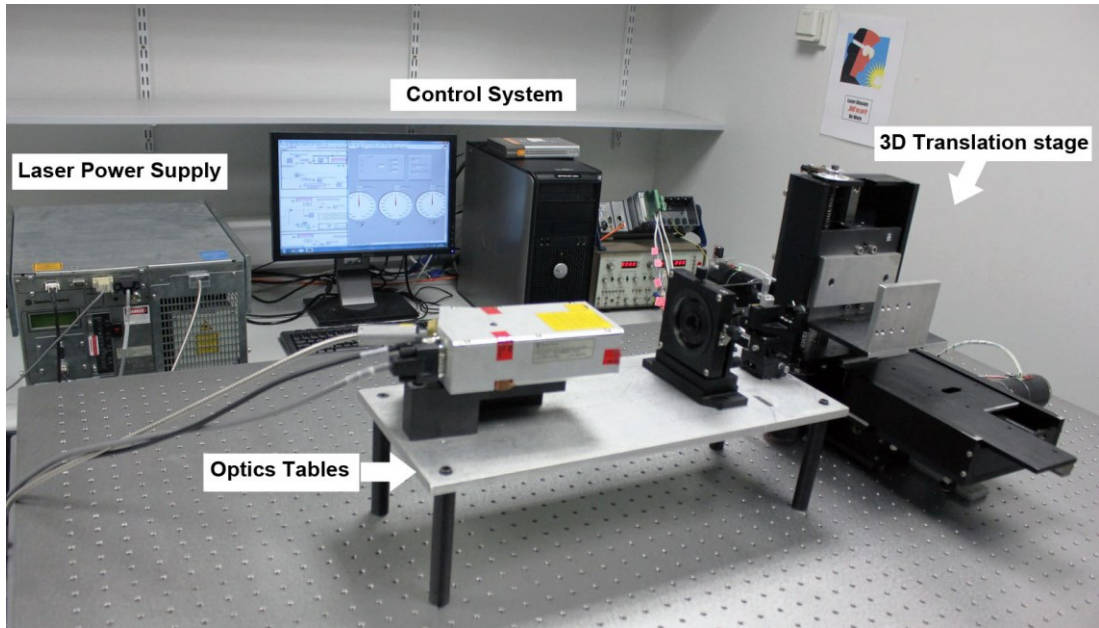
Figure 3-2: The Nd:YVO$_4$ laser system (with the enclosure removed).

A comprehensive description of the Nd:YVO$_4$ laser system, the Nd:YVO$_4$ laser power supply unit, and the optical table can be found in Appendix C, Appendix D, and Appendix E respectively. Selected specifications of the Nd:YVO$_4$ laser system are listed in Table 3-2.

Table 3-2: Specifications of the Nd:YVO$_4$ laser system.

Output power	< 2.5 W
Wavelength	1064 nm
Excitation	Radio frequency (RF)
Pulse energy, 110 kHz	>18 μJ
Pulse width, 110 kHz	80 ns
PRF range	Up to 1 MHz max

3D Translation stage

Previous positional problems with the Nd:YVO4 motion system included positioning skewness, that the hardware was incapable of giving the correct number of pulses (to the drivers of the stepper motors) during high speed motion, poor accuracy, and poor repeatability. The updated system included new Data Acquisition and Control hardware, new positional sensing elements and a significantly updated control program. These included quadrature rotary encoders and a CompactRIO FPGA unit. The CompactRIO FPGA unit was used to provide the driving frequency to all stepper motors (stages) and receive the feedback from the encoders simultaneously and in real time. This allowed the motion system to be used as a real time closed loop control system for the first time. Furthermore, it enabled the system to be capable of repeatable micrometre level accurate positioning as shown, later in this work. Figure 3-3 shows the 3D translation stage of the Nd:YVO4 laser system. A complete description of the 3D Translation stage can be found in Appendix F.
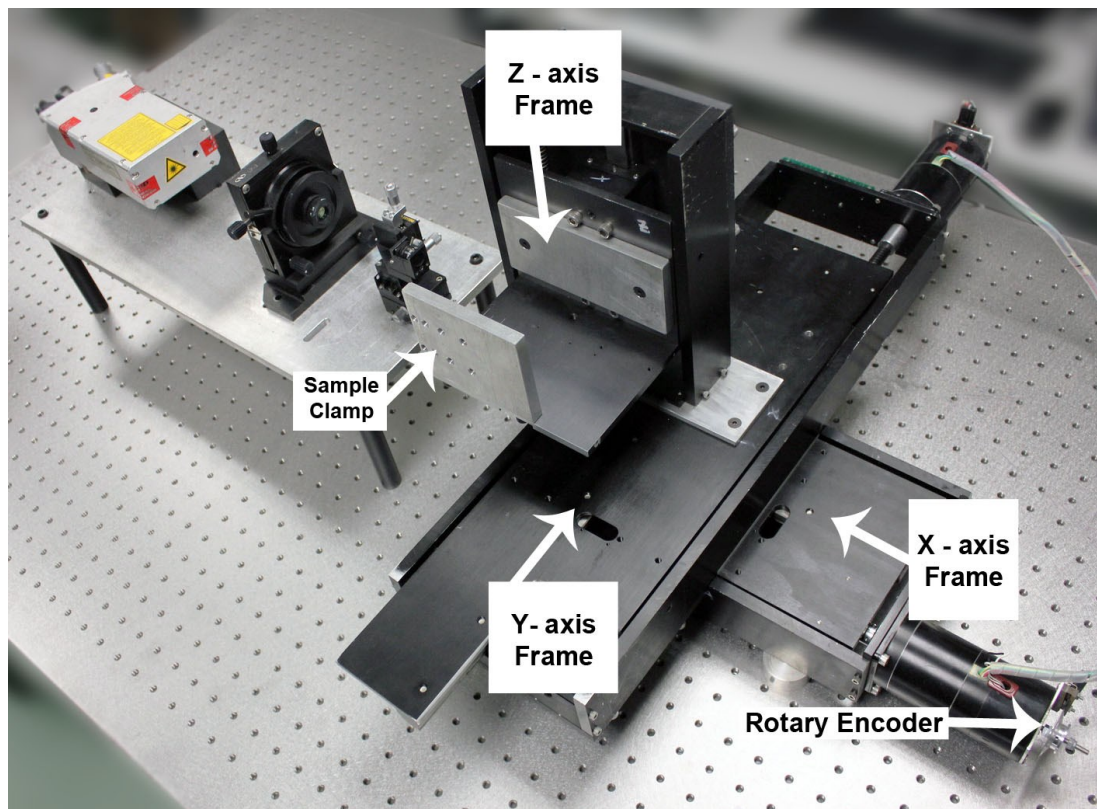
Figure 3-3: The 3D translation stage of Nd:YVO$_4$ laser system.

Laser System Control

Figure 3-4 shows the control system of the Nd:YVO$_4$ laser system. This system consisted of a control computer, motion system power supply (BWD MiniLab), a network switch (D-link), and a real time controller. The real time controller, consisted of National Instruments CompactRIO 9074 400 MHz 2M Gate FPGA (an integrated system of real-time controller and reconfigurable chassis), 8-channel, TTL digital input/output module; NI 9401, 32-channel, TTL digital input/output module; and a NI 9403 32-Ch, 5 V/TTL bidirectional digital I/O module.
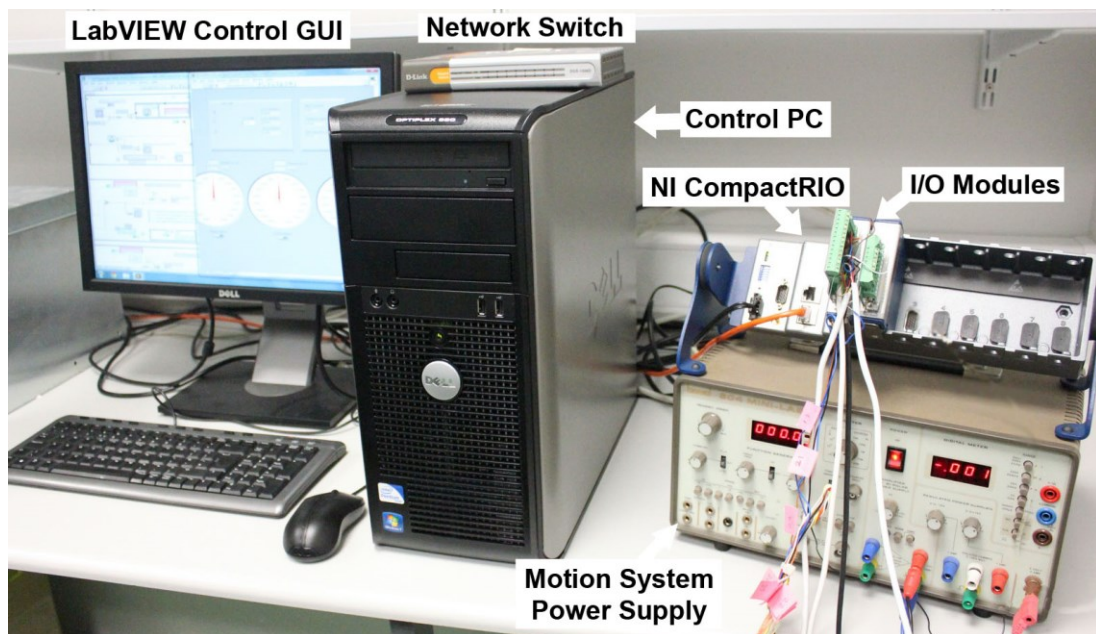
Figure 3-4: The control system of the Nd:YVO$_4$ laser system.

This real time controller was chosen carefully from a wide range of data acquisition, and instrument control products. This hardware was selected because it provided a real time combined monitoring, data logging, and control solution for the laser and motion control and can be programmed with NI LabVIEW software. Detailed descriptions of laser system control, control process layout, Nd:YVO4 laser power supply control, and motion system control can be found in Appendix G, Appendix H, and Appendix I respectively.

3.1.4   Nd:YAG Laser System

Another laser system, a Nd:YAG laser system, shown in Figure 3-5, is an in-house built and assembled system of 4 W maximum power and 1064 nm wavelength. This system was also developed for laser micromachining however, a galvanometer for X and Y positioning and a linear stage for Z positioning were used rather than a 3D translation stage. Laser firing and X-Y scanning were controlled by proprietary software WeldMark, which came with the laser and galvanometer.
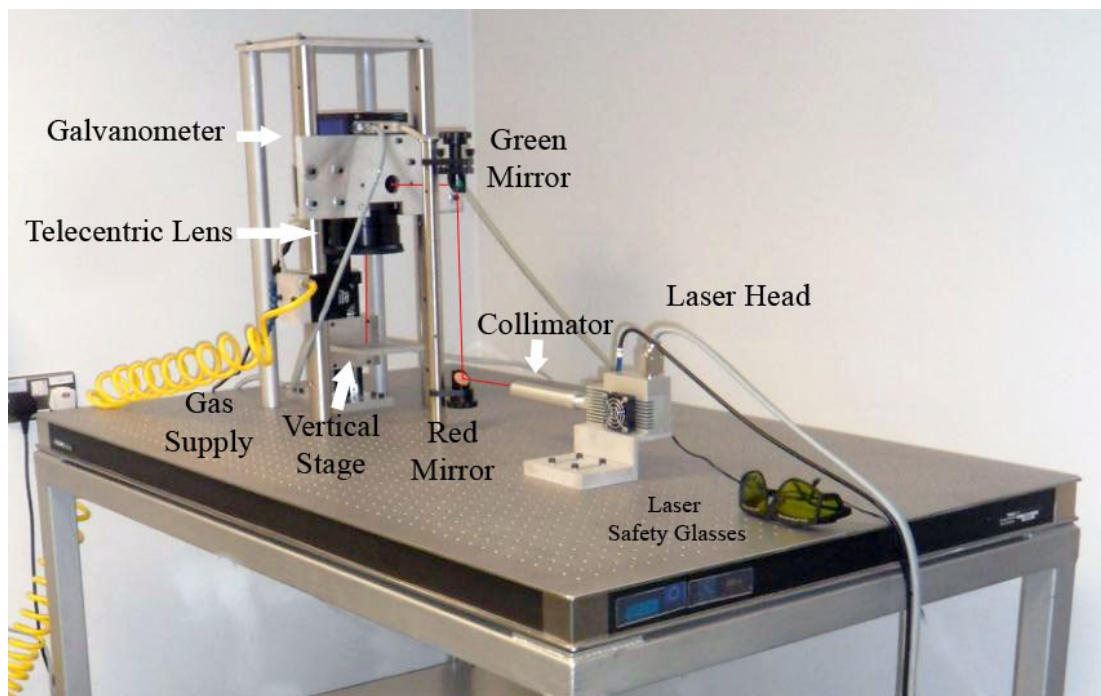
Figure 3-5: The Nd:YAG laser system (with the enclosure removed).

The author analysed the positional accuracy for micromachining with this laser system and compared it with that of the $Nd:YVO_4$ laser system. Selected specifications of the Nd:YAG laser (WEDGE 1064 HF) unit are listed in Table 3-3. A comprehensive description of the Nd:YAG laser system and its components can be found in Appendix J.

Table 3-3: Specifications of the Nd:YAG laser system (WEDGE 1064 HF) .

Output Power @ 100kHz	> 4 W
Wavelength	1064 nm
PRF range	Single shot to 100 kHz
Pulse width range	700 ps - 3 ns
Excitation	Radio frequency (RF)
Pulse energy	40 to 300 μJ
Polarization	Linear, 100:1
Cooling	Air cooled

3.1.5   Auxiliary Hardware

The modelling computer used was a DELL™ OPTIPLEX™ 780 with Intel® Core™ 2 Quad CPU Q8400 @ 2.66 GHz processor and 4 GB installed memory (RAM) and 64-bit Windows 7 operating system. This computer was used for the development of RSM and ANN predictive models. Full descriptions of stage micrometre can be found in Appendix K respectively.

3.1.6   CAD Processing Codes

LabVIEW is the National Instrument's (NI) graphical programming language. For this work, the solid/surface feature to be produced was designed in AutoCAD. For processing with the code developed, the CAD design must first be converted into STL format. The STL file format is the format used by rapid prototyping machines and provided a useful format for use in this work [196]. Using the STLOUT command in AutoCAD, the model design can be exported to an STL file. STL file format employs a method called "tessellation" for representing the CAD model surfaces as a closed volume mesh comprised of triangles.

Build files were created from the STL files which were fed to the real time controller to synchronously drive the 3D positioning stages and the Nd:YVO$_4$ laser firing. The developed build file was mainly based on slicing the STL file (tessellated model) in a

uniform manner at discrete distances, which could be specified in the developed STL file slicing program GUI. A detailed description of the CAD processing codes and GUIs can be found in Appendix L. The process of the developed algorithm used for preparing the build file is illustrated in Figure 3-6.
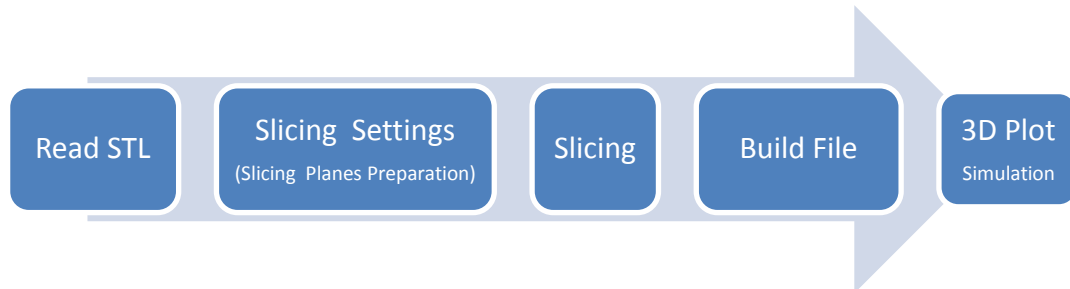
Figure 3-6: The flow chart of the CAD file processing code.

3.1.7 Nd:YVO$_4$ Laser System Positioning Control Code

After the CAD design had been processed and converted from STL format into a build file, the design is ready to be machined. Comprehensive descriptions of the automatic positioning control concept and the developed Nd:YVO$_4$ laser system motion control sub-codes and GUI can be found in Appendix M, and Appendix N respectively.

3.1.8 Nd:YVO$_4$ Laser System Laser Control Code

The development of a new code for controlling the laser operation was needed. The operation parameters of the T-Series laser power supply unit were controlled via RS232 serial communication. Commands to the T-Series power supply consisted of strings of semicolon terminated ASCII characters. For sending these commands, a LabVIEW serial port read-write code was developed. A comprehensive description of the OEM serial communication syntax and developed Nd:YVO$_4$ laser system laser control sub-codes and GUI can be found in Appendix O.

3.1.9 aNETka

Zurek et al. wrote a detailed ANN code in LabVIEW 5.1, called aNETka, and used it originally to investigate the magnetic properties of magnetic cores. This code allows

the generation of ANN models that are fully interconnected and of feed-forward structure with error back-propagation algorithm. This program allows a maximum of eight layers and 100 neurons per layer. Three activation functions (linear, sigmoid and tangent hyperbolic) are selectable with automatic data linear normalising between 0.05 and 0.95. This code effectively controls the training phase of the ANN in order to reach a selected Root Mean Square (RMS) error. This allows ANN models with very high degree of accuracy to be reached [197, 198]. aNETka operated according to error back-propagation learning. That consists of two passes through the different layers of the network: a forward pass and a backward pass. In the forward pass, an input vector is applied to the input layer of the network, and its effect propagates through the network layer by layer. Finally, a set of outputs is produced as the actual response of the network. During the forward pass, the synaptic weights of the networks are all fixed. During the backward pass, on the other hand, the synaptic weights are all adjusted in accordance with an error-correction rule. Specifically, the actual response of the network is subtracted from a desired (target) response to produce an error signal. This error signal is then propagated backward through the network against the direction of synaptic connections, hence the name "error back-propagation." The synaptic weights are adjusted to make the actual response of the network move closer to the desired response in a statistical sense [162].

There are many commercial software packages, which allow the use of ANN (MATLAB, QNET, etc.), but their main disadvantage is that they are "commercial". Since DCU has a site license for LabVIEW, then aNETka can be freely used without any additional cost. Moreover, aNETka is an open source code, so the source files can be modified as required.

aNETka was written in an old version of LabVIEW, and was therefore partly modified and updated to make it compatible with the current version of LabVIEW. aNETka consists of two main codes (Train aNETka, and Recall aNETka), and a library of subprograms all in one folder. All data handling is performed automatically during the execution, and the user is only asked to intervene if absolutely needed. A description of how to use the Train aNETka code is illustrated

in Appendix P, and a description of how to use the Recall aNETka is illustrated in Appendix Q.

3.2 Glass Experiments with CO_2 Laser System

In this section, the experimental design, the micro-channel width and depth measurement, and ANN model setup for the surface micro-channels on soda-lime glass using the CO_2 laser system are discussed.

3.2.1 Equipment and Materials Utilised

The laser system used was the CO_2 laser system presented in section 3.1.2. The in-house built laser surface profile scanning system was used for micro-channel width and depth measurement. The modelling computer used was the DELL™ OPTIPLEX™ 780 noted above. This computer was employed in the development of ANN predictive models. These predictive models were set up to predict the width and depth of laser machined micro-channels. A two-millimetre thick soda-lime glass sheet was the sample material.

3.2.2 Experimental Design

A series of experiments were performed to determine the relationship between the main laser emission parameters of the CO_2 laser and the dimensions of corresponding produced micro-channels. After initial screening experiments, a factorial design of experiments was conducted, using Design-Expert software, to analyse the outcomes of these laser micromachining parameters on the dimensions of the resulting micro-channels. Three process parameters analysed in this work were the laser power, PRF and translation speed of the glass sample. Each of these were analysed at three levels in the form of a 3^3 factorial design of experiments.

Table 3-4: Control parameters levels and their corresponding DoE coding.

Variables	Actual			Coded		
	Low	Mid	High	Low	Mid	High
P (W)	18	24	30	-1	0	1
PRF (Hz)	160	228	400	-1	-0.433	1
U (mm/sec)	5/3	15/3 = 5	25/3	-1	0	1

The low, middle, and high levels chosen for power, pulse repetition frequency, and Translation speed are shown in Table 3-4. The low level is represented by -1, the middle by 0 and the high level by 1. A slightly off-centre value of 228 Hz was chosen for the pulse repetition frequency. This is coded as -0.433 for the design of experiments which represents the degree of shift from the central position for this parameter. This shift from the central position was due to hardware capabilities of the laser system. Since millimetre per minute was the speed unit used in the motion control console, the fraction values of translation speed values measured in millimetre per second were practically justified.
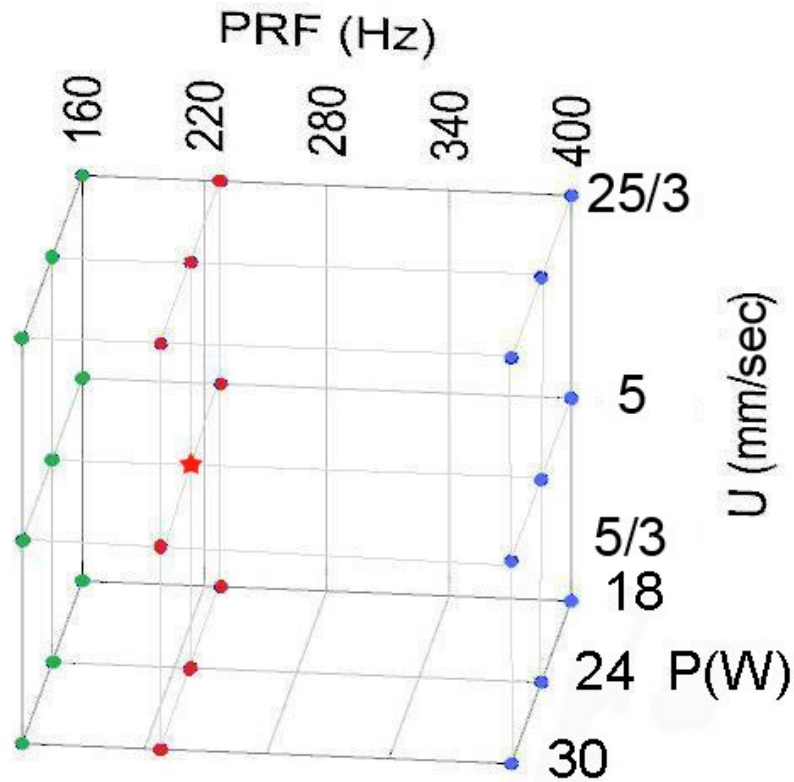
Figure 3-7: 3D representation of the investigated process control parameters.
★ indicates where five additional experiments were repeated.

There are 27 possible combinations of the three process parameters at the three levels. Figure 3-7 shows the distribution of designed experiments in the 3D experimental data space. For repeatability analysis, Experiment number 14 (the middle point, where (P=24 W, PRF=228 Hz, U=5 mm/sec)) was repeated five additional times, such that the total number of experiments conducted was 32 (=3^3+5). Table 3-5 shows a list of these 32 combinations of the process control parameters that were used in the conducted experiments. The run order, presented in Table 3-5 as "Run order", is a random order according to which experiments were conducted in order to reduce experimental bias errors.

Table 3-5: List of process control parameters of the experiments performed.

Std order	Run order	P W	PRF Hz	U mm/sec	Std order	Run order	P W	PRF Hz	U mm/sec
1	25	18	160	5/3	17	14	24	400	5
2	16	24	160	5/3	18	20	30	400	5
3	22	30	160	5/3	19	10	18	160	25/3
4	8	18	228	5/3	20	19	24	160	25/3
5	31	24	228	5/3	21	3	30	160	25/3
6	29	30	228	5/3	22	2	18	228	25/3
7	27	18	400	5/3	23	21	24	228	25/3
8	28	24	400	5/3	24	7	30	228	25/3
9	18	30	400	5/3	25	13	18	400	25/3
10	1	18	160	5	26	24	24	400	25/3
11	30	24	160	5	27	12	30	400	25/3
12	32	30	160	5	28	5	24	228	5
13	26	18	228	5	29	11	24	228	5
14	9	24	228	5	30	6	24	228	5
15	4	30	228	5	31	17	24	228	5
16	15	18	400	5	32	23	24	228	5

3.2.3 Experimental Procedure

The experiments were carried out according to the following procedure:

1- The soda-lime sheet was mounted on the XY stage of the CO_2 laser system.
2- A starting position near the bottom left corner of the glass sheet was set for the first channel.

3- The processing parameters, according to the run order sequence in Table 3-5 were fed into the control console.

4- To initiate laser processing, the laser beam and the XY stage were simultaneously and automatically switched on, by the control console, to fabricate a 15 mm long channel.

5- The XY stage moved the sample so that it was brought back to the starting position of current micro-channel and then moved to the starting position of the next micro-channel. This was achieved by moving the XY stage a 10 mm distance in the direction perpendicular to the axis of micro-channel.

6- The last three steps were repeated until all experiments in Table 3-5 were carried out.

7- Using a glass cutting tool, the glass sheet was cut to smaller sheets to facilitate post inspection, and micro-channels width and depth measurement.

8- To clean the micro-channels from any residuals, the samples were cleaned using water.

9- Using the laser surface profile scanning system, all micro-channels were scanned.

10- Using the scanning system LabVIEW GUI and for each micro-channel, a dimensional profile was taken, schematic of which is shown in Figure 3-8, then the width and depth were measured.

11- The measured data were typed into Excel spreadsheet files, to be used, at later stage, for the statistical analysis and process modelling [5].

3.2.4   Micro-Channels Width and Depth Measurement

The width and depth of every micro-channel were measured. Each of these experiments was performed three times to get an average value of these surface topography characteristics, and an indication of the degree of repeatability. The width and depth dimensions of the micro-channels for each experiment were measured at three different locations along the produced micro-channel. The measurement system used was an in-house built laser profilometer that had a 1.95 μm resolution in the X and Y-direction and a 0.5 μm resolution in the Z-direction

75

[199]. Average values and 95% confidence intervals for the micro-channels width and depth measurements were determined. Figure 3-8 shows a schematic of a micro-channel depicting the studied outcomes.

The point pair, between which the width was measured, was picked using the cursors, manually controlled over the laser profilometer scans on the scanning system LabVIEW GUI, and by looking at all views of the micro-channel. In some micro-channel scans, the build-up zone was higher than the unprocessed glass surface. Generally, the unprocessed glass surface was first found by moving the cursors in the Z-direction when viewing the scanned surface edge in the direction of the X-axis. Then the isometric view of the micro-channel was examined and the cursors moved again in the X and Y-direction until the locations defining the highest points on opposite edges of the micro-channel were found. This pair of points was recorded and the displacement between them was recorded as the micro-channel width. This procedure was repeated for three different locations along the micro-channel axis and the average was calculated. A similar procedure was followed to record the micro-channel depth [5].
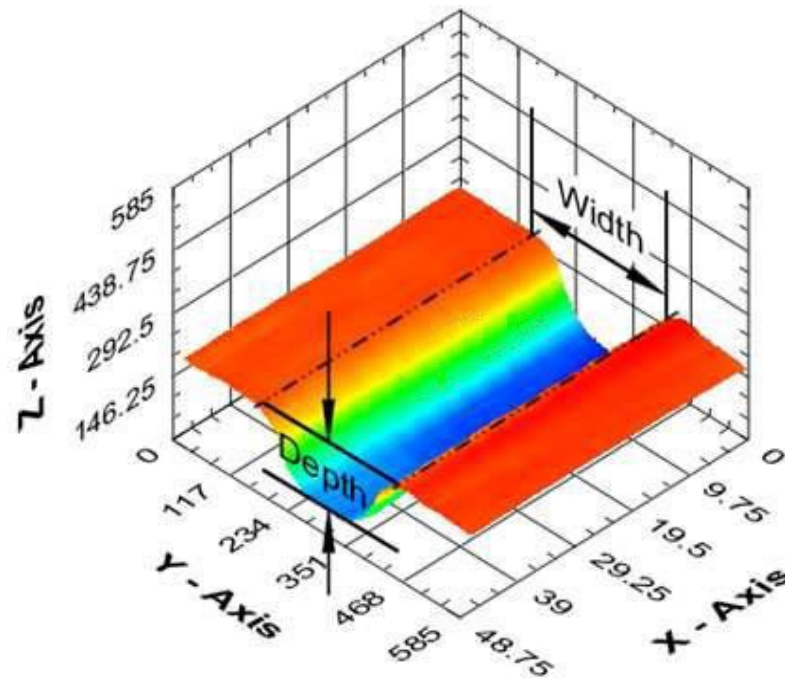
Figure 3-8: Micro-channel schematic highlighting the width and depth.

76

3.2.5   ANN Model Setup

The measurement results of the five repeated-experiments were averaged with their original experiment reducing the overall number of available data from 32 to 27 unique experiments. These measurement results provided the data set from which training sets were chosen for the subsequent ANN modelling.

Three ANN models were developed for each output (micro-channel width and depth) using the three inputs P, PRF, and U. These models were developed in order to examine the influence of changing the number and the selection of training data on the prediction capability of the ANN model. These ANN predictive models were based on three different training data sets. as follows:

- Model I: 24 randomly selected experiments (from the 27 experiments) were utilised as a training data set to train the network;

- Model II: the experiments from the eight corner points from the experimental data space and seven randomly selected experiments (15 in total) were utilised as a training data set to train the network;

- Model III: 15 randomly selected experiments were utilised as a training data set to train the network.

The remaining three experiments for model I, and 12 experiments for models II and III were utilised as confirmation experiments. These confirmation experiments were used for verification purposes in order to evaluate the predictive capabilities of the ANN predictive models. Figure 3-9 shows a representation of the training data distribution in 3D experimental data space, for (a) model I, (b) model II and (c) model III. The number of data available for training and verification was limited in this work to the 27 data points. The percentage of training experiments to overall data was set to a high level for model I compared to model II and III.
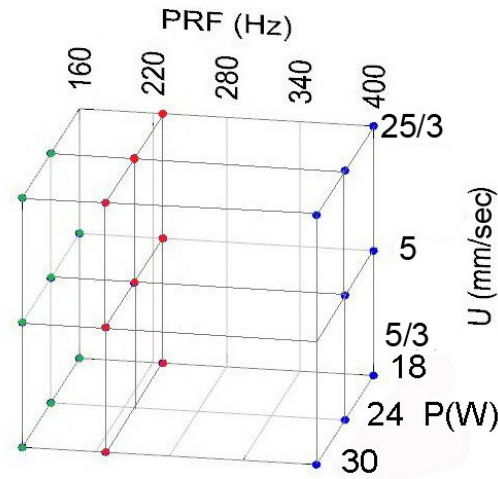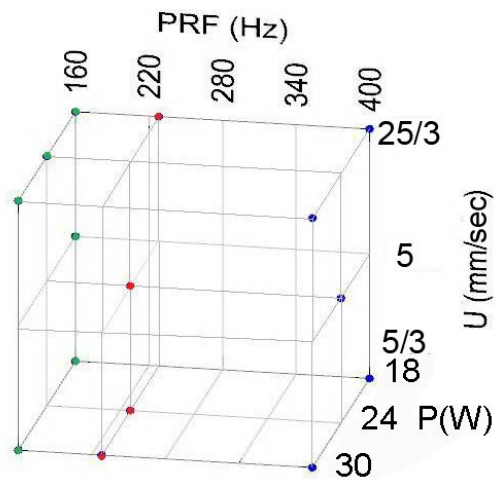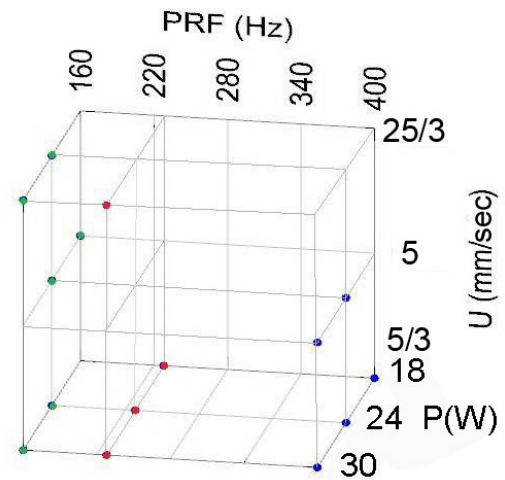
Figure 3-9: Representation of the training data
for (a) model I, (b) model II and (c) model III.

3.2.6   Configuration of ANN Models

The developed models were designed and run with the aNETka software in feed-forward back-propagation ANN mode. Due to the absence of a quantifiable method for a priori evaluation of the best network architecture, intensive trial and error examination was carried out in order to optimise the configuration of the ANN. Two ASCII text spreadsheet input files were used for each model. The first one contained the training data inputs and corresponding outputs for the training stage. The second one contained the confirmation experiments inputs and their outputs for the

verification stage, where the best network architecture is identified. As indicated in the literature review chapter, laser micromachining process is a quite complicated process for which to produce an accurate predictive model. Therefore, the number of hidden layers was varied between one and three in order to investigate the number of layers required to model the process. The number of nodes (neurons) in each of the hidden layers was varied between four to 80 neurons. A schematic description of the investigated ANN schemas is shown in Figure 3-10.
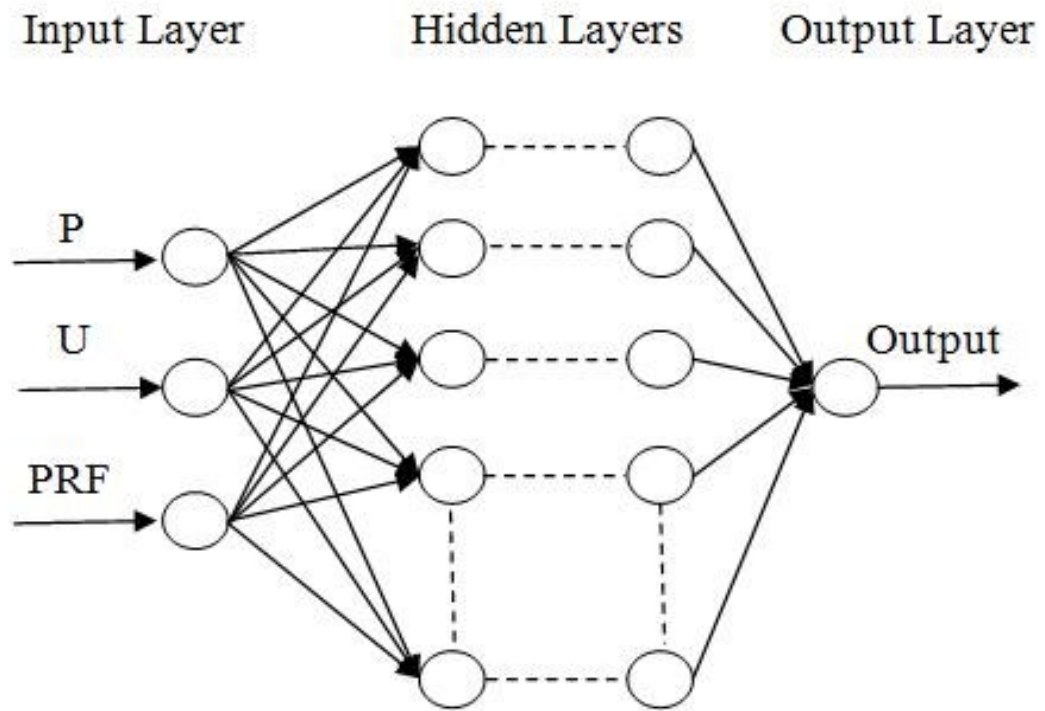
Figure 3-10: A schematic description of the investigated ANN schemas.

Inputs and outputs were linearly normalized, automatically within aNETka, in the range of 0.05–0.95. A transfer sigmoid function was utilised, since this nonlinear function has good generalisation capability. The learning rate parameter was set during simulation to control the magnitude of weight and bias updates. The selection of this value significantly affected the training time of the ANN. Another parameter, the momentum, was used to decrease the likeliness of the simulation becoming stuck in local optima. Experimentally, after screening trials, the learning rate was manually set at a value between 0.0001 and 6.0000 depending on the simulation during

training process and the momentum was fixed at a medium value of 0.8 for all ANN models.

In the training mode of aNETka, the training data was iteratively passed one by one through the ANN structure and the weights were automatically adjusted after each pass. In an effort to minimise the training error and avoid over training, only part (about 70%) of the training data was used to train the network, and the rest (about 30%) was randomly selected, by the aNETka, and set aside as test data set. This test data set was utilised as a validation set, a criterion to decide when to stop the training, and to test the generalisation capabilities of the ANN model being developed. The training interface of the aNETka code provided a graphical chart of real time RMS values. During the ANN model development, this graphical chart was unceasingly supervised so that ANN configurations with the highest prediction capability, i.e. lowest RMS, could be obtained for each model. If the training RMS and testing RMS decreased then the ANN was still learning (generalising). However, if the training RMS decreased and test RMS began to increase then the ANN would have begun to memorize (be over-trained). During training mode, models for which the RMS error increased during training were discarded. The process of model generation was then re-initialised to produce a better ANN model. Experimentally, after screening trials, only models with RMS error below 0.001% were accepted. The number of iterations was kept as low as possible during formulation of the ANN model. Approximately, 15-30 minutes was needed to achieve the target RMS value for each developed ANN setup/architecture.

3.3   Polymer Experiments with Nd:YVO$_4$ Laser System

In this section, the experimental design, the micro-channel width measurement and processing cost estimation, and ANN model setup for the internal micro-channels on polycarbonate and PMMA using the Nd:YVO$_4$ laser system is discussed.

3.3.1   Equipment and Materials Utilised

The Nd:YVO$_4$ laser system, presented in section 3.1.3, was used for internal micro-machining. The Reichart Microscope was used for the micro-channel width measurement. The modelling computer used was a DELL™ OPTIPLEX™ 780 as noted above. This computer was employed in the development of RSM and ANN predictive models. These predictive models were set up to predict the width of laser machined micro-channels and their associated cost. Ten-millimetre thick polycarbonate and PMMA 60×80 mm sheets were the sample materials.

3.3.2   Experimental Design

A series of experiments were designed to determine the relationship between the main laser process parameters of the Nd:YVO$_4$ laser, the machining process cost, and the dimensions of corresponding produced micro-channels. After initial screening experiments, a factorial design of experiments was carried out using Design-Expert software. This was done to analyse the outcomes of laser micromachining parameters on the dimensions and cost of the resulting micro-channels. The three process parameters analysed in this work were the laser power, PRF and translation speed of the processed sample. Each of these were analysed at three levels in the form of a 3^3 factorial design of experiments.

Table 3-6: Control parameters levels and their corresponding DoE coding.

Variables	Actual			Coded		
	Low	Mid	High	Low	Mid	High
P (W)	0.5	1.0	1.5	-1	0	1
PRF (Hz)	13	23	33	-1	0	1
U (mm/sec)	0.50	1.74	2.98	-1	0	1

The low, middle, and high levels were chosen for power, PRF and translation speed. Table 3-6 shows the experimental levels of the laser input parameters. The low level is represented by minus one, the middle by zero, and the high level by one.
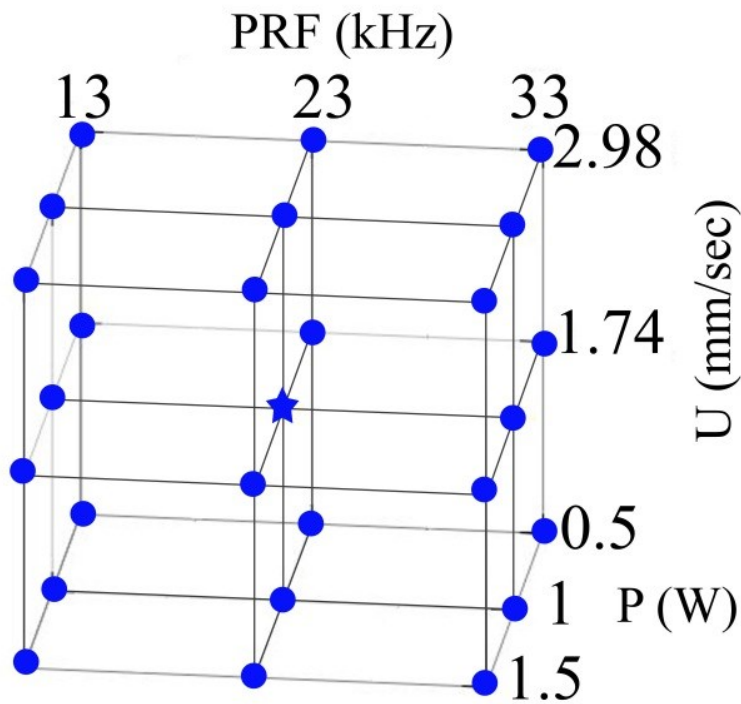
Figure 3-11: 3D representation of the investigated process control parameters.
★ indicates mid-point where five additional experiments were repeated.

There are 27 possible combinations of the three process parameters at the three levels. Figure 3-11 shows the distribution of designed experiments in the 3D experimental data space. For variability analysis, five additional experiments were

repeated at the middle point of the investigated ranges, where (P=1 W, PRF=23 kHz, U=1.74 mm/sec), such that the total number of experiments conducted was 32 (=3^3+5). Table 3-7 shows a list of these 32 combinations of the process control parameters that were used in the conducted experiments. The run order, presented in Table 3-7 as Run #), is a random order according to which the experiments were conducted in order to reduce experimental bias errors.

Table 3-7: List of the performed experiments.

Std order	Run order	P W	PRF kHz	U mm/sec	Std order	Run order	P W	PRF kHz	U mm/sec
1	23	0.5	13	0.5	17	1	1	33	1.74
2	15	1	13	0.5	18	16	1.5	33	1.74
3	11	1.5	13	0.5	19	4	0.5	13	2.98
4	20	0.5	23	0.5	20	9	1	13	2.98
5	14	1	23	0.5	21	8	1.5	13	2.98
6	32	1.5	23	0.5	22	7	0.5	23	2.98
7	2	0.5	33	0.5	23	21	1	23	2.98
8	17	1	33	0.5	24	12	1.5	23	2.98
9	28	1.5	33	0.5	25	27	0.5	33	2.98
10	24	0.5	13	1.74	26	10	1	33	2.98
11	22	1	13	1.74	27	26	1.5	33	2.98
12	30	1.5	13	1.74	28	6	1	23	1.74
13	3	0.5	23	1.74	29	31	1	23	1.74
14	18	1	23	1.74	30	13	1	23	1.74
15	5	1.5	23	1.74	31	25	1	23	1.74
16	29	0.5	33	1.74	32	19	1	23	1.74

3.3.3   Experimental Procedure

Micro-channels were produced in polycarbonate & PMMA sheets of 10 mm thickness. To facilitate post-development measurement, the distance between each two micro-channels was set to 2 mm. The sample position was set at the start of each experiment such that the focal plane of the laser is beyond the back surface plane along the X-axis. This enabled the laser micromachining process to be started with the focused laser spot on the back surface of the sample (see Figure 3-12).
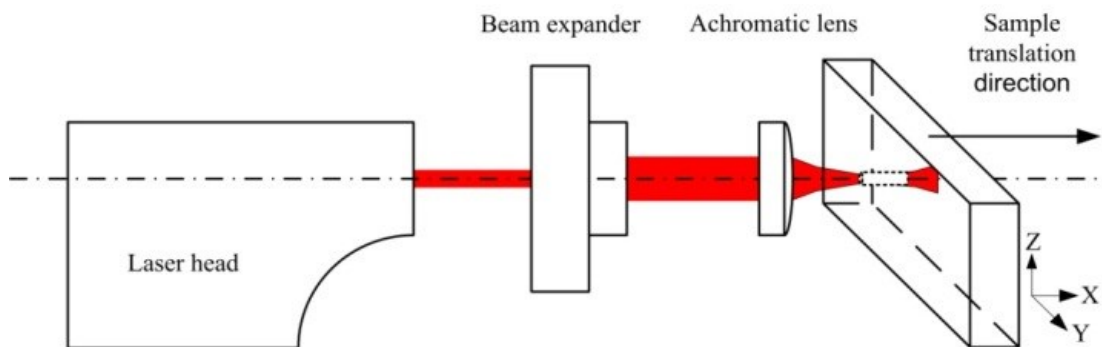
Figure 3-12: Laser micromachining optical components arrangement.

The sample was mounted on the 3D translation stage and then moved along the X-axis away from the laser source, creating the micro-channel from the back to the front of the sample. This novel direct writing procedure avoided the creation of surface micro-channels, which will require a difficult and rather fragile subsequent bonding. Figure 3-12 shows optical components setup and the work piece.

3.3.4   Micro-Channels Width Measurement

The micro-channel width is the transverse diameter perpendicular to the longitudinal direction (direction of laser firing) of the micro-channels machined within the polycarbonate blocks (see Figure 3-12). The micro-channel width (diameter) for each experiment was measured at three different locations along the produced micro-channel and the average values were determined. Theses dimensional measurements were carried out using Reichart optical microscope and OMNIMET image analysis software.

3.3.5 Micromachining Cost Estimation

Processing cost can be approximated as micromachining cost per length for a specific laser micromachining operation. In this approach, unplanned maintenances and breakdowns have not been taken into consideration. Furthermore, labour cost was not considered since the Nd:YVO$_4$ laser was for experimental purposes. However, labour cost should be considered when dealing with operational systems.

Table 3-8: Produced micro-channel estimated cost per hour breakdown.

Element of cost	Calculations	Cost €/hr
Laser power supply	(800 W) (€0.16/kW hr) (P/2) / 1000	0.064×P
DELL PC OPTIPLEX 380 & monitor	(140 W)(€0.16/kW hr) / 1000	0.0224
CompactRIO - control power	(8.2 W) (€0.16/kW hr) / 1000	0.0013
D-link network switch	(4.5 W) (€0.16/kW hr) / 1000	0.0007
BWD MiniLab - motion power	(43 W) (€0.16/kW hr) / 1000	0.0069
Diode replacement	(€ 11,410 / 10000 hr)	1.141
Maintenance labour	(12 hr/2000 hr operation) (€ 50/hr)	0.3
Total estimated micromachining cost per hour		1.4723 + 0.064×P

Table 3-8 presents a breakdown of the developed micro-channel estimated cost per hour. This estimation assumed a linearly proportional relationship between the electrical consumption of the laser power supply and the laser power emitted by the laser head. This justifies the division of the laser power values (in Watts) by two, the actual value of maximum Nd:YVO$_4$ laser power, for the laser power supply electrical consumption estimation. Several measurements of the Nd:YVO$_4$ laser power supply electrical consumption, using an electric meter, was done to test the assumption above-mentioned. All results were very close to the estimated values and confirmed that the assumption is reasonable and valid.

The electric consumption of the control computer, real time controller, network switch, and motion power supply were taken into account. Furthermore, after e-mail correspondence with the laser system manufacturer, they recommended a laser diode replacement after every ten thousand working hours and quoted it at € 11,410. Additionally, they recommended 12-hour maintenance for each two thousand operation time. Fifty euro was used as an estimate cost of maintenance labour per hour.

The kilowatt-hour energy cost was quoted by the electricity provider at € 0.16 (including tax). Some items of the Table 3-8 were divided over a thousand to reach a unit agreement among the items on €/hr. The total estimated operating cost per hour could be expressed, as a function of the output power, by $1.4723 + 0.064 \times P$.

$$\text{cost } [\text{€/m}] = \frac{1.4723 + 0.064 \times P \; \frac{€}{hr}}{(0.85) \times U \left[\frac{mm}{sec}\right]\left[3600 \; \frac{sec}{hr}\right]\left[\frac{m}{1000 \; mm}\right]}$$

$$= \frac{(0.481 + 0.021 \, P)}{U} \qquad\qquad 3\text{-}1$$

Assuming 85% utilisation, and converting all the units into SI units, the total approximated operating cost per unit length (measured in €/m) is given by Equation 3-1.

3.3.6   ANN Model Setup

The width measurement results of the five repeated-experiments were averaged with their original experiment, while the estimated micromachining cost per hour is the same for all of the five repeated-experiments. This allowed reducing the overall number of available data from 32 experiments to 27 unique experiments.

Polycarbonate ANN Models

The 27 experiments and their results (27 for width and 27 for micromachining cost) provided the data set from which training sets were chosen for the subsequent ANN

modelling. Three ANN predictive models were developed for the width and another three for micromachining cost estimation using the three inputs P, PRF, and U. These models were developed in order to examine the influence of changing the number and the selection of training data on the prediction capability of the ANN model. These ANN predictive models were based on three different training data sets as follows:

-Model I: 24 randomly selected experiments (from the 27 experiments) were utilised as a training data set to train the network;

-Model II: 14 experiments, selected according to the Face-Centred Cubic (FCC) Design, were utilised as a training data set to train the network;

-Model III: 13 experiments, selected according to the Box-Behnken Design, were utilised as a training data set to train the network.

All 27 experimental data were utilised as confirmation experiments. These confirmation experiments were used for verification purposes in order to evaluate the predictive capabilities of the ANN predictive models. Figure 3-13 shows a representation of the training data distribution in 3D experimental data space (a) for model I, (b) for model II, and (c) for model III. The number of data available for training and verification was limited to the 27 data points. The percentage of training experiments to overall data was set to a high level for model I compared to model II and III. The training set of models II & III were selected according to two popular designs; FCC Design & Box-Behnken Design respectively. These two designs were selected in order to investigate which design should be chosen in case a limited number of experiments are allowed. This scenario could be when carrying out the experiments is lengthy, expensive, difficult, or dangerous.
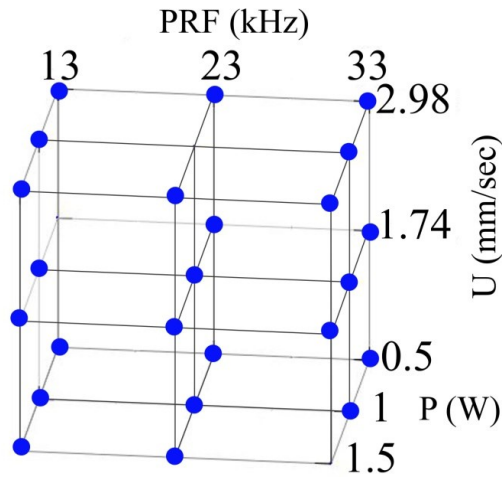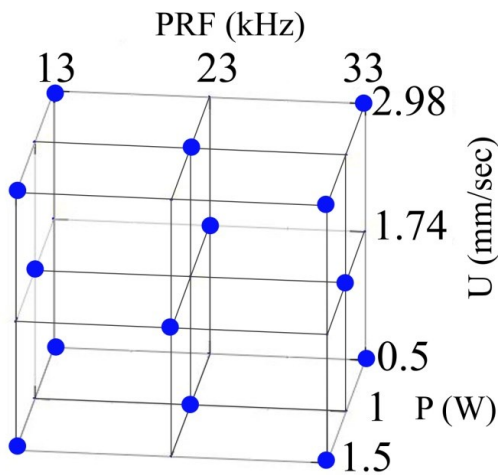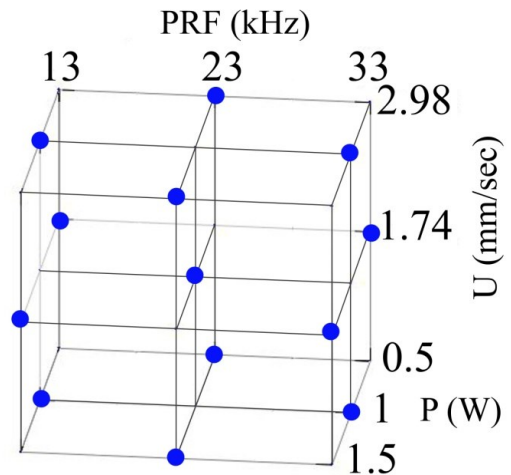
Figure 3-13: Schematic representation of the training data for (a) model I, (b) model II, and (c) model III.

PMMA ANN Models

The micro-channels dimensional measurement and micromachining cost estimation results (27 for width and 27 for depth) provided the data from which training sets were chosen. Four ANN predictive models were developed for the width and another four for micromachining cost estimation using the three inputs P, PRF, and U. These models were developed in order to examine the influence of changing the number

and the selection of training data on the prediction capability of the ANN model. These ANN predictive models were based on four different training data sets as follows:

-Model I: 24 randomly selected experiments (from the 27 experiments) were utilised as a training data set to train the network;

-Model II: 14 experiments, selected according to the Face-Centred Cubic (FCC) Design, were utilised as a training data set to train the network;

-Model III: 13 experiments, selected according to the Box-Behnken Design, were utilised as a training data set to train the network;

-Model IV: 14 randomly selected experiments were utilised as a training data set to train the network.

All 27 experimental data were utilised as confirmation experiments. These confirmation experiments were used for verification purposes in order to evaluate the predictive capabilities of the ANN predictive models. Figure 3-14 shows a representation of the training data distribution in 3D experimental data space (a) for model I, (b) for model II, (c) for model III, and (d) for model IV. The number of data available for training and verification was limited to the 27 data points. The percentage of training experiments to overall data was set to a high level for model I compared to model II, III and IV. The training set of models II & III were selected according to two popular designs; FCC Design & Box-Behnken Design respectively. These two designs along with model IV were selected in order to investigate which design should be chosen in case a limited number of experiments are allowed. This scenario could be when carrying out the experiments is lengthy, expensive, difficult, or dangerous.
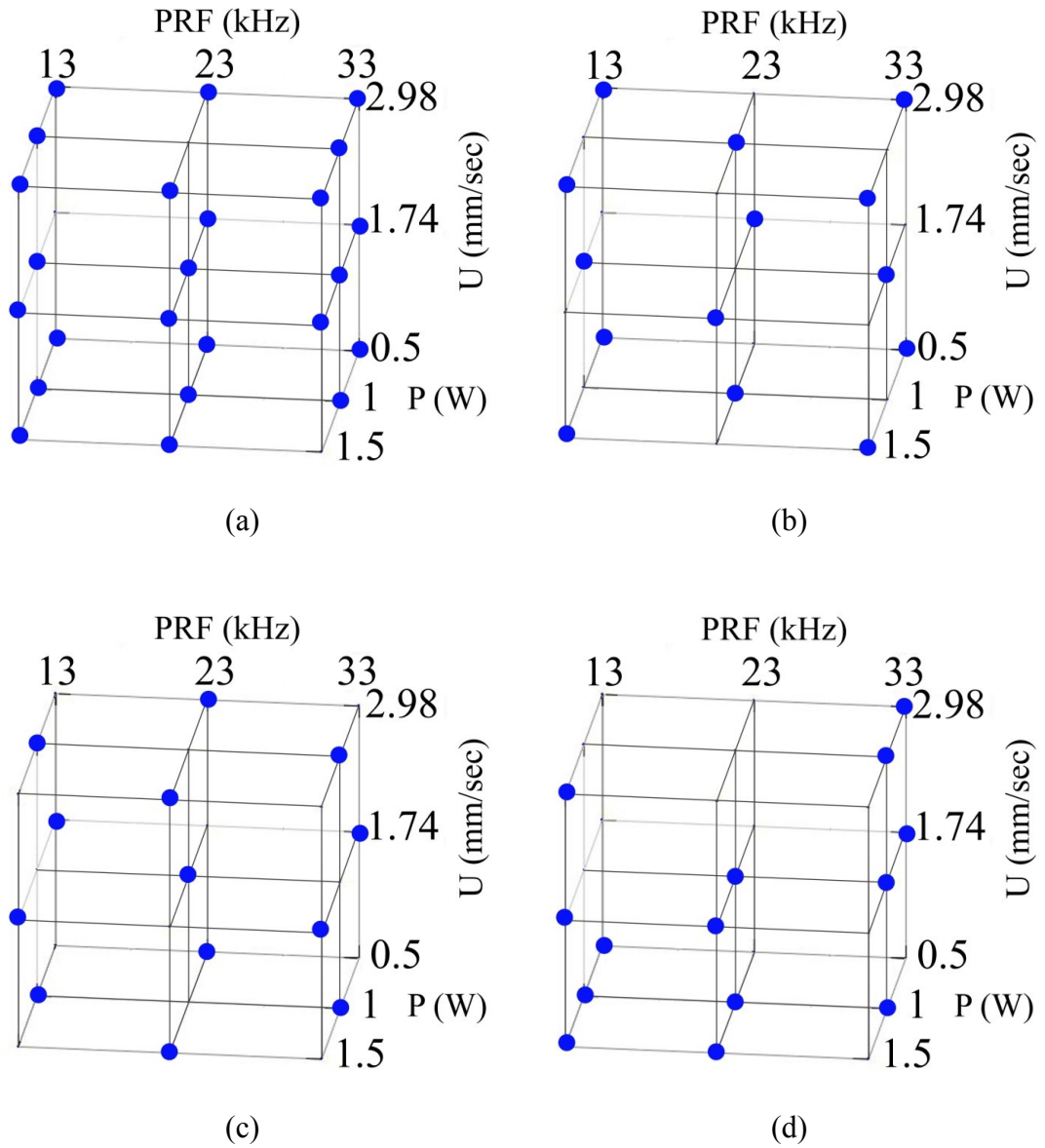
Figure 3-14: Schematic representation of the training data for (a) model I, (b) model II, (c) model III, and (d) model IV.

3.3.7 Configuration of ANN Models

The developed models were designed and run with the aNETka software in feed-forward back-propagation ANN mode. Due to the lack of a quantifiable procedure for theoretical appraisal of the best ANN architecture, an exhaustive trial-and-error study was performed to find the best ANN configuration for each model. Two ASCII text input files were prepared for each model. The first one contained the training

data inputs and corresponding outputs for the training stage. The second one contained all 27 experimental data inputs and their corresponding outputs for the verification stage. Laser micromachining process is a quite complicated process for which to produce an accurate predictive model, as mentioned in the literature review chapter. Therefore, the number of hidden layers was changed up to four and the number of neurons in each hidden layer was varied up to 100 neurons. A diagrammatic description of the examined ANN architectures is shown in Figure 3-10.

The sigmoid transfer function was used in all investigated ANN architectures for its good generalisation capability. Since the learning rate value controls the magnitude of weight and bias updates, the choice of this value meaningfully influences the training time of the developed ANN. Empirically, after screening trials, the learning rate value was manually varied between 0.0001 and 6 depending on the progress of the aNETka execution during the training process. To avoid and reduce the probability of the training runs being stuck in local optima, the momentum parameter was utilised and fixed at a medium value of 0.8 for all ANN training runs.

In the training mode of aNETka, the training data was iteratively passed one by one through the ANN structure and the weights were automatically adjusted after each pass. In an effort to minimise the training error and avoid over training, only part (about 70%) of the training data was used to train the network, and the rest (about 30%) was randomly selected, by the aNETka, and set aside as test data set. This test data set was utilised as a validation set, a criterion to decide when to stop the training, and to test the generalisation capabilities of the ANN model being developed. The training interface of the aNETka code provided a graphical chart of real time RMS values. During the ANN model development, this graphical chart was unceasingly supervised so that ANN configurations with the highest prediction capability, i.e. lowest RMS, could be obtained for each model. If the training RMS and testing RMS decreased then the ANN was still learning (generalising). However, if the training RMS decreased and test RMS began to increase then the ANN would have begun to memorize (be over-trained). During training mode, models for which the RMS error increased during training were discarded. The process of model

generation was then re-initialised to produce a better ANN model. Experimentally, after screening trials, only models with RMS error below 0.001% were accepted. The number of iterations was kept as low as possible during formulation of the ANN model. Approximately, 15-30 minutes was needed to achieve the target RMS value for each developed ANN setup/architecture.

3.4 Positional Analysis

In this section, the ISO standard, the experimental design and procedure, and the positional measurements, for both the Nd:YVO$_4$ laser system, and the Nd:YAG laser system, are discussed.

3.4.1 ISO Standard

The basic standard as a guideline for measuring the errors in machine tools is documented in International Organization of Standardization (ISO) 230-2 [200]. The purpose of this standard procedure is to standardise methods for testing the accuracy of machine tools. Furthermore, This ISO standard identifies test procedures used to determine the positioning accuracy and repeatability of numerically controlled axes. It does this by measuring individual axes on the machine, in this case a linear axis. The following definitions and formulas are as stated in the ISO documentation.

Definitions

Target position - Pi (i = 1 to m): The position to which the moving part is commanded to move. i identifies the particular position among other selected target positions along the axis.

Actual position - P_{ij} (i = 1 to m; j = 1 to n): The measured position reached by the moving part on the jth approach to the ith target position.

Positional deviation - x_{ij}: Actual position reached by the moving part minus the target position. It can be calculated according to Equation 3-2.

$$x_{ij} = P_{ij} - P_i \qquad\qquad 3\text{-}2$$

Unidirectional: The approach to a target position is always made in the same direction. The symbol ↑ signifies an approach in the positive direction and ↓ signifies an approach in the negative direction e.g. x_{ij} ↑ or x_{ij} ↓.

Bi-directional: the approach to the target position is made in either direction.

Expanded uncertainty: the result of a measurement that is likely to encompass a large portion of the distribution of values.

Coverage factor: This is a multiplier of the combined standard uncertainty in order to obtain an expanded uncertainty.

Temperature: All measurements were carried out at room temperature 20° C. If this was not the case, certain expansion coefficients may change. This could alter the effectiveness of the results attained.

Formulae

Mean unidirectional positional deviation at a position ($\bar{x}_i$ ↑ or $\bar{x}_i$ ↓): Arithmetic mean of the positional deviations obtained by a series of n unidirectional approaches to a position P_i. They can be calculated according to Equation 3-3 and Equation 3-4.

$$\bar{x}_i \uparrow = \frac{1}{n} \sum_{j=1}^{n} x_{ij} \uparrow \qquad\qquad 3\text{-}3$$

$$\bar{x}_i \downarrow = \frac{1}{n} \sum_{j=1}^{n} x_{ij} \downarrow \qquad\qquad 3\text{-}4$$

Mean bi-directional positional deviation at a position ($\bar{x}_i$): Arithmetic mean of the mean unidirectional positional deviations, $\bar{x}_i$ ↑ and $\bar{x}_i$ ↓ obtained from the two directions of approach at a position P_i. It can be calculated according to Equation 3-5.

$$\bar{x}_i = \frac{\bar{x}_i \uparrow + \bar{x}_i \downarrow}{2} \qquad\qquad 3\text{-}5$$

Reversal value at a position (B_i): Value of the difference between the mean unidirectional positional deviations obtained from the two directions of approach at a position P_i. It can be calculated according to Equation 3-6.

$$B_i = \bar{x}_i \uparrow - \bar{x}_i \downarrow \qquad\qquad 3\text{-}6$$

Reversal value of an axis (B): Maximum of the absolute reversal values $|B_i|$ at all target positions along or around the axis. It can be calculated according to Equation 3-7.

$$B = max.\,[|B_i|] \qquad\qquad 3\text{-}7$$

Mean reversal value of an axis $(\bar{B})$: Arithmetic mean of the reversal values B_i at all target positions along or around the axis. It can be calculated according to Equation 3-8.

$$\bar{B} = \frac{1}{m}\sum_{i=1}^{m} B_i \qquad\qquad 3\text{-}8$$

Estimator of the unidirectional axis repeatability of positioning at a position $(s_i \uparrow$ or $s_i \downarrow)$: Estimator of the standard uncertainty of the positional deviations obtained by a series of n unidirectional approaches at a position P_i. They can be calculated according to Equation 3-9 and Equation 3-10.

$$s_i \uparrow = \sqrt{\frac{1}{n-1}\sum_{j=1}^{n}\left(x_{ij} \uparrow - \bar{x}_i \uparrow\right)^2} \qquad\qquad 3\text{-}9$$

$$s_i \downarrow = \sqrt{\frac{1}{n-1}\sum_{j=1}^{n}\left(x_{ij} \downarrow - \bar{x}_i \downarrow\right)^2} \qquad\qquad 3\text{-}10$$

Unidirectional repeatability of positioning at a position $(R_i \uparrow$ or $R_i \downarrow)$: Range derived from the expanded uncertainty of unidirectional positional deviations at a position P_i using a coverage factor of 2. They can be calculated according to Equation 3-11 and Equation 3-12.

$$R_i \uparrow = 4s_i \uparrow \qquad\qquad 3\text{-}11$$

$$R_i \downarrow = 4s_i \downarrow \qquad\qquad 3\text{-}12$$

Bi-directional repeatability of positioning at a position (R_i): It can be calculated according to Equation 3-13.

$$R_i = max. [2s_i \uparrow + 2s_i \downarrow + |B_i|; R_i \uparrow; R_i \downarrow] \qquad\qquad 3\text{-}13$$

Unidirectional repeatability of positioning (R)**:** Maximum value of the repeatability of positioning at any position P_i along or around the axis. It can be calculated according to Equation 3-14 and Equation 3-15.

$$R \uparrow = max. [R_i \uparrow] \qquad\qquad 3\text{-}14$$

$$R \downarrow = max. [R_i \downarrow] \qquad\qquad 3\text{-}15$$

Bi-directional repeatability of positioning of an axis R: Maximum value of the repeatability of positioning at any position P_i along or around the axis. It can be calculated according to Equation 3-16.

$$R = max. [R_i] \qquad\qquad 3\text{-}16$$

Unidirectional systematic positional deviation of an axis $(E \uparrow$ or $E \downarrow)$ **:** The difference between the algebraic maximum and minimum of the mean unidirectional positional deviations for one approach direction $\bar{x}_i \uparrow$ or $\bar{x}_i \downarrow$ at any position P_i along or around the axis. They can be calculated according to Equation 3-17 and Equation 3-18.

$$E \uparrow = max. [\bar{x}_i \uparrow] - min. [\bar{x}_i \uparrow] \qquad\qquad 3\text{-}17$$

$$E \downarrow = max.[\bar{x}_i \downarrow] - min.[\bar{x}_i \downarrow] \qquad\qquad \text{3-18}$$

Bi-directional systematic positional deviation of an axis (E)**:** The difference between the algebraic maximum and minimum of the mean unidirectional positional deviations for both approach direction $\bar{x}_i \uparrow$ or $\bar{x}_i \downarrow$ at any position P_i along or around the axis. It can be calculated according to Equation 3-19.

$$E = max.[\bar{x}_i \uparrow; \bar{x}_i \downarrow] - min.[\bar{x}_i \uparrow; \bar{x}_i \downarrow] \qquad\qquad \text{3-19}$$

Range mean bi-directional positional deviation of an axis (M)**:** The difference between the algebraic maximum and minimum of the mean bi-directional positional deviations xi at any position Pi along or around the axis. It can be calculated according to Equation 3-20.

$$M = max.[\bar{x}_i] - min[\bar{x}_i] \qquad\qquad \text{3-20}$$

Unidirectional accuracy of positioning of an axis ($A \uparrow$ or $A \downarrow$) **:** Range derived from the combination of the unidirectional systematic deviations and the estimator of the standard uncertainty of unidirectional positioning using a coverage factor of 2. They can be calculated according to Equation 3-21 and Equation 3-22.

$$A \uparrow = max.\lfloor \bar{x}_i \uparrow + 2s_i \uparrow \rfloor - min.\lfloor \bar{x}_i \uparrow - 2s_i \uparrow \rfloor \qquad\qquad \text{3-21}$$

$$A \downarrow = max.[\bar{x}_i \downarrow + 2s_i \downarrow] - min.[\bar{x}_i \downarrow - 2s_i \downarrow] \qquad\qquad \text{3-22}$$

Bi-directional accuracy of positioning of an axis (A)**:** Range derived from the combination of the bidirectional systematic deviations and the estimator of the standard uncertainty of bi-directional positioning using a coverage factor of 2. It can be calculated according to Equation 3-23.

$$A = max.[\bar{x}_i \uparrow + 2s_i \uparrow; \bar{x}_i \downarrow - 2s_i \downarrow] - min.[\bar{x}_i \uparrow - 2s_i \uparrow; \bar{x}_i \downarrow + 2s_i \downarrow] \qquad \text{3-23}$$

Target Position Selection

The machine should be programmed to move between the target positions at a predetermined constant translation speed. In this work, positional analyses were carried out under a constant translation speed equals to 2 mm/sec, unless otherwise mentioned. The value of each target position can be selected without restrictions. However, it should take the general form presented in Equation 3-24.

$$P_i \;=\; (i-1)\,p + r \qquad\qquad \text{3-24}$$

Where i is the number of the current target position; p is an interval based on a uniform spacing of target points over the measurement travel; and r is a random number within $\pm$ the amplitude of possible periodic errors in the movement mechanism. It is used to ensure that these periodic errors are adequately sampled. Since this information is not available it is recommended to use a changing value of this random number, for each target position, between $\pm 30\ \%$ of P.

3.4.2   Positional Analysis of Nd:YVO$_4$ Laser System

Equipment and Materials Utilised

The laser system used was the Nd:YVO$_4$ laser system presented in section 3.1.3. The KEYENCE high-precession CCD laser displacement sensor system was used as a measurement system for actual movement measurement of the 3D translation stage of the Nd:YVO$_4$ laser system. This measurement system was chosen for its high resolution (1 μm) and, factory certified high repeatability (1 μm). Since the laser displacement sensor system was attached along the axis to be measured, there was no material processing needed.

Experimental Design

To study the positional analysis of the Nd:YVO$_4$ laser system 3D translation stage, the 3D translation stage should be programmed to move the stage along the axis

under test, and to position it at a series of target positions where it will remain at rest long enough for the actual position to be reached, measured and recorded.

Measurements shall be made at all the target positions according to the standard test cycle (see Figure 3-15), once along each of the three axes (X, Y, and Z). Each target position shall be attained three times in each direction along each axis.
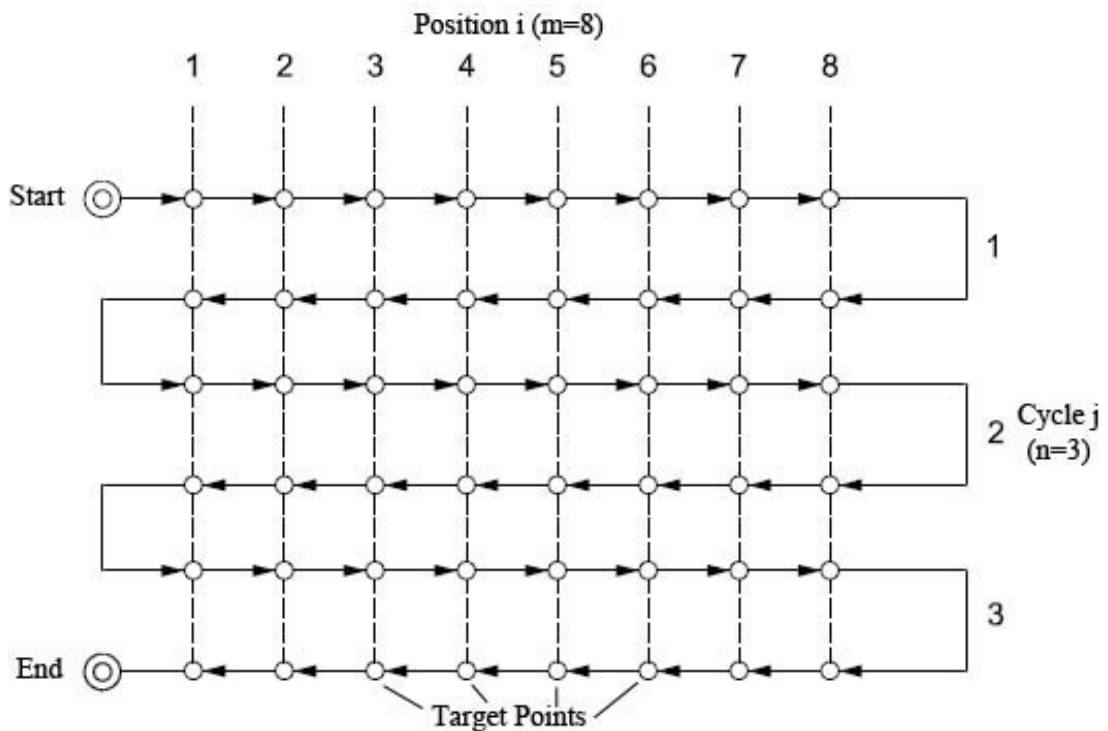
Figure 3-15: Nd:YVO$_4$ laser system standard test cycle.

Since the X-axis had a different working range from Y- and Z-axes, two different P values (target positions) were chosen, one along X-axis and another along Y- and Z-axes.

The P value for tests along the X-axis were chosen to be 2500 μm, since the working range of the X-axis, along laser firing axis and the achromatic lens (which has a focal length of 25.6 mm), was 20 mm. Thus, the examined travel range along the X-axis is 19869 μm.

Table 3-9: Nd:YVO$_4$ laser system target positions and spacings along X-axis.

No measurement		Target position μm								No measurement		Cycle
		1	2	3	4	5	6	7	8			
Spacings	0	188	2514	2153	2879	2242	2435	2481	2472	2505		
Start	→	→	→	→	→	→	→	→	→	→		
0		188	2702	4855	7734	9976	12411	14892	17364	19869	↓	1
	←	←	←	←	←	←	←	←	←	←		
↓	0	188	2702	4855	7734	9976	12411	14892	17364	19869		
	→	→	→	→	→	→	→	→	→	→		
0		188	2702	4855	7734	9976	12411	14892	17364	19869	↓	2
	←	←	←	←	←	←	←	←	←	←		
↓	0	188	2702	4855	7734	9976	12411	14892	17364	19869		
	→	→	→	→	→	→	→	→	→	→		
0		188	2702	4855	7734	9976	12411	14892	17364	19869	↓	3
End	←	←	←	←	←	←	←	←	←	←		

Table 3-9 shows the target positions and spacings along the X-axis, which were calculated according to Equation 3-24. On the other hand, since the working range along Y- and Z-axes was 65 mm, the P value to test the 3D translation stage along both of these axes was chosen to be 8000 μm. Thus the examined travel range along Y- and Z-axes is 63845 μm. Table 3-10 shows the target positions and spacings along Y- and Z-axes, which were calculated according to Equation 3-24.

Table 3-10: Nd:YVO$_4$ laser system target positions and spacings along Y- and Z-axes.

No measurement		Target position μm								No measurement		Cycle
		1	2	3	4	5	6	7	8			
Spacings	0	170	7617	8000	7982	8408	7819	7952	8206	7691		
Start	→	→	→	→	→	→	→	→	→	→		
0		170	7787	15787	23769	32177	39996	47948	56154	63845	↓	1
	←	←	←	←	←	←	←	←	←	←		
↓	0	170	7787	15787	23769	32177	39996	47948	56154	63845		
	→	→	→	→	→	→	→	→	→	→		
0		170	7787	15787	23769	32177	39996	47948	56154	63845	↓	2
	←	←	←	←	←	←	←	←	←	←		
↓	0	170	7787	15787	23769	32177	39996	47948	56154	63845		
	→	→	→	→	→	→	→	→	→	→		
0		170	7787	15787	23769	32177	39996	47948	56154	63845	↓	3
End	←	←	←	←	←	←	←	←	←	←		

Experimental Procedure

In this work, all positional tests were carried out in an unloaded condition (without a work piece), unless otherwise is mentioned. The KEYENCE high-precession CCD laser displacement sensor system has a measuring range of 10 mm. Therefore, the measuring range is only enough to measure one spacing distance (between two successive target positions in the positional measurement case along Y- and Z-axes). Consequently, to measure the next step distance, movement of this measurement system is needed. For this reason, the laser displacement sensor head was fitted with a linear guide rail. This was done to provide accurate, stable, and smooth linear guidance to the laser displacement sensor head

The laser displacement sensor assembly was positioned along the axis under test. A visible (laser diode), modulated point of light is projected onto a target surface as illustrated in Figure 3-16 for measurements along Y-axis.
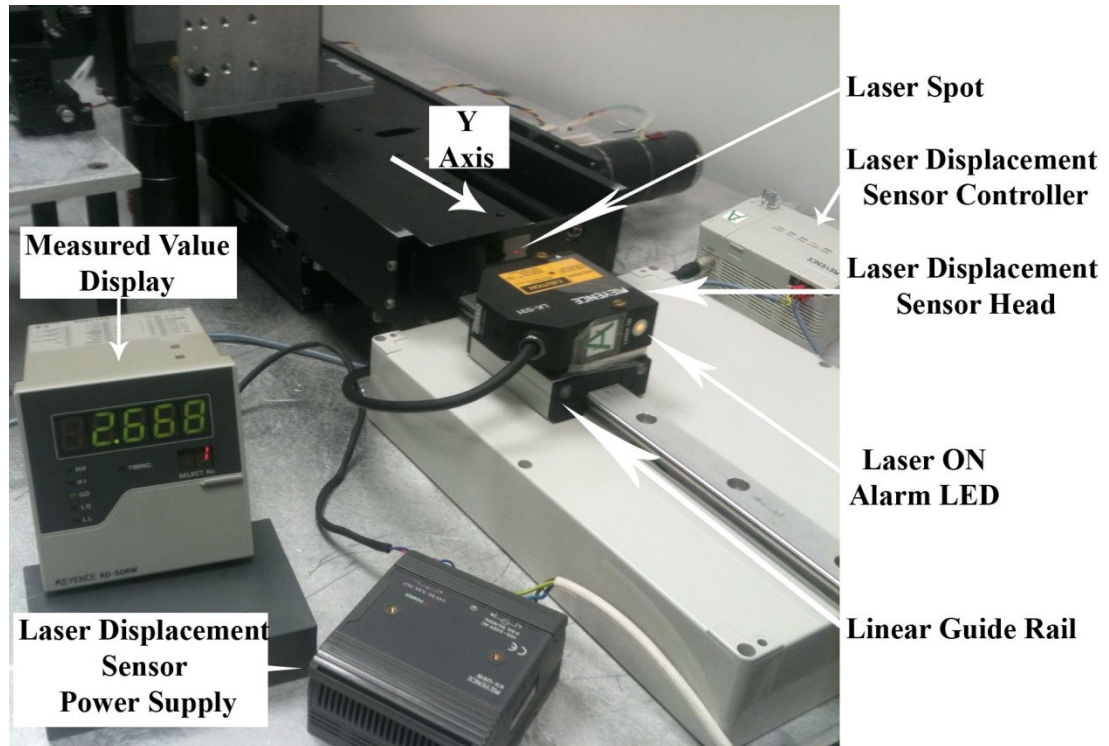
Figure 3-16: The laser displacement sensor assembly along Y-axis.

Hereinafter, the measurement setup and procedure carried out along Y-axis will be discussed. The same measurement setup and procedure were applied along X- and Z-axes.

All positional measurements, along Y-axis, started while the 3D translation stage is positioned within the first 10% of the travel range of the axis under test. Then the 3D translation stage was commanded, through the developed motion control code in LabVIEW, to move the stage along the Y-axis to the predetermined target positions successively. This allowed the 3D translation stage to remain at rest long enough for the actual position to be reached, measured and recorded. Since its measuring range was 10 mm (from -5.000 to +5.000 mm), the utilised measurement system was used to measure the spacing distances.

To illustrate this further, an example of moving the 3D translation stage along the Y-axis from the first target position to the second target position (second position spacing in the positive direction of the first cycle) will be demonstrated.
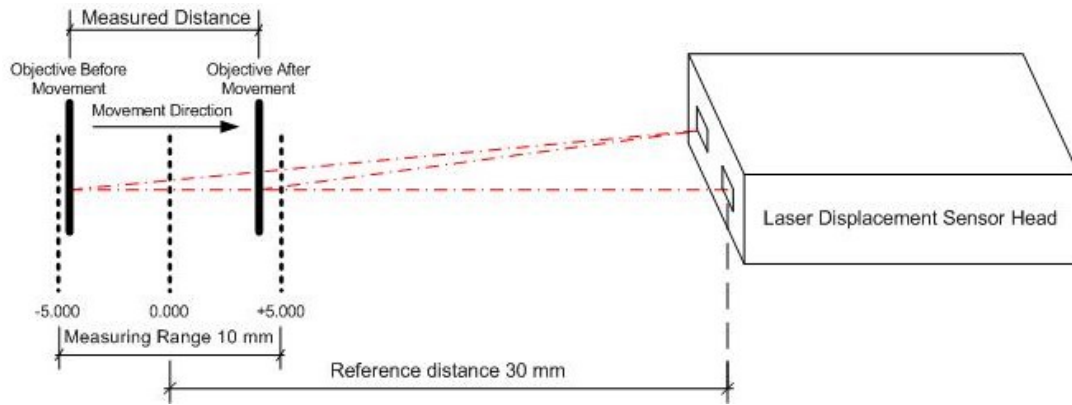
Figure 3-17: Utilised measurement procedure.

The measurement assembly was positioned, before moving the 3D translation stage, such that the measured value display (of the measurement system) is in the (-4.000 ~ -5.000 mm) range (for instance -4.475 mm). Then the 3D translation stage was commanded, through the developed motion control code in LabVIEW, to move 7617 μm (second position spacing) along the Y-axis. While the 3D translation stage is moving, the measurement system display will show the real time distance within the -5.000 and +5.000 mm range, which is illustrated in Figure 3-17. When the 3D translation stage reach its destination, the measurement system display should show a reading in the (2.500 ~ 5.000 mm) range (for instance 3.121 mm). So for the instance values mentioned above, it can be concluded that the measured 3D translation stage travelled distance equals to 7596 μm (4.475+3.121 mm) along the Y-axis, which is recorded on a measurement table, similar to Table 3-10, as a counterpart of the ideal distance (7617 μm).

Again, the measurement assembly was positioned, along the linear guide rail which is along the same stage axis under test, such that the measured value display (of the measurement system) is in the (-4.000 ~ -5.000 mm) range and the same procedure, mentioned above, is repeated to measure the third position.

After the measurement of the eighth position spacing, the measurement assembly kept stationary and the 3D translation stage is commanded to move 7691 μm along the Y-axis, then commanded to move the same distance in the negative part of the cycle. Then the measurement assembly was positioned such that the measured value display (of the measurement system) is in the (4.000 ~ 5.000 mm) range and the same procedure, mentioned above, is repeated to measure the eight position. And so forth, to complete all target positions movements and measurements of the 3D translation stage along the Y-axis.

3.4.3   Positional Analysis of Nd:YAG Laser System

Equipment and Materials Utilised

The laser system used was the Nd:YAG laser system presented in section 3.1.4. Since the motion system for moving the laser spot along X- and Y-axes was a galvanometer (laser beam two-axis deflection unit), it wasn't possible to measure the target positions on the laser system directly, as carried out with the $Nd:YVO_4$ laser system. Instead, an alternative procedure, which involved laser surface micromachining of voxels on glass sheet, was applied.

The Mitutoyo optical microscope was used for positional measurements of the Nd:YAG laser system. This measurement system was chosen for its high resolution (1 μm) and DIGIMATIC micrometre heads, which have large LCD displays for error-free reading of the two measuring slides.

For the positional measurements of the linear Z stage, the internal encoder of the PI precession positioning stage, presented in section Appendix J, was utilised.

Experimental Design

To study the positional analysis of the Nd:YAG laser system galvanometer, the galvanometer should be programmed to position the laser focal point along the axis under test (X or Y-axis), at a series of target positions where it will create a surface

voxel. The developed voxels will be measured later using the Mitutoyo optical microscope.

On the other hand, studying the positional analysis of the Nd:YAG laser system linear Z stage was not possible using the KEYENCE high-precession CCD laser displacement sensor system, since there was not enough room to setup the measurement system. As an alternative, the internal encoder of the Z stage (PI precession positioning stage), which has factory certified 0.012 μm resolution and 0.5 μm repeatability.

Voxels shall be micro-machined at all the target positions according to the standard test cycle (see Figure 3-18), once along each of the X- and Y-axes. Each target position shall be attained three times in each direction along each axis.
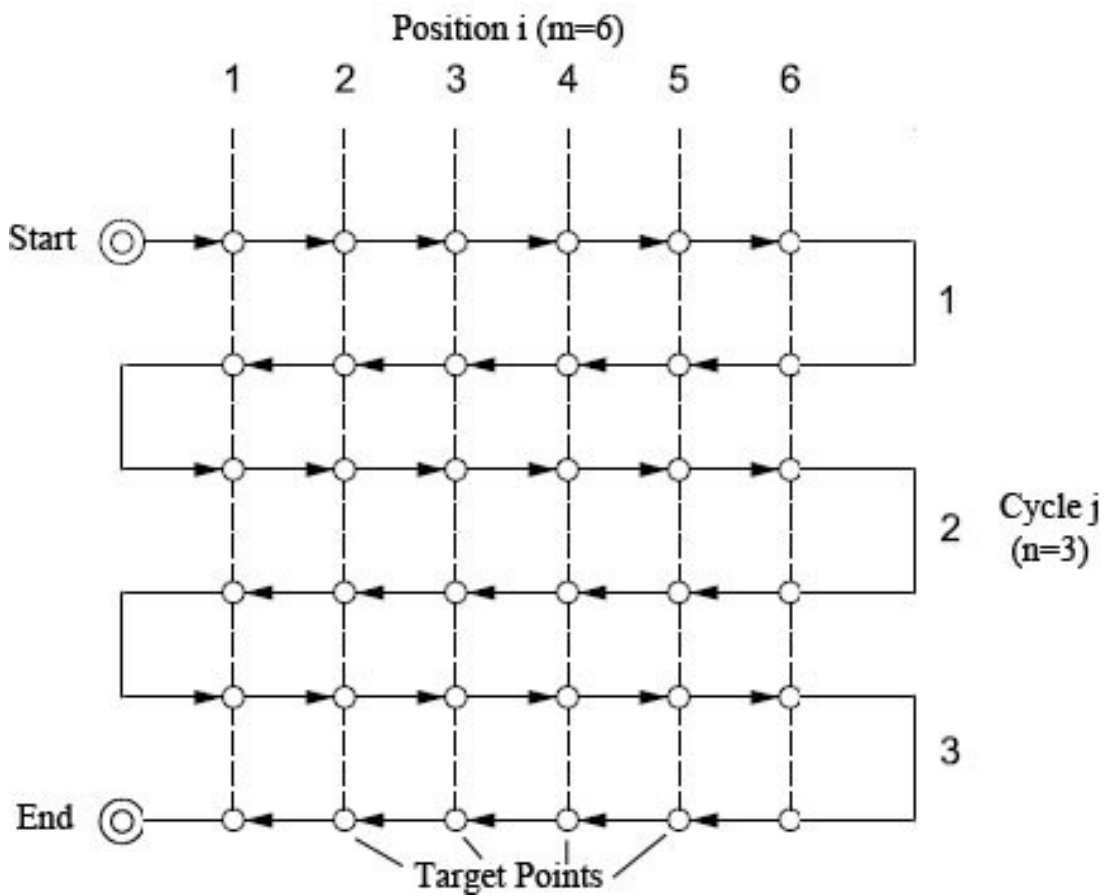
Figure 3-18: Nd:YAG laser system standard test cycle.

The P value was chosen to be 10000 μm, since the working range along the three axes was 60 mm. Thus, the examined travel range along the three axes is 19869 μm. Table 3-11 shows the target positions along the axis under test and for the three axes, which were calculated according to Equation 3-24.

Table 3-11: Nd:YAG laser system target positions and spacings.

No measurement		Target position μm						No measurement		Cycle
		1	2	3	4	5	6			
Spacings	0	430	9560	9910	9940	9900	9860	10370		
Start	→	→	→	→	→	→	→	→		
0		430	9990	19900	29840	39740	49600	59970	↓	1
	←	←	←	←	←	←	←	←		
↓	0	430	9990	19900	29840	39740	49600	59970		
	→	→	→	→	→	→	→	→		
0		430	9990	19900	29840	39740	49600	59970	↓	2
	←	←	←	←	←	←	←	←		
↓	0	430	9990	19900	29840	39740	49600	59970		
	→	→	→	→	→	→	→	→		
0		430	9990	19900	29840	39740	49600	59970	↓	3
End	←	←	←	←	←	←	←	←		

Since the galvanometer was controlled through the OEM WeldMark software, therefore finding the marking field corresponding (matching) target positions in the range of (-30 ~ 30 mm) was required. Table 3-12 shows the Nd:YAG laser system standard target positions and their corresponding platform target positions along X- and Y-axes.

Table 3-12: Marking platform corresponding target positions along X- and Y-axes.

No measurement	Positions						No measurement
	1	2	3	4	5	6	
0	430	9990	19900	29840	39740	49600	29970
-30000	-29570	-20010	-10100	-160	9740	19600	29970

Experimental Procedure

The galvanometer was controlled through the OEM WeldMark software, the marking platform corresponding target positions along X- and Y-axes were fed into the software as a visual design, like Figure 3-18, in the software GUI using the values from Table 3-12. When the laser spot reached the target position, the galvanometer scanning mirrors will stop at rest for a period enough for the laser to fire and develop the voxel. Then the laser stops and the galvanometer scanning mirrors will move the laser spot along the axis under test to the next target position and so forth.

After many screening trials, the laser setting that produced voxels of 10-15 μm (on average) in diameter, using the Nd:YAG laser system, was achieved. However, the Heat Affected zone (HAZ) was an additional 120 μm (on average) in diameter. Laser settings were optimised, through the screening trials, for the smallest voxel possible regardless of the developed HAZ size. For the subsequent measurement, the centre of each voxel was taken as a reference point for each developed voxel.

It was noticed that there was good symmetry and roundness of most voxels; this resulted in a higher level of confidence when taking measurements from the centre of each voxel. However, because of the anisotropic behaviour of the glass, around 60% of voxels did not share concentricity with the overall HAZ zone (both circular paths did not share a geometric centre), as shown in Figure 3-19. This figure shows a random target position developed voxel of 10 μm in diameter with a HAZ of around 200μm taken.
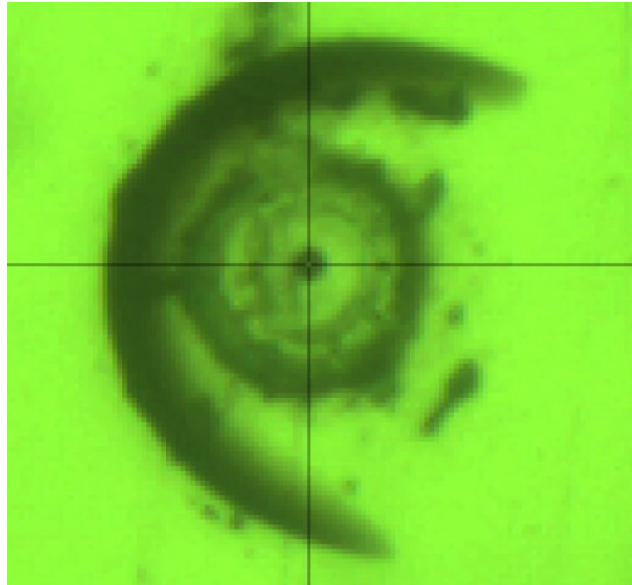
Figure 3-19: Magnified microscopic image of developed voxel on glass.

The Mitutoyo optical microscope was used to measure the distances between each two successive voxels. This microscope had imaging software, installed on the measuring computer, which had a very valuable magnification and cross hair features. These two features were significant for the measurement of the distance between the centres of each two successive voxels. Since there was no guides for positioning the glass sheet on the microscope coordinate measuring table, the movement of both two measuring slides (along X- and Y-axes), of the coordinate measuring table, was needed to reach the centre of the second successive voxel. Therefore, Pythagorean Theorem was applied to calculate the distance between each two successive voxels.

On the other hand, the linear Z stage (PI precession positioning stage) was controlled through the PI OEM software. The spacings of target positions were fed directly into the software GUI, one at a time. The same GUI contained the internal encoder reading value, for each spacing distance between each two successive target positions, after the movement is complete along the Z-axis.

3.4.4   Positional Analysis of the Mitutoyo optical microscope

Equipment and Materials Utilised

The 25 mm ruler of the calibrated and certified stage micrometre, presented in Appendix K, was used for positional measurements of the Mitutoyo optical microscope-measuring slide along the X-axis.

Experimental Design

The Mitutoyo optical microscope was used as a measurement system for the developed voxels' pattern on the glass sheet.
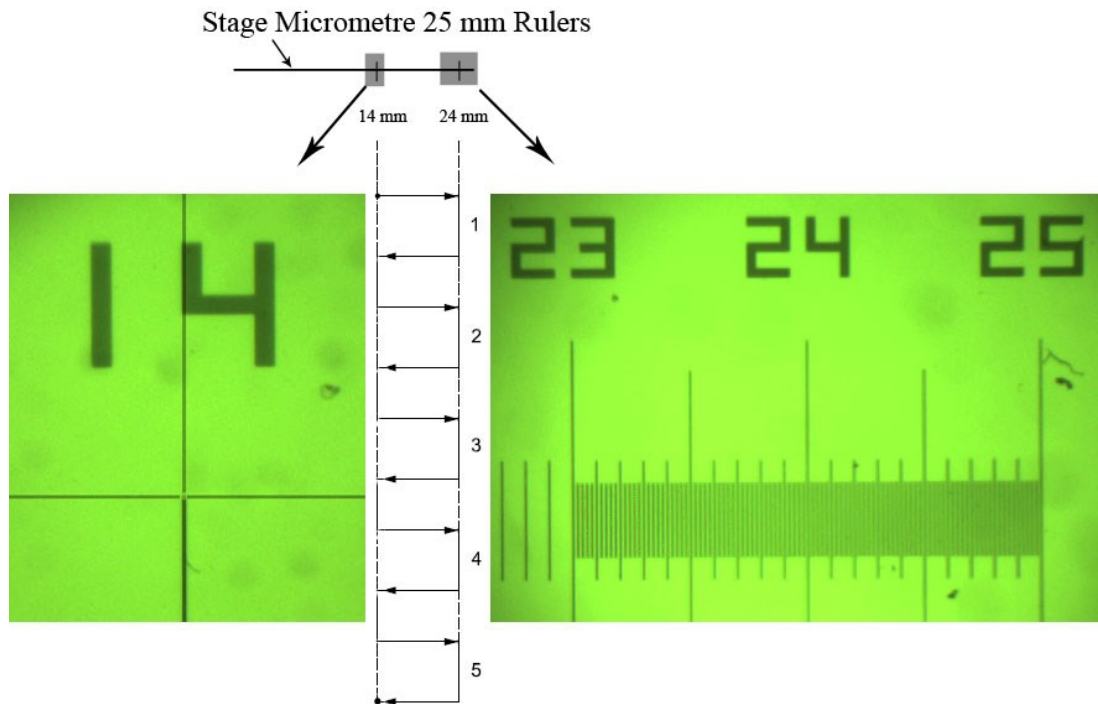
Figure 3-20: Mitutoyo optical microscope standard test cycle.

Since there was no information about the accuracy and repeatability of this measuring system, a positional analysis was required to certify that this microscope is sufficient as a measurement system. Since the measurements along the Y-axis were insignificant, with average less than 15 μm, therefore, a positional analysis study was needed just along X-axis. This was done against the 25 mm rulers of the certified stage micrometre, presented in Appendix K.

The standard test cycle, along X-axis (main axis used for measurements), was chosen to be of one target position (from 14 mm to 24 mm divisions on the 25 mm ruler of the stage micrometre) and five cycles as shown in Figure 3-20. This figure also shows 600% magnified microscopic images of the 14 mm and the 24 mm divisions. This magnification was extremely important for the accurate visual selection of the two utilised divisions.

Experimental Procedure

The stage micrometre was positioned on the Mitutoyo optical microscope measuring slides, so that the measuring starting point was set to the tip of the 14 mm. Then the measuring slides were manually moved, using the DIGIMATIC micrometre heads, so that the end measuring point is the tip of the 24mm where 0.02 mm divisions' increments could be found. This assisted in the alignment of the ruler against the micrometre stage. Then the reading of the DIGIMATIC micrometre LCD displays were taken for the first measured target position of the positive direction of the first cycle. Afterwards, the DIGIMATIC micrometre LCD displays was zero-set, then the same approach was applied from 24 mm to 14 mm for the negative direction of the cycle, and so forth.

Since there was no guides for positioning the stage micrometre on the microscope coordinate measuring table, the movement of both two measuring slides (along X- and Y-axes) of the coordinate measuring table was needed to reach the centre of the 24 mm division. Therefore, Pythagorean Theorem was applied to calculate the distance between 14 mm to 24 mm divisions.

CHAPTER 4

RESULTS & DISCUSSION

4.1 Introduction

This chapter presents and discusses the results of this work. The results presented in sections 4.2, 4.3, and 4.4 correspond directly to the experimental procedure details in sections 3.2, 3.3, and 3.4 respectively. Section 4.2 presents the CO_2 laser surface micro-channel micromachining of glass experiment results, section 4.3 presents the Nd:YVO$_4$ laser internal micromachining of polycarbonate and PMMA experiment results, and section 4.4 presents the positional analysis recorded from the investigated Nd:YVO$_4$ and Nd:YAG laser systems.

4.2 Glass experiments with CO_2 Laser System

Figure 4-1 shows micrographs of the produced micro-channels highlighting the width. Figure 4-1 (a), (b), and (c) show micro-channels produced at 18 W, 24 W and 30 W respectively. The PRF and U were fixed at 228 Hz and 8.33 mm/sec for production of these micro-channels. The corresponding micro-channel widths were respectively 222, 267, and 310 μm. Increasing power results in an increase of pulse energy and fluence that lead to an increased micro-channel width and depth.

Figure 4-1 (d), (e), and (f) show micro-channels produced at 160, 228 and 400 Hz respectively. The P and U were fixed at 24 W and 8.33 mm/sec for production of these micro-channels. The corresponding and decreasing micro-channel widths were 314, 267, and 187 μm. Pulse energy is calculated as average power; P divided by pulse repetition frequency; PRF. This inverse relationship shows that higher PRF

produced lower pulse energy and fluence that in turn resulted in decreased micro-channel width and depth.

(a)

(d)

(b)

(e)

(c)

(f)
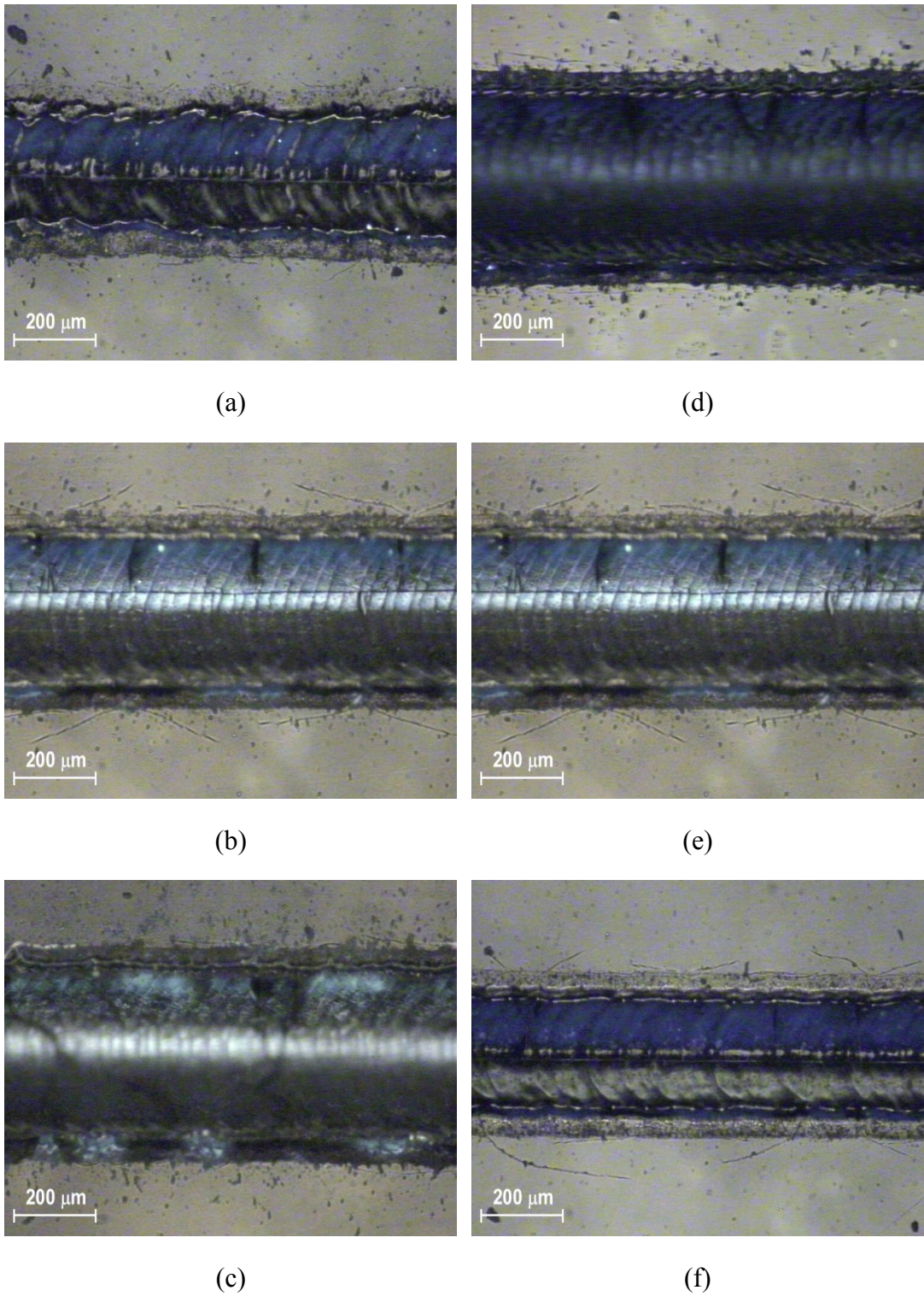
Figure 4-1: Plan view micrographs of selected laser-machined micro-channels.

111

4.2.1   ANN Prediction Models

To choose the best-developed ANN structure for each of the six ANN models (three for the width model and other three for the depth model), two statistical discriminating criteria were chosen to differentiate between the developed ANN structures.

The chosen statistical estimators were MPE (Mean Percentage Error), and E_∞ (absolute maximum percentage error). MPE is the computed average of percentage errors by which estimated predictions differ from actual values of the output being predicted. On the other hand, E_∞ indicates the worst prediction error for each model. In this case, E_∞ is valuable because the largest deviation allowable in laser micromachining applications is often limited to a maximum allowable amount of error. Percentage error e_i, MPE (Mean Percentage Error), and E_∞ (absolute maximum percentage error) were calculated according to the equations below:

$$e_i \;=\; 100 * \frac{(\widehat{y_i} - y_i)}{y_i}\,\% \qquad\qquad 4\text{-}1$$

$$\text{MPE} \;=\; \frac{1}{n}\sum_{i=1}^{n} e_i \qquad\qquad 4\text{-}2$$

$$E_\infty \;=\; \max_{i=1}^{n}\lvert e_i\rvert \qquad\qquad 4\text{-}3$$

Where n is the number of experiments, y is the actual value, and $\hat{y}$ is the predicted value.

After testing a large variety of hidden layer variations, it was found that the most accurate ANN model schemas were achieved with one hidden layer. This may be expected as multiple hidden layers are used for models of a deeply complex nature where response surfaces are of a higher order non-linear response [162]. Table 4-1 shows the number of neurons in the hidden layer that achieved the most accurate predictions of width and depth for models I, II, and III.

112

Table 4-1: Number of nodes in the hidden layer for width and depth models in I, II, and III models

ANN Model	Hidden layers	Width model	Depth model
I	1st	6	6
II	1st	20	10
III	1st	80	4

4.2.2 Actual Vs Predicted

The actual and predicted values of width and depth for I. II. III, and RSM are shown in Table 4-3. The bold numbers indicate accurately predicted values.

4.2.3 RSM Vs ANN

MPE and E_∞ were utilised in order to measure the difference between values produced by predictive models and the actual values. Furthermore, they were utilised as a measure of how well future outcomes are likely to be predicted by the investigated model. So practically, these estimators were used for the selection of the best ANN schemas for each model in addition to compare between the predictive models. Table 4-2 shows a side-by-side comparison between, I, II, III, and RSM models in terms of the chosen estimators.

Table 4-2: Comparison criteria for width and depth models in, I, II, III, and RSM models.

#	Width				Depth			
	RSM	I	II	III	RSM	I	II	III
MPE	0.02%	-0.13%	0.01%	6.61%	-0.33%	-0.97%	-0.08%	10.09%
E_∞	3.30%	2.40%	21.30%	101%	71.10%	14.00%	38.00%	189.60%

Table 4-3: Actual vs. predicted for RSM, I, II, and III, models.

#	Width (μm)					Depth (μm)				
	Actual	RSM	I	II	III	Actual	RSM	I	II	III
1	315	314.57	**315.00**	**315.00**	309.03	213	210.95	**213.00**	**213.00**	199.59
2	308	308.28	**308.00**	**308.00**	**308.00**	135	132.09	**135.00**	**135.00**	**135.00**
3	302	**302.00**	294.79	**302.00**	297.82	74	72.71	71.34	**74.00**	73.18
4	248	249.76	**248.00**	242.47	**248.00**	120	123.51	**120.00**	118.38	**120.00**
5	231	234.28	**231.00**	240.04	251.14	45	61.34	**45.00**	54.47	68.71
6	222	218.80	**222.00**	**222.00**	248.21	21	18.66	**21.00**	**21.00**	34.00
7	163	158.84	**163.00**	**163.00**	**163.00**	26	23.70	**26.00**	**26.00**	**26.00**
8	118	120.10	**118.00**	116.21	162.96	13	3.75	**13.00**	9.65	12.48
9	81	81.36	**81.00**	**81.00**	162.82	3	3.29	**3.00**	**3.00**	8.69
10	320	318.63	**320.00**	335.67	**320.00**	279	283.97	**279.00**	306.44	**279.00**
11	324	319.52	**324.00**	322.53	**324.00**	202	201.34	**202.00**	205.53	**202.00**
12	314	320.42	**314.00**	**314.00**	**314.00**	130	138.20	**130.00**	**130.00**	**130.00**
13	271	269.97	267.03	**271.00**	**271.00**	225	217.13	193.45	**225.00**	**225.00**
14	266	266.19	**266.00**	**266.00**	282.60	146	141.94	**146.00**	**146.00**	154.87
15	267	262.41	**267.00**	259.42	279.63	89	86.22	**89.00**	73.06	92.92
16	213	219.91	**213.00**	234.58	**213.00**	120	123.41	**120.00**	116.96	**120.00**
17	209	204.30	**209.00**	**209.00**	**209.00**	48	67.01	**48.00**	**48.00**	**48.00**
18	187	188.69	**187.00**	147.10	205.00	30	30.10	**30.00**	18.60	23.16
19	365	364.45	**365.00**	**365.00**	**365.00**	379	378.48	**379.00**	**379.00**	**379.00**
20	351	353.19	**351.00**	354.90	357.23	296	292.09	**296.00**	315.22	314.42
21	345	341.94	**345.00**	**345.00**	**345.00**	227	225.17	**227.00**	**227.00**	**227.00**
22	332	331.96	**332.00**	**332.00**	**332.00**	320	332.24	**320.00**	**320.00**	**320.00**
23	316	320.54	**316.00**	322.97	326.87	248	244.01	**248.00**	258.44	236.90
24	310	309.12	**310.00**	316.14	**310.00**	166	175.27	**166.00**	191.61	**166.00**
25	327	322.76	**327.00**	**327.00**	**327.00**	256	244.61	**256.00**	**256.00**	**256.00**
26	308	310.93	309.18	321.37	**308.00**	142	151.75	129.77	176.97	**142.00**
27	300	299.11	**300.00**	**300.00**	288.98	88	78.38	**88.00**	**88.00**	79.45

114

The lower the MPE and E_{∞} values indicate better prediction capability of the studied predictive model. Some MPE values were negative values; this means that the estimated (width or depth) predictions tend to be lower than their corresponding actual values. Table 4-2 shows that for both width and depth models, model II produced the lowest MPE value; while model I produced the lowest E_{∞} value. In Table 4-3, the ability of the predictive models to predict the training data as well as the confirmation experiments is shown. For ANN models, the ability of I, II, and III models to predict the confirmation experiments indicates the generalisation capability of the models since these confirmation experiments were not used in the formation of these models. The generalisation of model II can be seen to be better than model I or model III in that it has predicted the actual micro-channel widths and depths more accurately. This can be seen by comparing the individual predictions and more clearly by comparing the overall MPE illustrated in Table 4-2.

4.2.4   ANN Input Interactive Effect Prediction

ANN predictive models are capable of selecting the input parameters of a required dimensional output as well as predicting the interactive effect of the laser process control parameters on the dimensions of the resultant micro-channels.

To demonstrate this ability and using model II, micro-channel width and depth values were predicted for 2197 input data. These 2197 data inputs are all possible combinations (13^3) of the laser processing parameters listed in Table 4-4. All input data were prepared as ASCII text spreadsheet input file and along with the ANN model II trained configuration file were fed into the batch recall part of the aNETka software. aNETka software predicted the width and depth values for all input values. 507 ($3*13^2$) data points which corresponds to the mid-levels P=24W, PRF=280 Hz, and U=5 mm/sec were chosen and plotted as intensity plots using LabVIEW code developed specifically for this purpose.

Table 4-4: Laser control processing parameters investigated

#	P (W)	PRF (Hz)	U (mm/sec)
1	18	160	1.67
2	19	180	2.22
3	20	200	2.78
4	21	220	3.33
5	22	240	3.89
6	23	260	4.44
7	24	280	5
8	25	300	5.56
9	26	320	6.11
10	27	340	6.67
11	28	360	7.22
12	29	380	7.78
13	30	400	8.33

Figure 4-2 and Figure 4-3 show the bilateral influence of laser process control parameters laser power (P), Pulse Repetition Frequency (PRF), and translation speed (U) on width and depth respectively, while the third parameters set at the mid-level. The mid-levels were U=5 mm/sec, PRF=280 Hz, and P=24W. The results of this prediction demonstrate graphically the effect of changing two selected parameters on the dimensions of the micro-channels, while the third parameter was held constant at its average value.

These figures demonstrate the ability of ANN predictive models to offer a visual aid to select parameters or parameter ranges for a required output or output range. These graphs show simultaneously the combined effect of two parameters on the resulting dimension when the third parameter is held constant.

Figure 4-2 (a) shows the effect of Pulse Repetition Frequency (PRF) and laser power (P) on micro-channel width, while U=5 mm/sec. This figure shows that these two parameters are directly interacting with each other. Moreover, it graphically demonstrates that when Pulse Repetition Frequency (PRF) decreases and laser power (P) increases the resulting micro-channel width increases, and vice versa. Figure 4-2 (b) shows the effect of translation speed (U) and laser power (P) on micro-channel width, while PRF=280 Hz. This figure shows that these two parameters are hardly interacting with each other. Additionally, it clearly shows that when laser power (P) increases the resulting micro-channel width increases, while translation speed (U) has a marginal effect. Figure 4-2 (c) shows the effect of Pulse Repetition Frequency (PRF) and translation speed (U) on micro-channel width, while P=24W. This figure shows that these two parameters barely interacting with each other. Furthermore, this figure illustrates that when Pulse Repetition Frequency (PRF) decreases the resulting micro-channel width increases, while translation speed (U) has a minimal effect.

So Figure 4-2 (a), (b), and (c) graphically show that there is a direct relationship between laser power (P) and width, inverse relationship between Pulse Repetition Frequency (PRF) and width, and negligible effect of translation speed (U) on the width. Furthermore, required output width Figure 4-2 (a) can be used for initial selection of laser process parameters.

Figure 4-3 (a) shows the effect of Pulse Repetition Frequency (PRF) and laser power (P) on micro-channel depth, while U=5 mm/sec. This figure shows that these two parameters are directly interacting with each other. Moreover, it graphically demonstrates that when Pulse Repetition Frequency (PRF) decreases and laser power (P) increases the resulting micro-channel depth increases, and vice versa.

Figure 4-3 (b) shows the effect of translation speed (U) and laser power (P) on micro-channel depth, while PRF=280 Hz. This figure shows that these two parameters are directly interacting with each other. Additionally, it clearly shows that when translation speed (U) decreases and laser power (P) increases the resulting micro-channel depth increases, and vice versa.

Figure 4-3 (c) shows the effect of Pulse Repetition Frequency (PRF) and translation speed (U) on micro-channel depth, while P=24W. This figure shows that these two parameters directly interacting with each other. Furthermore, this figure illustrates that when Pulse Repetition Frequency (PRF) decreases and translation speed (U) decreases the resulting micro-channel depth increases, and vice versa.

So Figure 4-3 (a), (b), and (c) graphically show that there is a direct relationship between laser power (P) and depth, inverse relationship between Pulse Repetition Frequency (PRF) and depth, and inverse relationship between translation speed (U) and depth.
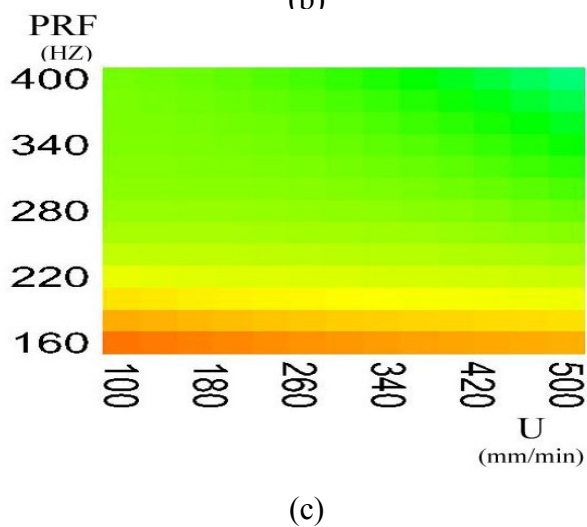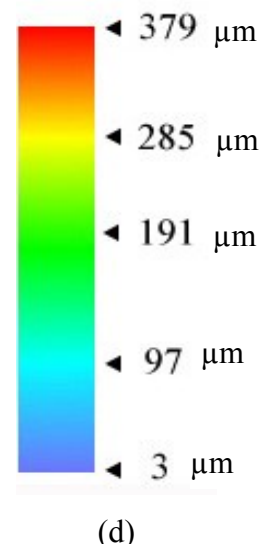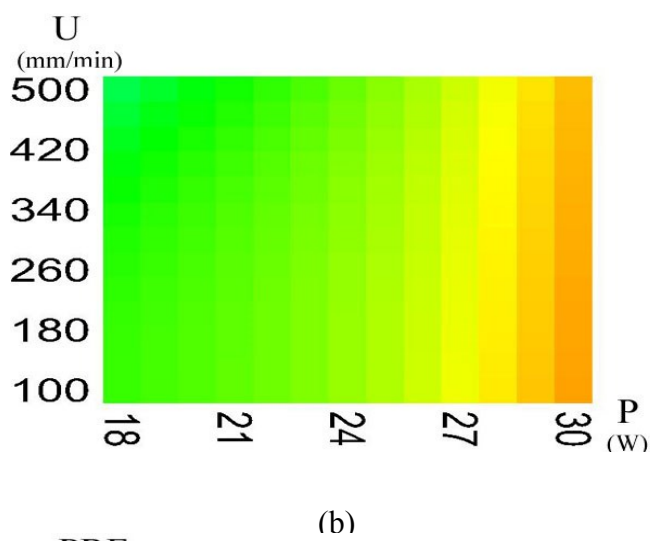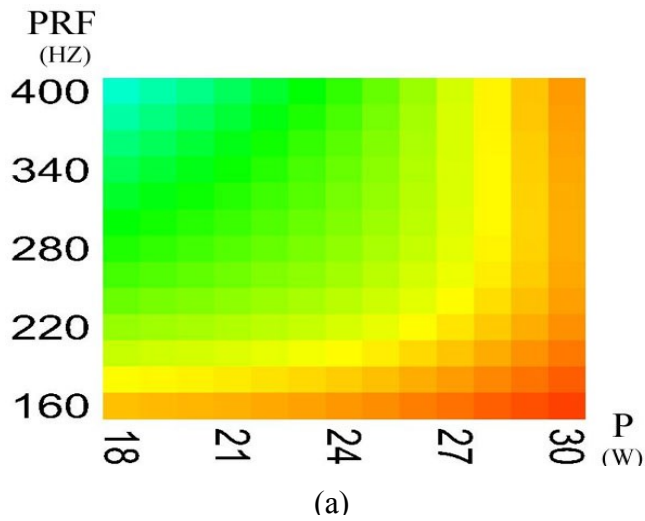
Figure 4-2: Showing interactive effect on micro-channel width for (a) PRF and P with U=5 mm/sec; (b) U and P with PRF=280 Hz; (c) PRF and U with P=24W; and (d) scale bar for dimensions.

119
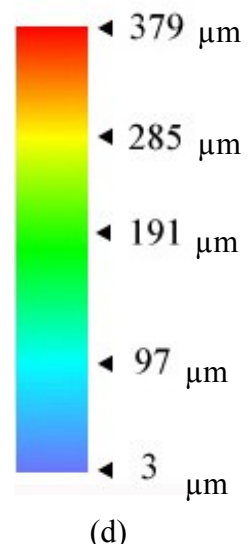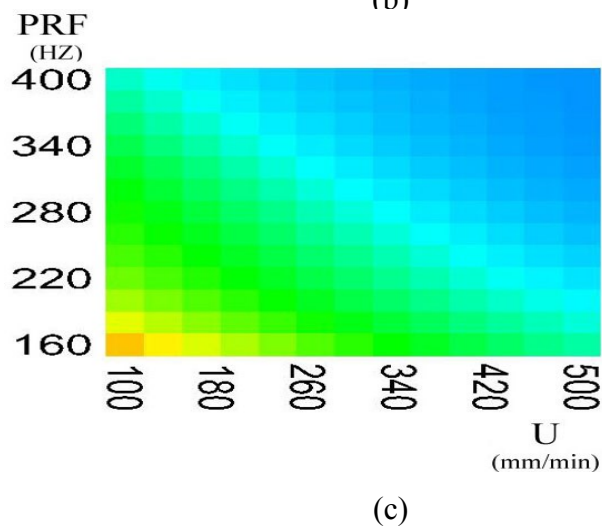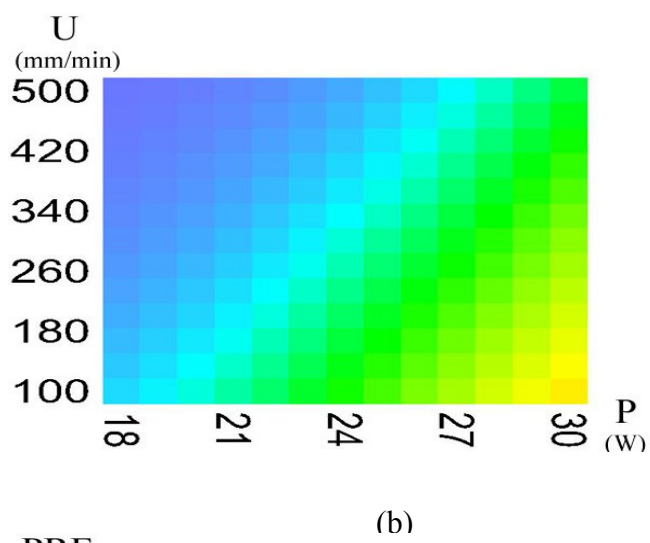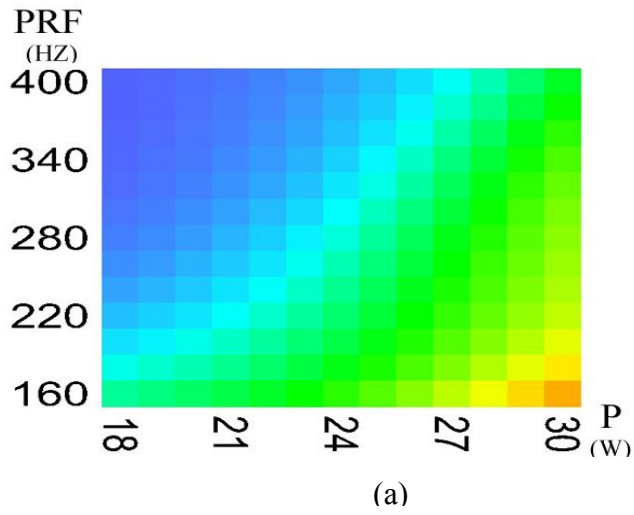
Figure 4-3: Showing interactive effect on micro-channel depth for (a) PRF and P with U=5 mm/sec; (b) U and P with PRF=280 Hz; (c) PRF and U with P=24W; and (d) scale bar for dimensions.

4.2.5   Discussion

A CO_2 laser system was used for the production of micro-channels in glass. A software package, called Design-Expert, was used to design the information gathering experiments and to develop the RSM predictive model [5, 127]. Predictive models were developed to relate the laser micromachining input parameters (laser power, PRF, and translation speed) to the output responses (machined micro-channel width and depth). Experiments, designed according to factorial Design of Experiments (DoE), were used to develop training and confirmation experiments sets for ANN predictive models. The influence of changing the number and the selection of training data set on the prediction capability of the developed ANN predictive model was investigated. Three sets of training data and another three sets of confirmation experiments were prepared for six ANN predictive models (three for width models and three for depth models). All ANN predictive models studied were of multi-layered feed-forward structure and back-propagation learning algorithm. The ANN architecture that achieved the lowest MPE for the confirmation experiments set was chosen for each ANN predictive model; see Table 4-1. It was found that the most accurate ANN model schemas were achieved with one hidden layer. This may be expected as multiple hidden layers are used for models of a deeply complex nature where response surfaces are of a higher order non-linear response [162].

The predicted dimensions from the RSM model and the three ANN predictive models were compared with the actual experimental data in terms of the MPE and the absolute maximum percentage error. The developed predictive models may be used to select the input parameters for required output dimensions or to predict the dimensions of the micro-channels based on set inputs.

Ranking predictive models (RSM, I, II, and III) according to their MPE, model II produced the lowest MPE, whereas RSM model was next best. Even though it has a larger training data set (24 for model I compared to 15 for model II), Model II showed lower MPE than model I. This indicates that the training data set is well chosen for model II. This may be because the training data set of model I is missing

one corner point of 3D experimental data space. On the other hand, model II has all the corner data points contained in its training data set. This highlights the importance of including the corner points of the 3D experimental data space in the model. Table 4-2 shows that the ranking according to MPE appears to be identical for width and depth.

Ranking predictive models (RSM, I, II, and III) according to their E_∞ (absolute maximum percentage error), Table 4-2 exhibits that model I produced the lowest absolute maximum percentage error. This result can be explained by the fact that this ANN model (model I) had the largest training data set (24 from the 27 available experimental data). So having the largest data set enabled this model to predict the confirmation experiments set with the least significant deviation. The RSM model ranked second with respect to the width prediction, while model II was second regarding depth prediction. The worse prediction from model III can be understood when it is considered that four of the eight corner points of the 3D experimental data space were not present in its training data set, so the prediction within the data space will not be sufficiently precise from this model.

Investigation of the combined effects (interaction) of the laser micromachining parameters is shown in the intensity plots of Figure 4-2 and Figure 4-3 for width and depth respectively. From these figures, it can be seen that the power has a large positive effect on the micro-channel widths and depths. On the other hand, the PRF has a negative effect on the micro-channel widths and depths. Translation speed however has little effect for micro-channel widths but some negative relation on micro-channel depths.

4.3   Polymer Experiments with Nd:YVO₄ Laser System

4.3.1   Polycarbonate Experiments

Micrographs of produced micro-channels

Figure 4-4 (a), (b) show micro-channels produced in polycarbonate at P = 0.5 W, PRF = 13 kHz, and P = 1.5 W, PRF = 23 kHz respectively. The translation speed U was fixed at 2.98 mm/sec for production of these micro-channels. The corresponding and increasing micro-channel widths were respectively 65.2, and 152.3 μm. Increasing power results in an increase of pulse energy and fluence which lead to an increased micro-channel width.
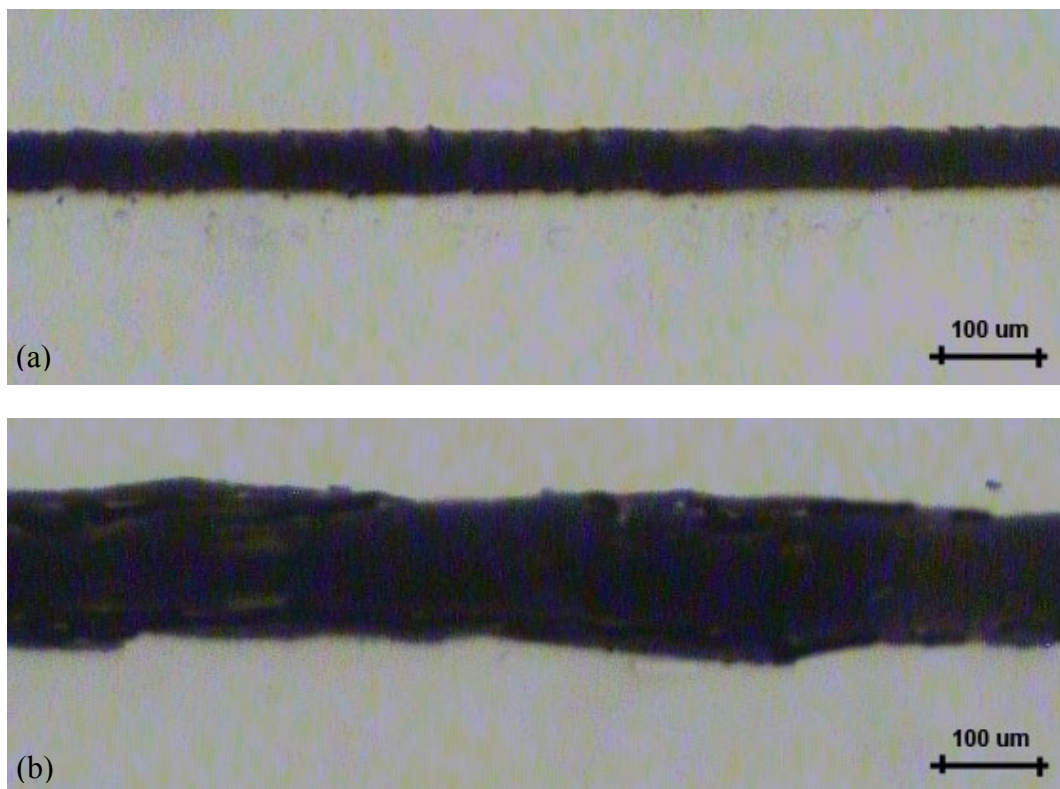
Figure 4-4: Plan view micrographs of two laser-machined micro-channels.

(a) at P = 0.5 W, PRF = 13 kHz, U = 2.98 mm/sec and

(b) at P = 1.5 W, PRF = 23 kHz, and U = 2.98 mm/sec.

RSM Analysis of Variance (ANOVA)

Analysis of variance (ANOVA) for width and cost models, developed using RSM, was carried out using Design-Expert software in order to test the significance of the regression models. The stepwise regression method was selected in order to eliminate the insignificant model terms automatically. The ANOVA for the two models summarises the analysis of each response in terms of sequential F-test, lack of fit test and show the significant model terms.

Table 4-5 and Table 4-6 show the ANOVA results for RSM width and cost models respectively. In addition, they show the other adequacy measures R^2, adjusted R^2 and predicted R^2. All the adequacy measures are close to one and indicate significant relationships considering a significance threshold of 0.001. The adequate precision ratios, being above four, in both models indicate adequate models discrimination.

Table 4-5: ANOVA analysis for the width model.

Source	Sum of Squares	d.f.	Mean Square	F Value	Prob > F
Model	93472.16	5	18694.43	141.7405	< 0.0001
P	60181.37	1	60181.37	456.293	< 0.0001
PRF	18902.16	1	18902.16	143.3155	< 0.0001
U	9581.894	1	9581.894	72.64958	< 0.0001
P×PRF	3550.08	1	3550.08	26.91658	< 0.0001
P×U	1256.653	1	1256.653	9.527901	0.0048
Residual	3429.191	26	131.8919		
Lack of Fit	3355.696	21	159.795	10.87115	0.0074
Pure Error	73.495	5	14.699		
Corrected Total	96901.35	31			

$R^2 = 0.965$, adjusted $R^2 = 0.958$, predicted $R^2 = 0.940$, adequate precision = 45.567.

Table 4-6: ANOVA analysis for the cost model.

Source	Sum of Squares	d.f.	Mean Square	F Value	Prob > F
Model	3.917822	4	0.979456	167972.2	< 0.0001
P	0.001875	1	0.001875	321.4944	< 0.0001
U	3.200602	1	3.200602	548888.9	< 0.0001
P×U	0.000926	1	0.000926	158.76	< 0.0001
U^2	0.71442	1	0.71442	122519.8	< 0.0001
Residual	0.000157	27	5.83E-06		
Lack of Fit	0.000157	22	7.16E-06		
Pure Error	0	5	0		
Corrected Total	3.91798	31			

$R^2 = 0.999$, adjusted $R^2 = 0.999$, predicted $R^2 = 0.999$, adequate precision = 904.922.

Analysis of variance indicated that the laser power (P), (PRF), translation speed (U), the two level interaction of laser power and pulse repetition frequency (P×PRF), and the two level interaction of laser power and translation speed (P×U), are the most significant model terms associated with width. Regarding cost model, the laser power (P), translation speed (U), the two level interaction of laser power and translation speed (P×U), and the second order effect of translation speed (U^2) are the significant model terms.

Development of Experiential and Mathematical Models

Constructing a mathematical model for the laser micro-machining process is an important step for understanding its behaviour, performance and for optimising the process itself. The experiential models for micro-channel width and micro-machining cost in terms of actual factors as established are shown below:

Width = 19.915 + 223.484 × P + 0.199 × PRF - 2.101 × U - 3.440
× P × PRF -16.505 × P × U

4-4

Cost = 1.429 + 0.045 × P - 1.008 × U - 0.0142 × P × U + 0.196 × U^2 4-5

While the following final mathematical models are in terms of coded factors:

Width = 136.49 + 57.82 × P - 32.41 × PRF - 23.07 × U - 17.20 × P × PRF - 10.23 × P × U   4-6

Cost = 0.29 + 0.010 × P - 0.42 × U – 0.008 × P × U + 0.30 × U^2 4-7

Interaction Effects of Control Parameters on the Responses

The influence of micro-machining parameters and their interaction effects can be analysed by using a 3D response graph. Figure 4-5, Figure 4-6, and Figure 4-7 show 3D response graphs for width and cost are drawn by varying two parameters and keeping the third parameter at constant middle level.
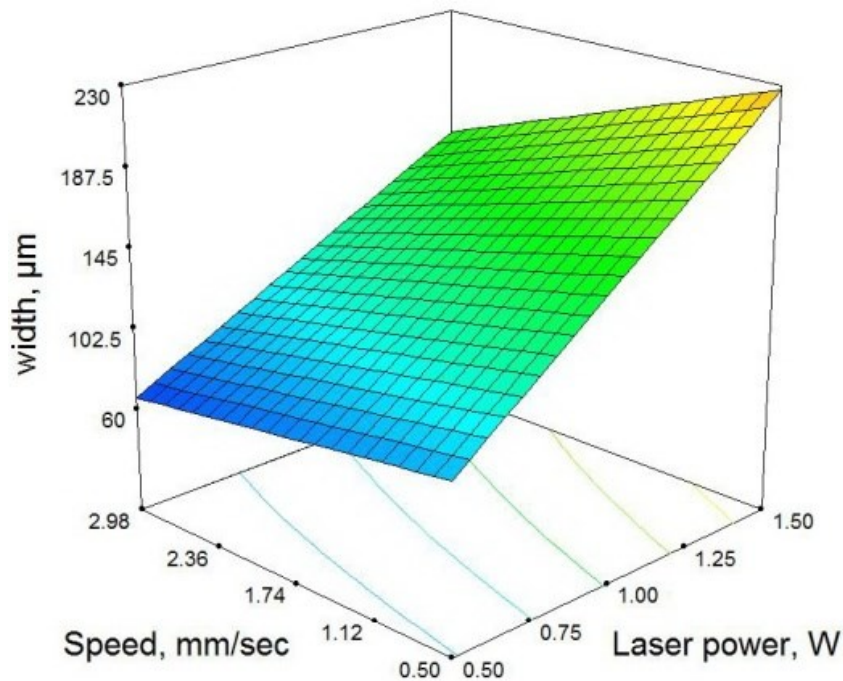
Figure 4-5: Interactive effect of U and P with PFR = 23 kHz on width.

Figure 4-5 show the interactive effect between translation speed (U), and laser power (P); while PRF = 23 kHz on the micro-channel width. This 3D graph shows that

126

increased laser power increases the micro-channel width. To a smaller extent, an increase in speed resulted in a decrease in micro-channel width.
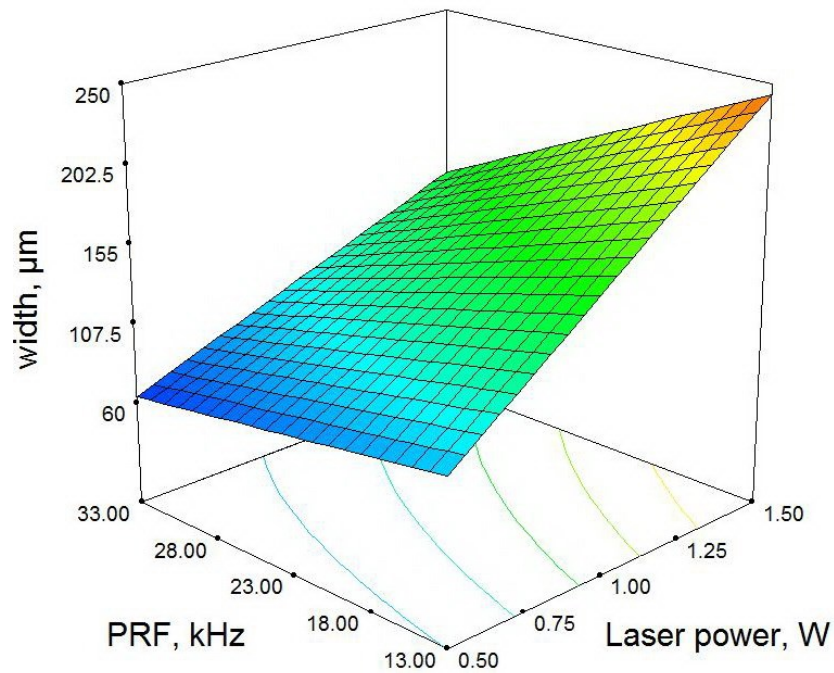
Figure 4-6: Interactive effect of P and PRF with U =1.74 mm/sec on width.

Figure 4-6 shows the interactive effect between PRF and laser power P; while translation speed U =1.74 mm/sec on micro-channel width. This graph looks similar to that of translation speed (U), and laser power (P), seen in Figure 4-5. Moreover, it shows that increased laser power increases the micro-channel width. To a lesser degree, an increase in PRF resulted in a decrease in micro-channel width.

Figure 4-7 show the interactive effect between laser power (P), and translation speed (U), while PRF = 23 kHz on the micromachining cost. This 3D graph shows that varying laser power has negligible effect on process cost. Furthermore, it demonstrates that the micro-machining cost significantly decreases by increasing the sample translation speed and insignificantly increases by increasing the laser power.
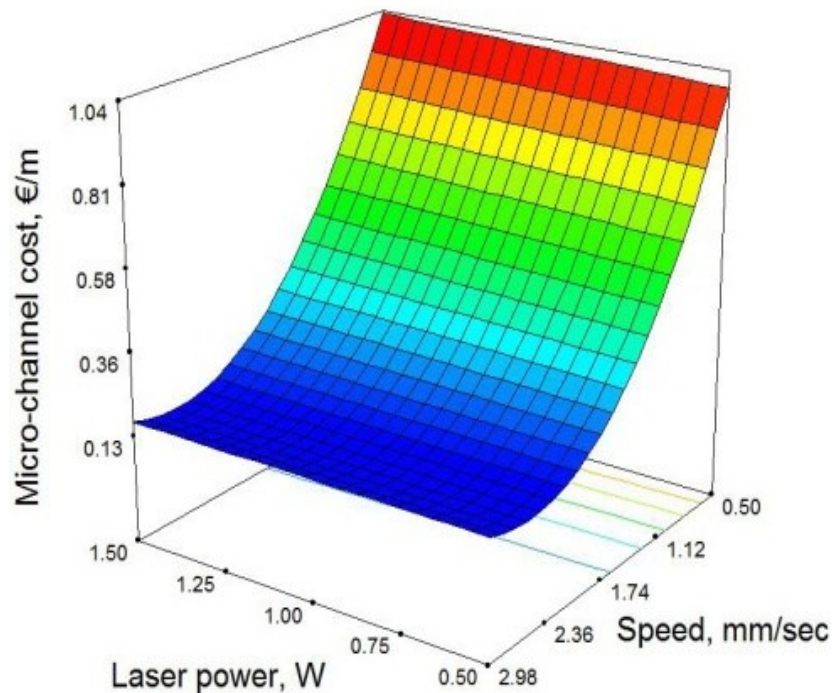
Figure 4-7: Interactive effect of P and U with PRF=23 kHz on cost.

ANN Prediction Models

To choose the best developed ANN structure for each of the six ANN models (three for the width model and other three for the cost model), several discriminating criteria are needed to differentiate between the ANN developed structures. Profound search in statistics was carried out to find estimators that can quantify the difference between values implied by a predictive model and the true values of the quantity being estimated. Three statistical estimators were found to be the best criterions that together can do the required work. These statistical estimators are MSE (Mean Squared Error), R^2 (The coefficient of determination), and MAPE (Mean Absolute Percentage Error).

MSE measures the average of the squares of the "errors." The error is the amount by which the predicted value (implied by a predictive model) differs from the actual value being predicted. R^2 offers a measure of how well future predictions are likely

to be predicted by the predictive model. MAPE is the average of summed absolute values of all the percentage errors and it produces a measure of relative overall fit.

MSE, R^2, and MAPE were calculated according to the Formulas below:

$$\text{MSE} = \frac{1}{n}\sum_{i=1}^{n}((y_i - \hat{y}_i)^2) \qquad\qquad 4\text{-}8$$

$$R^2 = \frac{\sum_{i=1}^{n}((\hat{y}_i - \bar{y})^2)}{\sum_{i=1}^{n}((y_i - \bar{y})^2)} \qquad\qquad 4\text{-}9$$

$$\text{MAPE} = \frac{1}{n}\sum_{i=1}^{n}\left|\frac{y_i - \hat{y}_i}{y_i}\right| \qquad\qquad 4\text{-}10$$

Where n is the number of experiments, y is the actual value, $\hat{y}$ is the predicted value, and $\bar{y}$ is the mean of actual values.

In this work and after trying a wide variety of hidden layer diversifications, it was discovered that the best ANN schemas, which has the lowest values of MSE and MAPE and the highest values of R^2, were obtained with one hidden layer for models I, and III, and two hidden layers for model II. Table 4-7 shows the number of neurons in the hidden layers that achieved best predictions of width and cost for models I, II, and III.

Table 4-7: Number of neurons in the hidden layers for width and cost models in I, II, and III models.

ANN Model	Hidden layers	Width model	Cost model
I	1st	6	4
II	1st	3	4
	2nd	3	-
III	1st	8	4

Actual Vs Predicted

The actual and predicted values of width and cost for RSM, I. II. and III models are shown in Table 4-8. The bold numbers indicate accurately predicted values.

Prediction Percentage Errors
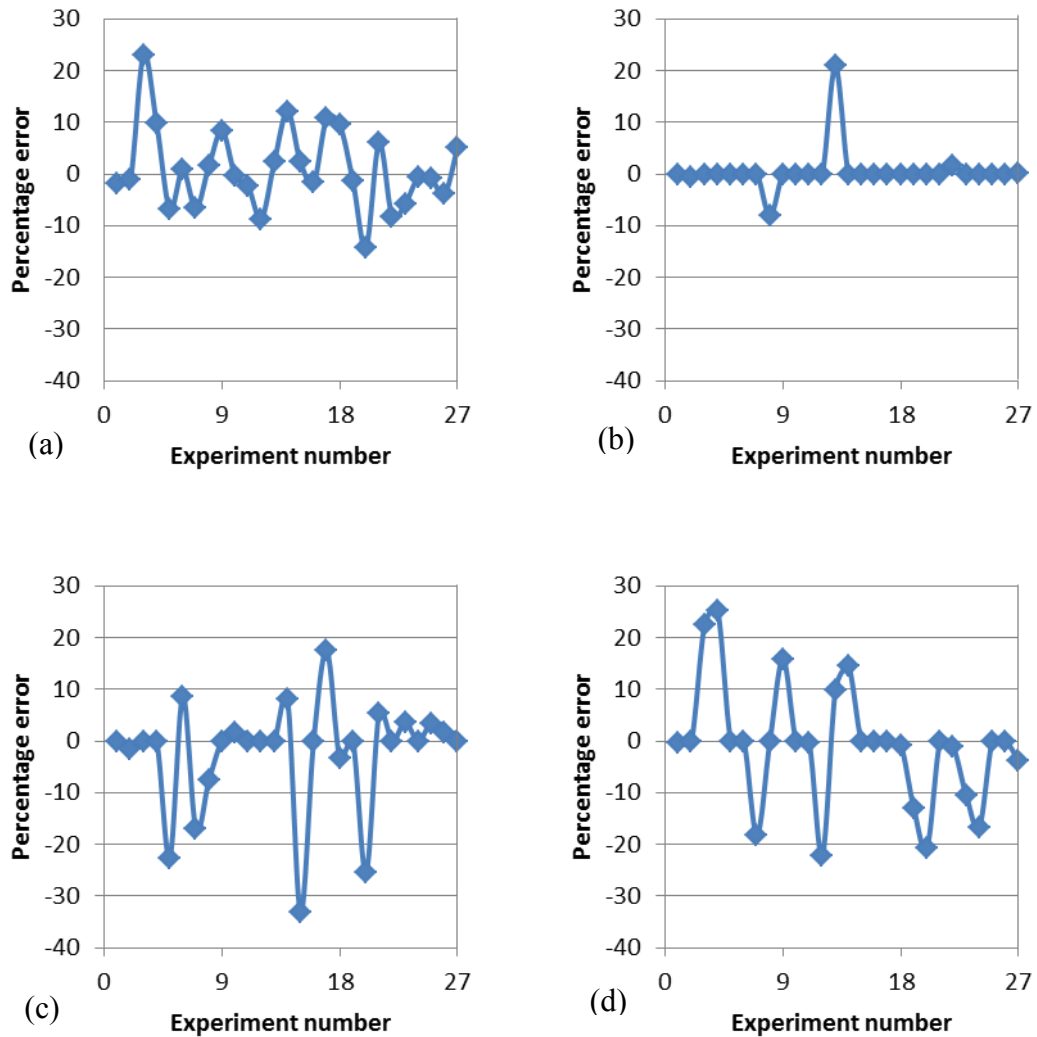
Figure 4-8: Percentage errors of predicted width values for (a) RSM, (b) model I, (c) model II, and (d) model III.

In order to compare visually between the width and cost actual values of and their RSM and ANN predicted counterparts, percentage errors were calculated according to formula 4-11.

130

Table 4-8: Actual vs. predicted for RSM, I, II, and III models.

#	Width (µm)					Cost (€/m)				
	Actual	RSM	I	II	III	Actual	RSM	I	II	III
1	116.0	105.9	**116.0**	**116.0**	90.3	0.991	0.993	**0.991**	**0.991**	**0.991**
2	180.3	191.1	**180.3**	190.0	**180.3**	1.012	**1.012**	**1.012**	**1.012**	**1.012**
3	263.2	276.4	263.7	**263.2**	253.4	1.033	1.031	**1.033**	**1.033**	1.028
4	99.6	99.3	**99.6**	101.3	**99.6**	0.991	0.993	**0.991**	**0.991**	**0.991**
5	152.9	167.4	**152.9**	147.7	151.7	1.012	**1.012**	**1.012**	**1.012**	**1.012**
6	245.0	235.4	**245.0**	249.0	**245.0**	1.033	1.031	**1.033**	**1.033**	1.028
7	80.9	75.5	**80.9**	67.1	66.2	0.991	0.993	**0.991**	**0.991**	**0.991**
8	123.5	126.3	**123.5**	82.6	**123.5**	1.012	**1.012**	**1.012**	**1.012**	**1.012**
9	193.0	177.2	196.3	**193.0**	190.9	1.033	1.031	**1.033**	**1.033**	1.028
10	85.0	86.3	78.1	78.5	**85.0**	0.283	0.279	**0.283**	0.282	**0.283**
11	163.5	161.3	**163.5**	**163.5**	142.1	0.289	**0.289**	**0.289**	**0.289**	**0.289**
12	238.7	236.4	**238.7**	246.9	**238.7**	0.295	0.299	**0.295**	**0.295**	**0.295**
13	72.7	79.8	**72.7**	**72.7**	91.1	0.283	0.279	**0.283**	0.282	**0.283**
14	139.9	137.6	**139.9**	**139.9**	**139.9**	0.289	**0.289**	**0.289**	**0.289**	**0.289**
15	207.4	195.4	**207.4**	214.8	185.5	0.295	0.299	**0.295**	**0.295**	**0.295**
16	56.5	55.9	56.2	55.6	**56.5**	0.283	0.279	**0.283**	0.282	**0.283**
17	89.0	96.5	**89.0**	**89.0**	103.1	0.289	**0.289**	**0.289**	**0.289**	**0.289**
18	122.3	137.1	**122.3**	132.2	140.0	0.295	0.299	**0.295**	**0.295**	**0.295**
19	65.2	80.2	**65.2**	**65.2**	79.8	0.165	0.167	**0.165**	**0.165**	0.166
20	169.2	145.0	**169.2**	126.0	134.1	0.169	**0.169**	**0.169**	**0.169**	**0.169**
21	211.2	209.8	210.8	**211.2**	176.0	0.172	0.170	**0.172**	**0.172**	**0.172**
22	79.0	73.6	**79.0**	61.1	**79.0**	0.165	0.167	**0.165**	**0.165**	0.166
23	118.4	121.2	143.1	**118.4**	130.1	0.169	**0.169**	**0.169**	**0.169**	**0.169**
24	152.3	168.8	**152.3**	178.8	**152.3**	0.172	0.170	**0.172**	**0.172**	**0.172**
25	50.8	49.8	**50.8**	**50.8**	50.6	0.165	0.167	**0.165**	**0.165**	0.166
26	79.6	80.2	**79.6**	86.5	**79.6**	0.169	**0.169**	**0.169**	**0.169**	**0.169**
27	113.4	110.6	**113.4**	**113.4**	112.9	0.172	0.170	**0.172**	**0.172**	**0.172**

$$\text{Percentage error} = \frac{100 * (\hat{y} - y)}{y} \qquad\qquad 4\text{-}11$$

Where y is the actual value, and $\hat{y}$ is the predicted value.

Width and cost predicted values percentage errors for RSM, I, II, and III models are shown in Figure 4-8 and Figure 4-9 respectively. These figures also provided a good visual comparison between the investigated predictive models.
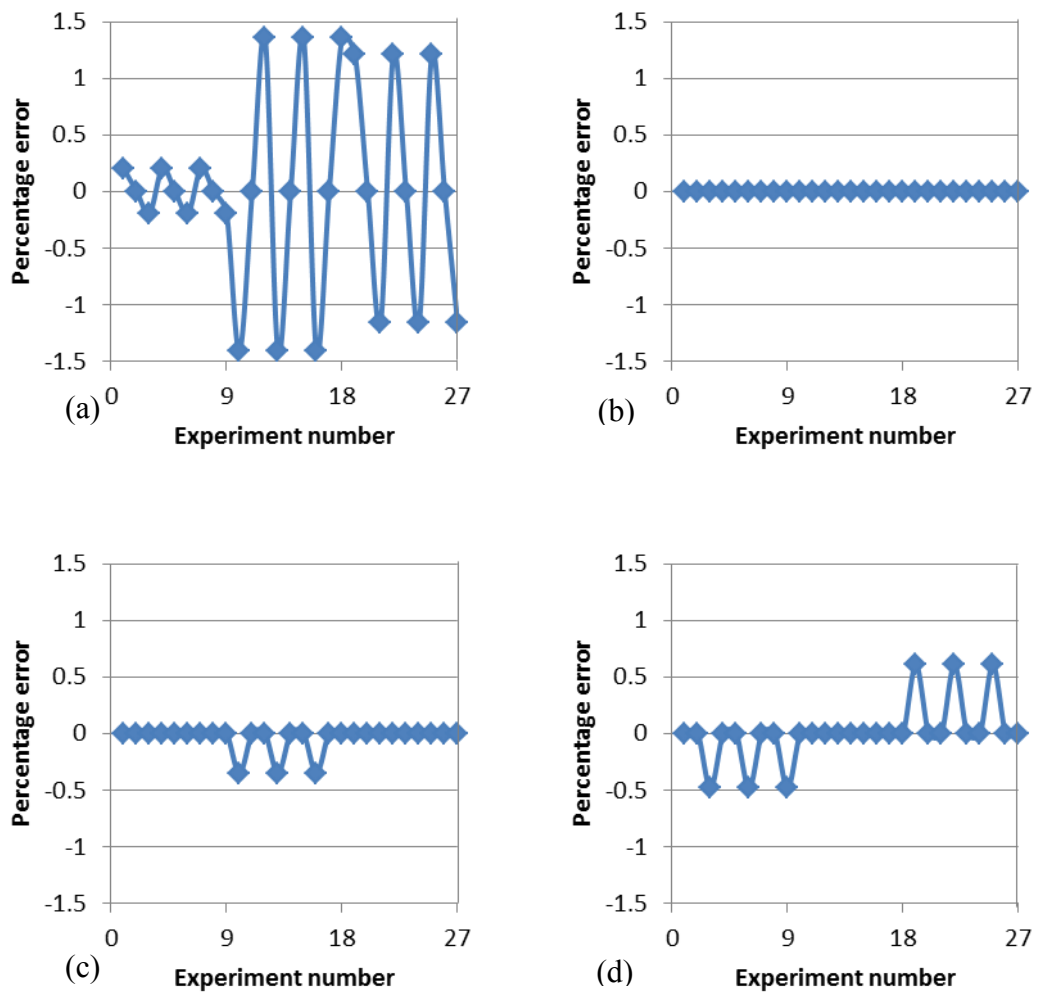
Figure 4-9: Percentage errors of predicted cost values for (a) RSM, (b) model I, (c) model II, and (d) model III.

RSM Vs ANN

MSE (Mean Squared Error), R^2 (The coefficient of determination), and MAPE (Mean Absolute Percentage Error) were utilised to quantify the difference between values produced by predictive models and the actual values. Besides, they were utilised as a measure of how well future outcomes are likely to be predicted by the investigated model. So effectively, these three estimators were used for the selection of the best schemas for each ANN model in the first place. Moreover, they were used to compare between the predictive models. Table 4-9 shows a side-by-side comparison between models RSM, I, II, and III in terms of the three chosen estimators.

Table 4-9: Comparison criteria of predictive models for width and cost.

Estimator	Width				Estimator	Cost			
	RSM	I	II	III		RSM	I	II	III
MSE	96.4	24.8	192.7	206.8	MSE	6×10^{-6}	8×10^{-11}	9×10^{-8}	3×10^{-6}
R^2	0.97	0.99	0.95	0.95	R^2	0.99	0.99	0.99	0.99
MAPE	5.8	1.2	6.0	7.2	MAPE	0.643	0.003	0.038	0.100

Table 4-10: Ranking of predictive models according to the comparison criteria.

Model	Width			Model	Cost		
Estimator	MSE	R^2	MAPE	Estimator	MSE	R^2	MAPE
1 (best)	I	I	I	1 (best)	I	I	I
2	RSM	RSM	RSM	2	II	II	II
3	II	II	II	3	III	III	III
4 (worst)	III	III	III	4 (worst)	RSM	RSM	RSM

Lower values of MSE and MAPE and higher values of R^2 indicate better model fit. Table 4-10 shows the RSM, I, II, and III models for width and cost prediction listed from best to worst.

Discussion

A Nd:YVO$_4$ micromachining laser system was used for the production of micro-channels in polycarbonate. To study the relationship between laser micromachining input parameters (laser power, PRF, and translation speed) and the output responses (the developed micro-channel width and corresponding micro-machining operating cost), RSM, and ANN predictive models were used. The Design-Expert software was used to develop an RSM predictive model and to design an arranged series of information-gathering experiments according to factorial Design of Experiments (DoE). Analysis of variance (ANOVA) for width and cost RSM models was carried out to test the significance of the regression models. ANOVA analysis in terms of sequential F-test, lack of fit test, and adequacy measures indicated that the constructed models are significant. Additionally, it signified the statistical significant model terms associated with width and cost RSM models.

RSM models were used along with the Design-Expert software to develop mathematical models that describe the width and cost models and to create 3D surface graphs that show the combined effects (interaction) of laser micromachining parameters on the responses, shown in Figure 4-5, and Figure 4-6. These intensity plots were developed by varying two parameters and keeping the third parameter at constant middle level. These figures showed that increased laser power increases the micro-channel width, while increased PRF decreases the micro-channel width. Besides, they revealed that the micro-machining cost significantly decreases by increasing the sample translation speed and insignificantly increases by increasing the laser power.

DoE experiments were used to develop training data sets for ANN predictive models. The influence of changing the number and the selection of training data on the prediction capability of the developed ANN predictive model was investigated.

134

Three sets of training data were prepared for six ANN predictive models (three for the width models and another three for the cost models). All studied ANN predictive models were of multi-layered feed-forward structure and back-propagation learning algorithm. MSE (Mean Squared Error), R^2 (The coefficient of determination), and MAPE (Mean Absolute Percentage Error) were used to quantify the difference between values implied by a predictive model and the true values of the quantity being estimated. Moreover, they were utilised as a basis for comparison between the developed ANN schemas. Furthermore, they provided a basis of comparison between all developed predictive models. ANN schema that achieved the lowest values of MSE and MAPE and the highest values of R^2 for all experimental data was chosen for each ANN predictive model (Table 4-7). It was found that the most accurate ANN model schemas were obtained with one hidden layer for models I and III, and two hidden layers for model II.

The predicted dimensions from the RSM model and the three ANN predictive models were compared with the actual experimental data in terms of MSE (Mean Squared Error), R^2 (The coefficient of determination), and MAPE (Mean Absolute Percentage Error). The developed predictive models may be used to select the input parameters for required output dimensions or to predict the dimensions of the micro-channels based on set inputs.

Ranking the models (RSM, I, II, and III) according to the three statistical estimators, Model I produced the lowest values of MSE and MAPE and the highest values of R^2. Therefore, model I was the best for width and cost models. This might be attributed to the high number of training data used in this model (24 out of 27 available experiments). This was the largest amount of training data compared to the other ANN models (14 for model II and 13 for model III). This enabled model I to predict the experimental data of width and operating cost with a narrow margin of error.

RSM was next best for width models, but came last for depth models. On the other side, Model II was next best for depth models and third better for width models and better than model III, even though both having almost the same number of training data but different training data set. This could be attributed to the fact that the

training data set in model II was chosen according to Face Centred Cubic Design that covers all the corner points from the experimental data space. While the rather worse prediction of the models that used Box-Behnken Design, could be because of the absence of the eight experimental data space's corner points from the training data set. So due to the lack of these influential points, the estimation within the data ranges will not be adequately exact from this model.

For micro-machining process prediction, the comparison showed that using a high number of ANN training data set would provide the best predictive tool. Well-chosen but limited number of ANN training data set would provide good, but not the best, predictive tool for models of a deeply complex nature where response surfaces are of high-order nonlinear response.

It can be seen clearly from Table 4-9 that values of the statistical estimators for cost prediction are a lot better than the values of their counterparts for width prediction. This can be attributed to the fact that production cost is proportional to its inputs and it was originally estimated using equation 3-1. Furthermore, this demonstrates the ability to utilise RSM and ANN as an arbitrary function estimation technique that uses experimentally observed data to "learn".

Table 4-10 shows that all statistical estimators came to an agreement; model I was the best, then RSM, then model II, and III, came last for the width model. With regard to the cost model, model I was the best, then model II, and III, and finally RSM came last. This agreement indicates that these estimators work together in harmony, and they were a good choice. These results empirically establish their use as criteria for selecting both the best ANN configuration for a developed model and comparison criteria for predictive models.

4.3.2   PMMA Processing

RSM Analysis of Variance (ANOVA)

Analysis of variance (ANOVA) for the RSM width and cost models was carried out using Design-Expert software in order to test the significance of the regression

models. The stepwise regression method was selected in order to eliminate the insignificant model terms automatically. The ANOVA for the two models summarises the analysis of each response in terms of sequential F-test, lack of fit test and show the significant model terms.

Table 4-11 and Table 4-12 show the ANOVA results for RSM width and cost models respectively. In addition, they show the other adequacy measures R^2, adjusted R^2 and predicted R^2. All the adequacy measures are close to one and indicate significant relationships considering a significance threshold of 0.001. The adequate precision ratios, being above four, in both models indicate adequate models discrimination.

ANOVA indicated that laser power P, PRF, translation speed U, the two level interaction of PRF and translation speed (PRF×U) and the second order effect of translation speed (U^2) are considered as the most significant model terms associated with width. Concerning the cost model, laser power (P), translation speed (U), the two level interaction of laser power and translation speed (P×U) and the second order effect of translation speed (U^2) are the model terms proven to be highly significant.

Table 4-11: ANOVA analysis for the width model.

Source	Sum of Squares	d.f.	Mean Square	F Value	Prob > F
Model	24012.86929	5	4802.573858	32.16069056	< 0.0001
P	1271.760556	1	1271.760556	8.516412011	0.0072
PRF	615.2252469	1	615.2252469	4.119888496	0.0527
U	9288.845	1	9288.845	62.2032432	< 0.0001
PRF×U	11737.5075	1	11737.5075	78.6008415	< 0.0001
U^2	1099.530988	1	1099.530988	7.363067576	0.0117
Residual	3882.594501	26	149.3305577		
Lack of Fit	3499.29227	21	166.6329652	2.173649819	0.1986
Pure Error	383.3022315	5	76.6604463		
Corrected Total	27895.46379	31			

$R^2 = 0.861$, adjusted $R^2 = 0.834$, predicted $R^2 = 0.782$, adequate precision = 23.584.

Table 4-12: ANOVA analysis for the cost model.

Source	Sum of Squares	d.f.	Mean Square	F Value	Prob > F
Model	3.917822	4	0.979456	167972.2	< 0.0001
P	0.001875	1	0.001875	321.4944	< 0.0001
U	3.200602	1	3.200602	548888.9	< 0.0001
P×U	0.000926	1	0.000926	158.76	< 0.0001
U^2	0.71442	1	0.71442	122519.8	< 0.0001
Residual	0.000157	27	5.83E-06		
Lack of Fit	0.000157	22	7.16E-06		
Pure Error	0	5	0		
Corrected Total	3.91798	31			

$R^2 = 0.999$, adjusted $R^2 = 0.999$, predicted $R^2 = 0.999$, adequate precision = 904.922.

Development of Experiential and Mathematical Models

Developing an experiential model is crucial for understanding the laser micro-machining process performance and its behaviour and for optimising the process itself. The mathematical models for micro-channel width and micro-machining cost in terms of actual factors as established by the Design-Expert software are shown below:

$$\text{Width} = 4.023 + 16.811 \times P + 4.973 \times PRF + 12.947 \times U - 2.522 \times PRF \times U + 7.685 \times U^2 \qquad \text{4-12}$$

$$\text{Cost} = 1.429 + 0.045 \times P - 1.008 \times U - 0.0142 \times P \times U + 0.196 \times U^2 \qquad \text{4-13}$$

While the following final mathematical models are in terms of coded factors:

$$\text{Width} = 80.07 + 8.41 \times P + 5.85 \times PRF - 22.72 \times U - 31.27 \times PRF \times U + 11.82 \times U^2 \qquad \text{4-14}$$

$$\text{Cost} = 0.29 + 0.010 \times P - 0.42 \times U - 0.008 \times P \times U + 0.30 \times U^2 \qquad \text{4-15}$$

Interaction Effects of Control Parameters on the Responses

The influence of micro-machining parameters and their interaction effects can be analysed by using 3D response graph. Figure 4-10, and Figure 4-11 show 3D response graphs for width and cost are drawn by varying two parameters and keeping the third parameter at constant middle level.
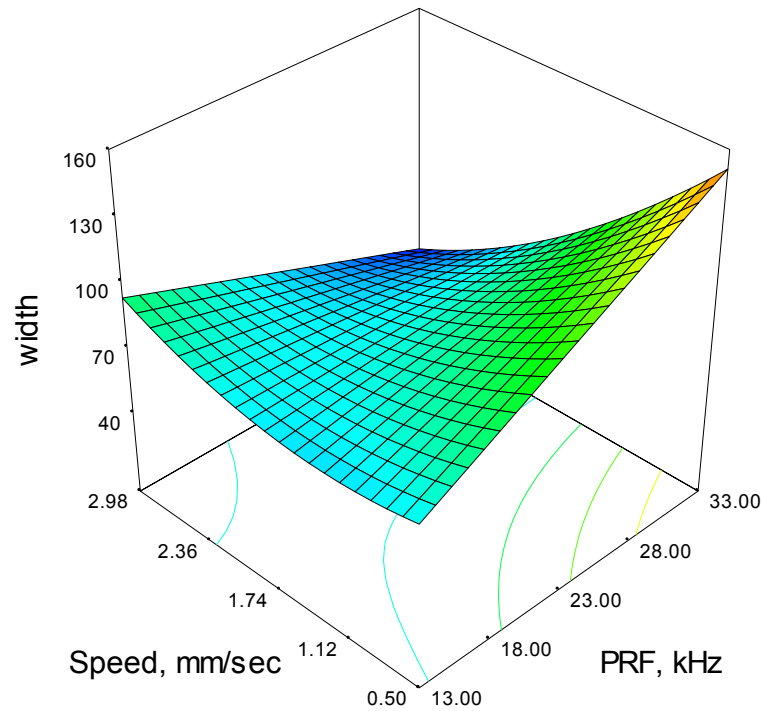
Figure 4-10: Interactive effect U and PRF with P = 1 W on width.

Figure 4-10 show the interactive effect between translation speed U, and PRF; while the laser power P = 1 W on the micro-channel width. This 3D graph shows that increased PRF at high level of speed decreased the width, whereas the opposite trend is noticed at the low level of sample translation speed. Besides, it shows that increased speed at high level of pulse repetition frequency decreased the width, whereas the opposite trend, to a lesser degree, was noted at the low level of PRF.

Figure 4-11 show the interactive effect between laser power (P), and translation speed (U), while PRF = 23 kHz on the micromachining cost. This 3D graph shows that varying laser power has negligible effect on process cost. Furthermore, it demonstrates that the micro-machining cost significantly decreases by increasing the sample translation speed and insignificantly increases by increasing the laser power.
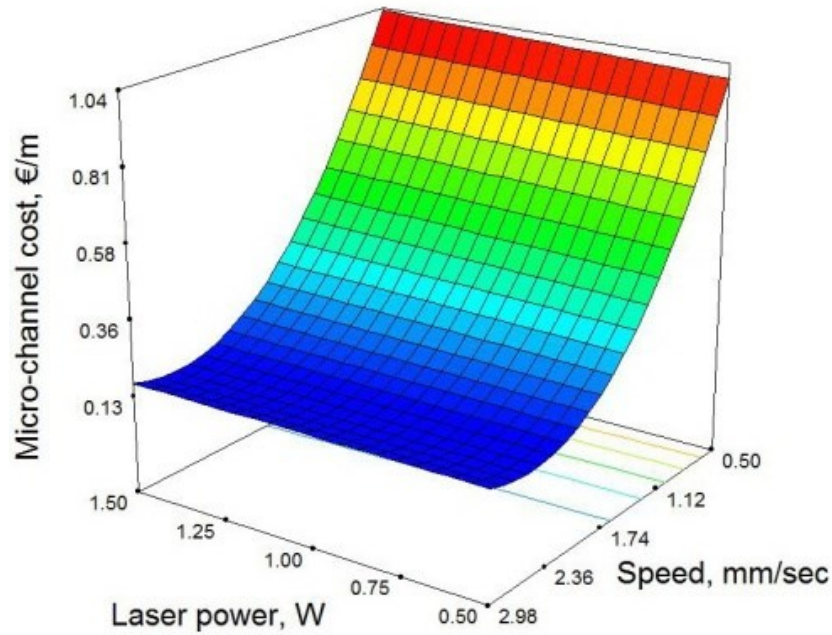
Figure 4-11: Interactive effect of P and U with PRF = 23 kHz on cost.

ANN Prediction Models

To choose the best developed ANN structure for each of the eight ANN models (four for the width model and other four for the cost model), several discriminating criteria are needed to differentiate between the ANN developed structures.

The three aforementioned statistical estimators MSE (Mean Squared Error), R^2 (The coefficient of determination), and MAPE (Mean Absolute Percentage Error) were utilised.

In this work and after trying a wide variety of hidden layer diversifications, it was discovered that the best ANN schemas, which has the lowest values of MSE and MAPE and the highest values of R^2, were obtained with one hidden layer for models I, II, and III and two hidden layers for model IV. Table 4-12 shows the number of neurons in the hidden layers that achieved best predictions of width and cost for models I, II, III, and IV.

141

Table 4-13: Number of neurons in the hidden layers for width and cost models in I, II, III, and IV models.

ANN Model	Hidden layers	Width model	Cost model
I	1st	6	4
II	1st	5	4
III	1st	8	4
IV	1st	4	5
	2nd	4	-

Actual Vs Predicted

The actual and predicted values of width and cost for RSM, I. II. III, and IV models are shown in Table 4-14. The bold numbers indicate accurately predicted values.

Table 4-14: Actual vs. predicted for RSM, I, II, III, and IV models.

#	Width (um)						Cost (€/m)					
	Actual	RSM	I	II	III	IV	Actual	RSM	I	II	III	IV
1	60.3	69.1	55.9	**60.3**	80.0	**60.3**	0.991	0.993	**0.991**	**0.991**	**0.991**	**0.991**
2	79.8	77.5	**79.8**	63.4	**79.8**	**79.8**	1.012	**1.012**	**1.012**	**1.012**	**1.012**	**1.012**
3	62.8	85.9	**62.8**	**62.8**	92.2	**62.8**	1.033	1.031	**1.033**	**1.033**	1.028	**1.033**
4	103.4	106.2	**103.4**	110.0	**103.4**	113.6	0.991	0.993	**0.991**	**0.991**	**0.991**	**0.991**
5	125.9	114.6	**125.9**	**125.9**	114.4	**125.9**	1.012	**1.012**	**1.012**	**1.012**	**1.012**	**1.012**
6	142.2	123.0	**142.2**	136.0	135.7	**142.2**	1.033	1.031	**1.033**	**1.033**	1.028	**1.033**
7	135.5	143.3	**135.5**	160.8	134.5	155.5	0.991	0.993	**0.991**	**0.991**	**0.991**	**0.991**
8	155.1	151.7	**155.1**	164.8	**155.1**	158.6	1.012	**1.012**	**1.012**	**1.012**	**1.012**	**1.012**
9	166.5	160.1	159.7	**166.5**	157.5	159.6	1.033	1.031	**1.033**	**1.033**	1.028	**1.033**
10	74.0	65.8	57.3	78.7	**74.0**	56.2	0.283	0.279	**0.283**	0.282	**0.283**	0.266
11	92.6	74.2	**92.6**	**92.6**	83.0	110.2	0.289	**0.289**	**0.289**	**0.289**	**0.289**	0.275
12	99.5	82.6	**99.5**	84.7	**99.5**	**99.5**	0.295	0.299	**0.295**	**0.295**	**0.295**	**0.295**
13	86.5	71.7	**86.5**	72.1	78.3	63.7	0.283	0.279	**0.283**	0.282	**0.283**	0.272
14	77.1	80.1	77.1	77.1	77.1	77.1	0.289	**0.289**	**0.289**	**0.289**	**0.289**	0.279
15	67.7	88.5	**67.7**	**67.7**	73.8	**67.7**	0.295	0.299	**0.295**	**0.295**	**0.295**	0.298
16	65.8	77.5	**65.8**	74.1	**65.8**	**65.8**	0.283	0.279	**0.283**	0.282	**0.283**	**0.283**
17	80.2	85.9	**80.2**	**80.2**	77.8	**80.2**	0.289	**0.289**	**0.289**	**0.289**	**0.289**	**0.289**
18	92.1	94.3	82.4	81.3	**92.1**	103.8	0.295	0.299	**0.295**	**0.295**	**0.295**	0.305
19	75.8	86.2	75.8	75.8	67.6	48.4	0.165	0.167	**0.165**	**0.165**	0.166	0.169
20	87.9	94.6	**87.9**	100.4	**87.9**	77.7	0.169	**0.169**	**0.169**	**0.169**	**0.169**	**0.169**
21	109.7	103.0	**109.7**	**109.7**	112.0	**109.7**	0.172	0.170	**0.172**	**0.172**	**0.172**	0.171
22	57.7	60.8	**57.7**	57.4	**57.7**	43.6	0.165	0.167	**0.165**	**0.165**	0.166	0.169
23	71.5	69.2	59.7	**71.5**	60.4	66.5	0.169	**0.169**	**0.169**	**0.169**	**0.169**	**0.169**
24	67.7	77.6	**67.7**	75.6	**67.7**	64.1	0.172	0.170	**0.172**	**0.172**	**0.172**	0.170
25	45.1	35.3	**45.1**	**45.1**	59.8	**45.1**	0.165	0.167	**0.165**	**0.165**	0.166	0.169
26	60.2	43.7	**60.2**	47.9	60.9	55.0	0.169	**0.169**	**0.169**	**0.169**	**0.169**	**0.169**
27	47.0	52.2	**47.0**	**47.0**	62.3	55.0	0.172	0.170	**0.172**	**0.172**	**0.172**	0.170

RSM Vs ANN

To quantify the difference between values produced by predictive models and the actual values MSE (Mean Squared Error), R^2 (The coefficient of determination), and MAPE (Mean Absolute Percentage Error) were utilised. These estimators can provide a measure of how well future outcomes are likely to be predicted by the investigated model. So practically, the same estimators were used to compare between the predictive models and for the selection of the best ANN configuration for each of the four ANN models. Table 4-15 shows a direct comparison between models RSM, I, II, III, and IV models in terms of the three chosen estimators.

Table 4-15: Comparison criteria for RSM, I, II, III, and IV models.

Estimator	Width					Estimator	Cost				
	RSM	I	II	III	IV		RSM	I	II	III	IV
MSE	128.0	21.5	77.3	87.5	112.2	MSE	6×10^{-6}	8×10^{-11}	9×10^{-8}	3×10^{-6}	3×10^{-5}
R^2	0.87	0.98	0.94	0.92	0.92	R2	0.99	0.99	0.99	0.99	0.99
MAPE	12.2	61.1	165.1	226.3	223.3	MAPE	0.643	0.003	0.038	0.100	0.120

Table 4-16: Ranking of predictive models according to the comparison criteria.

Model	Width				Model	Cost			
Estimator	MSE	R^2	MAPE	overall	Estimator	MSE	R^2	MAPE	overall
best	I	I	RSM	I	best	I	I	I	I
	II	II	I	II		II	II	II	II
	III	III	II	III		III	III	III	III
	IV	IV	IV	RSM		IV	RSM	RSM	RSM
worst	RSM	RSM	III	IV	worst	RSM	IV	IV	IV

144

Lower values of MSE and MAPE and higher values of R^2 indicate better model fit. Table 4-16 ranks RSM, I, II, III, and IV models for width and cost prediction from best to worst.

Discussion

A Nd:YVO$_4$ micromachining laser system was used for the production of micro-channels in PMMA. To study the relationship between laser micromachining input parameters (laser power, PRF, and translation speed) and the output responses (the developed micro-channel width and corresponding micro-machining operating cost), RSM and ANN predictive models were used. The Design-Expert software was used to develop an RSM predictive model and to design an arranged series of information-gathering experiments according to factorial Design of Experiments (DoE). ANOVA for width and cost RSM models was carried out to test the significance of the regression models. ANOVA analysis in terms of sequential F-test, lack of fit test, and adequacy measures indicated that the constructed models are significant. Additionally, it signified the statistical significant model terms associated with width and cost RSM models.

RSM models were used along with the Design-Expert software to develop mathematical models that describe the width and cost models and to create 3D surface graphs that show the combined effects (interaction) of laser micromachining parameters on the responses, shown in Figure 4-10, and Figure 4-11. These intensity plots were developed by varying two parameters and keeping the third parameter at constant middle level. These figures showed that increased PRF at high level of speed decreased the width, whereas the opposite trend is noticed at the low level of sample translation speed. Besides, it shows that increased speed at high level of PRF decreased the width, whereas the opposite trend, to a lesser degree, was noted at the low level of pulse repetition frequency. In addition, they revealed that the micro-machining cost significantly decreases by increasing the sample translation speed and insignificantly increases by increasing the laser power.

145

DoE experiments were used to develop training data sets for ANN predictive models. The influence of changing the number and the selection of training data on the prediction capability of the developed ANN predictive model was investigated. Four sets of training data were prepared for eight ANN predictive models (four for the width models and four for the cost models). All studied ANN predictive models were of multi-layered feed-forward structure and back-propagation learning algorithm. MSE (Mean Squared Error), R^2 (The coefficient of determination), and MAPE (Mean Absolute Percentage Error) were used to quantify the difference between values implied by a predictive model and the true values of the quantity being estimated. Moreover, they were utilised as a basis for comparison between the developed ANN schemas. Furthermore, they provided a basis of comparison between all developed predictive models. ANN schema that achieved the lowest values of MSE and MAPE and the highest values of R^2 for all experimental data was chosen for each ANN predictive model (Table 4-13). It was found that the most accurate ANN model schemas were obtained with one hidden layer for models I, II, and III, and two hidden layers for model IV.

The predicted dimensions from the RSM model and the four ANN predictive models were compared with the actual experimental data in terms of MSE (Mean Squared Error), R2 (The coefficient of determination), and MAPE (Mean Absolute Percentage Error). The developed predictive models may be used to select the input parameters for required output dimensions or to predict the dimensions of the micro-channels based on set inputs.

The overall ranking of (RSM, I, II, III, and IV) models according to the statistical estimators was completely identical for width and cost models. Model I produced the best results. This might be attributed to the high number of training data used in this model (24 out of 27 available experiments). This was the largest amount of training data compared to the other ANN models (14 for model II, 13 for model III, and 14 for model IV). This enabled model I to predict the experimental data of width and operating cost with a narrow margin of error.

Model II was next to best and better than model III, even though both having almost the same number of training data but different training data set. This could be attributed to the fact that the training data set in model II was chosen according to Face Centred Cubic Design that covers all the corner points from the experimental data space. While the rather worse prediction of the models that used Box-Behnken Design, could be because of the absence of the eight experimental data space's corner points from the training data set. So due to the lack of these significant points, the estimation within the data ranges will not be adequately precise from this model.

RSM was second to last and before model IV that came last. The slightly worse results of model IV can be attributed to the arbitrary selection of training set and the absence of crucial experimental data from the training data set. This outcome highlights the importance of the selection and design of the experimental data to produce a practical ANN model. Moreover, it is shown that ANN methodology can produce predictive models better than RSM model in terms of predictive capabilities when ANN training data set is chosen carefully even when only a limited number of experiments are allowed.

For micromachining process prediction, the comparison showed that using a high number of ANN training data set would provide the best predictive tool. Well-chosen but limited number of ANN training data set would provide good, but not the best, predictive tool for models of a deeply complex nature where response surfaces are of high-order nonlinear response.

Table 4-15 shows noticeably that the values of statistical estimator for cost prediction are much better than the values of their counterparts for width prediction. This can be justified since production cost is proportional to its inputs and it was originally estimated using Equation 3-1. Furthermore, this establishes the capability to employ RSM and ANN as an arbitrary function estimation technique that uses experimentally perceived data to "learn".

4.4 Positional Analysis

4.4.1 Positional Analysis of Nd:YVO$_4$ Laser System

Table 4-17, Table 4-19, and Table 4-21 are listing the ideal and measured spacings of the Nd:YVO$_4$ laser system along X-, Y-, and Z-axes respectively. The deviations were calculated according to Equation 3-2. On the other hand, Table 4-18, Table 4-20, and Table 4-22 present positional analysis results of Nd:YVO$_4$ laser system along X-, Y-, and Z-axes respectively. The positional analyses good results proven the potential capability of the developed 3D translation stage. The positional analysis study, along all three axes, yielded nearly identical results. This demonstrates that this translation stage is having the same positional properties and characteristics along all axes.

The positional analysis results showed that the reversal value (B), the mean reversal value ($\bar{B}$), the range mean bi-directional positional deviation (M), and the bi-directional systematic positional deviation (E) have an excellent maximum value of 49 μm for all the three axes. In terms of these four measures, results along X-axis were slightly better than results of Y-, and Z-axes.

Accuracy is the degree of closeness of measured values to the ideal values. On the other side, repeatability is the degree to which repeated movements under unchanged conditions show the same results. The accuracy and repeatability values revealed an excellent maximum value of 65 μm for all the three axes. X-, and Y-axes showed marginally better accuracy and repeatability values with a maximum of 61 μm.

Positional Analysis along X-axis

Table 4-17: Ideal and measured spacings along X-axis of the Nd:YVO$_4$ laser system.

i	Target positions		1	2	3	4	5	6	7	8
			188	2702	4855	7734	9976	12411	14892	17364
j	Ideal (μm)		188	2514	2153	2879	2242	2435	2481	2472
1	↓	actual	173	2500	2133	2893	2231	2444	2482	2462
		deviation	-15	-14	-20	14	-11	9	1	-10
	↑	actual	188	2525	2153	2879	2246	2457	2470	2471
		deviation	0	11	0	0	4	22	-11	-1
2	↓	actual	169	2506	2142	2889	2236	2424	2503	2469
		deviation	-19	-8	-11	10	-6	-11	22	-3
	↑	actual	191	2501	2172	2903	2259	2443	2463	2465
		deviation	3	-13	19	24	17	8	-18	-7
3	↓	actual	179	2497	2136	2906	2226	2453	2493	2465
		deviation	-9	-17	-17	27	-16	18	12	-7
	↑	actual	187	2518	2144	2889	2236	2435	2474	2455
		deviation	-1	4	-9	10	-6	0	-7	-17

Table 4-18: Positional analysis results of Nd:YVO$_4$ laser system along X-axis.

	i	1		2		3		4		5		6		7		8	
Target position P_i (µm)		188		2702		4855		7734		9976		12411		14892		17364	
Approach direction		↓	↑	↓	↑	↓	↑	↓	↑	↓	↑	↓	↑	↓	↑	↓	↑
Positional deviations (µm)	j=1	-15	0	-14	11	-20	0	14	0	-11	4	9	22	1	-11	-10	-1
	2	-19	3	-8	-13	-11	19	10	24	-6	17	-11	8	22	-18	-3	-7
	3	-9	-1	-17	4	-17	-9	27	10	-16	-6	18	0	12	-7	-7	-17
Mean unidirectional positional deviation $\bar{x}_i$ (µm)		-14.3	0.7	-13.0	0.7	-16.0	3.3	17.0	11.3	-11.0	5.0	5.3	10.0	11.7	-12.0	-6.7	-8.3
Estimator of standard uncertainty s_i (µm)		5.0	2.1	4.6	12.3	4.6	14.3	8.9	12.1	5.0	11.5	14.8	11.1	10.5	5.6	3.5	8.1
$2s_i$ (µm)		10.1	4.2	9.2	24.7	9.2	28.6	17.8	24.1	10.0	23.1	29.7	22.3	21.0	11.1	7.0	16.2
$\bar{x}_i - 2s_i$ (µm)		-24.4	-3.5	-22.2	-24.0	-25.2	-25.3	-0.8	-12.8	-21.0	-18.1	-24.4	-12.3	-9.3	-23.1	-13.7	-24.5
$\bar{x}_i + 2s_i$ (µm)		-4.3	4.8	-3.8	25.4	-6.8	31.9	34.8	35.4	-1.0	28.1	35.0	32.3	32.7	-0.9	0.4	7.8
Unidirectional repeatability $R_i = 4s_i$ (µm)		20.1	8.3	18.3	49.4	18.3	57.2	35.6	48.2	20.0	46.1	59.4	44.5	42.0	22.3	14.0	32.3
Reverse value B_i (µm)		15.0		13.7		19.3		-5.7		16.0		4.7		-23.7		-1.7	
Bidirectional repeatability $\bar{x}_i$ (µm)		29.2		49.4		57.2		48.2		49.1		59.4		55.8		32.3	
Mean bidirectional positional deviation R_i (µm)		-6.8		-6.2		-6.3		14.2		-3.0		7.7		-0.2		-7.5	
Axis deviation (mm)		Unidirectional ↓			Unidirectional ↑			Bidirectional									
Reverse value B		Not Applicable			Not Applicable			0.024									
Mean reversal value $\bar{B}$		Not Applicable			Not Applicable			0.005									
Range mean bidirectional positional deviation M		Not Applicable			Not Applicable			0.022									
Systematic positional deviation E		0.033			0.023			0.033									
Repeatability R		0.059			0.057			0.059									
Accuracy A		0.060			0.061			0.061									

150

Positional Analysis along Y-axis

Table 4-19: Ideal and measured spacings along Y-axis of the Nd:YVO$_4$ laser system.

i	Target positions		1	2	3	4	5	6	7	8
			170	7787	15787	23769	32177	39996	47948	56154
j	Ideal (μm)		170	7617	8000	7982	8408	7819	7952	8206
1	↓	actual	174	7654	8037	8001	8450	7865	7980	8251
		deviation	4	37	37	19	42	46	28	45
	↑	actual	169	7664	8043	7986	8436	7868	7976	8230
		deviation	-1	47	43	4	28	49	24	24
2	↓	actual	171	7664	8027	8013	8454	7863	7981	8240
		deviation	1	47	27	31	46	44	29	34
	↑	actual	172	7667	8025	8005	8444	7859	7968	8211
		deviation	2	50	25	23	36	40	16	5
3	↓	actual	168	7663	8026	8006	8440	7853	7975	8251
		deviation	-2	46	26	24	32	34	23	45
	↑	actual	171	7669	8039	8002	8451	7866	7958	8231
		deviation	1	52	39	20	43	47	6	25

Table 4-20: Positional analysis results of Nd:YVO$_4$ laser system along Y-axis.

	i	1		2		3		4		5		6		7		8	
Target position P_i (µm)		170		7787		15787		23769		32177		39996		47948		56154	
Approach direction		↓	↑	↓	↑	↓	↑	↓	↑	↓	↑	↓	↑	↓	↑	↓	↑
Positional deviations (µm)	j=1	4	-1	37	47	37	43	19	4	42	28	46	49	28	24	45	24
	2	1	2	47	50	27	25	31	23	46	36	44	40	29	16	34	5
	3	-2	1	46	52	26	39	24	20	32	43	34	47	23	6	45	25
Mean unidirectional positional deviation $\bar{x}_i$ (µm)		1.0	0.7	43.3	49.7	30.0	35.7	24.7	15.7	40.0	35.7	41.3	45.3	26.7	15.3	41.3	18.0
Estimator of standard uncertainty s_i (µm)		3.0	1.5	5.5	2.5	6.1	9.5	6.0	10.2	7.2	7.5	6.4	4.7	3.2	9.0	6.4	11.3
$2s_i$ (µm)		6.0	3.1	11.0	5.0	12.2	18.9	12.1	20.4	14.4	15.0	12.9	9.5	6.4	18.0	12.7	22.5
$\bar{x}_i - 2s_i$ (µm)		-5.0	-2.4	32.3	44.6	17.8	16.8	12.6	-4.8	25.6	20.7	28.5	35.9	20.2	-2.7	28.6	-4.5
$\bar{x}_i + 2s_i$ (µm)		7.0	3.7	54.3	54.7	42.2	54.6	36.7	36.1	54.4	50.7	54.2	54.8	33.1	33.4	54.0	40.5
Unidirectional repeatability $R_i = 4s_i$ (µm)		12.0	6.1	22.0	10.1	24.3	37.8	24.1	40.9	28.8	30.0	25.7	18.9	12.9	36.1	25.4	45.1
Reverse value B_i (µm)		-0.3		6.3		5.7		-9.0		-4.3		4.0		-11.3		-23.3	
Bidirectional repeatability $\bar{x}_i$ (µm)		12.0		22.4		37.8		41.5		33.8		26.3		36.1		58.6	
Mean bidirectional positional deviation R_i (µm)		0.8		46.5		32.8		20.2		37.8		43.3		21.0		29.7	
Axis deviation (mm)		Unidirectional ↓				Unidirectional ↑				Bidirectional							
Reverse value B		Not Applicable				Not Applicable				0.023							
Mean reversal value $\bar{B}$		Not Applicable				Not Applicable				-0.004							
Range mean bidirectional positional deviation M		Not Applicable				Not Applicable				0.046							
Systematic positional deviation E		0.042				0.049				0.049							
Repeatability R		0.029				0.045				0.059							
Accuracy A		0.059				0.060				0.060							

Positional Analysis along Z-axis

Table 4-21: Ideal and measured spacings along Z-axis of the Nd:YVO$_4$ laser system.

i	Target positions		1	2	3	4	5	6	7	8
			170	7787	15787	23769	32177	39996	47948	56154
j	Ideal (µm)		170	7617	8000	7982	8408	7819	7952	8206
1	↓	actual	168	7636	8002	7982	8411	7809	7938	8186
		deviation	-2	19	2	0	3	-10	-14	-20
	↑	actual	176	7625	7983	7973	8415	7844	7934	8193
		deviation	6	8	-17	-9	7	25	-18	-13
2	↓	actual	168	7618	7986	7962	8390	7799	7926	8198
		deviation	-2	1	-14	-20	-18	-20	-26	-8
	↑	actual	169	7641	7993	7989	8426	7844	7964	8199
		deviation	-1	24	-7	7	18	25	12	-7
3	↓	actual	174	7635	7990	7967	8421	7795	7934	8200
		deviation	4	18	-10	-15	13	-24	-18	-6
	↑	actual	171	7634	8008	7991	8415	7835	7959	8207
		deviation	1	17	8	9	7	16	7	1

Table 4-22: Positional analysis results of Nd:YVO$_4$ laser system along Z-axis.

	i	1		2		3		4		5		6		7		8	
Target position P_i (μm)		170		7787		15787		23769		32177		39996		47948		56154	
Approach direction		↓	↑	↓	↑	↓	↑	↓	↑	↓	↑	↓	↑	↓	↑	↓	↑
Positional deviations (μm)	j=1	-2	6	19	8	2	-17	0	-9	3	7	-10	25	-14	-18	-20	-13
	2	-2	-1	1	24	-14	-7	-20	7	-18	18	-20	25	-26	12	-8	-7
	3	4	1	18	17	-10	8	-15	9	13	7	-24	16	-18	7	-6	1
Mean unidirectional positional deviation $\bar{x}_i$ (μm)		0.0	2.0	12.7	16.3	-7.3	-5.3	-11.7	2.3	-0.7	10.7	-18.0	22.0	-19.3	0.3	-11.3	-6.3
Estimator of standard uncertainty s_i (μm)		3.5	3.6	10.1	8.0	8.3	12.6	10.4	9.9	15.8	6.4	7.2	5.2	6.1	16.1	7.6	7.0
$2s_i$ (μm)		6.9	7.2	20.2	16.0	16.7	25.2	20.8	19.7	31.6	12.7	14.4	10.4	12.2	32.1	15.1	14.0
$\bar{x}_i - 2s_i$ (μm)		-6.9	-5.2	-7.6	0.3	-24.0	-30.5	-32.5	-17.4	-32.3	-2.0	-32.4	11.6	-31.6	-31.8	-26.5	-20.4
$\bar{x}_i + 2s_i$ (μm)		6.9	9.2	32.9	32.4	9.3	19.8	9.1	22.1	31.0	23.4	-3.6	32.4	-7.1	32.5	3.8	7.7
Unidirectional repeatability $R_i = 4s_i$ (μm)		13.9	14.4	40.5	32.1	33.3	50.3	41.6	39.5	63.3	25.4	28.8	20.8	24.4	64.3	30.3	28.1
Reverse value B_i (μm)		2.0		3.7		2.0		14.0		11.3		40.0		19.7		5.0	
Bidirectional repeatability $\bar{x}_i$ (μm)		16.1		40.5		50.3		54.5		63.3		64.8		64.3		34.2	
Mean bidirectional positional deviation R_i (μm)		1.0		14.5		-6.3		-4.7		5.0		2.0		-9.5		-8.8	
Axis deviation (mm)		Unidirectional ↓				Unidirectional ↑				Bidirectional							
Reverse value B		Not Applicable				Not Applicable				0.040							
Mean reversal value $\bar{B}$		Not Applicable				Not Applicable				0.012							
Range mean bidirectional positional deviation M		Not Applicable				Not Applicable				0.024							
Systematic positional deviation E		0.032				0.028				0.041							
Repeatability R		0.063				0.064				0.065							
Accuracy A		0.065				0.064				0.065							

154

4.4.2   Positional Analysis of Nd:YAG Laser System

Table 4-23, Table 4-25, and Table 4-27 are listing the ideal and measured spacings of the Nd:YAG laser system along X-, Y-, and Z-axes respectively. The deviations were calculated according to Equation 3-2. On the other hand, Table 4-24, Table 4-26, and Table 4-28 present positional analysis results of Nd:YAG laser system along X-, Y-, and Z-axes respectively. The positional analysis study, along all three axes, yielded distinctly different results. This might be because of the two different components of the marking system (the galvanometer and the PI Z-stage). Therefore, this system does not have the same positional properties and characteristics along all axes. Thus, recommendation of micromachining along a specific axis can be given for a certain work to be developed.

The positional analysis results showed that the reversal value (B), the mean reversal value ($\bar{B}$), the range mean bi-directional positional deviation (M), and the bi-directional systematic positional deviation (E) have maximum values of 31 μm, 73 μm, and 9 μm along X-, Y-, and Z-axes respectively. Therefore, the PI Z-stage showed excellent results in comparison with the rather bad result along Y-axis.

Accuracy is the degree of closeness of measured values to the ideal values. The PI Z-stage showed an excellent Accuracy of 12 μm, while the accuracy along the X-axis was 53 μm, whereas the accuracy along the Y-axis was 92 μm. On the other side, repeatability is the degree to which repeated movements under unchanged conditions show the same results. The PI Z-stage showed an excellent repeatability of 9 μm, while the repeatability along the Y-axis was 31 μm, whereas the repeatability along the X-axis was 52 μm. this shows that the PI Z-stage has the best results. Moreover, it shows that X-axis has second best accuracy but relatively the worst repeatability. Additionally, it shows that Y-axis has second best repeatability but relatively the worst accuracy. In general and along all axes, the accuracy and repeatability of this system is excellent, except the accuracy value along the Y-axis, which can be categorised as good. The excellent performance of the Z-stage might justify the high cost of this PI stage, which was about € 4,000.

155

Positional Analysis along X-axis

Table 4-23: Ideal and measured spacings along X-axis of the Nd:YAG laser system.

i			1		2		3		4		5		6	
	Target positions		430		9990		19900		29840		39740		49600	
j	Ideal (µm)		430		9560		9910		9940		9900		9860	
			X	Y	X	Y	X	Y	X	Y	X	Y	X	Y
1	↓	X & Y	432	1	9531	22	9880	25	9923	20	9884	28	9851	28
		actual	432		9531		9880		9923		9884		9851	
		deviation	2		-29		-30		-17		-16		-9	
	↑	X & Y	430	1	9540	25	9879	27	9929	22	9888	29	9854	31
		actual	430		9540		9879		9929		9888		9854	
		deviation	0		-20		-31		-11		-12		-6	
2	↓	X & Y	433	0	9548	21	9881	28	9924	18	9889	31	9852	25
		actual	433		9548		9881		9924		9889		9852	
		deviation	3		-12		-29		-16		-11		-8	
	↑	X & Y	427	1	9544	18	9890	28	9925	24	9880	31	9849	24
		actual	427		9544		9890		9925		9880		9849	
		deviation	-3		-16		-20		-15		-20		-11	
3	↓	X & Y	436	0	9537	24	9886	24	9930	18	9899	32	9861	22
		actual	436		9537		9886		9930		9899		9861	
		deviation	6		-23		-24		-10		-1		1	
	↑	X & Y	425	1	9545	21	9905	25	9922	21	9894	27	9850	27
		actual	425		9545		9905		9922		9894		9850	
		deviation	-5		-15		-5		-18		-6		-10	

Table 4-24: Positional analysis results of Nd:YAG laser system along X-axis.

	i	1		2		3		4		5		6	
Target position P_i (µm)		430		9990		19900		29840		39740		49600	
Approach direction		↓	↑	↓	↑	↓	↑	↓	↑	↓	↑	↓	↑
Positional deviations (µm)	j=1	2	0	-29	-20	-30	-31	-17	-11	-16	-12	-9	-6
	2	3	-3	-12	-16	-29	-20	-16	-15	-11	-20	-8	-11
	3	6	-5	-23	-15	-24	-5	-10	-18	-1	-6	1	-10
Mean unidirectional positional deviation $\bar{x}_i$ (µm)		3.7	-2.7	-21.3	-17.0	-27.7	-18.7	-14.3	-14.7	-9.3	-12.7	-5.3	-9.0
Estimator of standard uncertainty s_i (µm)		2.1	2.5	8.6	2.6	3.2	13.1	3.8	3.5	7.6	7.0	5.5	2.6
$2s_i$ (µm)		4.2	5.0	17.2	5.3	6.4	26.1	7.6	7.0	15.3	14.0	11.0	5.3
$\bar{x}_i - 2s_i$ (µm)		-0.5	-7.7	-38.6	-22.3	-34.1	-44.8	-21.9	-21.7	-24.6	-26.7	-16.3	-14.3
$\bar{x}_i + 2s_i$ (µm)		7.8	2.4	-4.1	-11.7	-21.2	7.4	-6.8	-7.6	5.9	1.4	5.7	-3.7
Unidirectional repeatability $R_i = 4s_i$ (µm)		8.3	10.1	34.5	10.6	12.9	52.2	15.1	14.0	30.6	28.1	22.0	10.6
Reverse value B_i (µm)		-6.3		4.3		9.0		-0.3		-3.3		-3.7	
Bidirectional repeatability $\bar{x}_i$ (µm)		15.5		34.5		52.2		15.1		32.7		22.0	
Mean bidirectional positional deviation R_i (µm)		0.5		-19.2		-23.2		-14.5		-11.0		-7.2	
Axis deviation (mm)		Unidirectional ↓		Unidirectional ↑		Bidirectional							
Reverse value B		Not Applicable		Not Applicable		0.009							
Mean reversal value $\bar{B}$		Not Applicable		Not Applicable		0.000							
Range mean bidirectional positional deviation M		Not Applicable		Not Applicable		0.024							
Systematic positional deviation E		0.031		0.016		0.031							
Repeatability R		0.034		0.052		0.052							
Accuracy A		0.046		0.052		0.053							

Positional Analysis along Y-axis

Table 4-25: Ideal and measured spacings along Y-axis of the Nd:YAG laser system.

i		Target positions	1		2		3		4		5		6	
			430		9990		19900		29840		39740		49600	
j		Ideal (µm)	430		9560		9910		9940		9900		9860	
			X	Y	X	Y	X	Y	X	Y	X	Y	X	Y
1	↓	X & Y	430	1	9531	18	9855	15	9890	18	9845	21	9782	21
		actual	430		9531		9855		9890		9845		9782	
		deviation	0		-29		-55		-50		-55		-78	
	↑	X & Y	430	0	9538	15	9855	15	9891	17	9851	21	9782	24
		actual	430		9538		9855		9891		9851		9782	
		deviation	0		-22		-55		-49		-49		-78	
2	↓	X & Y	426	0	9536	18	9857	18	9884	18	9851	17	9786	19
		actual	426		9536		9857		9884		9851		9786	
		deviation	-4		-24		-53		-56		-49		-74	
	↑	X & Y	430	1	9535	19	9862	14	9889	17	9852	20	9783	20
		actual	430		9535		9862		9889		9852		9783	
		deviation	0		-25		-48		-51		-48		-77	
3	↓	X & Y	430	1	9537	17	9863	19	9893	17	9849	21	9792	21
		actual	430		9537		9863		9893		9849		9792	
		deviation	0		-23		-47		-47		-51		-68	
	↑	X & Y	430	1	9541	17	9863	18	9893	17	9844	21	9796	15
		actual	430		9541		9863		9893		9844		9796	
		deviation	0		-19		-47		-47		-56		-64	

Table 4-26: Positional analysis results of Nd:YAG laser system along Y-axis.

	i	1		2		3		4		5		6	
Target position P_i (μm)		430		9990		19900		29840		39740		49600	
Approach direction		↓	↑	↓	↑	↓	↑	↓	↑	↓	↑	↓	↑
Positional deviations (μm)	j=1	0	0	-29	-22	-55	-55	-50	-49	-55	-49	-78	-78
	2	-4	0	-24	-25	-53	-48	-56	-51	-49	-48	-74	-77
	3	0	0	-23	-19	-47	-47	-47	-47	-51	-56	-68	-64
Mean unidirectional positional deviation $\bar{x}_i$ (μm)		-1.3	0.0	-25.3	-22.0	-51.7	-50.0	-51.0	-49.0	-51.7	-51.0	-73.3	-73.0
Estimator of standard uncertainty s_i (μm)		2.3	0.0	3.2	3.0	4.2	4.4	4.6	2.0	3.1	4.4	5.0	7.8
$2s_i$ (μm)		4.6	0.0	6.4	6.0	8.3	8.7	9.2	4.0	6.1	8.7	10.1	15.6
$\bar{x}_i - 2s_i$ (μm)		-6.0	0.0	-31.8	-28.0	-60.0	-58.7	-60.2	-53.0	-57.8	-59.7	-83.4	-88.6
$\bar{x}_i + 2s_i$ (μm)		3.3	0.0	-18.9	-16.0	-43.3	-41.3	-41.8	-45.0	-45.6	-42.3	-63.3	-57.4
Unidirectional repeatability $R_i = 4s_i$ (μm)		9.2	0.0	12.9	12.0	16.7	17.4	18.3	8.0	12.2	17.4	20.1	31.2
Reverse value B_i (μm)		1.3		3.3		1.7		2.0		0.7		0.3	
Bidirectional repeatability $\bar{x}_i$ (μm)		9.2		15.8		18.7		18.3		17.4		31.2	
Mean bidirectional positional deviation R_i (μm)		-0.7		-23.7		-50.8		-50.0		-51.3		-73.2	
Axis deviation (mm)		Unidirectional ↓		Unidirectional ↑		Bidirectional							
Reverse value B		Not Applicable		Not Applicable		0.003							
Mean reversal value $\bar{B}$		Not Applicable		Not Applicable		0.002							
Range mean bidirectional positional deviation M		Not Applicable		Not Applicable		0.073							
Systematic positional deviation E		0.072		0.073		0.073							
Repeatability R		0.020		0.031		0.031							
Accuracy A		0.087		0.089		0.092							

159

Positional Analysis along Z-axis

Table 4-27: Ideal and measured spacings along Z-axis of the Nd:YAG laser system.

i	Target positions		1	2	3	4	5	6
			430	9990	19900	29840	39740	49600
j	Ideal (μm)		430	9560	9910	9940	9900	9860
1	↓	actual	430.8	9564.5	9909	9941.3	9896	9860
		deviation	1	5	-1	1	-4	0
	↑	actual	425.8	9561	9908.5	9943	9900	9858.8
		deviation	-4	1	-2	3	0	-1
2	↓	actual	430.8	9564.3	9909	9937.5	9900	9860.3
		deviation	1	4	-1	-3	0	0
	↑	actual	425.8	9561	9908.5	9943	9900	9859
		deviation	-4	1	-2	3	0	-1
3	↓	actual	430.8	9564.8	9909	9941	9896	9860
		deviation	1	5	-1	1	-4	0
	↑	actual	425.5	9562.5	9908	9942.5	9900	9859
		deviation	-5	3	-2	3	0	-1

Table 4-28: Positional analysis results of Nd:YAG laser system along Z-axis.

	i	1		2		3		4		5		6	
Target position P_i (μm)		430		9990		19900		29840		39740		49600	
Approach direction		↓	↑	↓	↑	↓	↑	↓	↑	↓	↑	↓	↑
Positional deviations (μm)	j=1	1	-4	5	1	-1	-2	1	3	-4	0	0	-1
	2	1	-4	4	1	-1	-2	-3	3	0	0	0	-1
	3	1	-5	5	3	-1	-2	1	3	-4	0	0	-1
Mean unidirectional positional deviation $\bar{x}_i$ (μm)		0.8	-4.3	4.5	1.5	-1.0	-1.7	-0.1	2.8	-2.7	0.0	0.1	-1.1
Estimator of standard uncertainty s_i (μm)		0.0	0.1	0.3	0.9	0.0	0.3	2.1	0.3	2.3	0.0	0.1	0.1
$2s_i$ (μm)		0.0	0.3	0.5	1.7	0.0	0.6	4.2	0.6	4.6	0.0	0.3	0.3
$\bar{x}_i - 2s_i$ (μm)		0.8	-4.6	4.0	-0.2	-1.0	-2.2	-4.3	2.3	-7.3	0.0	-0.2	-1.4
$\bar{x}_i + 2s_i$ (μm)		0.8	-4.0	5.0	3.2	-1.0	-1.1	4.1	3.4	2.0	0.0	0.4	-0.8
Unidirectional repeatability $R_i = 4s_i$ (μm)		0.0	0.6	1.0	3.5	0.0	1.2	8.4	1.2	9.2	0.0	0.6	0.6
Reverse value B_i (μm)		-5.1		-3.0		-0.7		2.9		2.7		-1.2	
Bidirectional repeatability $\bar{x}_i$ (μm)		5.4		5.2		1.2		8.4		9.2		1.7	
Mean bidirectional positional deviation R_i (μm)		-1.8		3.0		-1.3		1.4		-1.3		-0.5	
Axis deviation (mm)		Unidirectional ↓		Unidirectional ↑		Bidirectional							
Reverse value B		Not Applicable		Not Applicable		0.005							
Mean reversal value $\bar{B}$		Not Applicable		Not Applicable		-0.001							
Range mean bidirectional positional deviation M		Not Applicable		Not Applicable		0.005							
Systematic positional deviation E		0.007		0.007		0.009							
Repeatability R		0.009		0.003		0.009							
Accuracy A		0.012		0.008		0.012							

4.4.3   Positional Analysis of the Mitutoyo optical microscope

Table 4-29 lists the ideal and measured spacings of the Mitutoyo optical microscope. The deviations were calculated according to Equation 3-2. On the other hand, Table 4-30 presents positional analysis results of Mitutoyo optical microscope.

Since there was not multiple target positions, the positional analysis did not show the reversal value (B), the mean reversal value ($\bar{B}$), the range mean bi-directional positional deviation (M), or the bi-directional systematic positional deviation (E).

Accuracy is the degree of closeness of measured values to the ideal values. On the other side, repeatability is the degree to which repeated movements under unchanged conditions show the same results. The positional analysis showed identical values of accuracy and repeatability with a value of 5 μm. These excellent results support the utilisation of the Mitutoyo optical microscope as a measurement system.

Table 4-29: Ideal and measured spacings of the Mitutoyo optical microscope.

i	Target positions	1 ↓		1 ↑	
		14 mm → 24 mm		24 mm →14 mm	
j	Ideal (μm)	10000		10000	
		X	Y	X	Y
1	X & Y	10002	126	10002	127
	actual	10003		10003	
	deviation	3		3	
2	X & Y	10000	126	10001	124
	actual	10001		10002	
	deviation	1		2	
3	X & Y	10000	125	9999	128
	actual	10001		10000	
	deviation	1		0	
4	X & Y	10000	125	10000	126
	actual	10001		10001	
	deviation	1		1	
5	X & Y	10000	124	10000	124
	actual	10001		10001	
	deviation	1		1	

Table 4-30: Positional analysis results of Mitutoyo optical microscope.

	i	1	
Target position P_i (µm)		10000	
Approach direction		↓	↑
Positional	j=1	3	3
deviations (µm)	j=2	1	2
	j=3	1	0
	j=4	1	1
	j=5	1	1
Mean unidirectional positional deviation $\bar{x}_i$ (µm)		1.4	1.4
Estimator of standard uncertainty s_i (µm)		0.9	1.1
$2s_i$ (µm)		1.8	2.3
$\bar{x}_i - 2s_i$ (µm)		-0.4	-0.9
$\bar{x}_i + 2s_i$ (µm)		3.2	3.7
Unidirectional repeatability $R_i = 4s_i$ (µm)		3.6	4.6
Reverse value B_i (µm)		0.0	
Bidirectional repeatability $\bar{x}_i$ (µm)		4.6	
Mean bidirectional positional deviation R_i (µm)		1.4	
Axis deviation (mm)		Unidirectional ↓	Unidirectional ↑	Bidirectional
Repeatability R		0.004	0.005	0.005
Accuracy A		0.004	0.005	0.005

CHAPTER 5

CONCLUSIONS

5.1 Laser Micromachining Modelling

Modelling all the important factors that affect the resulting dimensions of laser micro-machined components by conventional analytical or numerical methods is not currently possible. In practice, when starting a new laser micromachining operation with requirement for specific part dimensions and new materials, the technician/operator performs a set of trial-and-error experiments to set the process control parameters related to the laser power, PRF, motion control and work piece material. This trial-and-error approach can be costly and time consuming especially for small batch production or prototyping, and does not ensure optimal process conditions for given manufacturing objectives [189].

In this work, micromachining process analysis was carried out to generate a deeper understanding of how the process variables affect the feature size, while the positional analysis was performed to understand how process variables can affect feature location.

In this work, DoE, RSM, and ANN modelling approaches were used to characterise the process and enabled micro-channel topology prediction from the CO_2 laser surface micromachining and the Nd:YVO$_4$ laser internal micromachining processes. The developed RSM and ANN predictive models may be used to select the input parameters for required output dimensions or to predict the dimensions of the micro-channels based on set inputs. In addition, the models are efficient predictive tools for estimating the investigated micro-machining outcomes. Direct comparisons between the predictive capabilities of the ANN and RSM predictive models were drawn.

From this work and within the limits of investigated parameters, it was concluded that the RSM approach could be utilised as a prediction and optimisation tool for

165

laser micromachining by constructing experiential and mathematical models. Experiments carried out according to factorial Design of Experiments (DoE) could actively assist in the selection of training data sets for the ANN predictive models. Changing the number and the selection of training data significantly affected the prediction capability of the developed ANN predictive model. ANN methodology produced predictive models that are better than an RSM in terms of predictive capabilities. This conclusion remained valid even when the ANN model has a carefully chosen limited number of experiments as a training data set. The ANN training data set chosen according to Face Centred Cubic Design, which covered the experimental data space's corner points, and more broadly encompassed the design space than training data sets chosen according to Box-Behnken Design or random selection.

Generally, predictive models over time may not work as well as when they were first implemented due to potential equipment deterioration. In this case, with RSM, all experiments need to be carried out again and the whole process of developing an RSM model needs to be repeated. On the ANN side, only the training experimental data points for the chosen model need to be re-captured again and used to re-train this ANN model structure. Therefore, for ANN approach there would be no necessity to go through the development of the ANN predictive model again.

The cost-based model only directly applies to evaluation of the micro-machining cost per length for the specific laser micro-machining operation performed in this work. This model will vary for other laser systems and other machining operations. The objective here however was to show the general comparative capability of ANN and RSM models to predict cost within micro-machining systems. It has been shown from this work that cost can be estimated for modelling and optimisation purposes.

These predictive models could be usefully employed in satisfying numerous industrial needs. These needs include situations when minimum scrap is acceptable or when structures with high degree of precision are demanded or where laser micromachining with minimal energy is required. All laser micromachining applications would benefit from optimising the geometry of the microstructure

166

utilising the above-mentioned concept, especially the production of micro-fluidic and lab-on-a-chip devices for chemical/analytical applications and in separation science.

There are many other modelling and optimisation techniques such as genetic algorithms, ant colony optimisation, grammatical evolution, simulated annealing, tabu search, stochastic tunnelling, differential evolution, particle swarm optimization, and fuzzy logic, which could also be applied to such a problem. Many of these techniques are more recently developed than the ANN or RSM modelling methods. This gives some confidence in the use of ANN and RSM for problem solving as presented in this work. However, it also opens the possibility for further research to investigate if any of these other techniques can be applied more easily or more successfully to solve such problems. ANN predictive models can be used to predict results that were not found from experimental work. By utilisation of any of the aforementioned optimisation techniques in conjunction with the ANN models, optimised process control parameter could be found for achieving target responses, boost the process performance, and improve the final product quality.

5.2   Positional Analysis Assessment for 1064 nm Laser Systems

The positional analysis study of the Nd:YVO$_4$ laser system, along all three axes, yielded nearly identical results. This demonstrated that this translation stage had the same positional properties and characteristics along all axes. The accuracy and repeatability values revealed an excellent maximum value of 65 μm for all the three axes. X and Y-axes showed marginally better accuracy and repeatability values with a maximum of 61 μm.

On the other hand, the positional analysis study of the Nd:YAG laser system, along all three axes, yielded distinctly different results. This might be because of the two different components of marking system (the galvanometer and the PI Z-stage). Therefore, this system does not have the same positional properties and characteristics along all axes. Thus, recommendation of micromachining along a specific axis can be given for certain micromachining job requirements. The PI Z-stage showed an excellent accuracy of 12 μm, while the accuracy along the X-axis was 53 μm, whereas the accuracy along the Y-axis was 92 μm. On the other side, the

PI Z-stage showed an excellent repeatability of 9 μm, while the repeatability along the Y-axis was 31 μm, whereas the repeatability along the X-axis was 52 μm. The PI Z-stage produced the best results in terms of accuracy and repeatability. The X-axis had second best accuracy but had the worst repeatability. Additionally, the Y-axis had the second best repeatability but the worst accuracy. In general and along all axes, the accuracy and repeatability of this system is excellent, except the accuracy value along the Y-axis, which can be categorised as good. The excellent performance of the Z-stage might justify the high cost of this PI stage (about €4,000). The excellent positional analysis results from the Mitutoyo optical microscope supported its utilisation as a measurement system.

In comparison, the 3D translation stage of the Nd:YVO$_4$ laser system showed more consistent results with maximum value of 65 μm along the three axes. The two motion systems of the two laser systems demonstrated a very good positional analysis result. Therefore, both systems can be utilised for precision micromachining applications. However, the lower cost of the in-house built 3D translation stage (about €3,000) of the Nd:YVO$_4$ laser system is an advantage in its favour.

This lack of literature on accuracy, repeatability, and resolution of laser preparation of microfluidic channels and micrometre scales could be partially due to the large number of process variables, which could affect these results. This in turn make it difficult to find the right parameters and settings required in order to obtain desired channel or voxel positioning within the resultant microstructure [118, 123].

Modelling the micromachining process allowed for finding the set of laser micromachining parameters of micro-channels predetermined geometry, whilst the positional analysis showed the developed motion system was capable of micrometre level accuracy and repeatability. This establishes the use of this work in precision micromachining applications, such as stage micrometre preparation, where the size and location of the feature is of critical importance.

The main conclusions of this work are summaries below.

✓ RSM and ANN can be used to predict micro-machined channel dimensions produced with CO_2 and Nd:YVO$_4$ laser systems

✓ RSM and ANN can be used to predict micromachining costs for the CO_2 and Nd:YVO$_4$ laser systems

✓ The ANN predictive models showed better approximation capabilities compared to RSM especially when

    ✓ a high number of training data was utilised, or

    ✓ a well-chosen limited number of training data was utilised

✓ A novel implementation of ANN which was shown to be capable for determining the interaction effects of laser micro-machining input parameters on the width and depth responses for the CO_2 laser system

✓ The control motion system for the Nd:YVO$_4$ was developed to be a real time closed loop control system

✓ The 3D translation stage and Nd:YVO$_4$ laser system, as well as the galvanometer and Nd:YAG laser system demonstrated micrometre level positional capability

✓ Accuracy and repeatability values were in general better for the galvanometer and Nd:YAG laser system (apart from bi-directional accuracy in the Y-axis)

✓ The lower cost, in house built, 3D translation stage however produced more consistent values of accuracy and repeatability across all three axes than the galvanometer system

5.3   Future Work

Future work may involve the following:

- The improvement of developed micro-channels' geometry quality and efficiency for the proposed applications.

This can be achieved by using specially doped polymers and glasses that could be chemically treated after irradiation with laser pulses. Alternatively, using an external oscillator in order to double or triple the frequency of the laser beam and consequently reduce its wavelength and make it more suitable for machining polycarbonate and PMMA polymers.

- The comparison of micromachining cost.

This can be achieved by comparing laser micromachining cost to other micro-channelling processes, taking into account other advantages of all the processes involved in the comparison such as the accuracy and the range of geometries that can be developed.

- The feasibility study on the applications of the developed micro-channels.

These applications include optical data storage, micro-fluidics, MEMS, optical telecommunication systems, and micro-sensors.

- The optimisation of developed micro-channels geometry using the utilised modelling techniques.

This can be carried out for the production of micro-fluidic and lab-on-a-chip devices, which can be used in chemical/analytical applications and in separation science.

An example of such an application is immobilising a monolithic polymers stationary phases within the micro-channels. Capacitively coupled contactless conductivity detection (C^4D), which is also known as contactless conductivity detection (CCD), can be used for detection of the target molecules. This method is a special type of conductivity-based detection where the sensing electrodes are not in direct contact

with the measured solution. In order to achieve this objective, the following work will be required:

  I. To develop internal micro-channels with different geometries in polycarbonate and PMMA polymers.
  II. To utilise the developed DOE and ANN prediction models in order to produce the micro-channels with a predetermined geometries.

References

1. Majumdar, J. and I. Manna, *Laser processing of materials.* Sadhana, 2003. **28**(3): pp. 495-562.

2. William, M., *Laser material processing*, 1991, Springer-Verlag, Berlin.

3. Hecht, J., *The laser guidebook,*1999: McGraw-Hill Professional.

4. Dahotre, N. and S. Harimkar, *Laser fabrication and machining of materials,*2007: Springer.

5. Issa, A., *Computational control of laser systems for micro-machining*, 2007, PhD Thesis, Dublin City University.

6. Bachmann, F., *Industrial laser applications.* Applied Surface Science, 1990. **46**(1-4): pp. 254-263.

7. Wang, S., C. Lee, and H. Chen, *Thermoplastic microchannel fabrication using carbon dioxide laser ablation.* Journal of Chromatography A, 2006. **1111**(2): pp. 252-257.

8. Juodkazis, S., K. Yamasaki, A. Marcinkevicius, V. Mizeikis, S. Matsuo, H. Misawa, and T. Lippert, *Micro-structuring of silica and polymethylmethacrylate glasses by femtosecond irradiation for Materials Science of MEMS applications*, in *Mat. Res. Soc. Symp. Proc.*2002. pp. B5.25.1 - B5.25.6.

9. Gower, M., *Industrial applications of laser micromachining.* Optics Express, 2000. **7**(2): pp. 56-67.

10. Alonso-Amigo, M., *Polymer microfabrication for microarrays, microreactors and microfluidics.* Journal of the Association for Laboratory Automation, 2000. **5**(6): pp. 96-101.

11. Kamata, M., M. Obara, R. Gattass, L. Cerami, and E. Mazur, *Optical vibration sensor fabricated by femtosecond laser micromachining.* Applied Physics Letters, 2005. **87**: pp. 051106.

12. Strickler, J. and W. Webb, *Three-dimensional optical data storage in refractive media by two-photon point excitation.* Optics letters, 1991. **16**(22): pp. 1780-1782.

13. Glezer, E., M. Milosavljevic, L. Huang, R. Finlay, T. Her, J. Callan, and E. Mazur, *Three-dimensional optical storage inside transparent materials.* Opt. Lett, 1996. **21**: pp. 2023-2025.

14. Glezer, E. and E. Mazur, *Ultrafast-laser driven micro-explosions in transparent materials.* Applied Physics Letters, 1997. **71**: pp. 882.

15. Kawata, Y., H. Ishitobi, and S. Kawata, *Use of two-photon absorption in a photorefractive crystal for three-dimensional optical memory.* Optics letters, 1998. **23**(10): pp. 756-758.

16. Schaffer, C., E. Glezer, N. Nishimura, and E. Mazur, *Ultrafast laser induced microexplosions: explosive dynamics and sub-micrometer structures.* Commercial Applications of Ultrafast Lasers, 1998: pp. 36-45.

17. Schaffer, C., N. Nishimura, and E. Mazur. *Thresholds for femtosecond laser-induced breakdown in bulk transparent solids and water*. 1998.

18. Toriumi, A., S. Kawata, and M. Gu, *Reflection confocal microscope readout system for three-dimensional photochromic optical data storage.* Optics letters, 1998. **23**(24): pp. 1924-1926.

19. Day, D., M. Gu, and A. Smallridge, *Use of two-photon excitation for erasable-rewritable three-dimensional bit optical data storage in a photorefractive polymer.* Optics letters, 1999. **24**(14): pp. 948-950.

20. Watanabe, M., S. Juodkazis, H. Sun, S. Matsuo, H. Misawa, M. Miwa, and R. Kaneko, *Transmission and photoluminescence images of three-dimensional memory in vitreous silica.* Applied Physics Letters, 1999. **74**: pp. 3957.

21. Watanabe, M., S. Juodkazis, H. Sun, S. Matsuo, and H. Misawa, *Two-photon readout of three-dimensional memory in silica.* Applied Physics Letters, 2000. **77**: pp. 13.

22. Yamasaki, K., S. Juodkazis, M. Watanabe, H. Sun, S. Matsuo, and H. Misawa, *Recording by microexplosion and two-photon reading of three-dimensional optical memory in polymethylmethacrylate films.* Applied Physics Letters, 2000. **76**: pp. 1000.

23. Schaffer, C. and E. Mazur, *Micromachining using ultrashort pulses from a laser oscillator.* Optics and Photonics News, 2001. **12**(4): pp. 20-23.

24. Hong, M., B. Luk'yanchuk, S. Huang, T. Ong, L. Van, and T. Chong, *Femtosecond laser application for high capacity optical data storage.* Applied Physics A: Materials Science & Processing, 2004. **79**(4): pp. 791-794.

25. EKSMA Co., Laser, optics, electronics, Glass Master Series Catalogue. *http://www.eksma.com*. 2010 [cited August-2012].

26. Bäuerle, D., *Laser processing and chemistry: recent developments.* Applied Surface Science, 2002. **186**(1-4): pp. 1-6.

27. Gattass, R., *Femtosecond-laser interactions with transparent materials: applications in micromachining and supercontinuum generation*, 2006, Harvard University Cambridge, Massachusetts.

28. Geissler, H. *Challenge of development and potential for glass processing by laser technology.* 2003. Glass Processing Days.

29. Herman, P., K. Chen, S. Ng, J. Zhang, D. Coric, P. Corkum, M. Mehendale, A. Naumov, and D. Rayner. *Photosensitivity in glasses: comparing ultrafast lasers with vacuum-ultraviolet lasers*. in *Conference on Lasers and Electro-Optics*. 2001.

30. Herman, P., K. Chen, P. Corkum, A. Naumov, S. Ng, and J. Zhang, *Advanced lasers for photonic device microfabrication.* RIKEN REVIEW, 2001: pp. 31-35.

31. Juodkazis, S., K. Yamasaki, A. Marcinkevicius, V. Mizeikis, S. Matsuo, H. Misawa, and T. Lippert. *Microstructuring of Silica and Polymethylmethacrylate Glasses by Femtosecond Irradiation for MEMS Applications*. 2001. Warrendale, Pa.; Materials Research Society; 2001.

32. Mizeikis, V., H. Sun, A. Marcinkevi ius, J. Nishii, S. Matsuo, S. Juodkazis, and H. Misawa, *Femtosecond laser micro-fabrication for tailoring photonic crystals in resins and silica.* Journal of Photochemistry & Photobiology, A: Chemistry, 2001. **145**(1-2): pp. 41-47.

33. Lupeanu, M., A. Rennie, D. Eggbeer, and C. Neagu. *Redesign of custom-fitted surgical guide with targeted functional analysis fabricated via SLM*. in *Prototyping and Manufacturing: Proceedings of the Twelfth Conference on Rapid Design*. 2011.

34. Morton, W., S. Green, A. Rennie, and T. Abram. *Surface finishing techniques for SLM manufactured stainless steel 316L components*. in *Innovative Developments in Virtual and Physical Prototyping: Proceedings of the 5th International Conference on Advanced Research in Virtual and Rapid Prototyping*. 2011.

35. Hitz, C., J. Ewing, and J. Hecht, *Introduction to laser technology,* 2001: Wiley-IEEE Press.

36. Ebendorff-Heidepriem, H., *Laser writing of waveguides in photosensitive glasses.* Optical Materials, 2004. **25**(2): pp. 109-115.

37. K. H. Leong, Innovative glass processing. *http://www.industrial-lasers.com/articles/2004/09/innovative-glass-microprocessing.html*. Industrial Laser Solutions 2004 [cited September-2012].

38. Clark-MXR, Inc., Ultrashort solutions for Science and Industry. *http://cmxr.com/index.htm*. 2011 [cited October- 2012].

39. Schaffer, C., A. Brodeur, J. García, and E. Mazur, *Micromachining bulk glass by use of femtosecond laser pulses with nanojoule energy.* Optics letters, 2001. **26**(2): pp. 93-95.

40. Schaffer, C., A. Brodeur, J. Garcia, W. Leight, and E. Mazur. *Micromachining optical waveguides in bulk glass using a femtosecondlaser oscillator*. in *Technical Digest: Conf. on Lasers and Electro-Optics (CLEO)*. 2000. San Francisco.

41. Homoelle, D., S. Wielandy, A. Gaeta, N. Borrelli, and C. Smith, *Infrared photosensitivity in silica glasses exposed to femtosecond laser pulse.* Optics letters, 1999. **24**(18): pp. 1311-1313.

42. Davis, K., K. Miura, N. Sugimoto, and K. Hirao, *Writing waveguides in glass with a femtosecond laser.* Optics letters, 1996. **21**(21): pp. 1729-1731.

43. Tong, L., R. Gattass, I. Maxwell, J. Ashcom, and E. Mazur, *Optical loss measurements in femtosecond laser written waveguides in glass.* Optics Communications, 2006. **259**(2): pp. 626-630.

44. Nolte, S., M. Will, J. Burghoff, and A. Tuennermann, *Femtosecond waveguide writing: a new avenue to three-dimensional integrated optics.*

Applied Physics A: Materials Science & Processing, 2003. **77**(1): pp. 109-111.

45. Shih, T., R. Gattass, C. Mendonca, and E. Mazur, *Faraday rotation in femtosecond laser micromachined waveguides.* Opt. Lett, 1996. **21**: pp. 1729-1731.

46. Miura, K., H. Inouye, J. Qiu, T. Mitsuyu, and K. Hirao, *Optical waveguides induced in inorganic glasses by a femtosecond laser.* Nuclear instruments & methods in physics research. Section B, Beam interactions with materials and atoms, 1998. **141**(1-4): pp. 726-732.

47. Hirao, K. and K. Miura, *Writing waveguides and gratings in silica and related materials by a femtosecond laser.* J. Non-Cryst. Solids, 1998. **239**(1): pp. 91-95.

48. Dumont, T., T. Lippert, A. Wokaun, and P. Leyvraz, *Laser writing of 2D data matrices in glass.* Thin Solid Films, 2004. **453**: pp. 42-45.

49. Qiu, J., K. Miura, H. Inouye, J. Nishii, and K. Hirao, *Three-dimensional optical storage inside a silica glass by using a focused femtosecond pulsed laser.* Nuclear Instruments and Methods in Physics Research Section B: Beam Interactions with Materials and Atoms, 1998. **141**: pp. 699-703.

50. Rossier, J.S., F. Reymond, and P.E. Michel, *Polymer microfluidic chips for electrochemical and biochemical analyses.* Electrophoresis, 2002. **23**(6).

51. Khan Malek, C., *Laser processing for bio-microfluidics applications (part I).* Analytical and bioanalytical chemistry, 2008. **385**(8): pp. 1351-1361.

52. Khan Malek, C., *Laser processing for bio-microfluidics applications (part II).* Analytical and bioanalytical chemistry, 2008. **385**(8): pp. 1362-1369.

53. He, D., Z. Zhang, Y. Huang, Y. Hu, H. Zhou, and D. Chen, *Chemiluminescence microflow injection analysis system on a chip for the determination of uric acid without enzyme.* Luminescence, 2005. **20**(4-5): pp. 271-275.

54. McGinty, S., G. O'Connor, and T. Glynn. *A comparative study of channel formation in polymer materials using VUV and UV nano-second laser sources for use in micro-fluidic applications.* in *Opto-Ireland 2005.* 2005.

55. Frazier, A., R. Warrington, and C. Friedrich, *The miniaturization technologies: Past, present, and future.* IEEE Transactions on Industrial Electronics, 1995. **42**(5): pp. 423-430.

56. Webb, C. and J. Jones, *Handbook of laser technology and applications.* 2004.

57. Sugioka, K., Y. Cheng, and K. Midorikawa, *Three-dimensional micromachining of glass using femtosecond laser for lab-on-a-chip device manufacture.* Applied Physics A: Materials Science & Processing, 2005. **81**(1): pp. 1-10.

58. Gower, M. *Laser micromachining for manufacturing MEMS devices.* in *MEMS Components and Applications for Industry, Automobiles, Aerospace, and Communication.* 2001.

59. Bao, M. and W. Wang, *Future of microelectromechanical systems (MEMS).* Sensors & Actuators: A. Physical, 1996. **56**(1-2): pp. 135-141.

60. Holmes, A. *Laser fabrication and assembly processes for MEMS.* in *Laser Applications in Microelectronic and Optoelectronic Manufacturing VI.* 2001.

61. Lawes, R., A. Holmes, and F. Goodall, *The formation of moulds for 3D microstructures using excimer laser ablation.* Microsystem Technologies, 1996. **3**(1): pp. 17-19.

62. Yung, K.C., S.M. Mei, and T.M. Yue, *Rapid prototyping of polymer-based MEMS devices using UV YAG laser.* Journal of Micromechanics and Microengineering, 2004. **14**: pp. 1682-1686.

63. The microscope depot. *http://www.microscope-depot.com/glossary.asp.* 2012 [cited September-2012].

64. Stage Micrometer Scale| Precision Calibration X-Y Glass Scale| High Measurement Accuracy IAM-2. *http://www.aig-imaging.com/mm5/merchant.mvc?Screen=PROD&Store_Code=AIIPI&Product_Code=IAM-2&Category_Code=Stage-Micrometer-Scales.* 2012 [cited Secember-2012].

65. Liu, X., D. Du, and G. Mourou, *Laser ablation and micromachining with ultrashort laser pulses.* IEEE journal of quantum electronics, 1997. **33**(10): pp. 1706-1716.

66. Weber, M., *Handbook of laser wavelengths,*1998: CRC press.

67. Herman, P.R., H. Higaki, E. Rouillon, and R.S. Marjoribanks. *Pondermotive-driven "acceleration" of etch rates for short-pulse laser micromachining of transparent glasses*. in *Lasers and Electro-Optics. CLEO 98. Technical Digest*. 1998.

68. Schaffer, C.B., J. Garcia, and E. Mazur, *Bulk heating of transparent materials using a high-repetition-rate femtosecond laser*. Applied Physics A: Materials Science & Processing, 2003. **76**(3): pp. 351-354.

69. Schaffer, C.B., A. Brodeur, and E. Mazur, *Laser-induced breakdown and damage to transparent materials*. Measurement Science and Technology, 2001. **12**: pp. 1784-1794.

70. Allcock, G., P.E. Dyer, G. Elliner, and H.V. Snelling, *Experimental observations and analysis of CO_2 laser-induced microcracking of glass*. Journal of Applied Physics, 1995. **78**(12): pp. 7295-7303.

71. Tran, D., H. Zheng, Y. Lam, V. Murukeshan, J. Chai, and D. Hardt, *Femtosecond laser-induced damage morphologies of crystalline silicon by sub-threshold pulses*. Optics and Lasers in Engineering, 2005. **43**(9): pp. 977-986.

72. Kuo, D., S. Vierk, O. Rauch, and D. Polensky, *Laser zone texturing on glass and glass-ceramic substrates*. IEEE Transactions on Magnetics, 1997. **33**(1 Part 2): pp. 944-949.

73. Sokolowski-Tinten, K., J. Bialkowski, A. Cavalleri, D. Von der Linde, A. Oparin, J. Meyer-ter-Vehn, and S. Anisimov, *Transient states of matter during short pulse laser ablation*. Physical Review Letters, 1998. **81**(1): pp. 224-227.

74. Bennett, T., D. Krajnovich, L. Li, and D. Wan, *Mechanism of topography formation during CO_2 laser texturing of silicate glasses*. Journal of Applied Physics, 1998. **84**(5): pp. 2897-2905.

75. McGinty, S., G. O'Connor, and T. Glynn. *Development of a prediction equation for depth, aspect ratio and trench roughness pertaining to excimer laser ablation of polymer materials*. in *Opto-Ireland 2005: Photonic Engineering*. 2005.

76. Zhao, J., J. Sullivan, and T.D. Bennett, *Wet etching study of silica glass after CW CO_2 laser treatment.* Applied Surface Science, 2004. **225**(1): pp. 250-255.

77. Watanabe, M., Y. Kuroiwa, and S. Ito, *Study of Femtosecond Laser Ablation of Multicomponent Glass.* Reports of the Research Laboratory, Asahi Glass, 2005. **55**: pp. 27-31.

78. Teoman, E. and D.L. Church, *TeoSys Engineering LLC, General Laser MicroMachining Principles.* 2003. **version 2**.

79. Matsuoka, Y., K. Wake, T. Nagashima, and N. Iehisa, *Glass processing using the fourth harmonic of nanosecond pulse Nd:YAG laser.* Applied Physics A: Materials Science & Processing, 2007. **87**(1): pp. 81-85.

80. Griot, M., *The practical application of light.* Melles Griot Catalogue for Optical Components, 2000.

81. Karam, R., I. Invenios, and R. Casler, *A new 3D, direct-write, sub-micron microfabrication process that achieves true optical, mechatronic and packaging integration on glass-ceramic substrates* Photonics Cluster (UK newsletter), 2004. **vol 7**.

82. Vasco, J., P. Bartolo, B. Silva, and C. Galo, *Laser micromachining for mould manufacturing: II. Manufacture and testing of mould inserts.* Assembly Automation, 2007. **27**(3): pp. 231-239.

83. Zheng, H.Y., H. Liu, S. Wan, G. Lim, S. Nikumb, and Q. Chen, *Ultrashort pulse laser micromachined microchannels and their application in an optical switch.* The International Journal of Advanced Manufacturing Technology, 2006. **27**(9): pp. 925-929.

84. Issa, A., D. Brabazon, and M. Hashmi, *3D transient thermal modelling of laser microchannel fabrication in lime-soda glass.* Journal of Materials Processing Tech., 2008. **207**(1-3): pp. 307-314.

85. Schaffer, C., A. Jamison, and E. Mazur, *Morphology of femtosecond laser-induced structural changes in bulk transparent materials.* Applied Physics Letters, 2004. **84**: pp. 1441.

86. Schaffer, C., A. Jamison, J. Garcia, J. Ashcom, and E. Mazur. *Morphology and mechanisms of femtosecond laser-induced structural change in bulk transparent materials*. 2001.

87. Schaffer, C., A. Brodeur, N. Nishimura, and E. Mazur. *Laser-induced microexplosions in transparent materials: microstructuring with nanojoules*. 1999.

88. Lenzner, M., J. Krüger, S. Sartania, Z. Cheng, C. Spielmann, G. Mourou, W. Kautek, and F. Krausz, *Femtosecond optical breakdown in dielectrics*. Physical Review Letters, 1998. **80**(18): pp. 4076-4079.

89. Ashcom, J. and E. Mazur. *Femtosecond laser-induced microexplosions in transparent materials*. in *Proceedings of the Lasers and Electro-Optics Society Annual Meeting 2001*. 2001.

90. Gu, M., J. Amistoso, A. Toriumi, M. Irie, and S. Kawata, *Effect of saturable response to two-photon absorption on the readout signal level of three-dimensional bit optical data storage in a photochromic polymer*. Applied Physics Letters, 2001. **79**: pp. 148.

91. Rothschild, M., D.J. Ehrlich, and D.C. Shaver, *Effects of excimer laser irradiation on the transmission, index of refraction, and density of ultraviolet grade fused silica*. Applied Physics Letters, 1989. **55**: pp. 1276.

92. Day, D. and M. Gu, *Formation of voids in a doped polymethylmethacrylate polymer*. Applied Physics Letters, 2002. **80**: pp. 2404.

93. Low, D. and L. Li, *An investigation into melt flow dynamics during repetitive pulsed laser drilling of transparent media*. Optics and laser technology, 2001. **33**(7): pp. 515-522.

94. Schaffer, C., A. Brodeur, J.F. Garcia, and E. Mazur. *Micromachining of bulk glass with tightly-focused femtosecond laser pulses*. in *Lasers and Electro-Optics Society 12th Annual Meeting. LEOS '99*. 1999.

95. Miura, K., J. Qiu, H. Inouye, T. Mitsuyu, and K. Hirao, *Photowritten optical waveguides in various glasses with ultrashort pulse laser*. Applied Physics Letters, 1997. **71**: pp. 3329.

96. Zhou, G., M. Ventura, M. Vanner, and M. Gu, *Use of ultrafast-laser-driven microexplosion for fabricating three-dimensional void-based diamond-lattice*

photonic crystals in a solid polymer material. Optics letters, 2004. **29**(19): pp. 2240-2242.

97. Beach, D., A. Shotwell, and P. Essue, *Applications of lasers and laser systems,*1993: Prentice-Hall, Inc.

98. Luxon, J.T., D.E. Parker, and P.D. Plotkowski, *Lasers in manufacturing: an introduction to the technology,*1987: IFS.

99. Zayhowski, J.J., *Passively Q-switched Nd:YAG microchip lasers and applications.* Journal of alloys and compounds, 2000. **303**: pp. 393-400.

100. Du, D., X. Liu, G. Korn, J. Squier, and G. Mourou, *Laser-induced breakdown by impact ionization in SiO^2 with pulse widths from 7 ns to 150 fs.* Applied Physics Letters, 1994. **64**(23): pp. 3071-3073.

101. Shah, L., M. Richardson, J. Tawney, and K. Richardson. *Femtosecond micro-machining of high index and photo-sensitive glasses in air*. in *Lasers and Electro-Optics.(CLEO 2000)*. 2000.

102. Luxon, J.T. and D.E. Parker, *Industrial lasers and their applications,*1985: Prentice-Hall Englewood Cliffs (NJ).

103. Shin, B., J. Oh, and H. Sohn, *Theoretical and experimental investigations into laser ablation of polyimide and copper films with 355-nm $Nd:YVO_4$ laser.* Journal of materials processing technology, 2007. **187**: pp. 260-263.

104. Lonzaga, J., S. Avanesyan, S. Langford, and J. Dickinson, *Color center formation in soda-lime glass with femtosecond laser pulses.* Journal of Applied Physics, 2003. **94**(7): pp. 4332-4340.

105. Beinhorn, F., J. Ihlemann, K. Luther, and J. Troe, *Plasma effects in picosecond-femtosecond UV laser ablation of polymers.* Applied Physics A: Materials Science & Processing, 2004. **79**(4): pp. 869-873.

106. Miller, J.C., *Laser ablation: principles and applications,*1994: Springer-verlag.

107. Radziemski, L.J. and D.A. Cremers, *Lasers-Induced Plasmas and Applications,*. Vol. 21. 1989: CRC.

108. Hwang, J.C.Y., *Femtosecond Laser-Induced Damage for Micromachining of Transparent Materials*, 2002, PhD Thesis, Harvard University.

109. Desai, A., D. Bokenkamp, X. Yang, Y.C. Tai, E. Marzluff, and S. Mayo. *Microfluidic sub-millisecond mixers for the study of chemical reaction kinetics*. in *International Conference on Solid State Sensors and Actuators. TRANSDUCERS'97 Chicago*. 1997.

110. Fermann, M.E., A. Galvanauskas, and G. Sucha, *Ultrafast lasers: Technology and applications,*. Vol. 80. 2002: CRC Press.

111. Nikumb, S., Q. Chen, C. Li, H. Reshef, H. Zheng, H. Qiu, and D. Low, *Precision glass machining, drilling and profile cutting by short pulse lasers*. Thin Solid Films, 2005. **477**(1): pp. 216-221.

112. Sauvain, E., J. Kyung, and N. Lawandy. *Photoinduced micron scale maskless etching in transparent glasses*. in *Lasers and Electro-Optics Society Annual Meeting. LEOS'94 Conference Proceedings*. 1994.

113. Lippert, T., *Laser application of polymers*. Polymers and Light, 2004: pp. 147-215.

114. Buerhop, C., B. Blumenthal, R. Weissmann, N. Lutz, and S. Biermann, *Glass surface treatment with excimer and CO_2 lasers*. Applied Surface Science, 1990. **46**(1): pp. 430-434.

115. Georgi, S. *Separating and structuring of brittle material by the use of laser radiation*. in *Fourth International Symposium on laser Precision Microfabrication*. 2003. International Society for Optics and Photonics.

116. Qin, S. and W.J. Li, *Process characterization of fabricating 3D micro channel systems by laser-micromachining*. Sensors and Actuators A: Physical, 2002. **97**: pp. 749-757.

117. Bratton, D., D. Yang, J. Dai, and C.K. Ober, *Recent progress in high resolution lithography*. Polymers for advanced technologies, 2006. **17**(2): pp. 94-103.

118. Wood, R.M., R.T. Taylor, and R.L. Rouse, *Laser damage in optical materials at 1.06 μm*. Optics & Laser Technology, 1975. **7**(3): pp. 105-111.

119. Giuliano, C.R., *LASER-INDUCED DAMAGE TO TRANSPARENT DIELECTRIC MATERIALS*. Applied Physics Letters, 1964. **5**(7): pp. 137-139.

120. Fan, C.H. and J.P. Longtin, *Modeling optical breakdown in dielectrics during ultrafast laser processing.* Applied optics, 2001. **40**(18): pp. 3124-3131.

121. Ready, J.F., *Effects of high-power laser radiation*Academic Press, 1971.

122. Schaffer, C.B., A. Brodeur, and E. Mazur, *Laser-induced breakdown and damage in bulk transparent materials induced by tightly focused femtosecond laser pulses.* Measurement Science and Technology, 2001. **12**(11): pp. 1784.

123. Vaidyanathan, A., T. Walker, and A. Guenther, *The relative roles of avalanche multiplication and multiphoton absorption in laser-induced damage of dielectrics.* IEEE journal of quantum electronics, 1980. **16**(1): pp. 89-93.

124. Singh, J.P. and S.N. Thakur, *Laser-induced breakdown spectroscopy,.* Vol. 47. 2007: Elsevier Science.

125. Blau, W.J., *Opto-Ireland 2002: Optics and Photonics Technologies and Applications,.* Vol. 4876. 2003: Society of Photo Optical.

126. Rossier, J.S., A. Schwarz, F. Reymond, R. Ferrigno, F. Bianchi, and H.H. Girault, *Microchannel networks for electrophoretic separations.* Electrophoresis, 1999. **20**(4-5): pp. 727-731.

127. Karazi, S.M., A. Issa, and D. Brabazon, *Comparison of ANN and DoE for the prediction of laser-machined micro-channel dimensions.* Optics and Lasers in Engineering, 2009.

128. Kozhukharov, V., D. Dimitrov, and D. Tonchev, *Interaction of CO_2 laser radiation with glasses.* Infrared Physics, 1989. **29**: pp. 415-422.

129. Olabi, A., G. Casalino, K. Benyounis, and M. Hashmi, *An ANN and Taguchi algorithms integrated approach to the optimization of CO_2 laser welding.* Advances in Engineering Software, 2006. **37**(10): pp. 643-648.

130. Pervolaraki, M., P. Dyer, and P. Monk, *Ablation studies using a diode-pumped $Nd:YVO_4$ micro-laser.* Applied Physics A: Materials Science & Processing, 2004. **79**(4): pp. 849-854.

131. Ben Azouz, A., S. Karazi, D. Brabazon, M. Vázques, M. Macka, and B. Paull. *Effect of laser processing parameters and glass type on topology of micro-channels.* in *Nano Science and Technology Institute NSTI-Nanotech Conference and Expo.* 2010. Anaheim, California, U.S.A.

132. Karazi, S.M., D. Brabazon, and A. Ben Azouz. *Dimensions and cost prediction modelling of Nd:YVO₄ laser internal micro-channel fabrication in PMMA*. in *Nano Science and Technology Institute NSTI-Nanotech Conference and Expo*. 2010. Anaheim, California, U.S.A.

133. Karazi, S. and D. Brabazon. *Analysis and prediction of dimensions and cost of laser micro-machining internal channel fabrication process*. in *EPJ Web of Conferences*. 2010. EDP Sciences.

134. Karazi, S.M. and D. Brabazon, *An artificial neural network for dimensions and cost modelling of internal micro-channels fabricated in PMMA using Nd:YVO₄ laser*, in *International Manufacturing Conference IMC28*-2011: Dublin City University, Dublin, Ireland. pp. 34-36.

135. Karazi, S.M. and D. Brabazon. *Evaluation of the effect of ND:YVO₄ laser parameters on internal micro-channel fabrication in polycarbonate*. in *International Conference on Neural Computation Theory and Applications NCTA*. 2011. University Paris-Est Créteil (UPEC), Paris, France.

136. Ben Azouz, A., S. Murphy, S.M. Karazi, M. Vasquez, and D. Brabazon, *Fast fabrication process of cyclic olefin copolymer microfluidic sensing systems*, in *15th international conference on advances in materials & processing technologies AMPT*2012: University of Wollongong, Wollongong, Australia.

137. Karazi, S.M. and D. Brabazon, *Control of laser micro-machining via artificial neural network (ANN) and response surface methodologies (RSM)*, in *15th Annual Sir Bernard Crossland Symposium*2012: Dublin City University, Dublin, Ireland.

138. Karazi, S.M., D. Brabazon, and A. Ben Azouz, *Laser micromachining control: numerical and statistical modelling techniques*, in *15th international conference on advances in materials & processing technologies AMPT*2012: University of Wollongong, Wollongong, Australia.

139. Dhupal, D., B. Doloi, and B. Bhattacharyya, *Optimization of process parameters of Nd:YAG laser microgrooving of Al ₂TiO₅ ceramic material by response surface methodology and artificial neural network algorithm*. Proceedings of the Institution of Mechanical Engineers, Part B: Journal of Engineering Manufacture, 2007. **221**(8): pp. 1341-1350.

140. The Quartz Page, Quartz Structure. *http://www.quartzpage.de/gen_struct.html*. 2012 [cited December-2012].

141. Holloway, D.G., *The physical properties of glass*. 1973.

142. Chemistry of Glass. *http://www.pilkington.com/pilkington-information/about+pilkington/education/chemistry+of+glass.htm*. 2012 [cited December-2012].

143. Soda-lime glass. *http://en.wikipedia.org/wiki/Soda_lime_glass*. 2012 [cited December-2012].

144. Soda Lime Flat Float Glass. *http://www.valleydesign.com/sodalime.htm*. 2012 [cited December-2012].

145. Bansal, N.P. and R.H. Doremus, *Handbook of glass properties*. 1986.

146. Mark, H., J. Zimmerman, N. Bikales, C. Overberger, G. Menges, and J. Kroschwitz, *Encyclopedia of Polymer Science & Engineering*. HF Mark, NM Bikales, CG Overberger, G. Menges, JI Kroschwitz, Eds., Wiley and Sons, New York, 1988. **II**: pp. 372.

147. Polycarbonate. *http://en.wikipedia.org/wiki/Polycarbonate*. 2012 [cited December-2012].

148. Acrylic Glass. *http://www.mecadi.com/en/literature_tools/encyclopedia/categorial/Definition/Acrylic_glass/*. 2012 [cited December-2012].

149. International Conference on Joining, P., *Joining Plastics 2006 : Conference Proceedings : Second International Conference on Joining PLastics : 25-26 April 2006, London, England*2006, Shrewsbury: Rapra Technology.

150. Data Table for PMMA. *http://www.matbase.com/material/polymers/commodity/pmma/properties*. 2012 [cited December-2012].

151. Antony, J., *Design of experiments for engineers and scientists,* 2003: Butterworth-Heinemann.

152. Katayama, S. and A. Matsunawa, *Solidification Behaviour and Microstructural Characteristics of Pulsed and Continuous Laser Welded Stainless Steels*. IFS(Publications) Ltd, 1986: pp. 19-25.

153. Cochran, W.G. and G.M. Cox, *Experimental designs*. 1957.

154. Eriksson, L., *Design of experiments: principles and applications,* 2008: MKS Umetrics AB.

155. Benyounis, K., *Prediction and optimization of residual stresses, weld-bead profile and mechanical properties of laser welded components*, 2006, PhD Thesis, Dublin City University.

156. Box, G.E.P. and K. Wilson, *On the experimental attainment of optimum conditions.* Journal of the Royal Statistical Society. Series B (Methodological), 1951. **13**(1): pp. 1-45.

157. Design of Experiments. *http://cms3.minitab.co.kr/board/minitab_data/7.%20DesignofExperimentsAll Topics.pdf*. 2005 [cited December-2012].

158. Montgomery, D.C., *Design and analysis of experiments,* 2008: Wiley.

159. Khuri, A.I. and J.A. Cornell, *Response surfaces: designs and analyses,*. Vol. 152. 1996: CRC.

160. Collins, M. and A. DeLucca, Neural Networks. *www.academic.marist.edu/~jzbv/architecture/Projects/S2002/NeuralNet2/C OA.PPT*. 2010 [cited June-2012].

161. Callan, R., *Essence of neural networks,* 1998: Prentice Hall PTR.

162. Haykin, S., *Neural networks: a comprehensive foundation,* 2008: Prentice Hall.

163. Bowen, W.R., M.G. Jones, and H.N.S. Yousef, *Prediction of the rate of crossflow membrane ultrafiltration of colloids: A neural network approach.* Chemical engineering science, 1998. **53**(22): pp. 3793-3802.

164. Varoonchotikul, P., *Flood forecasting using artificial neural networks,* Taylor & Francis, 2003: Balkema Rotterdam, The Netherlands.

165. Singh, Y. and P. Kumar, *Application of feed-forward neural networks for software reliability prediction.* SIGSOFT Software Engineering Notes, 2010. **35**(5): pp. 1-6.

166. Ahmad, A.M., S. Ismail, and D. Samaon. *Recurrent neural network with backpropagation through time for speech recognition*. in *International Symposium Communications and Information Technology, ISCIT*. 2004.

167.	Nagesh Kumar, D., K. Srinivasa Raju, and T. Sathish, *River flow forecasting using recurrent neural networks.* Water resources management, 2004. **18**(2): pp. 143-161.

168.	Kshirsagar, A. and M. Rathod. *Artificial Neural Network.* in *IJCA Proceedings on National Conference on Recent Trends in Computing.* 2012. Foundation of Computer Science (FCS).

169.	Ní Mhurchú, J., *Dead-end and crossflow microfiltration of yeast and bentonite suspensions: experimental and modelling studies incorporating the use of artificial neural networks*, 2008, Dublin City University.

170.	Aydiner, C., I. Demir, and E. Yildiz, *Modeling of flux decline in crossflow microfiltration using neural networks: the case of phosphate removal.* Journal of membrane science, 2005. **248**(1): pp. 53-62.

171.	Rumelhart, D.E., G.E. Hinton, and R.J. Williams, *Learning representations by back-propagating errors.* Cognitive modeling, 2002. **1**: pp. 213.

172.	Duda, R.O., P.E. Hart, and D.G. Stork, *Pattern classification.* 2nd ed. New York 2001.

173.	Fu, R.Q., T.W. Xu, and Z.X. Pan, *Modelling of the adsorption of bovine serum albumin on porous polyethylene membrane by back-propagation artificial neural network.* Journal of membrane science, 2005. **251**(1): pp. 137-144.

174.	Amari, S., N. Murata, K.R. Muller, M. Finke, and H.H. Yang, *Asymptotic statistical theory of overtraining and cross-validation.* Neural Networks, IEEE Transactions on, 1997. **8**(5): pp. 985-996.

175.	Maier, H.R. and G.C. Dandy, *Neural networks for the prediction and forecasting of water resources variables: a review of modelling issues and applications.* Environmental modelling & software, 2000. **15**(1): pp. 101-124.

176.	Lee, S., W. Park, H. Cho, W. Zhang, and M. Leu, *A neural network approach to the modelling and analysis of stereolithography processes.* Proceedings of the Institution of Mechanical Engineers, Part B: Journal of Engineering Manufacture, 2001. **215**(12): pp. 1719-1733.

177. Ye, J., X. Yuan, and G. Zhou. *Genetic algorithm for optimization design of diffractive optical elements in laser beam shaping*. in *Design, Fabrication, and Characterization of Photonic Devices II*. 2001.

178. De Deus, A. and J. Mazumder. *Two-dimensional thermo-mechanical finite element model for laser cladding*. 1996.

179. Wang, G.G. and S.Q. Xie, *Optimal process planning for a combined punch-and-laser cutting machine using ant colony optimization*. International Journal of Production Research, 2005.

180. Shen, H., Y. Shi, Z. Yao, and J. Hu, *Fuzzy logic model for bending angle in laser forming*. Materials Science and Technology, 2006. **22**(8): pp. 981-986.

181. Vitek, J., Y. Iskander, E. Oblow, S. Babu, S. David, P. Fuerschbach, and H. Smartt. *Neural network modeling of pulsed-laser weld pool shapes in aluminum alloy welds*. in *Conference: 5. international conference on trends in welding research*. 1998.

182. Chan, B., J. Pacey, and M. Bibby, *Modelling gas metal arc weld geometry using artificial neural network technology*. Canadian metallurgical quarterly, 1999. **38**(1): pp. 43-51.

183. Chan, B., M. Bibby, and N. Holtz. *Predicting the HAZ hardness of pipeline and tap fitting steels with artificial neural networks*. in *The fourth international conference on pipeline technology*. 2004. Australia: University of Wollongong.

184. Sterjovski, Z., D. Nolan, K. Carpenter, D. Dunne, and J. Norrish, *Artificial neural networks for modelling the mechanical properties of steels in various applications*. Journal of Materials Processing Tech., 2005. **170**(3): pp. 536-544.

185. Okuyucu, H., A. Kurt, and E. Arcaklioglu, *Artificial neural network application to the friction stir welding of aluminum plates*. Materials and Design, 2007. **28**(1): pp. 78-84.

186. Anawa, E. and A. Olabi, *Using Taguchi method to optimize welding pool of dissimilar laser-welded components*. Optics and laser technology, 2008. **40**(2): pp. 379-388.

187.   Benyounis, K. and A. Olabi, *Optimization of different welding processes using statistical and numerical approaches–A reference guide.* Advances in Engineering Software, 2008. **39**(6): pp. 483-496.

188.   Dragos, V., V. Dan, and R. Kovacevic. *Prediction of the laser sheet bending using neural network*. in *International Symposium on Circuits and Systems. Proceedings. ISCAS Geneva*. 2000.

189.   Yousef, B., G. Knopf, E. Bordatchev, and S. Nikumb, *Neural network modeling and analysis of the material removal process during laser machining.* The International Journal of Advanced Manufacturing Technology, 2003. **22**(1): pp. 41-53.

190.   Setia, R. and G. May, *Modeling and optimization of via formation in dielectrics by laser ablation using neural networks and genetic algorithms.* IEEE Transactions on Electronics Packaging Manufacturing, 2004. **27**(2): pp. 133-144.

191.   On Axis Performance Measures - Accuracy, Precision, & Resolution. *http://www.newport.com/servicesupport/Tutorials/default.aspx?id=86*. 2012 [cited December - 2012].

192.   Resolution, Accuracy and Repeatability, Engineering Reference. *http://www.aerotech.com/media/255855/complete%20engineering%20reference.pdf*. 2012 [cited December-2012].

193.   Koren, Y., *Robotics for engineers,*1985: McGraw-Hill Companies.

194.   Rofin, *DC015 industrial CO_2 Slab laser operating manual*, in *serial No. 2024/2024,*2002.

195.   Rofin website. *http://www.rofin.com/index.php?id=161&L=1*. 2009 [cited November-2012].

196.   Petik, A. *Some aspects of using STL file format in CAE systems*. in *Int Workshop CA System Technol*. 2000. Citeseer.

197.   Zurek, S., P. Marketos, and T. Moses, *LabVIEW as a tool for measurements, batch data manipulations and artificial neural network predictions.* Przegl d Elektrotechniczny, 2007. **83**(4): pp. 114-119.

198.   Zurek, S., A. Moses, M. Packianather, P. Anderson, and F. Anayi, *Prediction of power loss and permeability with the use of an artificial neural network in*

wound toroidal cores. Journal of Magnetism and Magnetic Materials, 2008. **320**: pp. 1001.

199.   Collins, D.A., *Development of a laser based surface profilometer using the principle of optical triangulation*, 2005, Master Thesis, Dublin City University.

200.   International Organization for Standardization, *Test Code for Machine Tools-part 2: Determination of Accuracy and Repeatability of Positioning Numerically Controlled Axes,*, 2006.

201.   Cohen, P.R., *Empirical methods for artificial intelligence,*. Vol. 139. 1995: MIT press Cambridge, MA.

202.   Clarke, G.M. and D. Cooke, *A basic course in statistics,*1998: Arnold New York.

203.   Wonnacott, T.H. and R.J. Wonnacott, *Regression: a second course in statistics,*1981: Wiley New York, NY.

204.   Hassan, E.M., *Feasibility and Optimization of Dissimilar Laser Welding Components*, 2008, Dublin City University.

205.   Design-Expert software, V., *Statistics Made Easy*, 2007, Stat-Ease Inc., Software, Training & Consulting.

206.   Akhnazarova, S., V. Kafarov, V.M. Matskovsky, and A.P. Repyev, *Experiment optimization in chemistry and chemical engineering,*1982: Mir Publishers.

207.   Draper, N.R., H. Smith, and E. Pownell, *Applied regression analysis,*. 3rd ed. Vol. 3. 1998: Wiley New York.

208.   Chatterjee, S. and A.S. Hadi, *Regression analysis by example,*. Vol. 607. 2006: Wiley-Interscience.

209.   MechTronic website. *http://www.mechtronic.co.uk/.* 2009 [cited July-2012].

210.   Jacobs, P.F., *Stereolithography and other RP&M technologies: from rapid prototyping to rapid tooling,*1995: Society of Manufacturing Engineers.

APPENDICES

Appendix A - General RSM Procedure

To perform an RSM for laser micromachining, the following sequential steps need to be performed in order to develop a mathematical model:

The identification of the key process input variables.

The key factors can be defined from the previous literature or by conducting a screening study. Normally, screening study is done by carrying out trial micromachining experiments changing one of the process parameters at a time. In this work, the significant process factors were determined from both the previous literature and a screening study. The process input factors are laser power, pulse repetition frequency, and translation speed.

The determination of each input ranges.

The screening study also helped finding the ranges of each factor. The criterion of selecting the working ranges was getting a smooth, uniform, and continuous micro-channel.

Design matrix development

The matrix depends on the selected experimental design scheme of RSM. For full 3^3 factorial design of experiments the design matrixes in coded values is shown in Table 6-1. The three levels are numerically coded as -1, 0, and +1. This matrix table was developed with the design expert software.

Table 6-1: Typical 3^3 factorial design of experiments coded values.

Std order	Run order	P	PRF	U
1	29	-1	-1	-1
2	11	0	-1	-1
3	13	1	-1	-1
4	27	-1	0	-1
5	6	0	0	-1
6	31	1	0	-1
7	30	-1	1	-1
8	10	0	1	-1
9	18	1	1	-1
10	5	-1	-1	0
11	17	0	-1	0
12	1	1	-1	0
13	24	-1	0	0
14	28	0	0	0
15	2	1	0	0
16	8	-1	1	0
17	15	0	1	0
18	7	1	1	0
19	23	-1	-1	1
20	19	0	-1	1
21	3	1	-1	1
22	25	-1	0	1
23	26	0	0	1
24	9	1	0	1
25	21	-1	1	1
26	12	0	1	1
27	22	1	1	1
28	4	0	0	0
29	32	0	0	0
30	14	0	0	0
31	20	0	0	0
32	16	0	0	0

Performing the experiment

In Table 6-1 "Std order" denotes to the standard order of experiments while "Run order" is a random order according to which the micromachining experiments were conducted in order to avoid experimental bias and systematic errors.

Recording the responses

All responses, geometry of developed micro-channels, were measured in sequential order for each experiment and each response. This was done using the Laser Profilometer for the CO_2 laser experiments, and Reichart optical microscope for the Nd:YVO$_4$ laser experiments. Usually, several measurements are taken for each experiment, if applicable, and then an average of at least three recorded measurements is calculated and considered for the subsequent analysis. On the other hand, the micromachining cost was estimated according to Equation 3-1 presented in section 3.3.5 so there was no need for the repetition and average.

Development of the mathematical model

The functional relationship representing any response of interest can be expressed as y = f (P, PRF, U) and Equation 2-8 becomes Equation 6-1:

$$y = a_0 + a_1 \times P + a_2 \times PRF + a_3 \times U + a_{11} \times P^2 +$$

$$a_{22} \times PRF^2 + a_{33} \times U^2 + a_{12} \times P \times PRF + \qquad 6\text{-}1$$

$$a_{13} \times P \times U + a_{23} \times PRF \times U$$

This mathematical model was developed with the design expert software.

Estimation of the coefficients in the model

Regression analysis is applied to specify the values of the coefficients in Equation 6-1. The design expert software was used to evaluate the coefficients for all responses of each experiment.

Testing the adequacy of the models developed

ANOVA (ANalysis Of VAriance) is a general method for studying sampled-data relationships [201, 202]. The method analyse the difference between two or more sample means by subdividing the total sum of squares. The purpose is to test for significant differences between class means, and this is done by analysing the variances. Analysis of variance (ANOVA) is similar to regression in that it is used to investigate and model the relationship between a response variable and one or more independent variables. In effect, analysis of variance extends the two-sample t-test for testing the equality of two population means to a more general null hypothesis of comparing the equality of more than two means, versus those that are not all equal [203, 204].

The adequacy of the developed models was tested using the analysis of variance (ANOVA) methodology. The p-value (or Prob.>F) of the model and of each term in the model can be figured using ANOVA. If the p-value of the model and of each term in the model does not exceed the level of significance ($\alpha = 0.05$ chosen for level of significance) then the model may be considered adequate within the confidence interval of $(1-\alpha)$, which equals to (1-0.05=95% confidence interval). For the lack-of-fit test, the lack of fit could be considered insignificant if the p-value of the lack of fit exceeds the level of significance.

$$SS_M = \sum_{i=1}^{n} (\hat{y_i} - \bar{y})^2 \qquad\qquad 6\text{-}2$$

$$SS_R = \sum_{i=1}^{n} (y_i - \hat{y_i})^2 \qquad\qquad 6\text{-}3$$

$$SS_T = \sum_{i=1}^{n} (y_i - \bar{y})^2 \qquad\qquad 6\text{-}4$$

$$SS_{PE} = \sum_{i=1}^{n_0} (y_i - \hat{y_i})^2 \text{ , for centre points only} \qquad 6\text{-}5$$

$$SS_{lof} = SS_R - SS_{PE} \qquad\qquad 6\text{-}6$$

$$R^2 = 1 - \left[\frac{SS_R}{SS_R + SS_M}\right] \qquad\qquad 6\text{-}7$$

$$Adjusted\ R^2 = 1 - \left[\left(\frac{SS_R}{df_R}\right) \times \left(\frac{SS_R + SS_M}{df_R + df_M}\right)^{-1}\right] \qquad\qquad 6\text{-}8$$

$$Predicted\ R^2 = 1 - \left[\frac{\sum_{i=1}^{n}(y_i - \widehat{y_{i,-i}})^2}{SS_R + SS_M}\right] \qquad\qquad 6\text{-}9$$

$$Adequate\ precision = \left[\frac{Max(\hat{y}) - Min\ (\hat{y})}{\sqrt{\dfrac{p \times MS_R}{n}}}\right] \qquad\qquad 6\text{-}10$$

$$MSE = \frac{1}{n}\sum_{i=1}^{n}(\widehat{y_i} - y_i)^2 \qquad\qquad 6\text{-}11$$

Where y is the actual value, $\hat{y}$ is the predicted value, $\bar{y}$ is the average value.

Using the design expert software, the statistical significance of the developed models and each term in the regression equation were inspected using statistical measure to achieve the best fit. These measures are the sequential F-test, lack-of-fit test and other adequacy measures. The adequacy measures were the coefficient of determination R^2, Adjusted R^2, Predicted R^2, and Adequate precision. Since statistics is beyond the scope of this work, therefor the theory behind these statistical measures will not be discussed further. The sum of squares can be calculated according to formulas from Equation 6-2 to Equation 6-6. On the other hand, the adequacy measures can be calculated according to formulas from Equation 6-7 to Equation 6-10. The mean square error is calculated according to Equation 6-11 [158, 159, 205-207]. Table 6-2 presents a sample of the ANOVA table used for analysis of the models developed in this work.

Table 6-2: ANOVA analysis table with all terms.

Source	Sum of Squares	d.f.	Mean Square	F Value	Prob > F
Model	SS_M	p	Each SS divided by its *df*	Each MS divided by MSE	From table or automatically from the software
P	SS_1	1			
PRF	SS_2	1			
U	SS_3	1			
P×PRF	SS_{12}	1			
P×U	SS_{13}	1			
PRF×U	SS_{23}	1			
P^2	SS_{11}	1			
PRF^2	SS_{22}	1			
U^2	SS_{33}	1			
Residual	SS_R	N-p-1			-
Lack of Fit	SS_{lof}	$N-p-n_0$			From Table
Pure Error	SS_E	n_0-1			-
Corrected Total	SS_T	N-1	-	-	-

R^2, adjusted R^2, predicted R^2, adequate precision.

Where P: Number of coefficients in the model.

N: Total number of runs (in this work, N=32).

n_o: Number of centre points.

df: Degree of freedom.

MSE: Mean Square error.

Model reduction

Generally, the full mathematical model representing the response of interest, Equation 6-2, has some insignificant model terms that need to be removed, terms that

have p-value greater that the level of significance α (α= 0.05 chosen for this work as level of significance). This elimination can be done manually or automatically [155, 205, 208]. The three automatic procedures of evaluating all possible regression equations are:

a) Forward selection procedure:

This procedure begins with only the constant term, and the first variable added is the one with the highest correlation with y. The variable will remain in the equation if its regression coefficient is significant. A new search for the second variable with highest correlation with y is started, after y has been adjusted for the effect of the first variable. The significance of the regression coefficient of the second variable is then tested. If the regression coefficient is significant, a search for a third variable is done in the same way. The procedure is accomplished when the last variable entered into the equation has an insignificant regression coefficient or when all variables are included. The test statistic for this selection process is the standard t or F-statistic, which is equal to t^2.

b) Backward elimination procedure:

In this procedure, the full equation is fitted and the variables are sequentially removed one at a time. The variable with the smallest contribution to the reduction of error is removed first, or the variable with the smallest regression coefficient to its standard error ratio (t ratio), and so forth. If more than one variable have an insignificant t ratio, the procedure operates by falling the variable with the smallest insignificant t ratio, the equation with the remaining variables is then fitted, and the new regression coefficient ratios are tested. The procedure is stopped when all the t ratios are significant or all except one variable has been removed.

c) Stepwise regression method:

This method is a forward selection with the possibility of removing a variable that might be added in an earlier stage, like the backward procedure, is considered. The calculations used for the inclusion and removal of variables are the same as for forward and backward procedures. This procedure has the advantage of assuming

different or similar levels of significance for inclusion or removal of variables from the regression equation. Since this procedure enjoys the benefits of the forward and backward procedures, this procedure was used for this work.

Development of the final reduced model

At this step, the final reduced model can be developed as determined by applying the adopted regression procedure. This model merely holds the significant terms and the terms that are necessary to preserve hierarchy. In addition, a reduced quadratic ANOVA table can be developed.

Post analysis

The response at any midpoint can be predicted using the developed model, only when this model is tested, checked, and found to be final adequate model. Moreover, this final model can be used to produce some important plots (such as 3D graphs, contours, and perturbation plots) to present the factors effect, interaction, and how they contribute to the response. Furthermore, the developed model can be employed to optimise the laser micromachining process.

Appendix B - CO$_2$ Laser System

Laser Beam

The beam delivery system is operating on 127 and 190 mm focal length. The machine beam system has a high-pressure nozzle assembly with four thumbscrew adjusters to keep the assist gas around the beam and replaceable copper nozzle allows a standoff distance between laser head and work piece. Premix laser gas is used for operating the laser machine. The gas consists of a 94 % mixture of (Carbon Dioxide, Helium, Nitrogen, and Xenon) and 6 % of Carbon Monoxide. The laser bottle contains 1500 standard litres [194, 195, 204]. Table 6-3 shows selected main specifications of the laser beam. The laser beam mode is TEM$_{00}$ and has a high quality factor of K > 0.9. The beam diameter was 20 mm at the laser output, diverging to 25 mm at 10 m distance. Practically, the focused spot diameter is 45 μm for the 127 mm focal length [5].

Table 6-3: Laser beam specifications.

Spatial mode	TEM00
Beam quality factor, K	> 0.9
Beam propagation parameter, M^2	1.11

Laser System Control

On the control software side, dedicated control software is installed as standard. On the control hardware side, There are two control units, the first one is the main laser control unit (by Rofin) which controls the laser machine only, and the other one is the control console (by MechTronic) which controls the entire laser system and overrides the settings on the main laser control unit. Therefore, the user-friendly, deskilled MechTronic control console was used to control the entire CO$_2$ laser system for machining the selected media. This control console allowed the

modification of operational parameters, such as laser power; P, and translation speed; U, by typing in their numerical values directly. While, the modification of the Pulse Repetition Frequency; PRF was indirectly accomplished by altering two dimensionless parameters (namely, the period and the divide) on the control console. All inputs were entered via the full colour TFT LCD touch screen, mounted at the front of the machine.

Motion System Control

The MTI 0505 motion system is the manufacturer-supplied motion control system for the CO_2 laser system. The same control console full colour TFT LCD touch screen was used for the simultaneous control of the motion system and the laser power supply. The motion control system is located on the side of the laser system in a temperature controlled electronic enclosure. The unit comprises an MTI multi-layer computer half-card and motion control card, designed and manufactured specifically by MTI. The unit is equipped with high-speed modem, 3.5" floppy drive and 5 GB hard drive, 4Mb ram, expandable to 32Mb, Digital Signal Processor, 486-DX5-133 host processor. The XY moving table system is particularly suitable for mixed job shop application given the Short, Fixed Beam Path and giving maximum beam stability. This translation stage is driven by DC brushless servomotors, directly connected to Precision Ball screws. This XY moving table has a machining area of 500 mm × 500 mm, a resolution of 1.25 μm by means of optical rotary encoders, a speed range from 1/60 mm/sec up to 250/3 mm/sec, in steps of 1 mm per min and acceleration value up to 2 m/s^2 at the beginning of the motion [5, 209].

Appendix C - Nd:YVO$_4$ Laser System

Laser Specifications

Neodymium-doped Yttrium Orthovanadate (Nd:YVO$_4$) is a crystalline material that regularly utilised as an active laser medium for diode-pumped solid-state lasers, grown by the Czochralski technique. This laser was chosen for this study due to its minimum temperature control requirements, its ability to retain short pulse output yet at very high repetition rate frequency (PRF), and its wavelength that is suitable for direct writing inside transparent media [56]. This laser unit was received as a donation from IBM Ireland. Selected specifications of the Nd:YVO$_4$ laser system are listed in Table 6-4.

Table 6-4: Specifications of the Nd:YVO$_4$ laser system .

Output power	< 2.5 W
Wavelength	1064 nm
Excitation	Radio frequency (RF)
Pulse energy, 110 kHz	>18 µJ
Pulse width, 110 kHz	80 ns
PRF range	Up to 1 MHz max

Appendix D - Nd:YVO$_4$ Laser Power Supply Unit

The Nd:YVO$_4$ Laser Power Supply

Spectra Physics T-series Nd:YVO$_4$ diode-pumped, fibre coupled, solid-state laser system, shown in Figure 6-1, was used. This T-Series laser included an exclusive proprietary coupling technology to a high power laser diode bar, called FC*bar*^{TM}. The Neodymium doped Yttrium Vanadium Oxide (Nd:YVO$_4$) was utilised as the lasing medium for the V-style laser heads.
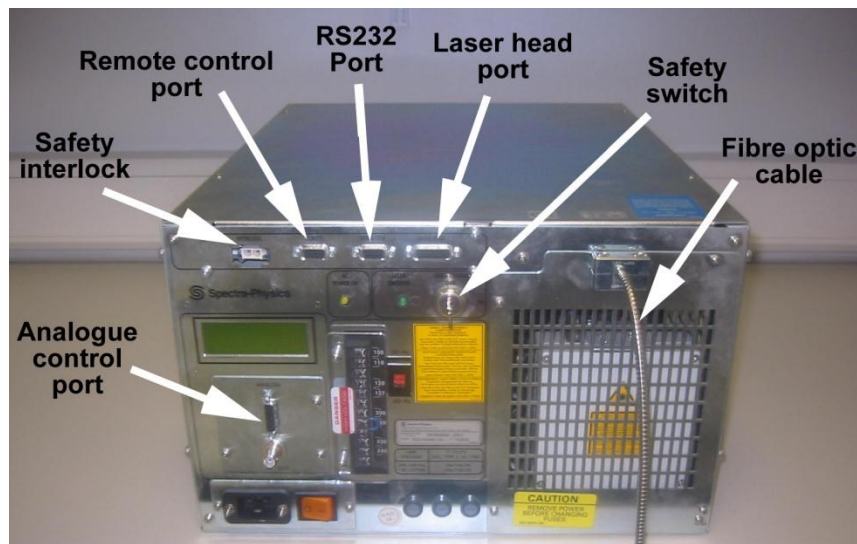
Figure 6-1: The Nd:YVO$_4$ laser power supply.

Spectra Physics laser model (T20 - V80 - 106Q) was used. This model number is descriptive and supplies some basic information about power supply, laser head, and output emission of the system as follows:

T20: the letter "T" represents that the power supply has an integrated "Total" thermal management system. The number "20" indicates that the laser can supply up to 20 Watts, which is the total available diode pump power that can be achieved with additional second laser diode bar added to the supply.

V80: the letter "V" denotes the folded v-shaped cavity resonator design of the laser head. The number "80" signifies the 80 ns nominal value of pulse width at 110 kHz pulse repetition frequency *PRF*.

106Q: the number "106" denotes the 1064 nm output wavelength. The letter "Q" indicates a Q-switched laser head.

Initially, an OEM simple DOS based program can be used to control the laser system through an RS232 serial port. Alternatively, an analogue control port on the power supply can be used to control the system using analogue and TTL signals.

Appendix E - Nd:YVO₄ Laser Optics Table
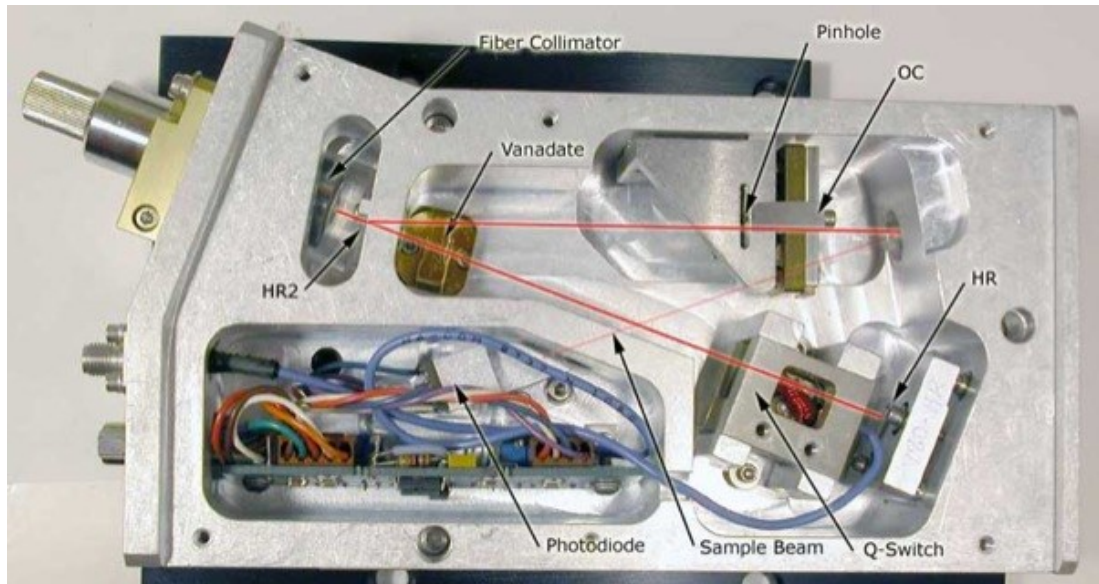
Figure 6-2: The V-style laser head with the top open.

The Three cables connected the laser head with the Nd:YVO$_4$ laser power supply, the laser head control cable (data cable), RF frequency cable (for pulse repetition frequency), and fibre optic cable, which carries the pumped diode light from the Nd:YVO$_4$ laser power supply to the laser head. Figure 6-2 shows the V beam path in the laser head that gives the V series heads their name.

The fibre optic cable conveyed the pumped laser light to the V-style laser head. In order to adjust the laser beam diameter at the focusing lens entrance, one variable 3X beam expander was used. An achromatic lens was employed for focusing the laser beam into the target media. This lens had a relatively considerable focal length, f = 25.6 mm, which enabled the internal machining in polymers media. To achieve the best focus of the laser beam, the achromatic lens was fitted with linearly fine-adjustable x-y-z translation stage for fine-alignment and displacement fine-tuning.
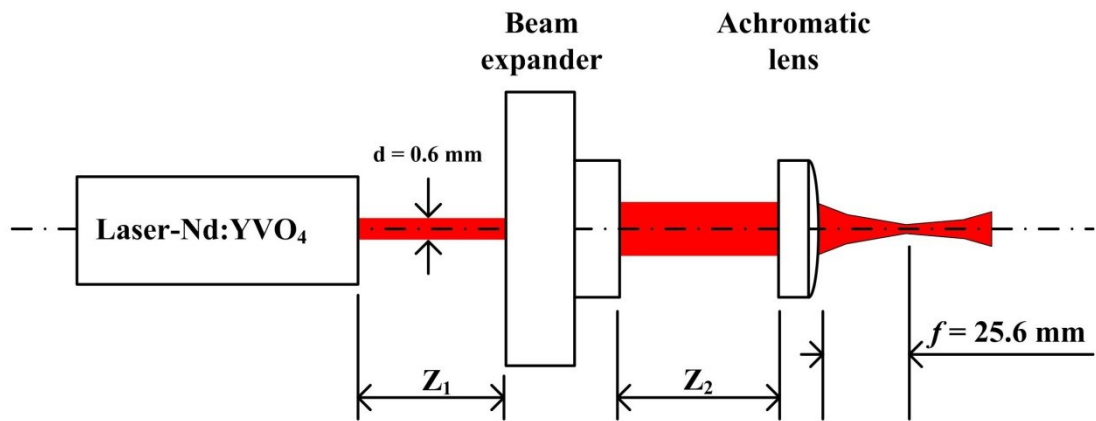
Figure 6-3: The optics setup of Nd:YVO4 laser system.

Figure 6-3 shows the optics setup of the Nd:YVO$_4$ laser system. The laser beam mode is TEM$_{00}$ and had a diameter of d = 600 μm at the laser head outlet, diverging to 848.53 μm after a distance Z$_1$ equals to 95 mm at the inlet of the beam expander. The beam expander magnification was set to two, thus the laser beam diameter was 1363.18 at the beam expander outlet. Then the laser beam slightly diverged to 1374.02 μm after a distance equals to Z$_2$ = 115 mm at the inlet of the achromatic lens. Practically, the focused spot diameter was 38.05 μm for the 25.6 mm focal length [5].

Appendix F - Nd:YVO$_4$ Laser System 3D Translation stage

The Nd:YVO4 motion system, and the CAD processing and laser control codes were originally developed by Ahmed ISSA [5]. However, the entire system endured several complicated problems, such as skewness, hardware incapable of giving the correct number of pulses (to the drivers of the stepper motors) during a very short time (high speed), poor accuracy, poor repeatability, and other issues. This is why the author significantly improved, updated, and extended the codes/programs contents and capabilities. Moreover, the author added quadrature rotary encoders and used a sophisticated hardware controller (Programmable Automation Controller (PAC) unit - CompactRIO with FPGA), which has given driving frequency to all stepper motors (stages) and got the feedback from the encoders simultaneously and in real time. This allowed the motion system to be a real time closed loop control system. Furthermore, it enabled the system to be capable of repeatable micrometre level accurate positioning as shown, later in this work, in the positional analysis section.

The translation stage was built so it can accommodate a maximum work piece size of 90 by 90 by 90 mm with practical maximum travel ranges of 20 by 65 by 65 mm on X, Y, and Z respectively. The 20 mm travel range on the X-axis was considered adequate since it was on the same axis of the focusing lens, which had a focal length of 25.6 mm.

Due to their basic control requirements and high degree of accuracy, three VEXTA two-phase PH268-21M2 stepper motors were used for the 3D translation stage. These 12 V two-phased stepper motors were lightweight, small sized, easy to install, and provided a good step angle of 1.8 degrees. Each motor was framed and coupled to a lead screw, through a metric flexible coupling, that converted the rotational motion into a linear motion.

Stepper motors need an electronic digital pulse signal in addition to voltage to turn the motor shaft by one step; this pulse is called the "step angle". To run the motor continuously, a continuous pulse train is needed to be sent to the stepper motor. Practically, a motor driver, which is an electronic circuit, is required to provide the necessary voltage and pulse train/frequency.
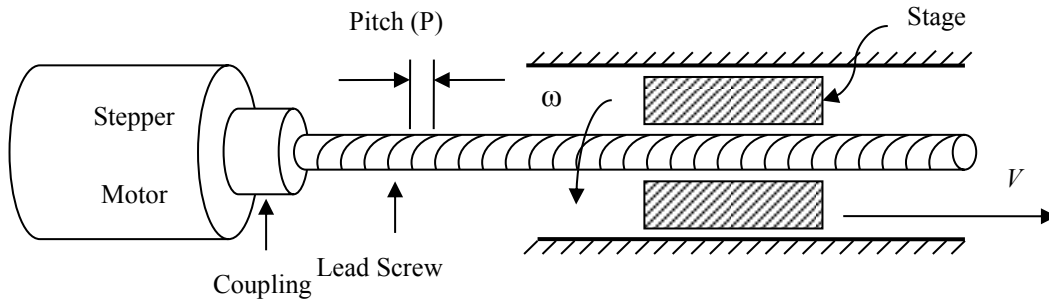
Figure 6-4: Mechanical setup of the linear stages.

The rotary movement of the stepper motors can be converted to linear motion of stage using a lead screw gear drive system, shown in Figure 6-4. Since each digital pulse signal will turn the stepper motor's shaft 1.8 degree, so N equals to 200 steps are the number of steps needed to rotate the motor's shaft one revolution (360 degrees). The smallest linear distance can be achieved, the distance resolution D_{RES}, is produced by the motor turning the shaft a single step. Taking into account that the lead screw used in this work had a pitch P = 1/4" = 6.35 mm, the distance between turns of a screw thread. This D_{RES} and the linear displacement D caused by n pulses sent to the stepper motor can be calculated according to formulas 6-12, and 6-13 respectively.

$$D_{RES} = P/N \qquad\qquad 6\text{-}12$$

$$D = n \times D_{RES} = n \times P/N \qquad\qquad 6\text{-}13$$

On the other hand, the stepper motor's rotational speed ω (rev/s) that runs with a pulse train frequency f (Hz), and the stepper motor's linear speed V (mm/s) caused by the lead screw can be calculated using the formulas 6-14, and 6-15 respectively.

$$\omega = 360 \times f/N \qquad\qquad 6\text{-}14$$

$$V = P \times f/N \qquad\qquad 6\text{-}15$$

Figure 6-5: The IM483 Micro-stepping Stepper Motor Driver.

An Intelligent Motion Systems, Inc. motor driver board (IM483), shown in Figure 6-5, was connected to each of the three stepper motors. This 12 V motor driver was chosen for its high performance, low cost, and having an advance electronic technique called micro-stepping. This technique further increase the stepper motor N value, consequently the stepper motor's positioning resolution, through regulating the level of the current running in the stepper motor winding. This driver can divide each standard/regular step up into 256 micro-steps; hence the N value can become 51200 micro-steps needed to rotate the motor's shaft one revolution (360 degrees) . According to formula 6-13 the standard/regular D_{RES} = 6.35 / 200 = 31.75 µm. However, using the micro-stepping technique the D_{RES} = 6.35 / 51200 = 0.124 µm.

In order to provide the feedback signal to the controller and measure the motional position of the stages, an AVAGO TECHNOLOGIES high-resolution rotary encoder was fitted to each axis of the translation stage. This electromechanical device uses optical sensors to provide electrical signals in the form of pulse trains, which can be translated into position and motion direction. This two-channel optical incremental quadrature encoder was chosen because it is TTL compatible, easy to mount on the current stepper motors, and has a remarkably high resolution of 2000 PPR (pulses per revolution). As shown in Figure 6-6, the encoder system consisted of the encoder module, the code wheel, and the two-channel encoder lead, which connected the encoder to the control system.

Figure 6-6: The encoder system's parts.

The modules consist of a lensed (LED) source and a detector IC enclosed in a small C-shaped plastic package. Due to a highly collimated light source and unique photo detector array, these modules are extremely tolerant to mounting misalignment. There is a single Light Emitting Diode (LED) included in each encoder module as its light source. The light is collimated into a parallel beam via a single polycarbonate lens located right over the LED. The integrated detector circuit (IC) is opposite to the

emitter. This integrated circuit contains multiple sets of photo-detectors and the signal processing circuitry needed to produce the digital waveforms. The code wheel rotates between the emitter and detector, causing the light beam to be interrupted by the pattern of spaces and bars on the code wheel. The code wheel design and radius will affect the arrangement pattern of photodiodes, which detect these interruptions. These detectors are also spaced such that a light period on one pair of detectors corresponds to a dark period on the adjacent pair of detectors. The photodiode outputs are then fed through the signal processing circuitry resulting in A, $\overline{A}$, B, and $\overline{B}$. Two comparators receive these signals and produce the final outputs for channels $\overline{A}$ and $\overline{B}$. Due to this integrated phasing technique, the digital output of channel A is in quadrature with that of channel B (90 degrees out of phase) .

In order to perform the required measurements using the quadrature encoders and to provide the needed feedback, the resulting A and B quadrature square-waves should be decoded to produce a count up or a countdown. The employed encoder is compatible with X1, X2, and X4 decoding techniques. In the X1 decoding, when channel A leads channel B, the count increment occurs on the rising edge of channel A. When channel B leads channel A, the decrement occurs on the falling edge of channel A. Figure 6-7 shows a quadrature cycle and the resulting increments and decrements for X1 encoding.
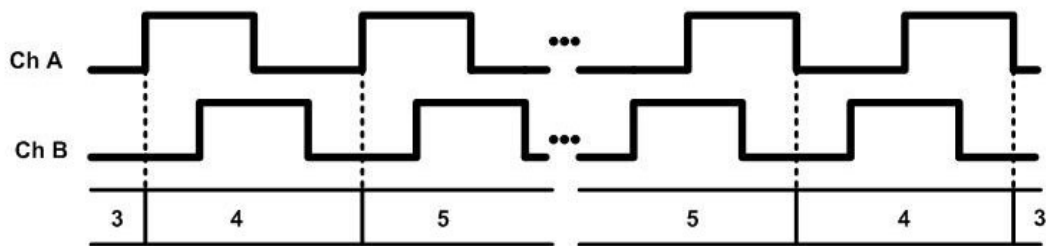
Figure 6-7: X1 decoding.

In the X2 decoding, when channel A leads channel B, the count increment occurs on each edge of channel A. When channel B leads channel A, the decrement occurs on each edge of channel A. Therefore, each cycle results in two increments or

decrements. Figure 6-8 shows a quadrature cycle and the resulting increments and decrements for X2 encoding.
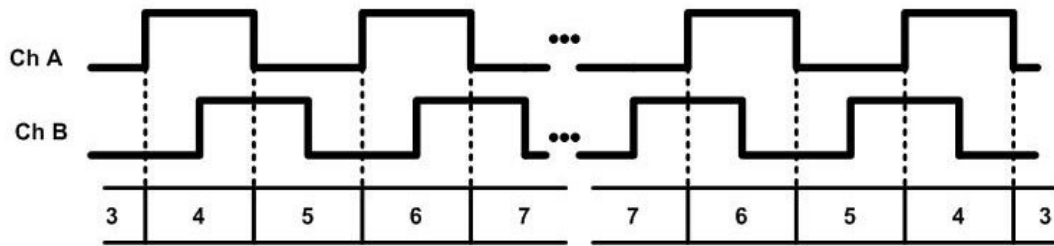
Figure 6-8: X2 decoding.

In the X4 decoding, the same behaviour holds for X2 encoding except the counter increments or decrements on each edge of channel A and channel B. The counter increments or decrements depending on which channel leads the other. So each cycle results in four increments or decrements. Figure 6-9 shows a quadrature cycle and the resulting increments and decrements for X4 encoding.
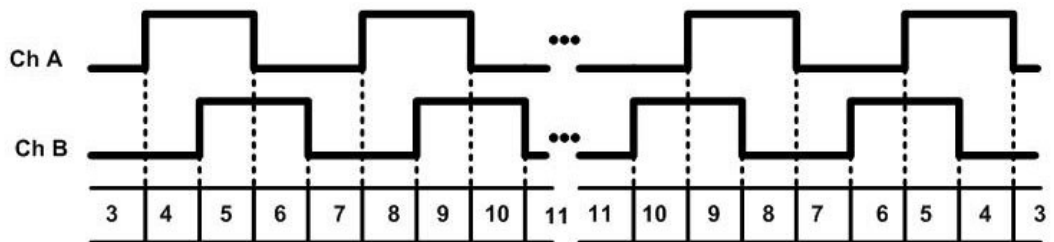
Figure 6-9: X4 decoding.

Since the encoder code wheel is mounted on the motor lead screw shaft which was of a pitch P = 1/4" = 6.35 mm, the full revolution of the code wheel corresponds to 6.35 mm. According to formula 6-13 the standard/regular encoder D_{RES} = 6.35 / 2000 = 3.175 µm. However, using the X4 decoding technique the 2000 PPR (pulses per revolution) will be decoded into 8000 counts per revolution, which means four-manifold resolution. In this case the encoder D_{RES} = 6.35 / 8000 = 0.794 µm. Therefore, to gain the full advantage of the encoders the X4 decoding was used.

Appendix G - Nd:YVO$_4$ Laser System Control

The control computer was a DELL™ OPTIPLEX™ 380 with Intel® Core™ 2 Dual CPU E5400 @ 2.7 GHz processor and 3.00 GB installed memory (RAM) and 32-bit Windows 7 operating system. This computer controlled the entire Nd:YVO$_4$ laser system (laser and motion systems) through LabVIEW 2009 code and graphical user interface (GUI) developed specifically for this work. The control computer communicated with the Nd:YVO$_4$ laser power supply through its serial communication port RS232. On the other hand, the control computer communicated with the NI CompactRIO through the Ethernet port.

The BWD MiniLab power supply provided the motors and their drivers with the DC voltage necessary for them to work properly. Moreover, it was utilised as a common ground point for the Nd:YVO$_4$ laser power supply, the motor drivers, and the real time controllers. The D-link network Ethernet switch was the telecommunication device that provided the data link layer (communication medium) between the controlling computer and the CompactRIO. Furthermore, it provides the control system with access to the internet so that the Laser system can be controlled remotely.

The real time controller, consisted of NATIONAL INSTRUMENTS NI CompactRIO 9074 (which is an integrated system of real-time controller and reconfigurable chassis), 8-channel, TTL digital input/output module; NI 9401, 32-channel, TTL digital input/output module; NI 9403.

This real time controller was chosen carefully from a wide range of data acquisition, and instrument control products. This hardware was selected because it by itself provides a real time combined monitoring, data logging, and control and can be programmed with NI LabVIEW software. Furthermore, it combines the reliability and ruggedness of a programmable logic controller (PLC), the performance, and

openness of a computer, and the flexibility of custom field-programmable gate array (FPGA) circuitry.

NI CompactRIO 9074 is an integrated system with a reconfigurable FPGA chassis and embedded real-time controller. This system has up to two million gate reconfigurable FPGAs, eight slots for NI I/O modules, up to 400 MHz real-time processor, and two Ethernet ports and RS232 serial port for connection to peripherals. The CompactRIO, which stands for Compact Real time Input and Output, and along with the two added NI I/O modules (NI 9401 and NI 9403) are regarded together as a programmable automation controller (PAC).

One TTL digital input/output module was not enough to provide the necessary hardware capabilities required to run the laser and motion system. Therefore, NI 9401 and NI 9403 were carefully chosen and together used to generate the frequencies and digital inputs and outputs desired. Practically, the FPGA technology in the CompactRIO enabled the generation of pulse train/frequency from a digital output a TTL digital input/output module using a unique and novel code in LabVIEW developed by the author especially for this purpose. Table 6-5 shows selected specifications of the two used NI I/O modules NI 9401 and NI 9403.

Table 6-5: NI I/O modules specifications.

Module	NI 9401	NI 9403
Logic	5 V/TTL	5 V/TTL
Channels	8	32
Sink/Source	Sink/Source	Sink/Source
I/O Delay Time	100 ns	7 µs
Signal Levels	5 V	5 V
Output Current per Channel	2 mA	2 mA
Connector Options	D-Sub	D-Sub

Appendix H - Nd:YVO$_4$ Laser System Control Process Layout

Control-wise, the laser system consisted mainly of the Nd:YVO$_4$ laser power supply system and the motion system which ,in turn, was made up of the motors (and their drivers) and the encoders (the feedback system). The control computer controlled, via the developed LabVIEW code and GUI (Graphical User Interface), controlled the whole laser system. It directly controlled the Nd:YVO$_4$ laser power supply and monitored the laser emission parameters through the RS232 cable. The laser's power supply transmitted the emission parameters to the laser head and hence to the external optics.

On the other hand, the NI real time controller triggered the laser ON/OFF, controlled the 3D translation stage, and processed the feedback data from the encoders. Moreover, the control computer was used to develop and process the CAD designs and feed the required laser and motion parameters via the developed LabVIEW code and GUI. So to facilitate the 3D translation stage's control on the control computer, the LabVIEW code and GUI were utilized to control the NI real time controller, which controlled the three stepper motors of the 3D translation stage via the three motor drivers. Figure 6-10 shows the developed 3D micromachining system's process flow diagram. Having a sub-micron linear resolution of the motors and the encoders with the real time controller and feedback system enabled the system to be capable of repeatable micrometre level accurate positioning.

Figure 6-10: Control process flow chart of the Nd:YVO$_4$ laser system.

Appendix I - Nd:YVO$_4$ Laser Motion System Control

The input/output or I/O is the communication between the information processing system (such as a computer, real time controller, etc.) and the system to be controlled/monitored. An output can be used to send a signal out from the information processing system, while the input can be used to receive a signal from the controlled/monitored system.

Since there is no need to run the motors at different speeds simultaneously, one frequency output was shared among the translation stage's three motors. On the other hand, one digital output to turn the motor (ON/OFF) and another to determine the motor rotation direction were needed for each motor (this digital output toggles the direction of rotation between CW and CCW, (ON) will move the stage away from the motor). That means seven digital outputs were needed from the real time controller for the motors. The NI 9401 module was employed to cover these seven digital outputs in addition to the digital output needed for the laser (ON/OFF) triggering signal.

Each encoder module needed two digital inputs and one digital output. The digital inputs were for channel A and channel B, while the digital output was set to constant on and used to supply the encoder with the proper voltage. That means that 9 digital inputs and outputs were needed for the encoder/feedback system alone and the NI 9403 module was employed to cover that. Table 6-6 shows the real time controller employed digital inputs and outputs and their description.

Table 6-6: The real time controller employed digital inputs and outputs.

Module	Digital I/O #	Function	Controlled device
NI 9401	DO 0	Motion frequency output	Motors
	DO 1	X-axis ON/OFF	
	DO 2	X-axis direction	
	DO 3	Y-axis ON/OFF	
	DO 4	Y-axis direction	
	DO 5	Z-axis ON/OFF	
	DO 6	Z-axis direction	
	DO 7	Laser ON/OFF	Laser power supply
NI 9403	DI 1	channel A of X-axis encoder	Encoders
	DI 2	channel B of X-axis encoder	
	DI 3	channel A of Y-axis encoder	
	DI 4	channel B of Y-axis encoder	
	DI 5	channel A of Z-axis encoder	
	DI 6	channel B of Z-axis encoder	
	DO 7	X-axis encoder voltage supply	
	DO 8	Y-axis encoder voltage supply	
	DO 9	Z-axis encoder voltage supply	

Appendix J - Nd:YAG Laser System

Nd:YAG Laser System

The author significantly contributed in the development of this laser with the objective of studying the positional analysis of this system and then comparing it with that of the Nd:YVO$_4$ laser system. Figure 6-11 shows the optics setup of Nd:YAG laser system.
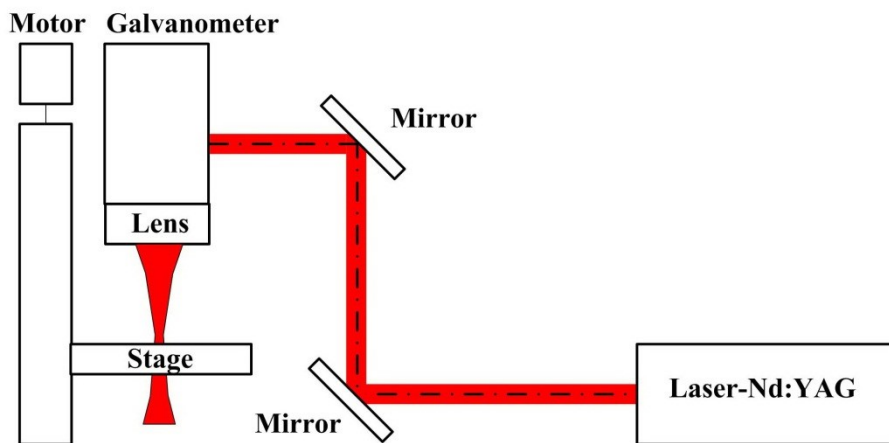
Figure 6-11: The optics setup of Nd:YAG laser system.

This system mainly consisted of the Nd:YAG laser pumping unit (WEDGE 1064 HF), laser head, optics, RAYLASE galvanometer (two-axis laser beam deflection unit), PI linear translation stage, Inert gas cover system, fume extraction system, control system, and accessories.

Laser Specifications

Neodymium-doped yttrium aluminium garnet (Nd:YAG) is a crystalline material. Besides, it is a very common host material in various forms of industrial lasers. This high peak power diode pumped solid-state (DPSS) laser (WEDGE 1064 HF) was carefully selected and bought from BRIGHT SOLUTIONS. This air-cooled short

pulse Q-switched DPSS laser was greatly preferred because it can emit more than 1 mJ, with pulse width 700 ps to 3 ns, resulting in a peak power up to 400 kHz.

Table 6-7: Specifications of the Nd:YAG laser system (WEDGE 1064 HF) .

Output Power @ 100kHz	> 4 W
Wavelength	1064 nm
PRF range	Single shot to 100 kHz
Pulse width range	700 ps - 3 ns
Excitation	Radio frequency (RF)
Pulse energy	40 to 300 μJ
Polarization	Linear, 100:1
Cooling	Air cooled

Beside its high output peak power, the low energy consumption and heat generation, allows efficient ablation and non-linear interaction with most materials . Selected specifications of the Nd:YAG laser (WEDGE 1064 HF) unit are listed in Table 6-7.

Appendix K - Stage micrometre

This calibrated and certified glass stage micrometre, shown in Figure 6-12, was utilised to make sure that this Mitutoyo microscope, which was used for positional measurements, is sufficient as a measurement system. This was carried out, since there was no information about the accuracy and repeatability of this microscope.

Figure 6-12: The utilised stage micrometre.

This stage micrometre has two scales on it (1" and 25 mm) with chrome deposition lines and a size of 1" x 3" x 0.110" thick. The 25 mm rulers is equally spaced and numbered 0 through 25. Each division between numbers 0 through 25 equals to 1.0 mm. Each division between numbers 20 through 23 is divided into 0.1 mm increments. Each division between numbers 23 through 25 is divided into 0.02 mm increments. On the other hand, the 1" ruler is numbered 0.0 through 1.0 every 0.100" division. 0.0" through 1.0" divided into 0.1" increments. 0.9" through 1.0" divided into 0.01" increments. The last two 0.01" increments are divided into 0.001" increments. Figure 6-13, and Figure 6-14 display the front and back sides of the stage micrometre certificate.

KLARMANN RULINGS, INC.
Precision Optical Patterns

P.O. Box 4795, Manchester, New Hampshire 03108
480 Charles Bancroft Highway, Litchfield, New Hampshire 03052
reticles.com   Email: sales@reticles.com

CERTIFICATE OF CALIBRATION

CUSTOMER	Buehler LTD. 41 Waukegan Road Lake Bluff, IL 60044
INSTRUMENT	Stage Micrometer P/N KR-814
MAKE	Klarmann Rulings, Inc.
SERIAL NUMBER	4421
DATE CALIBRATED	January 11, 2000
SUGGESTED RE-CALIBRATION DATE	January 11, 2005
CONDITION OF INSTRUMENT	__X__ GOOD ___ FAIR __ POOR

This is to certify that the above listed instrument has been calibrated by Klarmann Rulings, Inc.
Calibrated at 68.5 +/-2 Degrees F, Relative Humidity 35+/-5%.

The Standard used is as follows:
 KLARMANN RULINGS, INC. STAGE MICROMETER SERIAL NUMBER
 3548 TRACEABLE TO THE N.I.S.T. NUMBER 731/242156-88

Measuring Instrument:
 OLYMPUS STM MEASURING MICROSCOPE WITH AN OVERALL ACCURACY
 OF .00002"/.0004MM

The Quality Control Department of Klarmann Rulings, Inc. is in compliance with all requirements of
ANSI/NCSLZ540-1-1994. "American National Standard for Calibration". Our calibration system is reviewed and
tested by our Quality Control Manager once monthly in accordance with Klarmann Rulings, Inc. Quality Procedure
number 015. Our measuring instrument is calibrated four times yearly, using standards that are traceable to the N.I.S.T.
This certificate of calibration shall not be reproduced, except in full, without the written approval of Klarmann
Rulings, Inc.

Our measuring instrument was last calibrated on December 30, 1999.
Our next calibration is due on March 30, 2000.

The entire system is subject to review at any time by our Government Quality Assurance Representative.
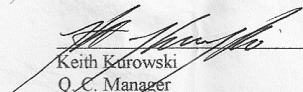
Keith Kurowski
Q.C. Manager

Figure 6-13: First page of the stage micrometre certificate.

Calibration Number: 4421
Date Calibrated: January 11, 2000
1" and 25mm Stage Micrometer per P/N KR-814
Actual readings are as follows:

1" SCALE			25mm SCALE					
SCALE	ACTUAL	SCALE		ACTUAL	SCALE	ACTUAL	SCALE	ACTUAL
0.100 =	0.10000"	1.00	=	01.0000mm	23.02 =	23.0200mm	24.02 =	24.0200mm
0.200 =	0.20000"	2.00	=	02.0000mm	23.04 =	23.0400mm	24.04 =	24.0400mm
0.300 =	0.30000"	3.00	=	03.0000mm	23.06 =	23.0600mm	24.06 =	24.0600mm
0.400 =	0.40000"	4.00	=	04.0000mm	23.08 =	23.0800mm	24.08 =	24.0800mm
0.500 =	0.50000"	5.00	=	05.0000mm	23.10 =	23.1000mm	24.10 =	24.1000mm
0.600 =	0.60000"	6.00	=	06.0000mm	23.12 =	23.1200mm	24.12 =	24.1200mm
0.700 =	0.70000"	7.00	=	06.9996mm	23.14 =	23.1400mm	24.14 =	24.1400mm
0.800 =	0.80000"	8.00	=	08.0000mm	23.16 =	23.1600mm	24.16 =	24.1600mm
0.900 =	0.90000"	9.00	=	09.0000mm	23.18 =	23.1800mm	24.18 =	24.1800mm
0.910 =	0.91000"	10.00	=	10.0000mm	23.20 =	23.2000mm	24.20 =	24.2000mm
0.920 =	0.92000"	11.00	=	10.9996mm	23.22 =	23.2204mm	24.22 =	24.2200mm
0.930 =	0.93000"	12.00	=	12.0000mm	23.24 =	23.2400mm	24.24 =	24.2400mm
0.940 =	0.94000"	13.00	=	13.0004mm	23.26 =	23.2600mm	24.26 =	24.2600mm
0.950 =	0.95000"	14.00	=	14.0004mm	23.28 =	23.2800mm	24.28 =	24.2800mm
0.960 =	0.96000"	15.00	=	15.0000mm	23.30 =	23.3000mm	24.30 =	24.3000mm
0.970 =	0.97000"	16.00	=	16.0000mm	23.32 =	23.3200mm	24.32 =	24.3200mm
0.980 =	0.98000"	17.00	=	17.0000mm	23.34 =	23.3400mm	24.34 =	24.3400mm
0.981 =	0.98100"	18.00	=	18.0000mm	23.36 =	23.3600mm	24.36 =	24.3600mm
0.982 =	0.98200"	19.00	=	19.0000mm	23.38 =	23.3800mm	24.38 =	24.3800mm
0.983 =	0.98300"	20.00	=	20.0000mm	23.40 =	23.4000mm	24.40 =	24.4000mm
0.984 =	0.98400"	20.10	=	20.1000mm	23.42 =	23.4200mm	24.42 =	24.4200mm
0.985 =	0.98500"	20.20	=	20.2000mm	23.44 =	23.4400mm	24.44 =	24.4400mm
0.986 =	0.98600"	20.30	=	20.3000mm	23.46 =	23.4600mm	24.46 =	24.4600mm
0.987 =	0.98700"	20.40	=	20.4000mm	23.48 =	23.4800mm	24.48 =	24.4800mm
0.988 =	0.98800"	20.50	=	20.5000mm	23.50 =	23.5000mm	24.50 =	24.5000mm
0.989 =	0.98900"	20.60	=	20.6000mm	23.52 =	23.5200mm	24.52 =	24.5200mm
0.990 =	0.99000"	20.70	=	20.7000mm	23.54 =	23.5400mm	24.54 =	24.5400mm
0.991 =	0.99100"	20.80	=	20.8000mm	23.56 =	23.5600mm	24.56 =	24.5600mm
0.992 =	0.99200"	20.90	=	20.9000mm	23.58 =	23.5800mm	24.58 =	24.5804mm
0.993 =	0.99300"	21.00	=	21.0000mm	23.60 =	23.6000mm	24.60 =	24.6000mm
0.994 =	0.99400"	21.10	=	21.1000mm	23.62 =	23.6200mm	24.62 =	24.6200mm
0.995 =	0.99500"	21.20	=	21.2000mm	23.64 =	23.6400mm	24.64 =	24.6400mm
0.996 =	0.99600"	21.30	=	21.3000mm	23.66 =	23.6600mm	24.66 =	24.6600mm
0.997 =	0.99700"	21.40	=	21.4000mm	23.68 =	23.6800mm	24.68 =	24.6800mm
0.998 =	0.99800"	21.50	=	21.5004mm	23.70 =	23.7004mm	24.70 =	24.7000mm
0.999 =	0.99900"	21.60	=	21.6000mm	23.72 =	23.7200mm	24.72 =	24.7200mm
1.000 =	1.00000"	21.70	=	21.7004mm	23.74 =	23.7400mm	24.74 =	24.7400mm
		21.80	=	21.8000mm	23.76 =	23.7600mm	24.76 =	24.7600mm
		21.90	=	21.9000mm	23.78 =	23.7800mm	24.78 =	24.7800mm
		22.00	=	22.0000mm	23.80 =	23.8000mm	24.80 =	24.8000mm
		22.10	=	22.1000mm	23.82 =	23.8204mm	24.82 =	24.8200mm
		22.20	=	22.2000mm	23.84 =	23.8400mm	24.84 =	24.8400mm
		22.30	=	22.3000mm	23.86 =	23.8600mm	24.86 =	24.8600mm
		22.40	=	22.4000mm	23.88 =	23.8800mm	24.88 =	24.8800mm
		22.50	=	22.5000mm	23.90 =	23.9000mm	24.90 =	24.9004mm
		22.60	=	22.6000mm	23.92 =	23.9200mm	24.92 =	24.9200mm
		22.70	=	22.7000mm	23.94 =	23.9400mm	24.94 =	24.9400mm
		22.80	=	22.8000mm	23.96 =	23.9600mm	24.96 =	24.9600mm
		22.90	=	22.9000mm	23.98 =	23.9800mm	24.98 =	24.9800mm
		23.00	=	23.0000mm	24.00 =	24.0000mm	25.00 =	25.0000mm
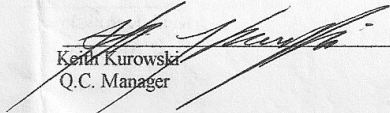
Keith Kurowski
Q.C. Manager

Figure 6-14: Second page of the stage micrometre certificate.

Appendix L - CAD Processing Codes and GUIs

The build file is the file that will be fed into the real time controller to drive the 3D positioning stage in the Nd:YVO$_4$ laser system. The developed build file was mainly based on slicing the STL file (tessellated model). The process of the developed algorithm used for preparing the build file is illustrated in Figure 6-15.
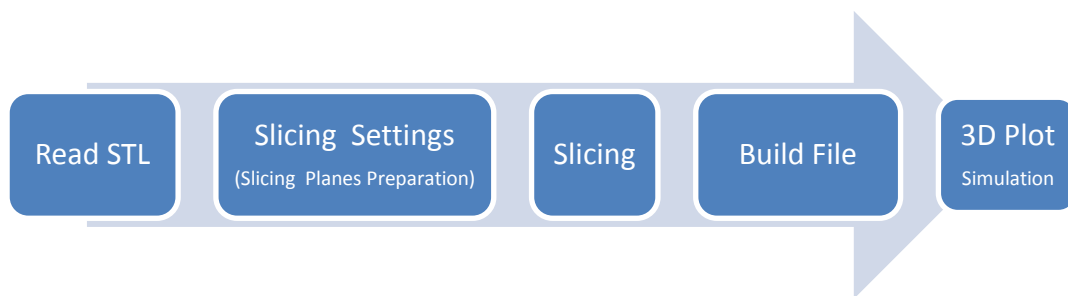
Figure 6-15: The flow chart of the CAD file processing code.

This process was programmed according to "State Machine" architecture in LabVIEW. In other words, the programmed code will perform a specific action for each state in the diagram in a systematic manner. Furthermore, it will automatically convert the input STL file into the final output build file with minimal interaction from the user. The GUI was carefully designed to provide as simple and user friendly interface as possible. A "3D sphere" feature design sample will be used, from this section on, to illustrate the developed CAD processing code and GUI.

"Read STL" State

Slicing technique is the method used to produce a build file from the STL file [210]. For slicing, only the coordinates of the three vertices, which define each facet (triangle), were needed. So there was a need to remove the redundant data contained in the STL file. Therefore, the two main purposes of the "Read STL" step were to

remove the redundant data of the STL file and to save the filtered data in a text file. The filtered text output of the "read STL" step was called the "source file".

After opening the developed CAD processing code, the "STL file path" and the "Output file name" input strings should be provided before running the CAD processing code. STL file path" is the location of the input STL file to be converted. On the other hand, the "Output file name" is the user chosen name of the final build file to be created.
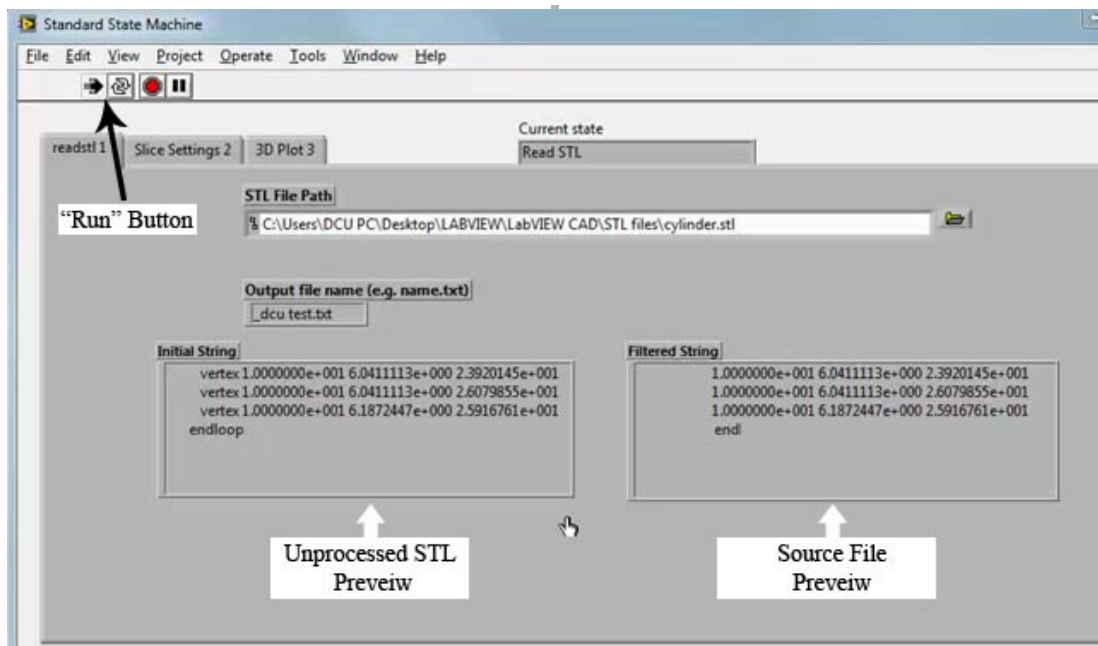
Figure 6-16: The "Read STL" state front panel.

The location of the output "build file" was not required as it was programmed to be related to the location of the input STL file. Figure 6-16 shows the read STL state of the LabVIEW state machine GUI. This interface provides a "facet" preview of the unprocessed STL file and the source file. The source file contains only the coordinates of the facet's three vertices and the word "end" between each two facets and the word "eof", which means End Of File, at the very end of the filtered file.

How the Code Works

1. It reads the first seven lines in the STL file. These lines contain the coordinates of the first facet, they will for example read:

solid sphere

facet normal -0.16 -0.18 -0.90

outer loop

vertex 1.40000 1.40000 0.00000

vertex 1.40000 1.51177 0.15111

vertex 1.21177 1.60000 0.15111

endloop

2. It looks for a matched string in these lines "outer loop", this marks the beginning of the facet vertices' details. Then it deletes the matched string and the preceding text. After that it passes the remaining string.

3. It looks for another matched string "endloop" in the remaining string; this marks the end of the facet vertices' details. The program then deletes the match string and the text after this. After that it passes the remaining string.

4. The remaining string contains three lines; each line begins with the word "vertex" followed by three numbers that resemble the coordinates of the vertex. The "vertex" words are also deleted so that the string only contains three lines of coordinate readings.

5. A fourth line is added to the previous string, this line reads "end" marking the end of the first facet's details. These four lines are written to an output text file.

6. This ends the first iteration in the program; the second loop iteration processes the following seven lines from the STL file and so on. In each iteration, steps 2 to 5 are repeated.

7. This algorithm is followed till the last seven lines are processed from the STL file. In this last loop an extra line is added to the string in step 5, reading "eof" which marks the end of file.

The program terminates its operation at the end of the STL file. The output text file contains all the facets' details but in a reduced form. The size of the file is thus reduced by half and it is more easily used in the slicing program.

"Slice Settings" State

The user defines the slicing parameters, which are going to be used in processing the design, in this state. The front panel of this state is shown in Figure 6-17. There is a five seconds time delay to let the user define the layer spacing and the direction of slice. The intersection direction of the slicing might be along X (X planes), Y (Y planes), or Z (Z planes). The spacing should be a reasonable value compared to the dimensions of the shape. The process parameters and the source file are fed into another two, transparent to user, sub-codes. The actual slicing is done in the Planes.vi and Intersection.vi sub-codes.
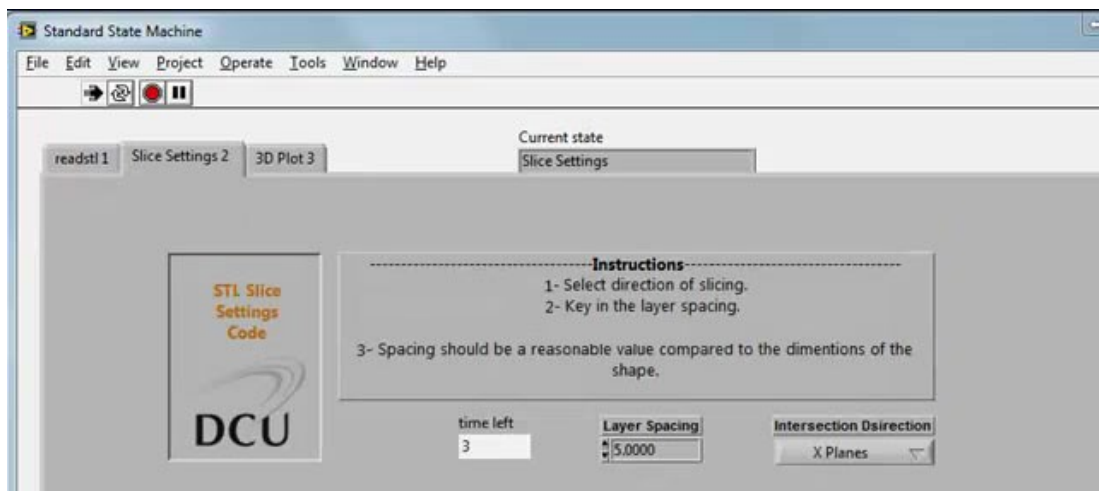
Figure 6-17: The "Slice Settings" state front panel.

How to Use The Code

The input variables used in this program are shown in Figure 6-17. These include:

1. Intersection Direction: Defines the direction of slicing, the user can choose between X, Y and Z direction.

2. Layer Spacing: Defines the spacing between the slicing planes. The value chosen is usually a compromise between the best quality and a reasonable build file size.

How the Code Works

1. It takes the first facet's data from the source file, and saves the X, Y and Z coordinates in three individual arrays.
2. Step 1 is repeated till the end of the source file. At the end, there are three arrays (X-values, Y-values and Z-values).
3. The three arrays, the Intersection Direction and the Layer Spacing value are fed as inputs to the Planes code and the Slicing code.

Planes Code

This code examines the CAD design limits and the layer spacing to generate the slicing planes; X Planes, Y Planes, or Z Planes according to the direction of slice. This code is self-executing, and transparent to the user. The slicing planes are then used in the Slicing code.

How the Code Works

Here the procedure is explained for generating Z Planes, it is exactly the same for the other two directions.

1. It finds the minimum and maximum values in the Z values arrays. The difference between them defines the length in the Z direction.
2. The length in Z direction is divided by the layer spacing; it gives the number of planes required.
3. The Z Planes are generated in a loop that has the count of the number of planes calculated in step 2. Starting with the minimum Z value and adding the layer spacing every time to the preceding value and saving the value in an array until the maximum Z value is reached.
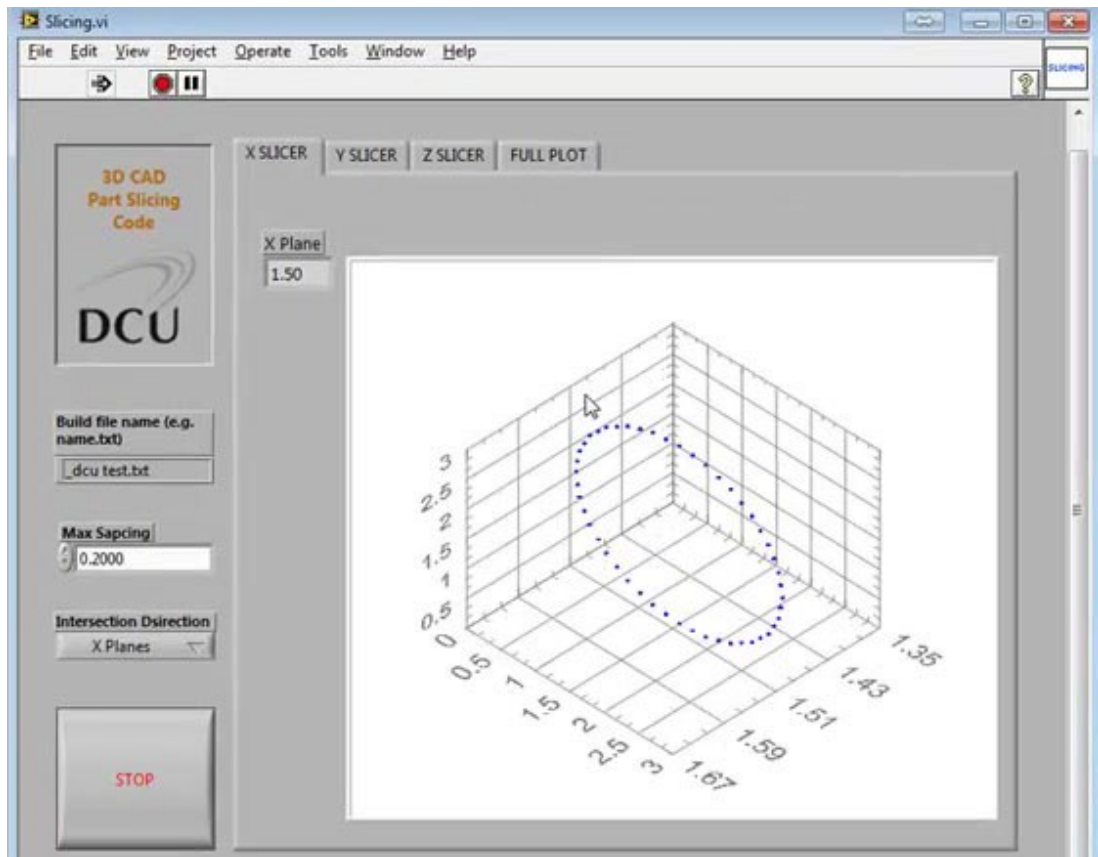
Figure 6-18: Sample planar contour of a sphere.

"3D Plot" State

This is the final state in the CAD processing code. A real-time computer simulation of the laser micromachining process is presented in this state. To test the CAD design under different conditions, it is necessary to run simulations on a computer. Furthermore, this virtual reality simulation is used to envisage the output pattern. The complete sliced sphere geometry treated in this illustration is shown in Figure 6-19.
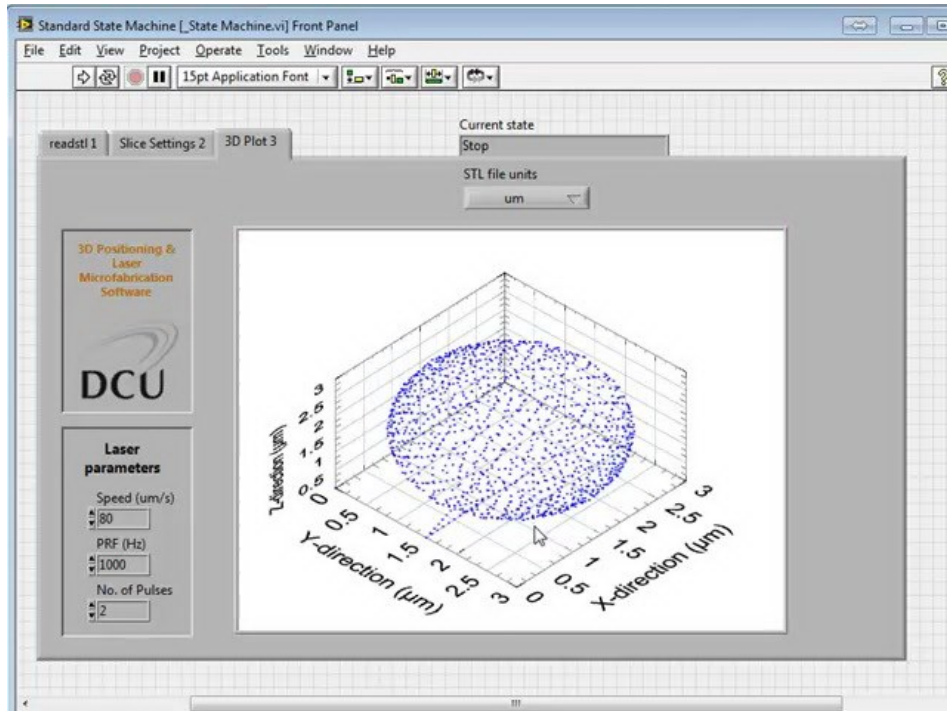
Figure 6-19: Full plot of the sphere.

After this state the code will stop and an output build file will be created. The generated planar contours give the fully sliced 3D CAD design, which can be written to a build text file. Each planar contour data points are clustered and a line with the word "PLANE" indicates the end of the planar contour data points, as shown in Figure 6-20.
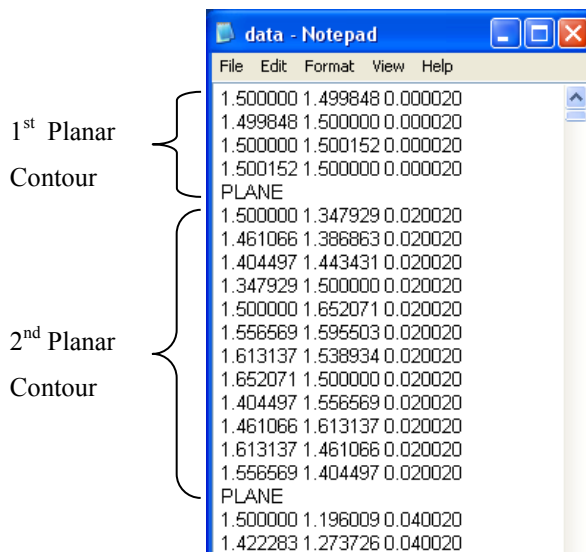
Figure 6-20: Part of the sphere build file.

XL

Appendix M – Automatic Positioning Control Concept

The following explains the automatic positioning control concept:

1. At the beginning, the 3D translation stage is at home position and the X, Y and Z coordinates are set to (0, 0, 0).
2. The first line from the build file is read, it contains X1, Y1 and Z1 (the coordinates of the first point).
3. If the line reads "PLANE" signifying the beginning of a new planar contour. Then go back to step 2. That means that all points of the same plane are considered.

Note1: Dx is the difference between the current and the previous x coordinates. This represents the distance in micrometres that the work piece has to be displaced in the x direction. Same applies to Dy and Dz for y and, z coordinates.

4. Dx, Dy and Dz are calculated in the first loop they equal (X1-X, Y1-Y, Z1-Z) these values resemble the displacement required in the x, y and z directions respectively.

Then the program enters into a structure that contains 3 sequences, each sequence performs the displacement in one direction. Taking the x direction for example:

i.   If Dx = 0 the code will jump to sequence-Y (displacement in Y direction), then sequence-Z.
ii.   A TRUE-Boolean signal (Enable X) is sent to DIO 1 which is the digital ON/OFF of X-axis motor driver.
iii. Depending on the sign of Dx, a Boolean signal (Direction X) is sent to DIO 2 which is the digital direction input on the motor driver.
iv.   Direct a pulse train at the calculated frequency, calculated from the frequency generator code, to Step Clock Input pin on the motor driver.

v.   When the X encoder digital output reading reached the required Dx, the code will stop the X-axis motor and reset the encoder digital output reading. Then code proceeds to sequence-Y.

5. When the displacement has taken place in the 3 directions, a TRUE-Boolean is sent to DIO 16 which is connected to the analogue control socket on the laser power supply unit. This signal fires the laser for a predetermined period of time, enough to develop the required damage in the processed sample.

6. The current X, Y and Z coordinates are saved in a shift register. They will take the place of the previous coordinates in the next loop. The code loops back to step 2.

7. This algorithm is repeated until the line read from the build file reads "eof", the program will terminate its operation.

Note2: In the Z planes case, the code will take the first z intersection plane and move the stage Dx then Dy to reach the first point then the laser fires. Afterwards, move the stage to next Dx then Dy to reach the second point then the laser fires again. When all the points are done in this plane, the code will process the second intersection plane and so on.

Appendix N - Nd:YVO$_4$ Laser System Motion Control Sub-Codes and GUI

Positioning Control Code

After the CAD design has been processed and converted from STL format into a build file, the design is ready to be machined. Two different codes were developed to control the 3D positioning translation stage using LabVIEW; namely automatic and manual. Both have almost the same and only differ in how the x, y, and z coordinates are fed into the positioning control code. The automatic code takes the x, y and z coordinates from the build file, as an array, and moves the 3D positioning translation stage (work piece) automatically according to them. A description of the automatic positioning control concept can be found in Appendix M. This code is almost finished and in final stage. Finalising the code is one of the future work objectives. On the other hand, the manual code, which will be discussed, is complete and working.

The mathematical relations discussed in section 0 were used in the developed control codes. These mathematical equations were used to calculate the appropriate frequency for driving the stepper motor that corresponds to an appropriate linear speed. Figure 6-21 shows the front panel of the control code of the 3D positioning translation stage.
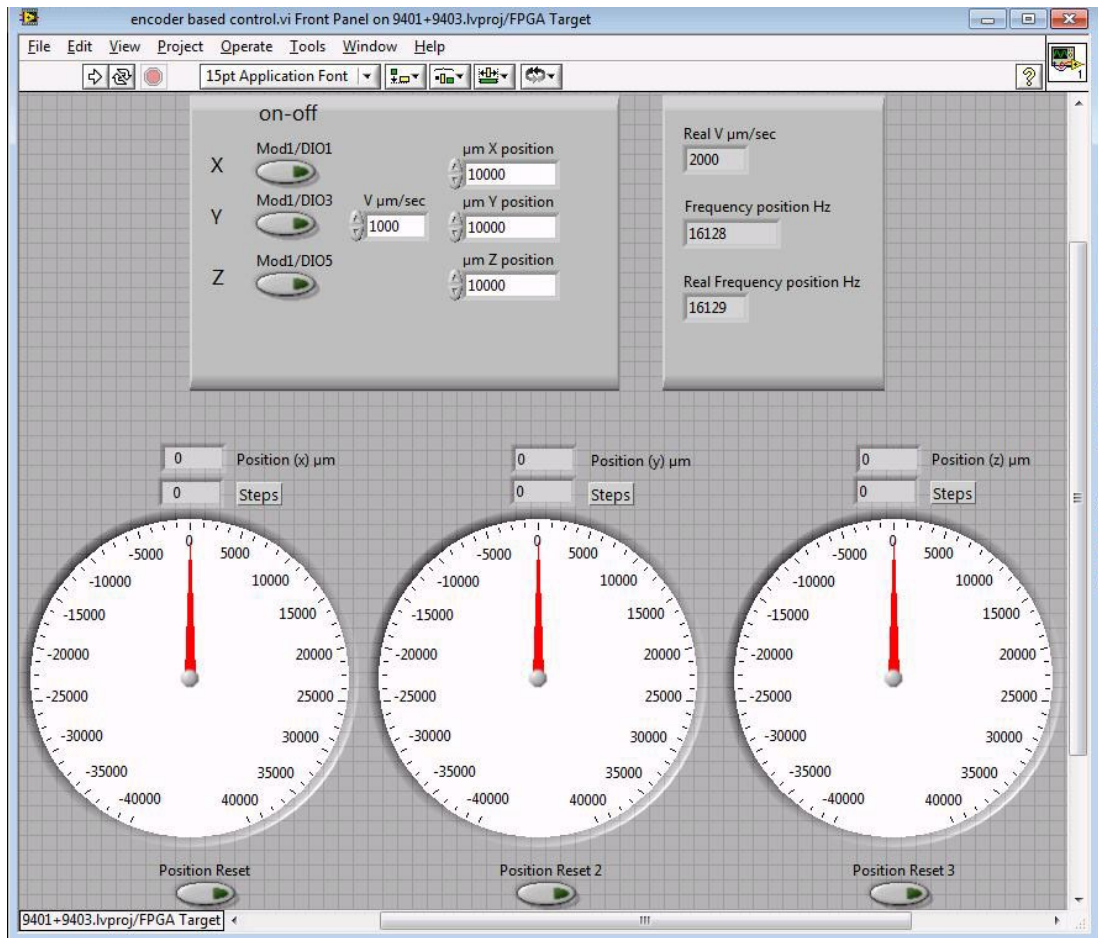
Figure 6-21: The front panel of position control code.

Motion Control Methodology

All inputs and outputs were digital from the two added NI I/O modules (NI 9401 and NI 9403). As shown in Figure 6-21, the inputs were three ON/OFF buttons for X, Y, and Z stages, the digital input of the linear speed, and the three digital inputs of the required movement on X, Y, and Z stages. On the other hand, the outputs were the digital display of the actual output values of linear speed and frequency, and the gauge and digital display of the actual distance travelled on the X, Y, and Z stages.

The whole code was developed to run using the real-time controller and the FPGA module, since only this combination is capable and powerful enough to generate the required clock frequencies for such a high-precision 3D positioning stage.

Reset Code

Upon running the motion control code and clicking the "run" button, the digital inputs, of X,Y, Z positions, and speed; V, are set to default initials values, as shown in Figure 6-21. However, all digital outputs will be reset, as shown in Figure 6-22. This "Reset" while loop structure will run first automatically for one time only and stop right afterwards.
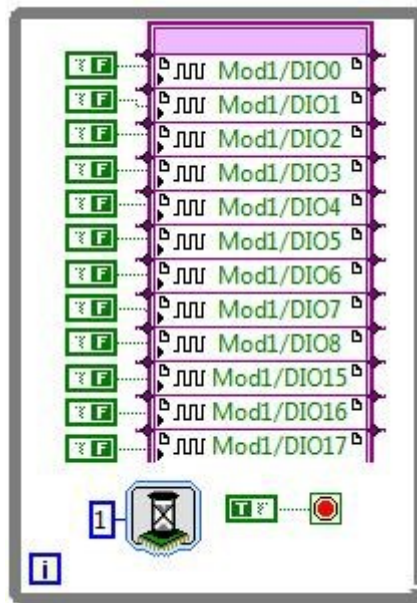
Figure 6-22: The block diagram of the "Digital outputs reset".

Frequency Generator Code

The frequency generator and validator code will run next. This code takes the linear speed value and finds the matching clock frequency of the real-time controller, using the mathematical relations discussed in section 0, to generate the proper continuous square pulse train. The continuous square pulse train is acquired by alternating a digital output between on and off, as shown in Figure 6-23.
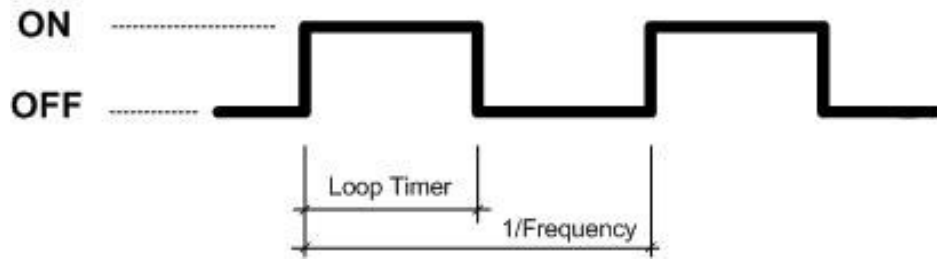
Figure 6-23: Digital output square pulse train.

This pulse train drives the three steppers motors on the 3D positioning translation stage, and determines the speed of the stage. Higher stage speed requires higher more pulses within a period of time, hence higher frequency. Then the code checks the generated pulse train and presents the actual output values of linear speed and frequency, as shown at the top right part of the Figure 6-21. The block diagram of the frequency generator novel code is shown in Figure 6-24.
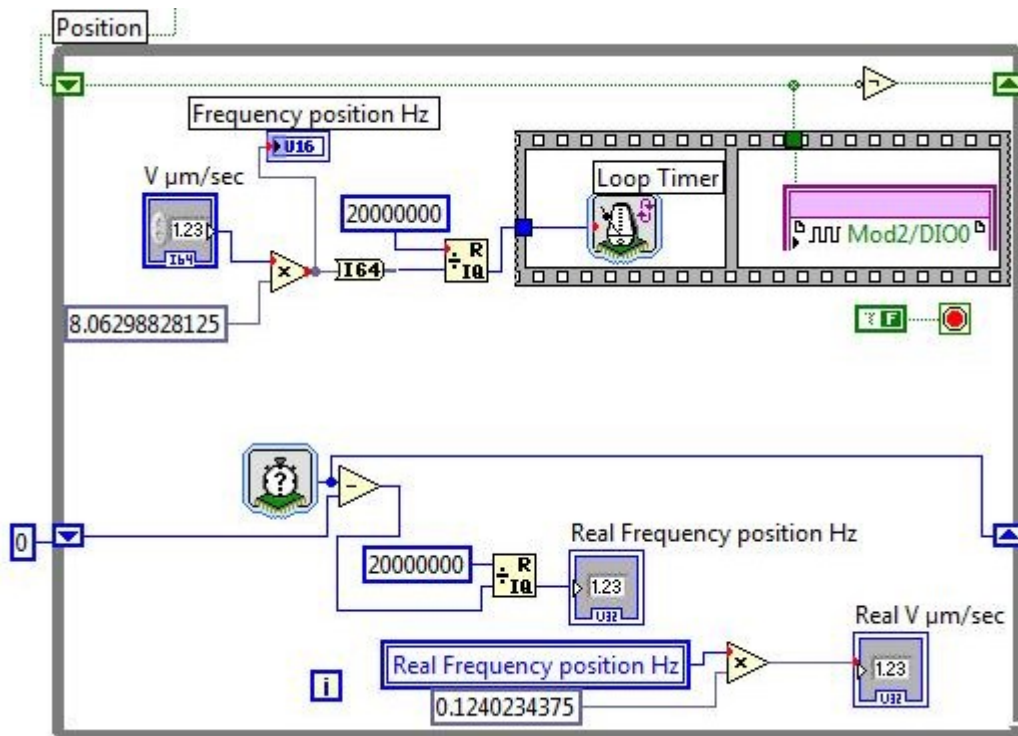
Figure 6-24: The block diagram of the pulse train (frequency) generator.

Encoder Feedback Code

Since there were three encoders, one for each axis, three identical codes were developed. Each one of the three codes has the related encoder inputs. The block diagram of the X-axis quadrature encoder code is shown in Figure 6-25. This code was developed to calculate the position of the related sub-stage (X, Y, or Z) based on quadrature encoder X4 encoding.
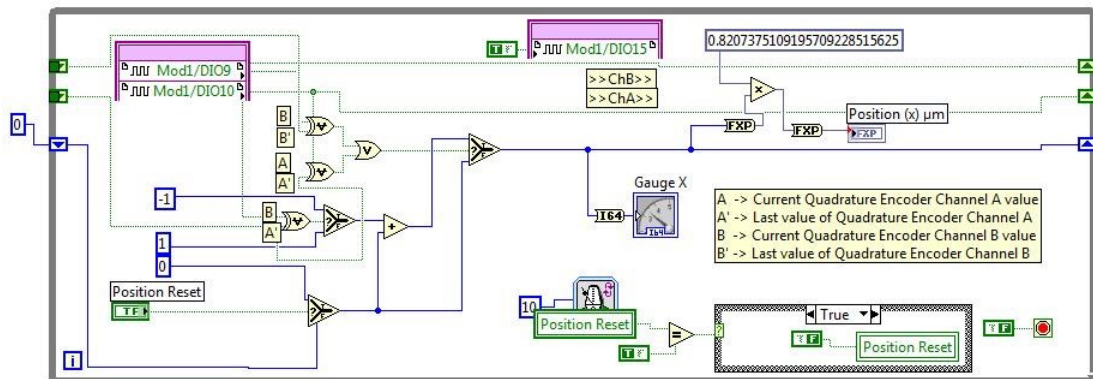
Figure 6-25: The block diagram of the quadrature encoder on X-axis.

In order to detect the change in state of the encoder output channel, the XOR is performed between the present and the previous values of each channel. An increment or decrement of the position counter will occur, if the state of either one of the channels has changed. To determine whether to increment or decrement the position, an XOR between the previous state of Channel A and the present state of Channel B is performed. If the previous state of Channel A is the same as the present state of Channel B then an increment is the position count has happened, and vice versa. In other words, if the pulse on channel A leads Channel B the position count is incremented by four, otherwise it is decremented by four. Figure 6-9 clearly illustrates this graphically.

Main Real-Time Position Control Code

Figure 6-26 shows the block diagram of the main code, where the real-time control is taking place. Each stepper motor has two inputs, one for turning it ON/Off, and another for direction. It was proposed that the positive direction of each stage is away

of its motor. The manual motion control methodology will be illustrated through an example of moving the 3D translation stage of 10 mm distance along the X-axis at 1 mm/sec linear speed.
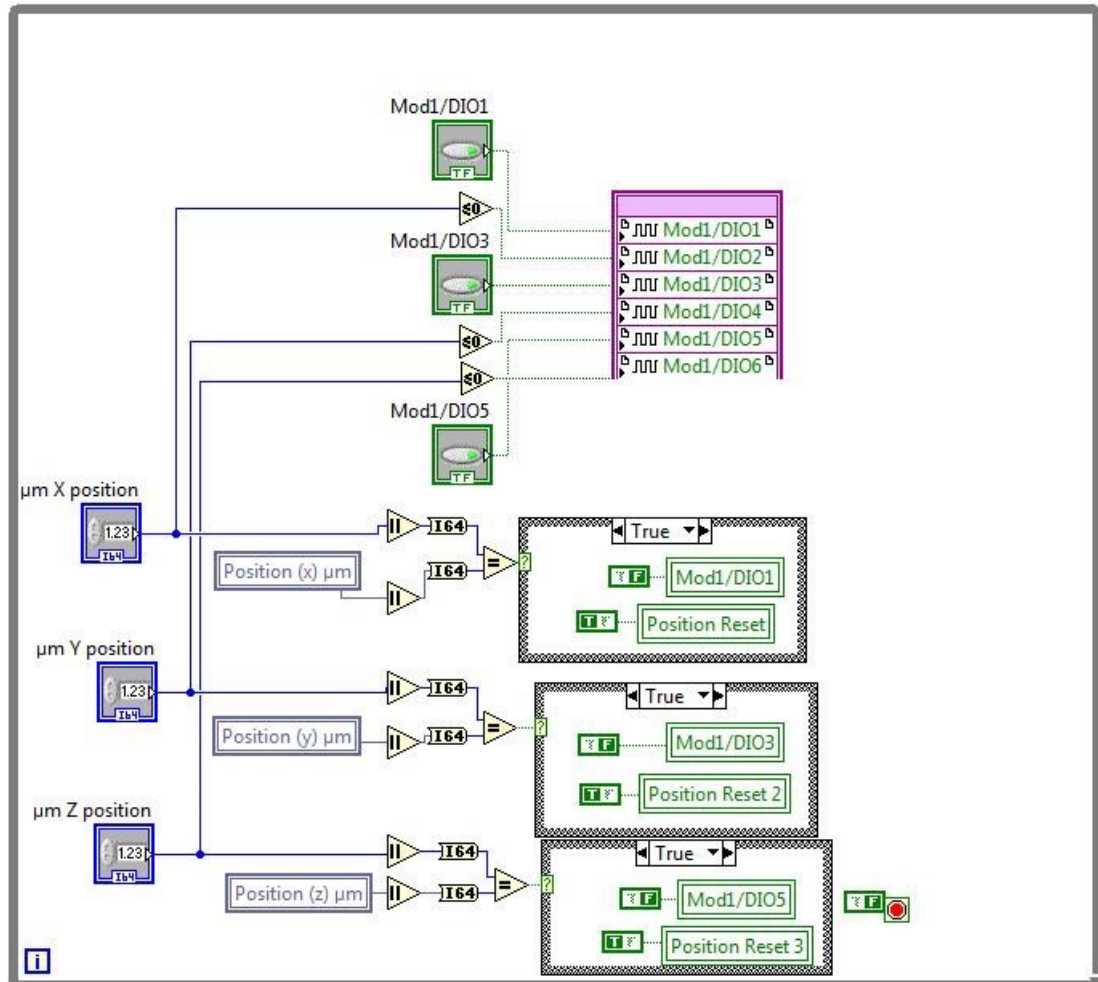
Figure 6-26: The block diagram of the main real-time control code.

After entering a value of 1000 μm/sec in the linear speed input box (V μm/sec) and 10000 μm in the X-axis required displacement (μm X position) and clicking the X ON/OFF button afterwards, the main position control code will be triggered. It will direct the pulse train, created in the frequency generator code, to the X-axis. The sub-Stage along the X-axis will move away from the motor, since the displacement has a positive value. Upon moving this stage, the related X-axis encoder feedback code will detect this movement and monitor this movement in real-time, till the stage travels the required 10 mm. This is carried out by comparing the actual travelled

XLVIII

displacement of the X stage with the value entered in the "X-axis required displacement" and when they equal, the code will reset the X ON/OFF automatically to OFF, and reset the reading of the X encoder digital display to zero.

Appendix O - Nd:YVO$_4$ Laser System Laser Control Sub-Codes and GUI

The development of a new code for controlling the laser operation was needed. The operation parameters of the T-Series laser power supply unit can be controlled via RS232 serial communication. This section shows the OEM serial communication syntax, which was utilised as a basis of the developed LabVIEW laser control code.

RS232 Communication Codes

Commands to the T-Series power supply consist of strings of semicolon terminated ASCII characters. For sending these commands, a LabVIEW serial port read-write code was developed. The default Serial Port Configuration settings were chosen according to in the laser catalogue. These settings were 9600 Baud, 8 Data Bits,1 Stop Bit, and No Parity Bits.

Initial Settings Code

This code runs automatically after clicking the run button of the laser control code. This code reads the initial values of the operation parameters from the laser power supply. The front panel of this code, as shown in Figure 6-27, appears in the middle of the screen. Then the code terminates and its front panel closes automatically.
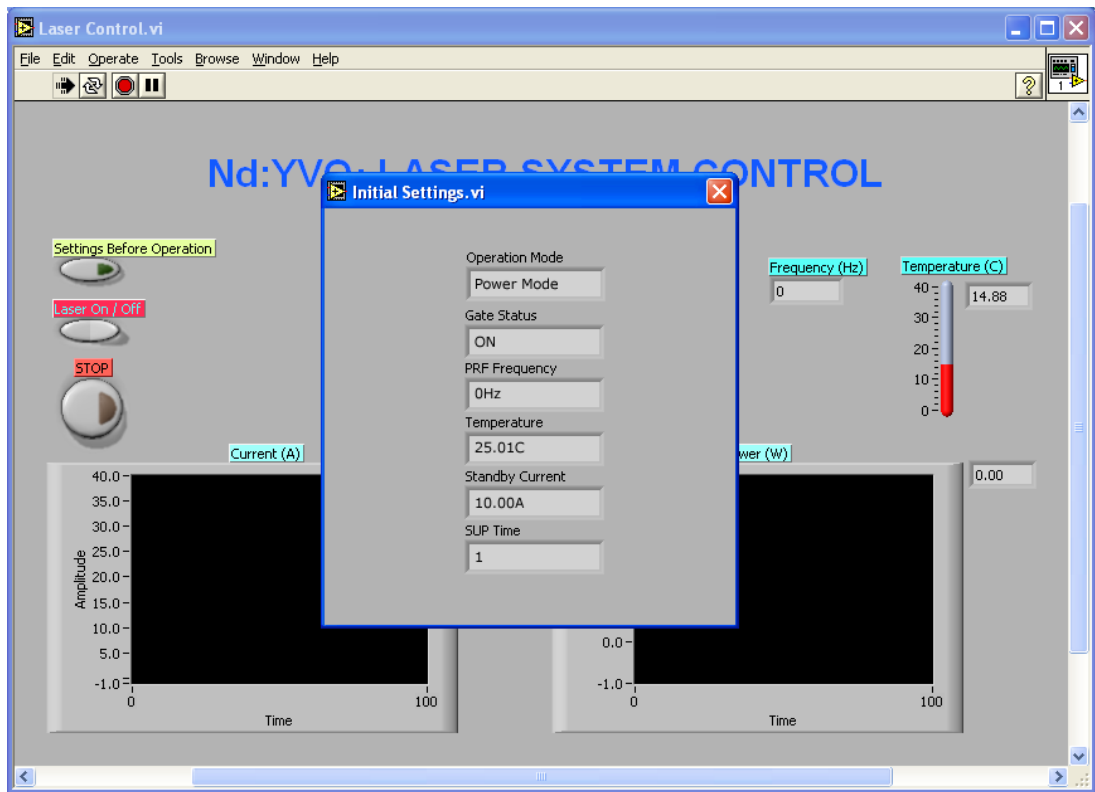
Figure 6-27: Initial settings code front panel displayed on stand up.

Settings before Operation Code

After the "Initial Settings" front panel closes, the laser main control code displays the current, power and temperature levels of the laser diode as shown in Figure 6-28.
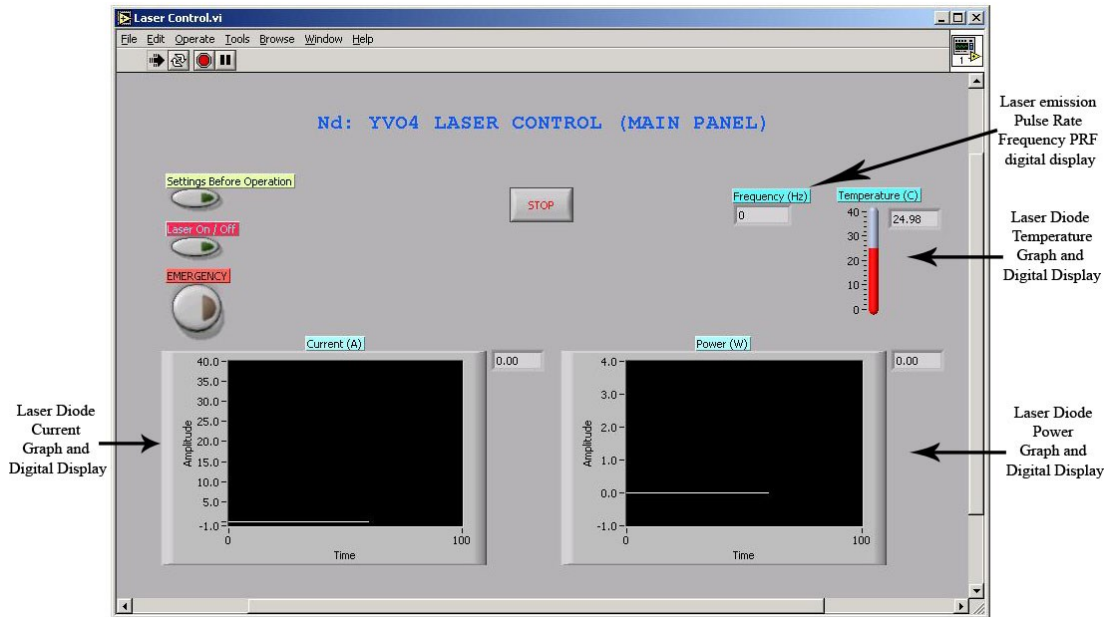
Figure 6-28: Laser control code front panel.

The laser emission parameters can be changed by clicking on the "Settings before Operation" button. When this button is clicked, the front panel of the "Settings" code will appear in the middle of the screen as shown in Figure 6-29.

On the left part of the front panel, the previously recorded initial parameters are listed to be a reference to the user. On the right, inputs of the same parameters are listed to allow any user required change of these setting. Since the diode is usually off before running the program, there are no initial values for the diode current and power. After the required change is entered the "EXIT" button should be clicked. Then the new settings are sent to the laser power supply unit via the serial port and the "settings before operation" front panel closes.
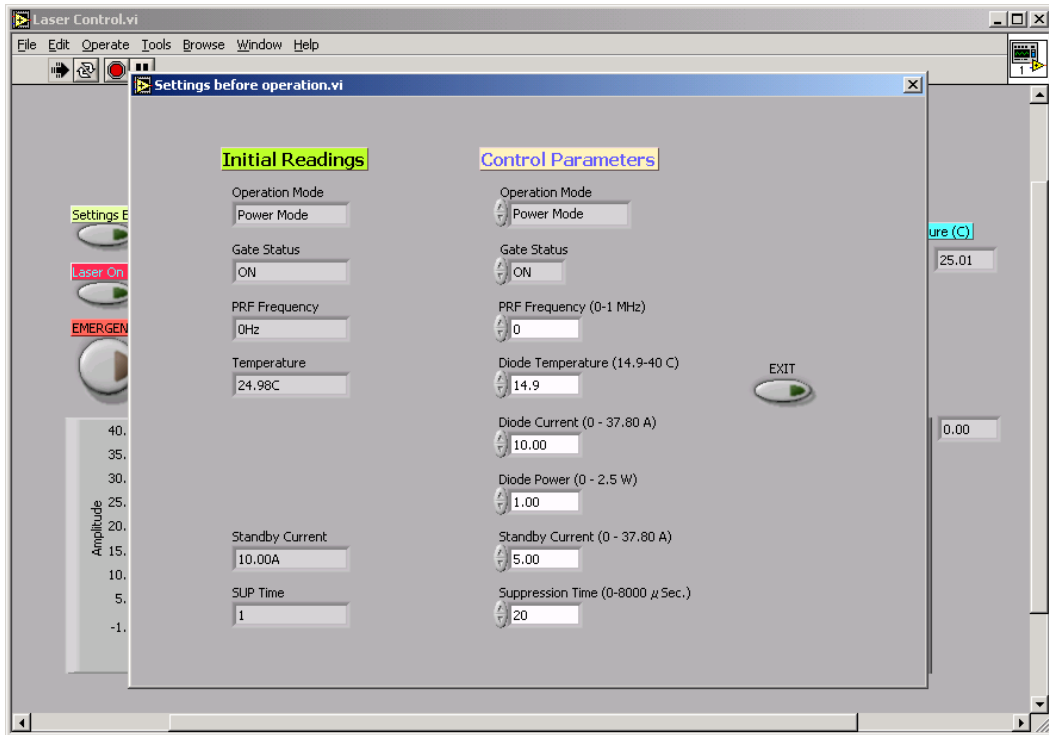
Figure 6-29: Front panel of the "Settings before Operation".

Laser Main Control Code

Before the laser emission takes place (running the main laser code), "Initial Settings" and "Settings before Operation" codes should run sequentially. The monitoring displays of the laser control front panel are presented in Figure 6-30. These monitoring displays are the diode current, power, and temperature graphs and digital displays, and the |laser emission Pulse Rate Frequency *PRF* digital display. On the other hand, the control buttons were the "Settings before Operation" button, the "Laser ON/OFF" button; which switches the laser emission ON or OFF, the "EMERGENCY" button; which terminates laser emission and program all at once if any unforeseen emergency should arise, and the "STOP" button; for normal termination of the program after the operator switches the laser diode off.
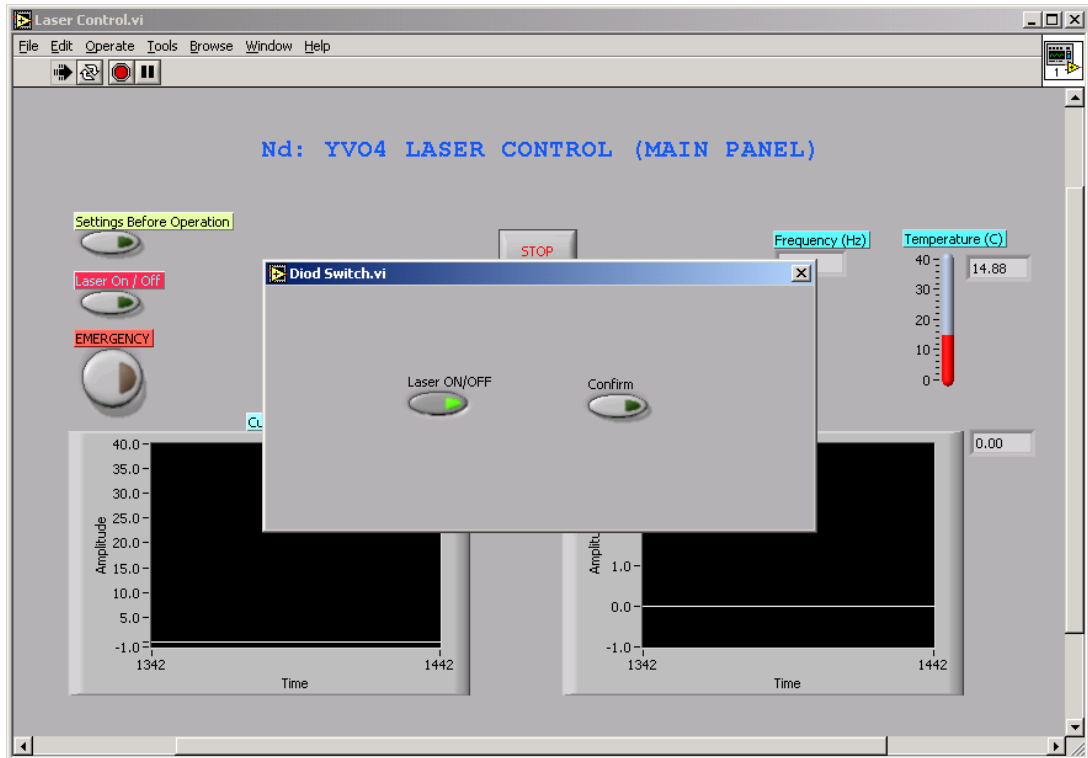
Figure 6-30: The front panel of the "Diode Switch" confirmation box.

To run the laser, the "Laser ON/OFF" button should be clicked. A confirmation box, in the middle of the screen, will appear, as shown in Figure 6-30. This confirmation is the front panel of "Diode Switch" code. Once the operator clicked the confirm button, the command was sent and the front panel closed. The laser emission then started at the predefined settings. Figure 6-31 shows the front panel of the laser main control code after the laser emission was turned on.
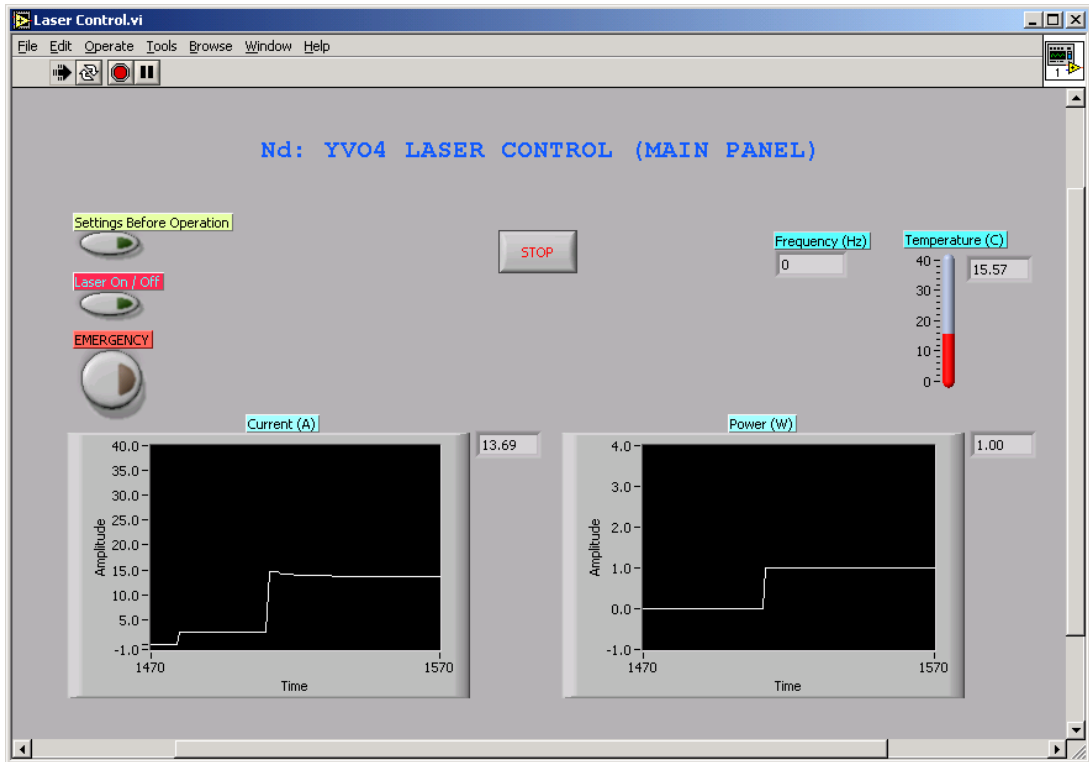
Figure 6-31: The front panel of the laser main control code while laser diode is ON.

Appendix P – aNETka Training Mode

aNETka training mode –Train aNETka code

Before any prediction or approximation can take place, aNETka has to be trained. This is achieved by running Train aNETka code.

After running the Train aNETka code, it will ask about the following configurations:

a) ANN configuration

This is a one-dimensional array. The top field means number of inputs, the middle fields are hidden layers and the most bottom field (does not have to be the last in the array) is the number of outputs.
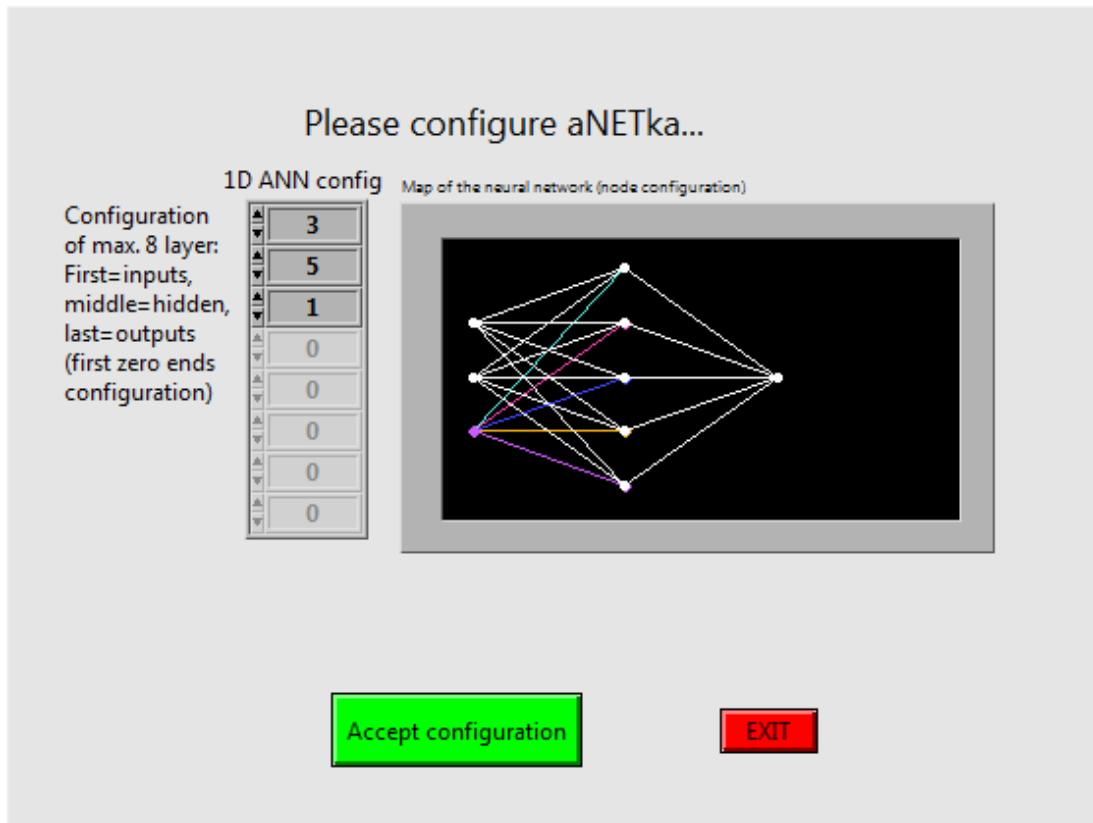
Figure 6-32: ANN configuration/architecture dialog box.

There have to be at least three layers. First zero in the array disables all the inputs below. For convenience, the graphical representation of chosen configuration is displayed on the right, as shown in Figure 6-32. After selecting required configuration green button should be pressed for acceptance. Pressing the red button will close the dialog box and terminate the main program. Figure 6-32 shows an ANN configuration of 3 input, eight hidden layers, and one output.

b) Activation function

One of three options can be selected: Linear, Sigmoid, and Tangent hyperbolic, as shown in Figure 6-33.
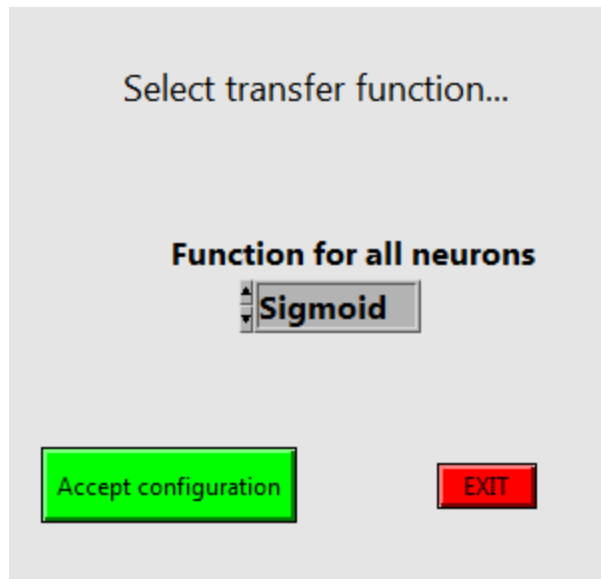
Figure 6-33: Activation function selection dialog box.

c) Input data

A standard windows dialog box will appear asking the user to specify the input data file. For the training mode, the input data must be saved in a suitable format: ASCII text spreadsheet file, tab delimited, with the first row containing captions for each column, as shown in Figure 6-34. The Microsoft Excel format or similar is unsuitable, however the file has to be exported to a text file (with .txt extension).
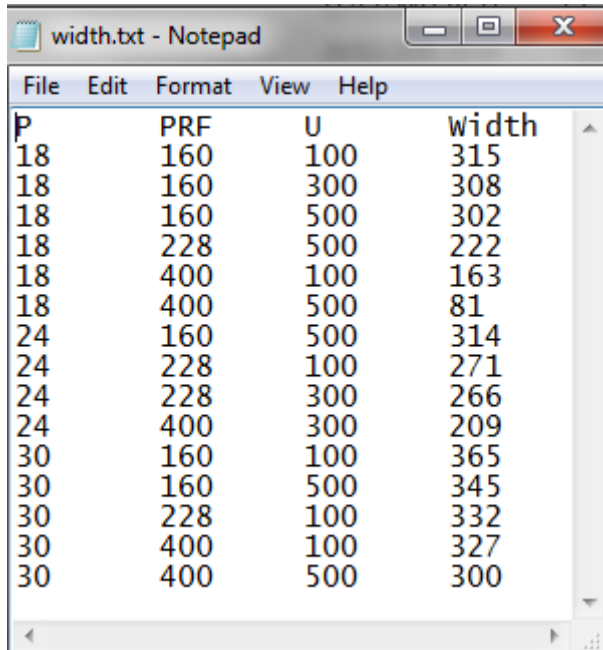
Figure 6-34: sample of aNETka input data file.

The program will ask for the input file. After opening, the content will be displayed as illustrated in Figure 6-35.
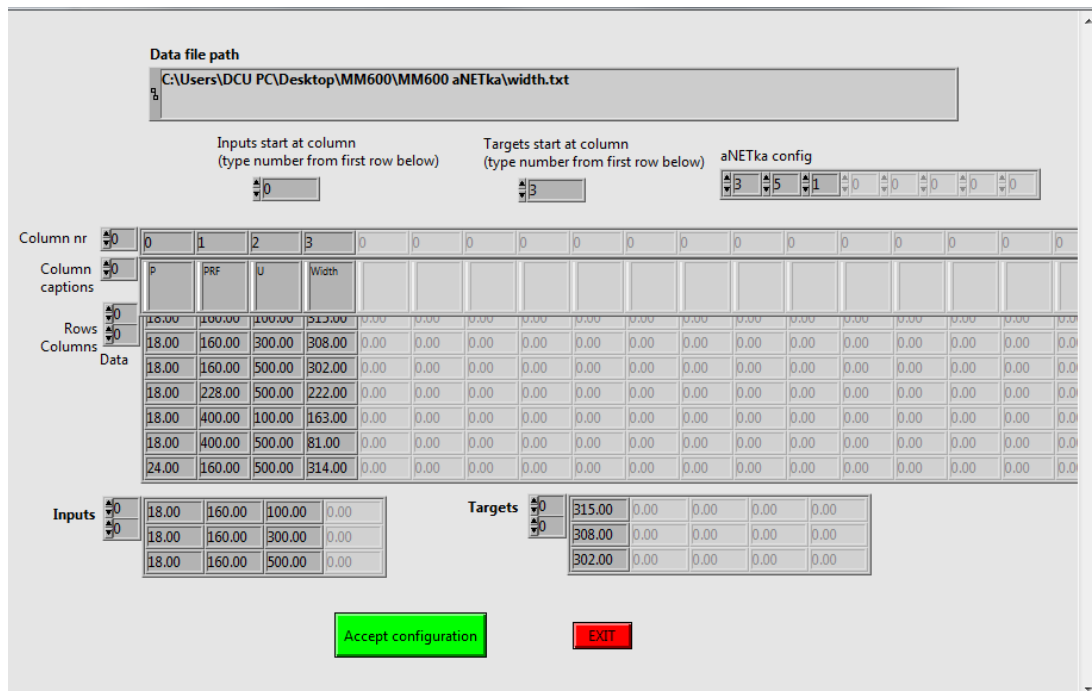
Figure 6-35: aNETka training mode input data dialog box.

The configuration of ANN in top right corner reminds about the number of required inputs and outputs. The largest table in the window contain all the data from the input file. First row contains all the indices for the data in order to simplify the selection. Second row contains all the captions and further rows contain the actual input and target data. The two indices above the largest table signify the beginning of the input and target columns. The choice of inputs and targets can be verified by the look at the two small tables at the bottom of the screen. If the data table is large, and does not fit in the screen, then the screen can be scrolled and/or the table can be scrolled, by clicking the index Columns on the left of the largest table.

d) Test cases

The number of test cases can be selected to any positive number that is less than the total number of cases, as shown in Figure 6-36.
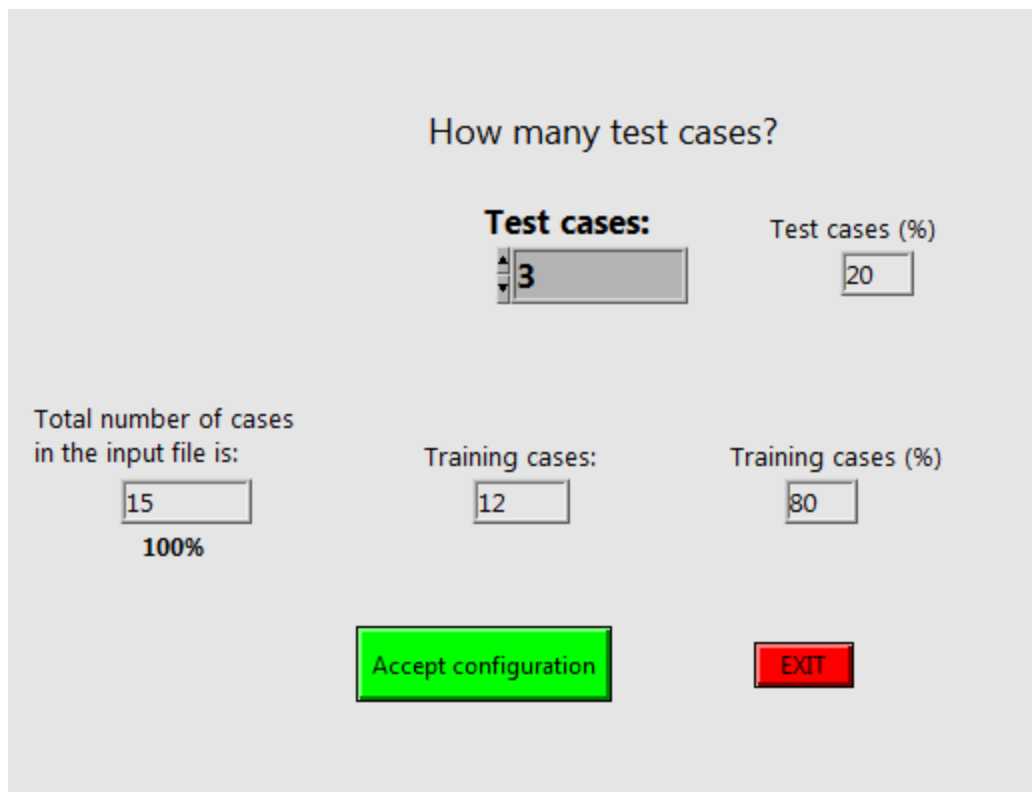
Figure 6-36: Number of test cases dialog box.

e) Learning rate

Learning rate parameter decides how quick the network should be able to learn; therefore, it should be set to some "medium" value. Since it is difficult to decide numerically when the learning rate should be increased or decreased, an automatic change of learning rate during the learning process was included in the aNETka code. Start the automatic learning rate after some predefined number of iterations aNETka Watch the learning process and Change the learning rate in order to decrease the ANN error. This change will be up to predefined maximum value and down to a predefined minimum value, as shown in Figure 6-37.
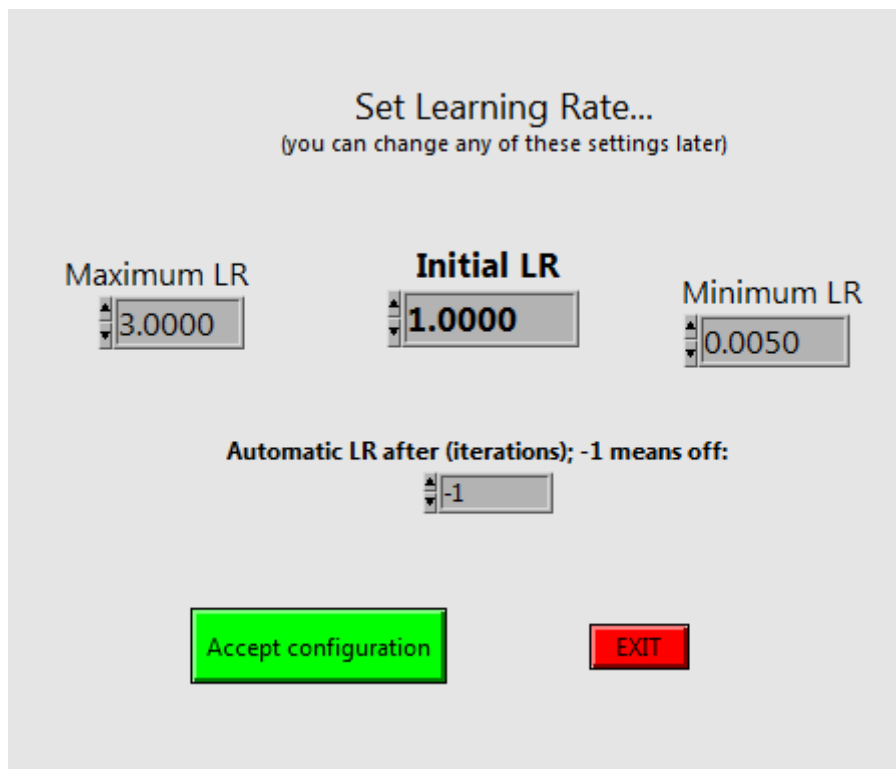
Figure 6-37: Set learning rate dialog box.

f) Iterations and other values.

In this dialog box, shown in Figure 6-38, there are four values to be set: total number of iterations to execute, total RMS percentage error (combined for all ANN outputs) at which the training should stop,

momentum and screen update (the screen will be refreshed after the number of iterations specified; small values may slow down the execution, large values will result in no control over the training process).
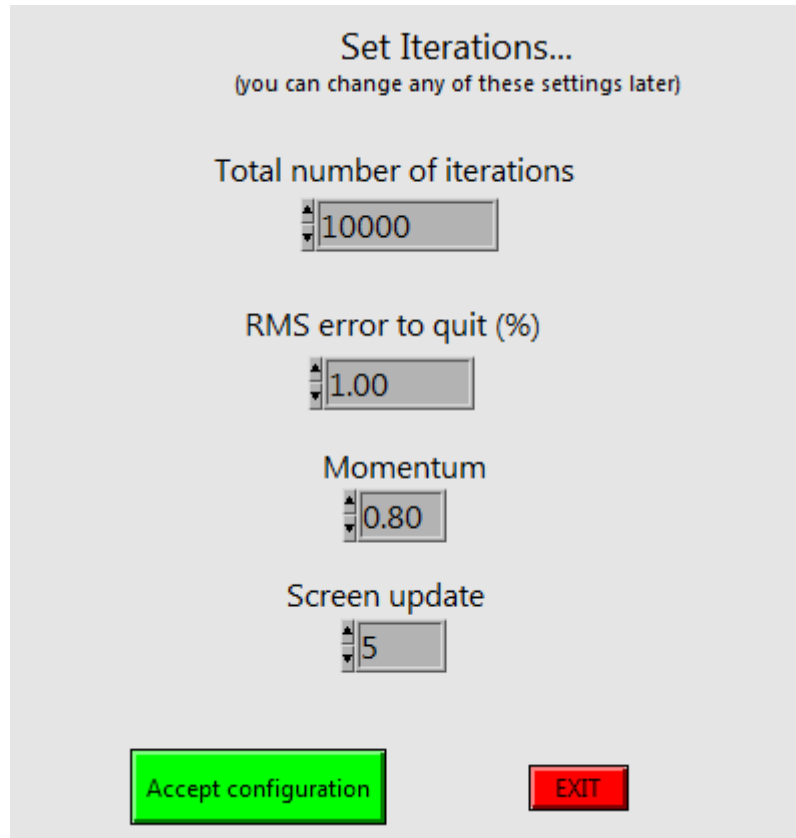
Figure 6-38: Set iterations dialog box.

After pressing the green button in the last dialog box, shown in Figure 6-38, the main screen of the training program will appear and training will start immediately. The main screen of the training program contains several indicators, as shown in Figure 6-39.
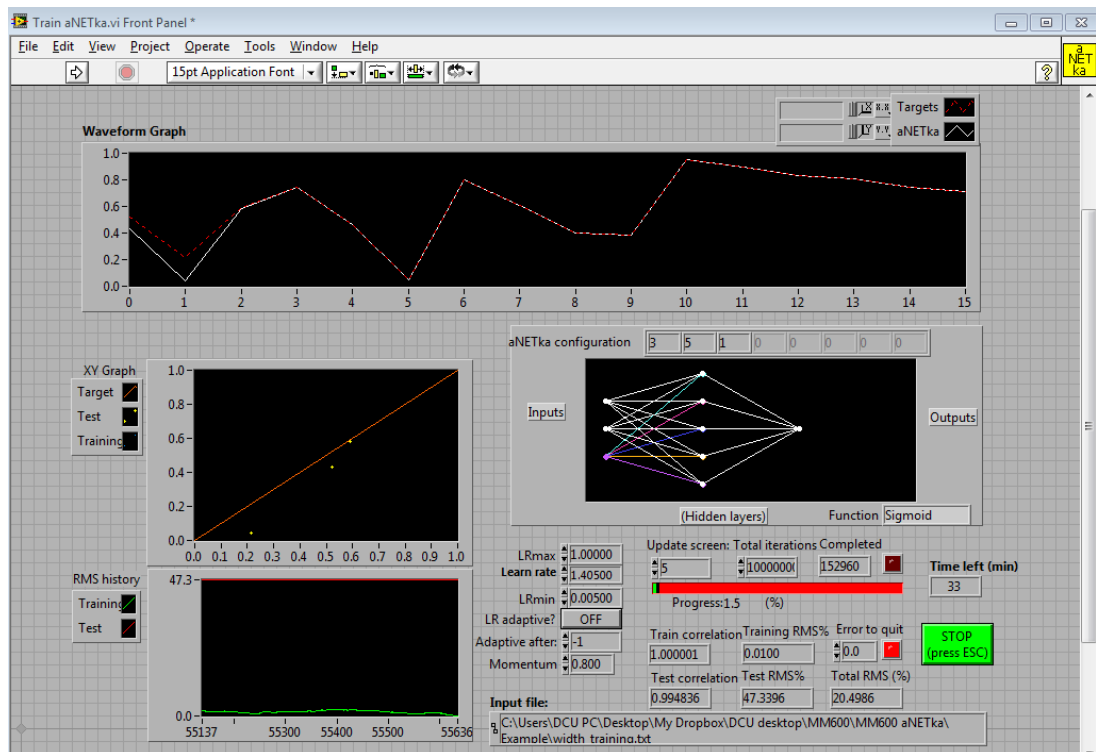
Figure 6-39: The main screen of the aNETka training code.

Apart from the values chosen during the configuration process described above the following are displayed:

- **Waveform graph:** This graph presents all the outputs of ANN as a single waveform graph. It provides quick visual representation of how far is the trained ANN from the target values. Any part of the graph can be easily zoomed by using the tools provided at the top of the graph.

- **XY Graph:** it presents the same data as the Waveform graph, but in different way (actual vs. predicted). The user can see not only all the data, but also how far the training cases (blue dots) are and the test cases (yellow spots) from the target values (red 45º straight line).

- **Function**: shows the utilised activation function.

- **aNETka configuration**: Graphical representation of chosen ANN configuration.

- **RMS history:** This is a running graph (maximum number of displayed iterations is 500), which presents the history of RMS % errors for training set (green curve) and test set (red curve). This graph allows user to decide if the ANN is being over-trained.

LXIII

- **Progress bar**: The bar displays the completed iterations as a green field, and the iterations to be completed as a red field. The percentage amount of iterations to complete is displayed just below the bar.
- **Correlation (train and test)**: The correlation gives an idea about the degree of "agreement" with the target data. Correlation equals to one denotes perfect match.
- **Train RMS % error**: The RMS percentage error is calculated for the training data. The RMS % error is calculated as:

$$RMS\% = \sqrt{\left(\sum\left[\left(\frac{y - \hat{y}}{y}\right)^2\right]\right)} \qquad \text{6-16}$$

Where y is the actual value, $\hat{y}$ is the predicted value, and N is the number of values.

- **Test RMS % error**: The RMS percentage error is calculated for the test data according to equation 6-16.
- **Total RMS % error**: The RMS percentage error is calculated for the whole set of data (training and test data) according to equation 6-16.
- **Red LED next to Iterations:** If the total number of iterations is reached, the program stops and this LED is turned on.
- **Red LED next to RMS to quit**: As above but indicates that the program was terminated because of RMS condition.
- **STOP button**: The program can be stopped at any time by pressing this button.

Note: The main program can stop because of three reasons: total number of iterations reached, RMS error reached or STOP button pressed. In any of those cases, the program terminates immediately and a standard Windows dialog box will appear asking the user to specify the desired name and location of the trained ANN output file for saving purpose. It is advised to save the output file name with a ".txt" extension; so that it can be easily open in order to check the developed ANN configuration. This file normally have information about the number of neurons, input file details, the captions of input and output data, ANN configurations, and

connections' weights [197]. Figure 6-40 shows a sample of aNETka trained file. These data will be used for the aNETka recall mode.

Figure 6-40: Sample of aNETka trained file.

Appendix Q - aNETka Batch Recall Mode

---

aNETka batch recall mode –Recall aNETKa (batch) code

In batch recall mode, the input data (for which the results/outputs are required) has to be saved in exactly the same format as in training mode. After running the "recall aNETka (batch)" code, two successive standard windows dialog box will appear asking the user to specify the trained aNETka file, and the input data file. Figure 6-41 shows an aNETka recall mode Input data sample. The outputs are calculated immediately for the input data set. The targets are not presented to the network, and they are not even selected in the configuration process.

Figure 6-41: aNETka Recall mode input data dialog box.

In order to simplify the data processing, the output file is copied to the same location, name of the new file is modified to contain string "(aNETka)", and the

calculated/predicted outputs are added as a last column in the file, as shown in Figure 6-42.

Figure 6-42: Sample of aNETka recall mode output/predicted data file.

The main screen of the aNETka recall mode, which contains waveform graph, configuration graph, configuration array and files paths, is shown in Figure 6-43.
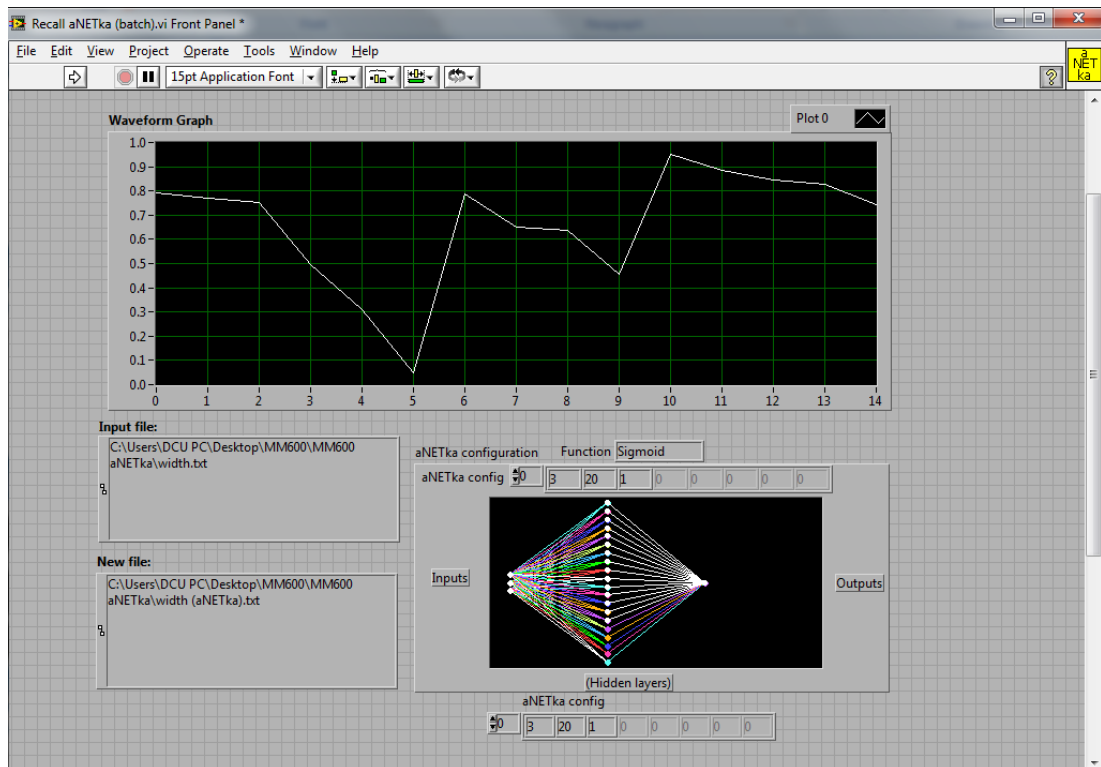
Figure 6-43: The main screen of the aNETka recall mode.

Note1: It is important that the data, with which the trained network is recalled, is within the limits used for the training.

Note2: the number of input values has to match the number of input values used in training. Greater number of inputs will be truncated down to required value, but lower number of inputs will result in completely wrong outputs from the ANN [197].